Charles University in Prague
Faculty of Mathematics and Physics

DOCTORAL THESIS

Ondřej Maršálek

Structure and dynamics of electronic defects in liquid water

Institute of Organic Chemistry and Biochemistry
Academy of Sciences of the Czech Republic

Supervisor: prof. Mgr. Pavel Jungwirth, DSc.

Study programme: Physics
Specialization: Biophysics, Chemical and Macromolecular Physics

Prague, 2012

First and foremost, I would like to thank my advisor Pavel Jungwirth for being the best thing that can happen to a young scientist. I would also like to thank my collaborators, from whom I have learned a lot. In particular, working with Frank Uhlig is always a pleasure.

I am grateful to my parents and family for their support and understanding and to Irene for being the best thing that can happen to a young man.

I hereby declare that this thesis is my own work, based on the sources and literature listed in the appended bibliography.

I understand that my work relates to the rights and obligations under the Act No. 121/2000 Coll., the Copyright Act, as amended, in particular the fact that Charles University in Prague has the right to conclude a license agreement on the use of this work as a school work pursuant to Section 60 paragraph 1 of the Copyright Act.

Prague, July 15, 2012 Ondřej Maršálek

CONTENTS

Title: Structure and dynamics of electronic defects in liquid water
Author: Ondřej Maršálek
Institute: Institute of Organic Chemistry and Biochemistry, Academy of Sciences of the Czech Republic
Supervisor: prof. Mgr. Pavel Jungwirth, DSc.
Supervisor's e-mail address: pavel.jungwirth@uochb.cas.cz

Abstract: In this thesis we present ab inito molecular dynamics simulations of two different electronic defects in water. Photoionization of liquid water produces a cationic hole, which undergoes ultrafast dynamics and forms the hydrated proton and the hydroxyl radical as its products. We study both the dynamics and spectroscopy of this process. The hydrated electron is a key intermediate in radiation chemistry of aqueous systems. We simulate its equilibrium properties in anionic water clusters as well as the dynamics of vertical electron attachment to cold and warm clusters. The hydrated electron reacts with a hydrated proton to form a hydrogen atom. We examine this reaction at a finite temperature in a larger cluster as well as in more detail in a smaller cluster. Because both of the electronic defects studied here are challenging open-shell species, we put emphasis on benchmarking and testing our computational setup. Six published articles are attached to the thesis.

Keywords: density functional theory, self-interaction correction, ab inito molecular dynamics, hydrated electron, cationic hole, water ionization, photoionization, vertical electron attachment

Název práce: Struktura a dynamika elektronických defektů v kapalné vodě
Autor: Ondřej Maršálek
Ústav: Ústav orgaincké chemie a biochemie, Akademie věd České republiky
Vedoucí doktorské práce: prof. Mgr. Pavel Jungwirth, DSc.
e-mail vedoucího: pavel.jungwirth@uochb.cas.cz

Abstrakt: V této práci předkládáme ab initio molekulárně dynamické simulace elektronických defektů v kapalné vodě. Fotoionizací kapalné vody vzniká kationtová díra, která ultrarychlým procesem reaguje na hydratovaný proton a hydroxylový radikál. Studujeme dynamiku i spektroskopii tohoto procesu. Hydratovaný elektron je klíčovým meziproduktem v radiační chemii vodných roztoků. Simulujeme jeho rovnovážné vlastnosti v záporně nabitých vodních klastrech i dynamiku vertikálního záchytu elektronu teplými a studenými klastry. Reakcí hydratovaného elektronu a hydratovaného protonu vzniká vodíkový atom. Tuto reakci zkoumáme za konečné teploty ve větším klastru a detailněji v klastru menším. Protože oba zde studované elektronické defekty jsou náročné systémy s otevřenou slupkou, klademe důraz na ověření nastavení výpočtů. K práci je přiloženo šest publikovaných článků.

Klíčová slova: teorie funkcionálu hustoty, selfinterakční korekce, ab initio molekulární dynamika, hydratovaný elektron, kationtová díra, ionizace vody, fotoionizace, vertikální záchyt elektronu

CHAPTER

ONE

INTRODUCTION

Ionization processes in aqueous systems play an important role in diverse contexts, including nuclear waste storage and remediation, exposure to natural radioactivity, or medical imaging and therapy [28].

1.1 Electron initiated processes

A cascade of processes is initiated by primary high-energy electrons passing through liquid water. As an electron ionizes the liquid, it creates secondary electrons, which have enough energy to cause further ionization. Due to the proximity of these events, ionization spurs are created in the liquid. Finally, low energy electrons are created, whose kinetic energy is below 10 eV and is thus not sufficient to cause ionization. These electrons can take part in further processes, causing damage. If they couple to the solvent and thermalize, they become hydrated electrons, e^-_{aq}. These hydrated electrons have a finite lifetime in water due to reactions with different solvated species. Even in neat water, they will react with dissolved oxygen gas, hydrated protons which are present due to the finite pH of water, or even water molecules themselves. Understanding the reactivity of hydrated electrons is important, because it is this quenching which prevents direct damage (e.g. to DNA) by the electrons and because some of the products may be undesirable or dangerous. Note that some authors use the term “low-energy electrons” to mean something different, namely low binding energy, even in the context of hydrated electrons [92].

While the full radiation chemistry of such systems is rich and complicated [28], we will focus on two species here — the hydrated electron and the cationic hole left after the removal of an electron.

1.2 Photoionization of liquid water

An important way to create the two species of interest is by a photon with sufficiently high energy — photoionization of water. Although such radiation can in general cause damage to hydrated species (such as DNA or proteins) by ionizing them directly, our focus here is indirect radiation damage — ionization of the solvent and subsequent chemical damage by the radicals created in that process. This is important, because the concentration of water in a typical aqueous system is significantly higher than the concentration of any solute. Strictly speaking, the term ionization means a complete removal of an electron from the system, but we use it here also for the situation in a condensed system where the electron gets ejected sufficiently far from the ionization site. A schematic view of water photoionization is as follows:

$$\begin{gathered} \mathrm{H_2O} + \hbar\omega \rightarrow \mathrm{H_2O}{\cdot}^{+} + \mathrm{e}^{-}_{\mathrm{CB}}, \\ \mathrm{H_2O}{\cdot}^{+} + \mathrm{H_2O} \rightarrow \mathrm{OH}{\cdot} + \mathrm{H_3O}^{+}, \\ \mathrm{e}^{-}_{\mathrm{CB}} \rightarrow \mathrm{e}^{-}_{\mathrm{aq}}. \end{gathered}$$

First, water gets ionized by an incident photon and a conduction-band (CB) electron is ejected. The cationic radical reacts by proton transfer with another water molecule, forming a hydrated proton and a hydroxyl radical. This radical is responsible for a large part of indirect radiation damage subsequent to photoionization of water. The ejected electron is initially delocalized. Assuming that it stays in the aqueous system and does not have enough energy for further ionization, it eventually couples to the solvent and localizes, forming the ground state hydrated electron.

1.3 Experimental studies

Let us now review a selection of experimental results relevant to this work. Measurements of properties of the hydrated electron have traditionally been done on anionic water clusters, as such a setup allows the use of techniques that require vacuum, notably photoelectron spectroscopy. These clusters are prepared using supersonic expansion, electrospray, or condensation in a cold buffer gas. The details of the preparation vary and influence the properties of the resulting clusters, but one common feature of all the techniques is that the clusters are always cold and solid.

The first photoelectron spectra of water cluster anions were reported by Coe et al. [15]. Measurements of different cluster sizes allow the extrapolation of vertical binding energies to the bulk limit, assuming an internally bound electron. Later experiments report several isomers of these clusters [111, 16], where each isomer is extrapolated separately, giving different values at the bulk limit. These isomers are assigned as a dipole bound electron for the most weakly bound isomer III, a surface bound electron assigned as isomer II and isomer I, which extrapolates to the vicinity of the expected bulk value of vertical binding energy. Isomers II and III are considered to be metastable by most authors. Although there is a temperature mismatch between the clusters and the liquid at ambient conditions, this discrepancy is usually not discussed. An experiment with a different setup, where the clusters come into contact with close to room-temperature buffer gas and are then kept in a trap at a T=10 K [65], reports a significantly lower abundance of the weakly bound isomers. Most recent results show that co-expansion with neon, rather than argon, increases the temperature of the clusters and changes the relative abundances of the different isomers when compared to the previous experiments — again, more internally bound electrons are observed [116]. For a representative plot of the measured binding energies, see Figure 2 of reference 65.

Recently, the liquid microjet technique has enabled the application of photoelectron spectroscopy to the surface of liquid water and aqueous solutions [115]. The first experiment to report the bulk vertical binding energy 3.3 eV from such a setup [90] also reported a long-lived feature at a low binding energy of 1.6 eV, attributed to an electron on the surface of liquid water. This measurement was motivated by the extrapolation of the surface state, isomer II, reported in anionic water clusters. Other microjet experiments soon followed, reporting bulk vertical binding energies of 3.2 eV [94], 3.4 eV [64] and 3.6 [89]. None of these have found evidence of weakly bound surface species, which has been attributed to differences in the experimental setup by some authors [1]. An experiment designed specifically for maximum surface sensitivity in order to search for these states found only a transient signal that disappears on the sub-picosecond timescale [11].

In search of the surface state, Sagar et al. have applied second harmonic generation spectroscopy to the surface of water in which hydrated electrons were created [82]. The similarity of signals in measurements with a free surface and with a surface coated in surfactants suggests that there is not a significant part of the excess electron density protruding out of the surface of water.

Gaudel et al. made an attempt to experimentally detect the presence of H_2O^+ and measure its decay time [29], but recent evidence, both experimental and theoretical, suggests that H_2O^+ was not generated with the setup used and that the measured signal was an artefact [118].

1.4 Computational studies

Computational treatment of ionization processes is challenging for several reasons. The open-shell nature of both positively and negatively charged electronic defects imposes restrictions on the electronic structure method that can be used. Issues with delocalized or quasi-degenerate states further complicate the situation. When electronic eigenstates get close in energy, it may be necessary to go beyond the Born-Oppenheimer approximation to treat the system properly.

If these challenges are overcome, or suitable approximations taken, computation can provide spatial and temporal resolution that is unavailable to experimental techniques. In preparing a simulation, one has full control over the system, which means that its composition as well as initial conditions can be set exactly as desired. Any measurable properties can be calculated at any chosen time, including the correlated evaluation of several properties for the same configuration, which tends to be problematic experimentally.

1.4.1 Hydrated electron

The hydrated electron is an inherently quantum species and it is thus not possible to evaluate its interactions using an empirical force field. Broadly, there are two possible approaches that one can take. In mixed quantum-classical calculations, the system is split into the molecular part, which is treated using an empirical force field, and the single excess electron treated fully quantum mechanically. This is effectively a QM/MM type of calculation, where the QM part contains only the one excess electron. Molecular dynamics of this system can be performed thanks to the relatively low computational demands of the approach. A pseudopotential must be parametrized for the interaction of the excess electron with the water molecules. The other approach is to use one of the many available quantum chemical methods, including density functional theory, Hartree-Fock theory, or post-Hartree-Fock correlated methods. Due to the computational demands of this approach, research in this areas has focused mainly on static idealized structures or optimizations of small clusters. Several groups have performed ab initio molecular dynamics simulations based on density functional theory.

Mixed quantum-classical models

The first pseudopotential calculations [84, 81] were done using path integral molecular dynamics for the excess electron. Later work uses a different parametrization of the pseudopotential and solves the Schrödinger equation of the excess electron on a Cartesian grid [102, 101]. This model comes to the conclusion that measured properties of anionic water clusters should be interpreted so that the electron resides at the surface of the cluster in all isomers [104]. A recent model includes self-consistent polarization of the water molecules and compares more favorably to quantum chemical calculations [49, 47]. In contrast with the previous one, it shows different positions of the electron within the cluster, with internal solvation becoming dominant as the temperature of the cluster is increased [47]. The parametrization procedure of the pseudopotential is similar in all cases — a Hartree-Fock calculation of a single water molecule — with the details and the analytic forms being different between the various models. The properties of the resulting hydrated electron turn out to be rather sensitive to these details, for example the coordination number varies between 4 and 6 [43]. This problem is exemplified by the most recent parametrization [57], which finds that the structure of the hydrated electron is strikingly different than reported previously. In this model, the electron does not reside in a polarized cavity, but rather overlaps with water molecules in a region where the density of the liquid is increased. This proposition has sparked heated discussions in the literature [103, 48, 58] as well as at conferences.

Quantum chemical calculations

Quantum chemical calculations, especially those using high quality correlated methods have the ability to describe the hydrated electron accurately. Here we mention only some examples from the rich literature on the subject. Due to the computational demands, this approach is usually limited to optimizations of idealized and small systems [87] or single-point calculations on geometries obtained using more affordable methods [88]. If high accuracy is required, second-order Møller–Plesset perturbation theory (MP2) may be insufficient [42] and higher quality (and higher cost) methods must be used [113]. For reactions and excited states of the hydrated electron, it might be necessary to consider multi-reference methods [91].

Ab initio molecular dynamics

Ab inito molecular dynamics shares with the above approaches the methods used for the evaluation of interactions, but goes further in the treatment of nuclei by performing molecular dynamics at a finite temperature. Density functional theory is the most common choice of electronic structure method, however, this is not a principal limitation but rather a practical matter — other quantum chemical methods are significantly more expensive.

Pioneering ab initio molecular dynamics simulations of the hydrated electron used the Car-Parrinello method and a relatively small periodic system of 32 water molecules [10, 9]. The properties of the excess electron at different thermodynamic states were explored.

Simulations of an anionic cluster of 32 water molecules have been done in collaboration with our group [26].

Recently, simulations of relatively large clusters have been performed, but the limited length of trajectories makes even rough convergence of the results somewhat questionable [7].

1.4.2 Water photoionization

Calculations of photoionization of water have focused on cluster systems. Pieniazek et al. have used the high-quality equation of motion method [55] to inspect the details of the water dimer and water pentamer cations [79, 78]. These calculation have also been used as a reference for the tuning of density functional methods, as will be discussed later in this thesis. The dynamics of the water pentamer after vertical ionization has been explored using a tuned range-separated density functional [63]. The same process has been studied also in the larger water 17-mer using the Hartree-Fock method [27]. The authors had to resort to using an excited stated of their Hartree-Fock calculation to force the cationic hole inside the cluster, which is not discussed in the paper.

1.5 Road map

The results presented in this thesis follow six papers by the author of the thesis and coworkers, which are referenced where appropriate and attached at the end of the thesis.

The rest of the thesis is organized as follows. In the next chapter, we will review the computational methods used for the presented work, looking at both nuclear motion and electronic structure calculation. As water is a disordered liquid at ambient conditions, it is important to capture finite-temperature effects appropriately. We use molecular dynamics to achieve that, as well as to obtain dynamical trajectories of non-equilibrium processes. Because calculation of the electronic structure of open-shell systems that contain an electronic defect is challenging, we dedicate a large part of the work to the development and benchmarking of computational setups that are both efficient and sufficiently accurate. In the two following chapters, we will proceed to show results of simulations of ionization of neat water. The removal of an electron from an aqueous system leaves behind a cationic hole. We will follow its dynamics in a condensed periodic system until the formation of its products — the OH radical and the H_3O^+ cation. If the ejected electron stays in an aqueous system and thermalizes, it forms the hydrated electron. We will look at this localization process in a cluster, which serves as a suitable proxy to the bulk process and also contributes to the understanding of the physics of anionic water clusters. To illustrate problems with the interpretation of cluster measurements, we compare the results to the same process at low temperatures, as cold clusters are what is usually available experimentally. Since the hydrated electron is a very reactive species and has a finite lifetime in aqueous solutions, it is important to understand its quenching. We look at the most elementary of these processes — the reaction with a hydrated proton which creates a hydrogen atom. The hydrated electron is also of great interest by itself and we examine its equilibrium properties at ambient temperature both in clusters and the aqueous bulk. In the last chapter, we will draw conclusions from the current work and suggest extensions and possible future directions.

CHAPTER

TWO

COMPUTATIONAL METHODOLOGY

In this chapter we will review the computational methods used in this work. Presenting all the material in full would require much more space than is available here. We will therefore restrict the discussion to the basic outline of each method, focus on aspects relevant for this work and refer to literature for details.

Broadly, there are two categories of computational methods that we need to consider. The Born-Oppenheimer approximation separates nuclear and electronic degrees of freedom in a way that leaves nuclear positions only as parameters in the electronic problem. Further, the quantum nature of atomic nuclei is neglected, as is appropriate for many situations at ambient conditions. Within this set of approximations, atomic nuclei are treated as classical particles moving on potential energy hypersurfaces corresponding to eigenstates of the electronic part of the system. Thus, firstly, we need to deal separately with the problem of obtaining reliable electronic energies and gradients with respect to nuclear positions for any given set of nuclear coordinates. Secondly, given these energies and gradients, we need to solve the problem of navigating the resulting potential energy hypersurfaces in a way that is computationally efficient and physically meaningful. These areas are to a large extent independent and the methods needed in each can be discussed separately.

In this work, we restrict our attention to dynamics on the ground-state potential energy hypersurface. Although, generally speaking, this is an approximation, for many processes it is entirely appropriate. For both electronic defects discussed in this thesis, the separation between the ground state and the first excited state is sufficient once the system is relaxed. Even though this is not the case in the initial stages of their dynamics (electron attachment or photoionization of water), we limit ourselves to the ground state even for these processes, as an approximation. Any treatment of non-adiabatic processes would complicate the simulations extremely and would require reliable calculation of excited states and non-adiabatic couplings. The ground-state electronic structure is challenging already and the quality of excited states could not be guaranteed without significant methodological development, which is far beyond the scope or time scale of the work presented here.

Depending on the desired result, the nuclear motion can have the form of optimization (local minimum, transition state or transition path) or dynamics at a finite temperature. Although a combination of methods was used in this work, a vast majority of the results was obtained using molecular dynamics, with optimizations being of an auxiliary character. Consequently, we will focus only on ab initio molecular dynamics in the following text and refer the reader to one of the standard texts for the treatment of nuclear optimization methods [17].

2.1 Molecular dynamics

The term "molecular dynamics" is used to describe a method, or rather a class of methods, to treat the motion of atoms and molecules at a finite temperature. Despite the name, it is perhaps more accurately described as "nuclear dynamics", as it is the motion of atomic nuclei that is central to the method, while their combination into molecules is secondary and given entirely by the approximation in which we choose to treat interactions. Here, we will focus exclusively on a classical description of atomic nuclei, although the term "molecular dynamics" is sometimes also used for quantum methods. At the heart of the method lie the equations of motion of classical mechanics. The positions of nuclei of a molecular system of interest are evolved in time from a chosen initial condition using these equations of motion, by solving them numerically. The resulting trajectory is then analyzed to obtain dynamic or thermodynamic properties of the system of interest, assuming that the system is ergodic. This is indeed the case for most systems of interest, especially in the liquid phase. A time average over the trajectory can then be identified with an ensemble average over the appropriate phase-space distribution $\rho(\mathbf{q},\mathbf{p})$. For a quantity $a(\mathbf{q},\mathbf{p})$ on phase space, we have

$$\langle a \rangle = \lim_{T\to\infty} \int_0^T \mathrm{d}t\, a(\mathbf{q},\mathbf{p}) = \frac{\int \mathrm{d}\mathbf{q}\mathrm{d}\mathbf{p}\, \rho(\mathbf{q},\mathbf{p}) a(\mathbf{q},\mathbf{p})}{\int \mathrm{d}\mathbf{q}\mathrm{d}\mathbf{p}\, \rho(\mathbf{q},\mathbf{p})}. \tag{2.1}$$

Systems with high barriers or glassy behavior need a more careful treatment than is provided by direct molecular dynamics.

Although all the properties of the system are determined by the interaction — the shape of the potential energy hypersurface on which the dynamics occurs — in this section we will simply assume that we have a suitable method to obtain it for our system of interest and focus only on the nuclei.

While this simplified outline of the method might seem straightforward, it easily gets rather complicated when one needs to consider different types of boundary conditions, temperature and pressure coupling, constraints, and the numerical properties of the methods, all of which are important in practical calculations. Literature covering the molecular dynamics method includes references 2, 25, 100.

2.1.1 Types of molecular dynamics simulations

There are two principal types of molecular dynamics simulations that one can perform. In non-equilibrium simulations, a perturbation is introduced to the system such that it undergoes dynamics that is then analyzed. This perturbation can either take the form of an initial condition or a continual influence, for example an external field. In equilibrium simulations, the system evolves freely, sampling an equilibrium ensemble at a given thermodynamic state point. From such simulations, we can extract both thermodynamic quantities and equilibrium dynamic properties, for example time correlation functions.

2.1.2 Initial conditions

To start a molecular dynamics simulation, an initial condition is needed. That is, the positions and velocities of all atoms need to be specified.

For equilibrium simulations, velocities v of atoms of mass m are usually drawn at random from the Maxwell distribution at temperature T,

$$f(v) = \sqrt{\frac{m}{2\pi k_B T}} \exp(-\beta m v^2/2). \tag{2.2}$$

Positions are either taken from a previous simulation or are generated in some systematic way, for example on a regular grid. An equilibration simulation must then be performed before production data is collected.

For non-equilibrium simulations, initial conditions are usually taken as a sample from a previous equilibrium simulation and supplemented with a suitable perturbation that will take the system out of equilibrium.

2.1.3 Boundary conditions

Finite systems do not need any special treatment of boundaries, they simply use open boundary conditions. The simulation of condensed systems would, however, be impractical with finite systems, as they would have to be very large to minimize surface effects. For these reasons, periodic boundary conditions are used. In general, the atoms of the system are placed in a rhomboid and the distances between them are measured as if the central box was replicated infinitely in all directions and only interaction with the nearest replica of each atom was considered. For short-ranged interactions, including only the direct interaction over this distance is sufficient, which is called the minimum image convention.

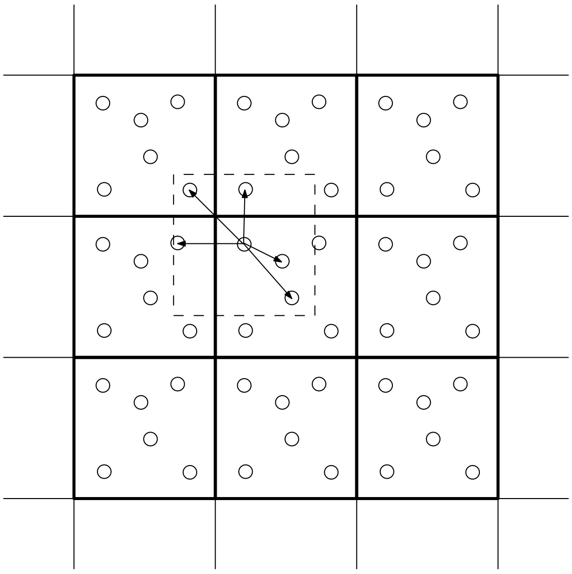

Figure 2.1 An illustration of periodic boundary conditions in two dimensions for a system of six particles. The central box is drawn together with its first eight replicas. Distances of one atom to the nearest replicas of all the other atoms are shown.

For long-ranged interactions, like electrostatics, extra effort is needed to calculate a sum over the periodic replicas. The coordinates of the atom can, but do not have to, be returned to the primary box at regular intervals. As long as distances are measured correctly, it is of no consequence for the simulation and only plays a role for the output and visualization of atomic positions. Figure 2.1 shows an illustration of periodic boundary conditions in two dimensions. Periodic boundary conditions can also be applied only in one or two directions, allowing simulations of wires or slabs, which are useful for the study of interfaces. For some simulations, special boundary conditions are needed. These include fixed layers of atoms for the simulation of surfaces of solids or slip boundary conditions for the simulation of shear flow.

2.1.4 Constraints

Some molecular dynamics simulations utilize constraints which fix certain internal degrees of freedom at their equilibrium values. Typically, covalent bond lengths and certain angles are constrained. This is well justified for covalent bonds in their ground state and allows for a simpler evaluation of interactions as well as for an increase of the integration time step, as it removes the highest frequency motion from the system. In this work, no constraints were used.

2.1.5 Thermostats and barostats

Simply evolving the system in time using classical equations of motion results in constant-energy trajectories. While this might be appropriate for non-equilibrium simulations, thermodynamically, such trajectories sample the microcanonical ensemble, in the context of molecular dynamics usually called NVE. Often, we are interested in the thermodynamics of a canonical ensemble, either at constant volume (NVT) or at constant pressure (NpT). Approaching these with a microcanonical ensemble would require prohibitively large simulations and it is much more practical to sample canonical ensembles directly. This requires extra effort in the form of modified equations of motion that will sample such ensembles.

Thermostats provide temperature coupling and maintain a defined average temperature by modifying velocities of atoms, barostats provide pressure coupling and maintain a defined average pressure by modifying the size of the simulation cell. Pressure coupling is only applicable in simulations with at least one periodic dimension, it is meaningless for simulations of finite isolated systems, for example molecular clusters. The basic ideas of thermostats and barostats are the same. One possible way to do either is the extended ensemble approach. Extra degrees of freedom are introduced to the system and coupled to the atomic degrees of freedom. Total energy of the extended system is conserved, while the energy of the original system fluctuates in such a way that a constant temperature and/or pressure is maintained. This follows the way the canonical ensemble is often derived in thermodynamics. The Parrinello-Rahman barostat [74] is an example of a pressure coupling method based on this approach, while the Nose-Hoover thermostat [46] and its more robust extension Nose-Hoover chains [68] are examples of temperature coupling methods. Another possibility is the introduction of a stochastic process that modifies the appropriate variables. Numerical propagators of Langevin dynamics make use of this approach for thermostatting [105]. The Andersen thermostat [3] provides a very simple way to sample the canonical ensemble. At each molecular dynamics step, each atom is, with a certain probability, reassigned a new velocity drawn at random from the Maxwell distribution. A combination of velocity rescaling with a stochastic process results in a particularly efficient and robust thermostat which, unlike other velocity rescaling thermostats, samples the canonical ensemble correctly [12]. This method is usually called CSVR, for “canonical sampling through velocity rescaling”.

2.1.6 Numerical solution of equations of motion

The equations of motion, including any thermostats or barostats and constraints, must be solved numerically, with forces on individual atoms provided as input. Although numerical mathematics provides a plethora of methods, certain requirements restrict the numerical propagators used in practice to a narrow class. Because the evaluation of interaction by far dominates a typical molecular dynamics simulation, it is crucial that the method of choice needs only one evaluation of forces at each step. Further, methods that are at least approximately symplectic have certain desirable properties, notably time reversibility, which make them suitable for molecular dynamics simulations.

The widely used Verlet [112] and velocity Verlet methods [93] and their equivalent leap frog method [24, 2] belong to this category, although originally they were not derived with symplecticity as a target, but rather simply from a Taylor expansion. In the case of the velocity Verlet algorithm, we get for each time step

$$\mathbf{x}(t+\Delta t) = \mathbf{x}(t) + \mathbf{v}(t)\Delta t + \frac{\mathbf{F}(\mathbf{x}(t))}{2m}\Delta t^2, \tag{2.3}$$

$$\mathbf{v}(t+\Delta t) = \mathbf{v}(t) + \frac{\mathbf{F}(\mathbf{x}(t+\Delta t)) + \mathbf{F}(\mathbf{x}(t))}{2m}\Delta t. \tag{2.4}$$

Later formulation based on the Trotter expansion of the formal exact solution of the equations of motion expressed using the Liouville operator rederives these traditional methods and also shows the way to more advanced propagators [99, 67]. These include multiple time step methods as well as robust treatment of temperature and pressure coupling in the presence of holonomic constraints [117].

To sketch the basic idea of this approach, let us start with the Liouville operator L, which is given by

$$iL = \{\ldots, H\} = \dot{\mathbf{q}} \cdot \nabla_{\mathbf{q}} + \dot{\mathbf{p}} \cdot \nabla_{\mathbf{p}} \tag{2.5}$$

and can be used to express the time evolution of an arbitrary function on phase space,

$$\dot{f}(\mathbf{q}, \mathbf{p}) = \{f, H\} = iLf(\mathbf{q}, \mathbf{p}). \tag{2.6}$$

Solving this equation formally, we get

$$f(t) = \exp\left(iL(t-t_0)\right) f(t_0) = U(t-t_0)f(t_0). \tag{2.7}$$

Because the two terms in L do not commute, the exponential has to be approximated using Trotter expansion. There are many ways to do this and they will produce different numerical propagators. As an example, the above velocity Verlet propagator can be obtained as

$$U_{velocity\ Verlet}(\Delta t) = \exp\left(\frac{i\Delta t}{2}\dot{\mathbf{p}} \cdot \nabla_{\mathbf{p}}\right) \exp(\Delta t \dot{\mathbf{q}} \cdot \nabla_{\mathbf{q}}) \exp\left(\frac{i\Delta t}{2}\dot{\mathbf{p}} \cdot \nabla_{\mathbf{p}}\right). \tag{2.8}$$

Using a good numerical propagator that keeps any conserved quantities constant is crucial for the quality of the whole simulation. The time step of this numerical integration must be chosen based on the physical properties of the underlying potential energy hypersurface so that the numerical integration is stable.

2.2 Density functional theory

Density functional theory is an electronic structure method that uses electron density in real space as the fundamental quantity. Although approximations based on electron density have been known since the early days of quantum mechanics [96, 23], it was not until 1964 that this approach has received significant attention. Hohenberg and Kohn have published a set of theorems, showing rigorously that the ground-state wavefunction of the system is a unique functional of the density [45]. As a consequence, all other properties, notably the energy, are also functionals of the density. A paper by Kohn and Sham that followed [53] provided a formulation that includes a very good approximation for the kinetic energy term, making practical calculations possible. Although the exact full functional is unknown, simple approximations to the exchange-correlation part were discovered quickly and enabled surprisingly accurate electronic structure calculations at a modest computational cost. Nowadays, Kohn-Sham density functional theory is the standard for many applications, especially for larger and condensed systems where other methods are either unavailable or prohibitively computationally expensive. Research of new approximate exchange-correlation density functionals is very active, as is development of new efficient computational methods of solution of Kohn-Sham equations. Details of density functional theory and its computational realization can be found for example in references 73, 52, 13, 17.

2.2.1 Kohn-Sham equations

The basic contributions to the total electronic energy functional are the kinetic energy term $T[n]$, the external potential term (atomic nuclei and any external fields) $V[n]$, and the electron-electron interaction energy $V_{ee}[n]$, which is usually split into the classical electrostatic self-energy $V_H[n]$, sometimes called Hartree energy, and the non-classical exchange-correlation energy $V_{XC}[n]$:

$$E[n] = T[n] + V[n] + V_{ee}[n] = T[n] + V[n] + V_H[n] + V_{XC}[n]. \tag{2.9}$$

The very first term constitutes the major problem of density functional theory in this formulation, as it is not known. Various approximations exist and are used in the context of orbital-free density functional theory even today, but are not very reliable by the standards of quantum chemistry.

The Kohn-Sham formulation improves on this by introducing a very good approximation for the kinetic energy term, at the cost of a more complicated representation of the system. Specifically, it maps the real system to a fictitious system that has identical electron density, but is non-interacting and electrons occupy individual orbitals. The density is simply

$$n(\mathbf{r}) = \sum_i f_i \langle \psi_i | \mathbf{r} \rangle \langle \mathbf{r} | \psi_i \rangle, \tag{2.10}$$

where f_i are occupation numbers. For the equivalence, the system needs an effective potential that will produce, as its eigenstates, orbitals that in turn produce a density that is identical to that of the real system. It is important to keep in mind that these orbitals are entirely auxiliary and the Kohn-Sham formulation says nothing about their relation to the real system, other than through the density. The kinetic energy of the non-interacting system can be written in terms of the individual orbitals as

$$T_s[n] = \sum_i f_i \frac{p^2}{2m} |\psi_i\rangle, \tag{2.11}$$

which is a very good approximation to the full kinetic energy. The remaining correlated kinetic energy, $T_c = T - T_s$, is included in the exchange-correlation functional in the Kohn-Sham formulation, making the energy functional

$$E[n] = T_s[n] + V[n] + V_H[n] + V_{XC}^{KS}[n]. \tag{2.12}$$

To satisfy the density-matching condition, the effective potential must be set to

$$v_s = v + v_H + v_{XC}, \tag{2.13}$$

where the terms on the right-hand side are potentials of the corresponding energies. The resulting Kohn-Sham equations for the orbitals then have the form

$$\left[\frac{p^2}{2m} + v_s \right] |\psi_i\rangle = \epsilon_i |\psi_i\rangle, \tag{2.14}$$

where ϵ_i are the eigenvalues of the orbitals $|\psi_i\rangle$ which reproduce the real density.

Without going into details, we note that there exists also a generalized Kohn-Sham formulation of density functional theory, which includes a known part of the interaction in the fictitious system [85]. This is useful for the construction of hybrid functionals.

Because the effective potential depends on the orbitals through the density, these equations need to be solved iteratively until self-consistency, within certain convergence criteria, is reached. This is the so-called self-consistent field (SCF) cycle.

In analogy with Hartree-Fock theory, the equations need to be formulated slightly differently depending on the spin polarization of the system. For a closed-shell system, we have the restricted Kohn-Sham equations with all orbitals doubly occupied. For spin polarized systems, there are two possibilities. Unrestricted Kohn-Sham equations have two sets of singly occupied orbitals, one for each spin component. Restricted open-shell Kohn-Sham (ROKS) equations have a single set of orbitals with different occupations and use one density for each spin component to evaluate the energy. We note that although generalized Hartree-Fock theory exists, of which the unrestricted and restricted theories are special cases, no such formulation or implementation of density functional theory is known to us.

2.2.2 Basis sets for Kohn-Sham orbitals

In practical calculations, each of the single-electron orbitals $|\psi_i\rangle$ needs to be expanded in a suitable basis set.

A common choice, especially in programs intended for quantum chemistry, is the linear combination of atomic orbitals (LCAO) approach. These atom-centered orbitals can be any analytic or numerically tabulated functions. The most common choice, however, is a linear combination of Gaussians in the radial coordinate multiplied by spherical harmonics in the angular coordinates. The reason for the popularity of this choice is the efficiency of evaluation of integrals involving these basis functions and the relatively low number of basis functions needed to obtain reasonably converged results. We note, however, that systematic convergence of computed properties with respect to basis set size is problematic in the LCAO approach.

Although LCAO functions are normally centered on atoms, there are no technical reasons preventing their placement in off-atom positions. In practice, this is rarely done, although the approach does exist in literature in the form of bond functions [18] or floating Gaussian orbitals [39]. It is also used in the parametrization of pseudopotentials for single-electron models of the solvated electron [102]. In this work, we found a use of this concept that seems to increase both the quality and computational efficiency of our simulations. As the hydrated electron is rather diffuse when compared to electron density in molecules, basis functions with low exponents are needed for its proper description. Traditionally, this would be achieved by the so-called augmentation functions — additional diffuse basis functions placed on atoms. This approach works well in quantum chemistry for relatively small finite systems, but starts having difficulties as the size of the system increases. In a condensed system, the overlap of diffuse functions from nearby atoms is significant — the different basis functions are getting close to linear dependence. That complicates SCF convergence or even makes it impossible. We choose to use a regular fixed grid of ghost atoms (no atomic core, only a location for basis functions) to place additional spherical functions in the system. This provides good support for the diffuse parts of the electron while only modestly increasing computational cost. It has the additional advantage of being uniform in space, which means that the quality of description of the diffuse density does not decrease as we go farther from atomic nuclei. With a suitable combination of grid spacing and Gaussian exponent, this approach is superior to augmentation functions in terms of convergence for the size of systems investigated here. It is at least comparable in terms of quality of description in cases where convergence is possible. We denote this type of augmentation of the basis set ggg (grid of Gaussian ghosts) in the names of basis sets.

In solid-state physics, plane waves are a very common choice as a basis set for Kohn-Sham orbitals. They provide a uniform quality of description suitable for condensed-phase systems. Several parts of the energy functional can be evaluated very efficiently using plane waves. This approach takes advantage of the efficiency of the Fast Fourier Transform algorithm to bring the electron density to a real-space grid, where the exchange-correlation part of the functional can be evaluated (see below).

Other basis sets are used in implementations of density functional theory as well. These approaches include real-space grids [22], discrete variable representation [61] or the finite element method [75].

Density fitting, sometimes also called resolution of identity, is used to speed up both density functional theory and (post-)Hartree-Fock calculations. While it is normally used in the context of Gaussian basis sets to substitute sums over three-index integrals in place of four-index integrals, the fitting basis can be entirely different. The Gaussians and plane waves method [60] is one such case where Kohn-Sham orbitals are expanded using LCAO with Gaussian radial functions and electron density is then collocated on a grid and represented using plane waves. This representation is then used to evaluate most of the terms of the Kohn-Sham Hamiltonian. This combination enables a very compact representation of the Kohn-Sham orbitals together with an efficient evaluation of matrix elements thanks to the global grid and plane waves.

2.2.3 Practical density functionals

Although the elegance of density functional theory is appealing, it does not provide a recipe for the actual exchange-correlation functional, it merely guarantees its existence and certain properties. Practical calculations rely on the construction of approximate functionals, which is guided by some of the known properties of the unknown exact functional and by benchmarking against experimental quantities or other calculations. As stated above, most of the total energy functional is known — the non-interacting kinetic energy is a very good approximation to the total kinetic energy, the interaction with the external potential (nuclear point charges and any applied fields) is known exactly and the classical electrostatic self-interaction of the electron density covers a large part of the electron-electron interaction. What remains is the exchange-correlation functional, which in Kohn-Sham density functional theory serves as a garbage can of the full functional, where the unknown parts are gathered — the missing part of the interacting kinetic energy density and the non-classical part of the electron-electron interaction, exchange and correlation energy. Because Kohn-Sham density functional theory is by far more common than the original orbital-free density functional theory, it is this functional that most practical exchange-correlation functionals endeavor to approximate.

Surprisingly, even local or semi-local approximations to the exchange-correlation functional provide at least satisfactory and often very good results. In the local density approximation (LDA), the exchange-correlation energy is simply an integral over the whole system of a local function of the electron density. LDA is derived from the uniform electron gas and parametrized to its properties. Gradient-corrected and generalized gradient approximations (GGA) also use a local function, which in addition to electron density also depends on its derivatives. The specific functional form often shows remarkable physical insight of its authors rather than a rigorous derivation in a systematic way. Any parameters that need to be set are determined either by tuning the functional to properties of atoms, molecules or solids (e.g. BLYP [8, 59]), or by targeting some of the known exact properties of the unknown true exchange-correlation functional (e.g. PBE [77]). It is customary to name density functionals using the initials of their authors. Approximate functionals can be generalized in a straightforward way for spin-polarized systems, where there are two electron densities, one for each spin component.

Semi-local functionals are known to suffer from the self-interaction error. This error is particularly severe for open-shell systems, where the unpaired electron contributes most of the magnitude of the error. A simple illustration of this problem is provided by one-electron systems, for example the hydrogen atom. Due to the approximations taken in the exchange-correlation functional, exchange energy does not cancel entirely electrostatic self-energy and correlation energy is non-zero even though there is only a single electron in the system. Based on this observation, a systematic way of removing the self-interaction error was suggested [76] — the self-interaction correction (SIC). More recently, the correction has been applied only to the spin density of the system and scaled to match reference data [20, 110]. It is beneficial, although not necessary, to apply this correction within a restricted open-shell Kohn-Sham scheme. The scaling parameters need to be determined by benchmarking against a suitable reference.

One very popular approach to the construction of approximate functionals is the addition of a fraction of exact (Hartree-Fock) exchange in place of (semi-)local exchange. The resulting scaled hybrid functional is relatively expensive, at least by the standards of GGA density functional theory. However, many computed properties are significantly improved. B3LYP, perhaps the most commonly used functional in quantum chemistry, is of this type, PBE0 is another. Another approach to hybrid functionals is based on the splitting of the electron-electron interaction into a short-range and a long-range part, for example using the error function,

$$\frac{1}{r} = \frac{\mathrm{erf}(\gamma r)}{r} + \frac{\mathrm{erfc}(\gamma r)}{r}, \tag{2.15}$$

Where γ is a free parameter that needs to be set. The short-range part is then evaluated as exact exchange, while the long-range part is approximated as in the original, nonhybrid functional. The resulting functionals are called range-separated hybrids [6] and have similar computational demands as scaled hybrids, although they can take advantage of the short range of the expensive exact exchange. Hybrid functionals have not been used for any of the main results presented here, but they have been used for comparison and benchmarking and for a project that is currently in progress and not yet published. As especially range-separated hybrids look very promising in initial calculations for both types of electronic defects studied here, this direction should certainly be pursued further, especially in light of increasing hardware performance and recent algorithm and implementation advances [37, 38]. With these, the use of hybrid functionals becomes feasible even for molecular dynamics of condensed systems in periodic boundary conditions.

Because exchange-correlation functionals are non-linear, there is no way to express the resulting exchange-correlation energy in terms of individual basis functions and the functionals need to be evaluated numerically. Two different types of grids are used for this purpose in implementations of density functional theory. In quantum chemical programs, grids in spherical coordinates centered on atoms are usually chosen and space is divided into regions covered by different grids using for example Voronoi partitioning. This approach is suitable for isolated systems. In programs intended primarily for solid-state physics or condensed systems in general, a global Cartesian grid is often used. This is often the same grid that is used for other parts of the calculation, like electrostatic energy.

None of the commonly used semi-local or hybrid functionals are able to describe long-range dispersion interactions. A functional that includes fully non-local correlation would be needed to achieve that. While such functionals exist [19], they tend to be significantly more expensive computationally and not as well parametrized for general purposes. A large part of dispersion interactions can be recovered by suitably parametrized two- and possibly three-atom interactions applied as a correction. Several methods using this concept exist [33, 34, 35, 36, 97, 51], with differences in the exact functional form and the way they are parametrized. The idea is the addition of pair (and optionally triplet) interactions to, for example, a GGA density functional and a suitable scaling of the original GGA energy and forces. The basic pairwise interaction has the form

$$u(r) = \mathrm{f}(r)\frac{C_6}{r^6}, \tag{2.16}$$

where $\mathrm{f}(r)$ is a suitably chosen short-range damping function, C_6 is an interaction constant that needs to be determined and $1/r^6$ is the asymptotic behavior of the dispersion interaction between two atoms.

2.2.4 Approximations to the nuclear potential

The nuclear potential, which serves as an external potential for the Kohn-Sham equations, is simply the Coulomb potential of a set of point charges with the magnitude of the charge set based on the chemical elements of the atoms. It is possible to evaluate the energy in this potential exactly, but it is often neither practical nor needed in actual computations. As the Coulomb potential is very steep close to the nuclei, the energy density in regions close to the nuclei is high and the electron density is relatively stiff when exposed to the presence of other atoms in the system. In the valence regions of atom, the situations is exactly the opposite — the energy density is much lower and the electron density is more easily polarized. As it is the valence region that, to a large extent, determines properties of molecular systems and changes in total energy upon change of nuclear configuration, approximations are often taken to make practical calculations more efficient without significant impact on results. One such option is the so-called frozen core approximation, where orbitals containing a suitably chosen number of core electrons are frozen in their neutral-atom states — they do not undergo relaxation when positions of nuclei change. A very common option is the complete removal of the core electrons and the introduction of an effective potential that represents the atomic nucleus and the core electrons. These resulting potentials are called pseudopotentials or effective core potentials. At longer distances, they look like bare charges, but close to the nuclei, they are softer and some have non-local parts to account for the repulsion by the implicit core electrons. This has the advantage that the resulting electron density is smoother and thus easier to represent using any type of basis set. Further, relativistic effects are usually only significant for core electrons, which means they can be covered by pseudopotentials without adding complexity to the calculation. Norm-conserving pseudopotentials modify the orbitals within a certain element-specific augmentation radius around the nuclei, but keep the normalization as well as the values of orbitals outside the augmentation radius. Ultrasoft pseudopotentials relax the requirement of conserved norm of each orbital at the expense of being technically more involved.

2.3 Ab initio molecular dynamics

The term ab inito molecular dynamics is usually used for any calculation where the forces and energies for a molecular dynamics simulation are obtained from an electronic structure calculation, leaving aside whether the method is truly without (semi-)empirical parameters or not. This terminology is used to put ab initio molecular dynamics in contrast with molecular dynamics based on empirical force fields or semi-empirical methods, although in practice there is a spectrum of methods that covers the whole range between the two extremes of entirely empirical to entirely ab initio. An important feature of ab inito calculated interactions is that they allow for the making and breaking of chemical bonds, although the quality of description must of course be checked for a given combination of method and chemical reaction. Some authors distinguish the terms ab initio molecular dynamics and first-principles molecular dynamics. We do not make that distinction in this work as we do not find it useful. A good overview of various aspects of ab inito molecular dynamics with focus on density functional theory can be found in reference 70.

Ab initio molecular dynamics rose in popularity and importance with the introduction of the Car-Parrinello method [14]. This approach made practical calculations more computationally efficient while maintaining the advantages of density functional theory. Instead of full electronic relaxation at each geometry, electrons in Kohn-Sham orbitals are given fictitious masses and are included in the dynamics of the system. With suitable settings, adiabatic separation between electronic and nuclear degrees of freedom can be maintained and the nuclei move close to the electronic potential energy hypersurface, though not exactly on it.

In the presented work, the Car-Parrinello method is not used. We use Born-Oppenheimer molecular dynamics, where electronic relaxation is, within convergence criteria, complete at each geometry along the trajectory. Although this might look obviously more expensive at first sight, there are several factors that need to be considered. The time step in this approach is limited only by the highest frequencies present in nuclear motion, whereas in Car-Parrinello molecular dynamics it needs to be shorter because of the relatively low fictitious electronic masses, compared to nuclear masses. Further, iterative methods for the solution of Kohn-Sham equations have advanced since the introduction of Car-Parrinello molecular dynamics. Together with efficient extrapolation of the Kohn-Sham wavefunction [54, 56], this can bring the total number of SCF iterations for a given length of simulation time to a comparable or even lower level. For these reasons, Born-Oppenheimer molecular dynamics should be the method of choice when an efficient implementation is available, as there is no need to worry about the adiabatic separation of the electronic and nuclear subsystems and the possible energy flow between them.

Even though density functional theory is by far the most common choice for the evaluation of potential energy hypersurfaces in ab initio molecular dynamics, as explained above, it is not the only possibility. The decoupling between nuclear and electronic degrees of freedom is complete in Born-Oppenheimer molecular dynamics and any method that provides gradients can be used, the only limitation being its computational cost. As an example, dynamics of small water clusters based on MP2 energies and forces is becoming more common [71, 72]. As the Car-Parrinello method performs fictitious dynamics of electronic orbitals, it can only be used in conjunction with methods where the whole electronic energy is evaluated using orbitals.

2.4 Analysis of simulation results

> *"It is nice to know that the computer understands the problem. But I would like to understand it too."* — Eugene Wigner

After a simulation is performed, there is still one last step remaining before it is useful for anything. The resulting data must be analyzed and quantities of interest must be extracted. Sometimes this is straightforward, as in the case of potential energy, while for other quantities the postprocessing needed is much more involved, as in the case of electron or spin density and derived quantities.

One class of properties, available in all molecular dynamics simulations, is those derived from the phase-space trajectory of the system — positions and momenta as a function of time. In equilibrium molecular dynamics, the time dependence is irrelevant and the trajectory is used simply as an ensemble of structures. Temperature is determined from kinetic energy using the equipartition theorem for N atoms in three dimensions,

$$E_k = \sum_{i=1}^{N} \frac{\mathbf{p}_i^2}{2m_i} = \frac{3}{2} N k_B T. \tag{2.17}$$

Potential energy is determined from positions using the method chosen to evaluate interaction. If a given thermostatting scheme has an energy associated with the thermostat, this can be evaluated too and used as a way to check the quality of integration. For an exact solution, the sum of the three terms must remain constant in time and any deviation serves as a measure of inaccuracy of the numerical solution of equations of motion. An important quantity derived from positions is the pair correlation function, $g(\mathbf{r})$, which is defined for each pair of species in the system, including self-correlation. This quantity provides information on the structure of the system. It expresses the probability of finding a partner particle in a given position relative to the reference particle, normalized to an uncorrelated ideal gas. Thus, by definition, the pair correlation function of an ideal gas would be a constant function that is equal to one everywhere. Usually, only the radial coordinate is considered, giving a radial distribution function, $g(r)$, but for species whose orientation can be fixed, a spatial distribution function can be considered as well. We note that the terminology regarding pair correlation functions varies somewhat in literature and is not entirely consistent.

For molecular dynamics simulations based on electronic structure calculations, another class of quantities exists, those derived from the electronic structure of the system at each molecular dynamics step. The details of what is available obviously depend on the specific chosen method. With most methods, one of the wide spectrum of population analyses [17] can be used to reduce the charge distribution to point charges that approximate it. In density functional theory, we have the Kohn-Sham orbitals and therefore also the total electron density and, for spin-polarized systems, the spin density. These densities are three-dimensional scalar functions represented either on a regular grid or in an LCAO representation. As such, they can be used for visualization, using either two-dimensional cuts or isosurfaces of the three-dimensional data. They usually need to be processed further to obtain quantitative information on the system. The electronic potential energy and its derivatives with respect to nuclear positions are used to drive ab initio molecular dynamics. The difference of energies between two different charge states is the vertical ionization potential or vertical electron affinity. As the hydrated electron is the most weakly bound species in a typical aqueous system, its vertical detachment energy (VDE), an important experimental observable, can be calculated this way, as it is simply the vertical ionization potential of the system. The rest of the ionization spectrum could be calculated as excited states of the ionized system [80], although this is not needed in this work. Note that the resulting spectrum should not be interpreted as the photoionization spectrum of the system, as it does not account for the possibly different cross-sections of the different states.

For systems with an excess electronic charge, it is useful to look at some basic characteristics of the position and shape of the distribution of that excess charge. In this work, we identify the spin density of the open-shell system as the excess charge. Another possibility would be to use the difference density between the neutral and the charged system. If a restricted open-shell calculation is used for the charged system, the difference between the two possible definitions is the relaxation density of the paired Kohn-Sham orbitals. Looking at the first several moments of the distribution of the excess charge, we start with its normalization to unity,

$$\int\limits_{\mathbb{R}^3} s(\mathbf{r})\mathrm{d}\mathbf{r} = 1. \tag{2.18}$$

The position of the excess charge is characterized by the first moment of the distribution,

$$\mathbf{r}_c = \int\limits_{\mathbb{R}^3} \mathbf{r}s(\mathbf{r})\mathrm{d}\mathbf{r}. \tag{2.19}$$

Further, we want to describe the size and shape of the spin distribution around that central position. For this, we use the gyration tensor, defined as

$$\mathbf{S} = \int\limits_{\mathbb{R}^3} (\mathbf{r} - \mathbf{r}_c)(\mathbf{r} - \mathbf{r}_c)s(\mathbf{r})\mathrm{d}\mathbf{r}. \tag{2.20}$$

This tensor has eigenvalues λ_x^2, λ_y^2 and λ_z^2. Using these, we can express the radius of gyration r_g, which is a measure of the size of the distribution,

$$r_g^2 = \lambda_x^2 + \lambda_y^2 + \lambda_z^2. \tag{2.21}$$

The same quantity could also be calculated as

$$r_g^2 = \int\limits_{\mathbb{R}^3} (\mathbf{r} - \mathbf{r}_c)^2 s(\mathbf{r})\mathrm{d}\mathbf{r} \tag{2.22}$$

without the need for the full gyration tensor. However, we do calculate the full tensor, as it is also useful to describe the shape of the distribution. For this, we follow reference 95 and define asphericity as

$$b = \lambda_z^2 - \frac{1}{2}(\lambda_x^2 + \lambda_y^2), \tag{2.23}$$

acylindricity as

$$c = \lambda_y^2 - \lambda_z^2, \tag{2.24}$$

and finally, using the above, relative shape anisotropy as

$$\kappa^2 = \frac{b^2 + \frac{3}{4}c^2}{r_g^4}. \tag{2.25}$$

The last one is a measure of an overall deviation from a symmetric distribution and assumes values between 0 and 1. A purely linear distribution would have $\kappa^2 = 1$, for a regular planar structure $\kappa^2 = 1/4$ and for a distribution with tetrahedral or higher symmetry $\kappa^2 = 0$. It is also useful to calculate the radial profile of the distribution with respect to its center, by integrating over the angles,

$$s(R) = \int s(R, \theta, \varphi) R^2 \sin(\theta) \mathrm{d}\varphi \mathrm{d}\theta, \tag{2.26}$$

where $R = |\mathbf{r} - \mathbf{r}_c|$.

For simulations of clusters, we would like to define a quantity that describes the distance of the excess electron from the molecular part of the system. One possibility is simply to measure the distance between the center of mass of the cluster $\mathbf{r}_{COM}$ and the center of the distribution of the excess electron $\mathbf{r}_c$,

$$d_{COM} = \left| \mathbf{r}_c - \mathbf{r}_{COM} \right|. \tag{2.27}$$

Another possible definition is the average distance of the excess electron from the center of mass of the cluster,

$$d_{avg} = \int_{\mathbb{R}^3} \left| \mathbf{r} - \mathbf{r_{COM}} \right| s(\mathbf{r}) \mathrm{d}\mathbf{r}. \tag{2.28}$$

While for some configurations these definitions give similar values, for others (like a symmetric distribution on the surface of the cluster), they differ substantially.

For the purpose of identifying different regions of the system where the excess electron resides, we perform the following partitioning in our latest unpublished work. The region of the central cavity (once it is established that a cavity exists) is determined using Voronoi decomposition. Regions of significant overlap with water molecules are those, where the electron density of the neutral system exceeds a certain suitable threshold. The sensitivity of the result to this setting needs to be tested. Regions in the liquid that are not inside water molecules but are also outside the central cavity, can in principle also contain a part of the density of the excess charge, which we call the diffuse part. For configurations that are close to an open surface, there can be another region — outside the liquid. To define the boundary, we use the method of Willard and Chandler [114].

2.5 Specific choices for this work

While the above gives a general overview of the methods that we have used in this work, specific choices still need to be made for many parameters. For all the ab initio molecular dynamics we have used the Quickstep module of the CP2K program package [109]. There are two reasons why the systems treated in this work present a unique computational challenge, which most programs fail to address. The size, both spatial and temporal, of the simulations needed requires high computational efficiency. The Gaussians and plane waves method and its implementation in CP2K represent the state of the art in this respect. This is especially important for condensed systems in periodic boundary conditions. The other reason is the open-shell configuration of the two systems of interest and the specific density functional theory methods they require, which are all implemented in CP2K. In the near future, the introduction of linear scaling methods [106] promises the ability to simulate also very large systems, given sufficient computational resources. At the same time, CP2K also provides all the methods need for the treatment of nuclei, molecular dynamics and optimization methods, which are largely unproblematic, but it is certainly helpful to have them available without having to combine multiple programs.

2.5.1 Density functional theory

In the CP2K implementation of density functional theory, there is a global Cartesian grid that must cover the whole system. For cluster systems, open boundary conditions are created by making the simulation box large enough for the electronic density to become negligibly low at the box boundaries. For a cluster of 32 water molecules, a cubic box with an edge length of 20 Å is sufficient. This must be supplemented with a suitable Poisson solver. Several different ones are available in CP2K, including one based on wavelets [31, 30]. This solver is able to treat finite systems in open boundary conditions or systems with two-dimensional periodicity, even charged ones, without any extra demands on the size of the box. For simulations in periodic boundary conditions, a conventional Poisson solver based on fast Fourier transformation is used. The spacing of the grid on which the electronic density is represented, or the equivalent cutoff of the plane wave representation, is dictated by the steepness of the underlying (pseudo)potential. In our setup, well converged energies and forces are obtained with a plane-wave cutoff of 280 Ry.

We use the dual-space norm-conserving Goedecker-Teter-Hutter pseudopotentials [32]. They give optimal efficiency for calculations using plane waves, but their non-local part can be applied on a real space grid, which is more efficient than doing it in reciprocal space for large systems. For a water molecule, two core electrons of the oxygen atom are represented implicitly by the pseudopotential and further the bare point charges of the hydrogen atoms are smeared into Gaussians so that they can be collocated on the global grid.

For most of our calculations, we employ the BLYP-D2 exchange-correlation functional — the Becke semi-local exchange functional [8] together with the Lee-Yang-Parr semi-local correlation functional [59], supplemented by the dispersion correction of Grimme [34]. In earlier work, we also used the Perdew-Burke-Ernzerhof functional [77], with negligible differences between the two, as far as the main conclusions are concerned. However, BLYP-D2 has been shown to improve significantly on both the structure, as measured by the radial distribution function, and the density of pure BLYP water [83, 4]. Pure GGA functionals are know to overstructure liquid water, which has traditionally been masked by setting the temperature to about 350 K, rather than 300 K. With BLYP-D2, this is no longer needed.

Liquid water is well described by the molopt-TZV2P basis set. This is a generally contracted basis set with quality comparable to a triple-ζ basis set with two polarization functions, which has been optimized for condensed molecular systems [108]. Although it contains very diffuse Gaussian functions, they are always part of contractions and do not contribute independently. The introduction of an excess charge to the system places additional requirements on the basis set, especially in the case of clusters. The addition of diffuse basis functions centered on atoms, a standard approach in LCAO calculations, provides good description of the diffuse states of the hydrated electron, at the expense of computational efficiency. The overlap between diffuse Gaussian functions on neighboring atoms is high and results in the need for more conservative SCF methods and an increase of the number of SCF iterations needed to achieve convergence. In some cases, convergence becomes impossible, often after some number of molecular dynamics steps, which further complicates practical calculations. The ggg approach explained earlier fixes these issues while providing at least equally good description of the diffuse parts of the electronic density. Specifically, we use a grid spacing of 2 Å and a Gaussian exponent of $\zeta = 0.189$ Å^{-1}. For the cluster calculations, this results in the addition of 1000 functions, increasing the total number of basis function by more than 50 %. Because the computational expense of this setup is not dominated by the LCAO part of the calculation, this seemingly large increase results only in a modest performance decrease when compared to a non-augmented calculation. Compared to a traditionally augmented calculation, the performance is clearly superior for the reasons stated above.

We apply the self-interaction correction to the singly-occupied orbital in a restricted open-shell Kohn-Sham calculation. This correction can also be applied to the spin density in an unrestricted calculation, which produces almost identical results in our case. The first approach is, however, more robust, as it does not allow for spontaneous overpolarization of the system driven by the correction. It is important that the correction is part of the functional that is self-consistently minimized at each molecular dynamics step, rather than being applied post-SCF, as is the case in some other implementations. The self-consistent case is computationally more difficult, as it requires minimization of a functional that depends explicitly also on one of the orbitals, not only on the total electron density. There are two parameters in this self-interaction correction. The first one, a, scales the electrostatic part of the correction. The second one, b, scales the exchange-correlation part of the correction. Their optimal values need to be determined for each specific open-shell species. For the OH radical in solution as well as for the water dimer cation, the optimal values are $a = 0.2$, $b = 0.0$. This motivates the use of the same values also for the cationic hole in bulk water, as discussed in detail later. For calculations with both the hydrated proton and hydrated electron present in the system, the values $a = 0.3$, $b = 0.2$ benchmark favorably against MP2 calculations. For systems with the hydrated electron only, we have done calculations with both of these sets of values.

Kohn-Sham equations are solved iteratively until predefined convergence criteria are reached. This determines the quality of both the electronic energy and the forces on individual atoms. Together with the time step, it also determines the quality of the molecular dynamics simulation, which is the important criterion. We use a threshold of 10^{-6} or 10^{-7} for the electronic gradient, as defined in the CP2K program. Orbital transformation, an efficient SCF method that avoids matrix diagonalization [107] reaches the solution in shorter time than traditional methods. The iterative procedure also needs an initial guess. For the first step of molecular dynamics or for a single-point calculation, this is usually taken to be the combination of unperturbed atomic solutions. For subsequent molecular dynamics steps, one can take advantage of the solution converged for the previous geometry, which differs only very little. Therefore, such an initial guess is significantly better than when atomic solutions are used. Even better, several previous solutions can be considered and extrapolated. There are different methods to do this and different properties of the system can be used for the extrapolation — the electronic density, the LCAO density matrix multiplied by the overlap matrix, or others. Interestingly, the most efficient method available in CP2K, is based on the always stable predictor-corrector method devised for efficient simulations with polarizable empirical force fields [54]. Typically, three to five previous steps are used for the extrapolation.

As an example of the performance of this setup in practice, we report the real time per molecular dynamics step of the anionic cluster of 32 water molecules. On a computer cluster with nodes with two dual-core AMD Opteron 2214 CPUs running at 2.2 GHz with Infiniband interconnect, running on 6 nodes for a total of 24 cores, it takes about 90 seconds to complete a molecular dynamics step once the extrapolation pipeline is saturated. On the HLRN ICE1 supercomputer, running on a total of 32 cores, one molecular dynamics step takes about 45 seconds. Each node has two quad-core Intel Xeon Harpertown E5472 CPUs running at 3 GHz and quad data rate Infiniband. A significant portion of our simulations had to be run on clusters without fast interconnect, limiting the scale of the runs to eight cores, with proportionally slower performance. All calculations are run fully from memory for performance reasons.

In the latest work on the hydrated electron in bulk liquid water, we employ a technique know as QM/MM — quantum mechanics and molecular mechanics. Although this is the established term for the approach, it would be more appropriate to call it quantum chemistry and empirical force field. Its basic idea is a split of the system into two parts, where interactions within one of them are treated using a quantum chemical method, for example density functional theory, and interactions within the other are treated using an empirical force field, which is much cheaper to evaluate. This must be supplemented with a suitable coupling scheme to evaluate the interaction between the two regions. The method provides high quality description of local interactions around a challenging species, while also decreasing the influence of the finite size of the simulation box, as the region described using an empirical force field can easily be made large without much impact on the computational cost of the whole simulation.

2.5.2 Molecular dynamics

Molecular dynamics is performed with a time step $\Delta t = 0.5$ fs, which is dictated by the highest frequency in the system, the vibrations of OH bonds in water. Together with the above SCF convergence settings, this results in good energy conservation and sufficient integration quality. Energy conservation is measured by the drift of either total energy in an NVE simulation or of a conserved quantity in an NVT simulation, if the thermostat used has one. In equilibrium simulations, we use a thermostat to sample the canonical ensemble. Specifically, we use the CSVR method with a time constant of 50 fs. Non-equilibrium simulations then use samples from these distributions as the starting nuclear configuration, together with a change of electronic charge. Depending on the sign of the change, this results in the simulation of either vertical electron attachment or photoionization. This dynamics should proceed at constant total energy, although thermostat use has little effect on very fast processes. For simulations of the hydrated electron where we are not interested in the initial localization process, but rather want to sample equilibrium, we use a shortcut for the initial condition. First, we run a simulation with a halide anion, which creates a suitable polarized cavity in the liquid. This anion is then removed and the charge of the system is set so that an excess electron is present in the system. In practice, this electron always localizes in the pre-created cavity, as its structure is very similar to the equilibrium cavity needed for the electron. Subsequent equilibration of that system is therefore faster than without a cavity. For simulations of cold clusters, structures taken from dynamics at 300 K are energy minimized and used as initial conditions for anionic clusters at a low temperature in the range 30–50 K. Alternatively, structures from 300 K anionic water clusters are taken, minimized and then run at a low temperature to obtain a different kind of cold anionic water clusters, as discussed later in the thesis. Although a more careful protocol of preparation of cold clusters could certainly be devised, we do not consider it a limitation here, as the purpose is to address qualitative differences, rather than to obtain specific quantitative results. Initial conditions for ab initio molecular dynamics simulations are taken from simulations with empirical force fields. A certain amount of equilibration is then needed to quench the transition between the potential energy hypersurfaces obtained with the two different methods.

CHAPTER

THREE

DYNAMICS FOLLOWING PHOTOIONIZATION OF WATER

As explained in the introduction, vertical ionization leaves behind a cationic hole, regardless of the ionized species. For the previously stated reasons, we focus here on water ionization, which leads to indirect radiation damage in aqueous systems. As we will see, the initial cationic hole is delocalized over several water molecules. For this reason, understanding ionization of water itself will be important also for species with an ionization potential close to that of water.

Work on this problem was published in a paper that is attached to this thesis [118].

3.1 Photoionization of water clusters

Although we are interested in bulk behavior, it is useful to start by considering small water clusters and their ionization. This provides an opportunity to work on computational methodology that will eventually be used for bulk simulations in periodic boundary conditions. For small clusters, reliable quantum chemical methods are available and computationally feasible. These can serve as a benchmark for cheaper methods that can be used for ab inito molecular dynamics of condensed systems.

Our colleagues have published a study of the water dimer cation [79], which serves as a good starting point for further simulations. They used EOM-IP-CCSD(T)/6-311++G** as the reference method for the electronic structure of this system. The equation of motion for ionization processes method [55] uses a Hartree-Fock calculation of the neutral as a starting point for a subsequent coupled clusters calculation of the cation, overcoming challenges that this type of systems poses for conventional post-HF methods. The results clearly show that plain GGA density functional theory is unsuitable for the treatment of this open-shell system, when judged by relative energies of different geometries of the water dimer cation. On the other hand, the addition of the self-interaction correction for the singly-occupied orbital improves the results considerably, bringing relative energies into quantitative agreement with the reference. The recommended scaling parameter values of the self-interaction correction $a = 0.2$ and $b = 0.0$, which were determined for the OH radical in solution [110], work well also in this case. Such a match is remarkable, as this challenging system is not described properly by significantly more expensive methods, including Hartree-Fock and single-reference post-HF correlated methods. The addition of the self-interaction correction for the singly-occupied orbital increases the computational cost only slightly and, importantly, does not change the scaling behavior of the method. Further, in the water pentamer cation, EOM-IP-CCSD/6-311++G** shows that the spin population is distributed over two water molecules [78]. This delocalization can be used as an additional benchmark for condensed-phase methods. Again, SIC-DFT with $a = 0.2$ and $b = 0.0$ emerges as a good choice, as it captures this delocalization while being cheap enough to be used for ab initio molecular dynamics.

Photoionization of the water dimer removes the electron from the hydrogen bond donor, rather than the acceptor. A proton is immediately transferred in a barrierless process to the acceptor, forming an OH radical and and an H_3O^+ cation. This is the first approximation of the same process in bulk water, but the delocalization of the cationic hole in the water pentamer already tell us that there might be more to the story.

Ultimately, water clusters are not suitable for the study of ionization of bulk water. That is the case even for large clusters that have an interior region. The presence of the open surface decreases the local ionization potential of the interfacial water molecules. Therefore, photoionization will always remove electrons from the surface of the cluster, making access to the bulk process imposible. For this reason, the only way to proceed is to perform calculations of a three-dimensional periodic system.

3.2 Photoionization of bulk water

Having established that our method of choice benchmarks favorably against the reference in small water clusters, we can proceed to apply this method to a bulk water system. The results of these simulations form the core of the published work [118].

3.2.1 Benchmarking on bulk water

We can start by performing further benchmarking by taking the water pentamer configuration of reference 78 and comparing the spin density obtained using different methods to the density from EOM-IP-CCSD. Figure 7 of the paper shows isosurfaces of the spin density obtained with different density functional methods as well as pure Hartree-Fock. The reference spin density is delocalized over the two water molecules donating hydrogen bonds to the central one. This feature is reproduced by a self-interaction-corrected density functional as well as by a hybrid functional with a sufficiently high percentage of exact exchange. A plain GGA density functional overestimates the delocalization, spreading the spin density also on the other water molecules. Hartree-Fock completely localizes the cationic hole on a single water molecule.

Now we can apply the same methods to configurations taken as samples from equilibrium dynamics of bulk water at 300 K. For obvious reasons, EOM-IP-CCSD is unavailable for this purpose. The resulting spin densities are shown in Figure 6 of the paper and are consistent with what we have seen for clusters. The cationc hole is delocalized, with the largest degree of delocalization seen with a pure GGA functional. Adding the self-interaction correction decreases this delocalization, as does mixing in some amount of exact exchange. A pure Hartree-Fock calculation again shows the cationic hole fully localized. It is clear from these results, that a range of hybrid functionals going from pure GGA to pure Hartree-Fock spans the whole spectrum from extremely delocalized to fully localized. We note that the structure of liquid water itself is represented poorly with Hartree-Fock [98], making it an unsuitable candidate to begin with.

To provide even more benchmarking information before proceeding to the results, we look at the dynamics following vertical photoionization, using different methods. As a measure of localization we plot the largest Mulliken spin population on a single oxygen atom as a function of time. While Mulliken populations do not provide robust quantitative information, they serve well as a simple indicator of the hole being localized. For this to be the case, the maximum spin population on a single oxygen atom must be close to unity. If this is not true, then the hole is, by definition, delocalized. Figure 3.1 shows the time evolution of maximum Mulliken spin population on an oxygen atom during molecular dynamics obtained using different electronic structure methods. That means that the nuclear trajectories are different, each following the interactions provided by the given method. Increasing the amount of exact exchange shortens the localization time, with a pure Hartree-Fock calculation showing a localized spin density from the very beginning, consistent with the previous single-point benchmark. Importantly, the GGA functional BLYP never localizes the hole and the proton transfer reaction never occurs. This is in strong conflict with experimental data. Although the details of this reaction are not know experimentally, it is well established that it happens on a timescale shorter than about 100 fs. The self-interaction corrected GGA density functional BLYP-SIC, on the other hand, provides results comparable to a hybrid functional with a suitable ammount of exact exchange added in. At the same time, it is much cheaper computationally, as the dependence on the spin density of the singly-occupied orbital is much faster to account for than a full Hartree-Fock calculation which is needed for a hybrid functional.

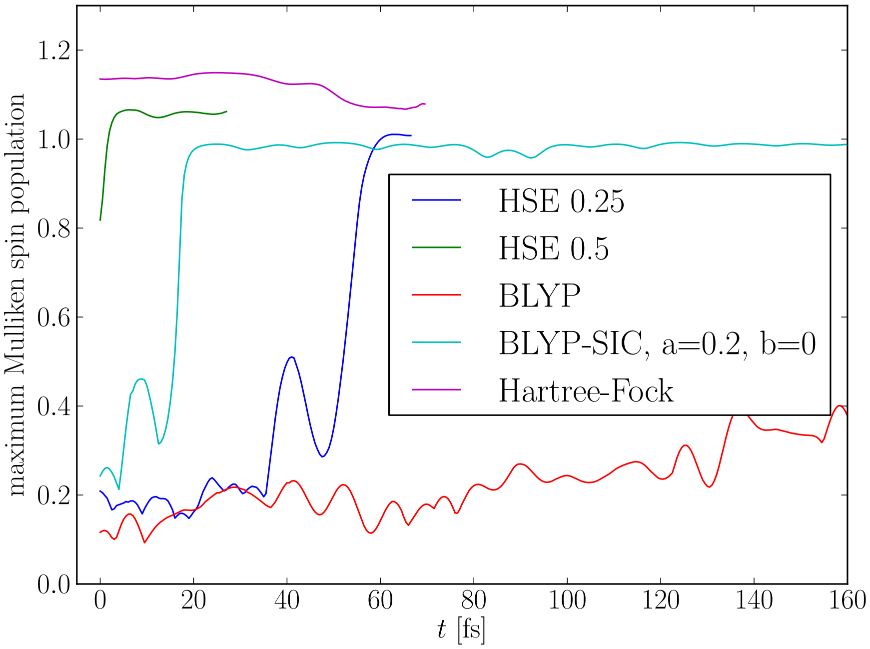

Figure 3.1 Time evolution of maximum Mulliken spin population on a single oxygen atom for different electronic structure methods.

3.2.2 Dynamics following photoionization of liquid water

Having confirmed self-interaction corrected density functional theory as a method that is suitable for the treatment of photoionization of bulk water using ab initio molecular dynamics, we proceed to the actual results. We have produced a total of 22 trajectories and analyzed in detail the dynamics of the system following vertical ionization. Snapshots of the system along one such trajectory, showing isosurfaces of the spin density, are show in Figure 1 of the paper. We observe ultrafast localization of the hole followed by the formation of a hydrated proton and an OH radical. As before, we can follow the maximum Mulliken spin population on a single oxygen atom, for all the trajectories. These are plotted in Figure 2 of the paper, together with the average in black and an arbitrary threshold for localization. The exact value of that threshold is not really important, due to the steepness of the curves. Figure 3 of the paper provides a view of the process from the perspective of the atomic nuclei. It shows the distance between the spin and the charge, again for all the trajectories. This distance is zero before any proton transfer has occured. After it has occured, it is the distance between the oxygen atom that holds the spin density and the oxygen atom that has the excess proton (measured simply by distance). Due to this definition, the distance changes in jumps, as the proton moves from one oxygen atom to the next. There are recrossings in most trajectories, as we treat the nuclei as classical particles and the proton shuffles back and forth before settling at the new oxygen atom. This defines our reaction interval — between the first and the last proton transfer for a jump between a pair of oxygens. To put the electronic and nuclear information together, in Figure 4 of the paper we correlate the reaction interval with the spin localization time. The result clearly shows that the reaction starts as soon as the spin density is localized on a single water molecule, identifying H_2O^+ as an extremely reactive transient species that is only populated for a very short time in each trajectory. This is a crucial result that has important consequences for the experimental search for the spectroscopic signature of this process.

To model the spectroscopy of this process, calculations of electronically excited states were performed by our collaborators on this project. These calculations use snapshots along the ab initio molecular dynamics trajectories every 2 fs. For each snapshot a QM/MM calculation is performed, where the reactive trimer is treated explicitly and the rest of the waters is included as point charges. The reactive trimer is defined as the water molecule on which the spin density will localize and the two water molecules to which it donates hydrogen bonds — those to which it could transfer a proton. An EOM-IP-CCSD/6-311++G** calculation is performed in this setup to calculate the electronic excitation spectrum of the system. The time-resolved spectra along all the trajectories are then averaged. Because the choice of the trimer artificially limits the delocalization of the initial hole, we mask out the contribution of the spectrum from a given trajectory until the time the spin density is localized in that trajectory. This removes the strong and spurious contribution of the part of the trajectory where the hole is artificially localized. Both the full and masked spectrum is shown in Figure 8 of the paper. Our experimentalist colleagues discuss the comparison of the computed spectrum with the measured spectrum that they have obtained. Spectra from two different measurements are shown in Figure 9, together with the modelled spectrum displayed over matching wavelength ranges. Due to the significant challenges described in detail in the paper, a clear spectroscopic signature of this ultrafast process could not be measured.

After careful benchmarking of the electronic structure method, we have studied the process of photoionization of liquid water. We have found that the rate-limiting step of the ultrafast reaction producing a hydrated proton and an OH radical is the previously unknown localization of the initially delocalized cationic hole. Based on this result, we can update the outline of the process of water ionization given in the introduction as

$$\begin{aligned}
(\mathrm{H_2O})_\mathrm{n} + \hbar\omega &\rightarrow (\mathrm{H_2O})_\mathrm{n}{\cdot}^{+} + \mathrm{e}^{-}_{\mathrm{CB}}, \\
(\mathrm{H_2O})_\mathrm{n}{\cdot}^{+} &\rightarrow (\mathrm{H_2O})_{\mathrm{n}-1} + \mathrm{H_2O}{\cdot}^{+}, \\
\mathrm{H_2O}{\cdot}^{+} + \mathrm{H_2O} &\rightarrow \mathrm{OH}{\cdot} + \mathrm{H_3O}^{+}.
\end{aligned}$$

3.3 Development of density functionals

The development of density functionals is an active area of research in general, but the demand for new and improved functionals is especially high for difficult systems like the water radical cation discussed here. Although we have seen that the self-interaction correction performs well for our purpose, it still is a correction that, moreover, needs to be parametrized. It would be useful to have available a functional that is more robust, and we have seen from the benchmarks that scaled hybrid functionals could work well.

Range-separated hybrid functionals have previously been successfully used for symmetric radical cations [62], which is relevant to our problem — individual water molecules have similar local environments and the cationic ground state is quasi-degenerate. The process of tuning of the functional — the setting of the range separation parameter γ to a value that is optimal, in some sense, for a given system can improve results dramatically [5]. The target of this tuning can be any property of interest, but the so-called self-tuning is especially attractive, because it does not need any external input. It relies on the ionization potential theorem, a known property of the exact functional, which states that the highest eigenvalue of the Kohn-Sham system is equal to the negative of the ionization potential,

$$\epsilon_{HOMO} = -IP. \tag{3.1}$$

This theorem is almost always severely violated by semi-local functionals. Tuned range-separated hybrid functionals that satisfy it tend to have many good properties, including those related to charge or spin delocalization. In Figure 3.2, we plot the two values that should be equal as a function of the range separation parameter for one particular geometry of the water dimer. As changing γ constitutes changing the functional and thus properties like energy, it is important that a set of calculations is done with a single value. This is critical if such a functional is to be used for ab initio molecular dynamics, where changing γ on the fly would introduce spurrious forces. Moreover, it would make the calculation very expensive if the self-tuning procedure would have to be performed at regular intervals along the trajectory. Previously, ab initio molecular dynamics has been done with the optimal value obtained for geometries of local minima of potential energy [63].

As for the choice of specific functionals, it is preferable to pick one that is constructed from a GGA functional in a straightforward way, with no paramters other than γ, so that the effect of range separation can be studied independently of other influences. The BNL functional [6] as well as the long-range corrected modifications of common GGA functionals, LC-BLYP and LC-PBE, fulfill this requirement.

With the above motivation, we propose a way to tune a functional for an ensemble of structures and use the resulting range separation parameter for subsequent ab initio molecular dynamics of that system. Because different geometries will have different optimal values of γ, we have to find some compromising method of satisfying the ionization

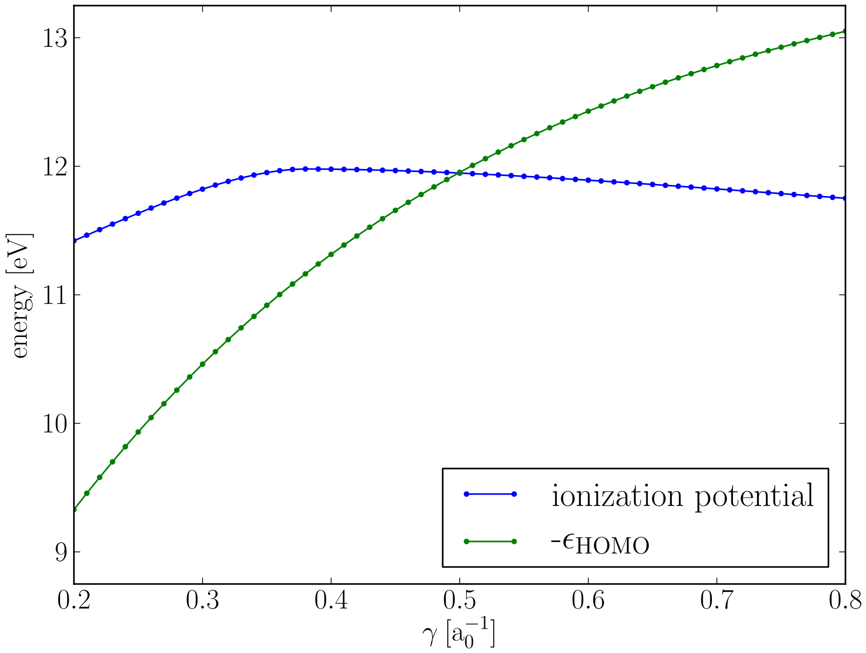

Figure 3.2 The ionization potential and the negative of the eigenvalue of the highest occupied Kohn-Sham orbital as a function of the range-separation parameter γ for the water dimer in its minimum energy geometry (one water molecule hydrogen-bonded to the other) calculated using the LC-BLYP functional.

potential theorem. One possibility would be to use the average of optima for different geometries, but this does not account for the magnitude of the error that using this value will introduce on average. Therefore, a better way is to find such a value of γ that minimizes the deviation from the ionization potential theorem when averaged over the ensemble. A priori, it is not clear that such a value should even exist. In principle, the optimal values for different geometries could be so different that it would make this approach useless. Before this procedure can be performed, we need to obtain the ensemble of structures. This can be done using molecular dynamics driven by a method known to give a good ground-state potential energy hypersurface for the given system. For water, BLYP-D2 fits that description well, although for small systems like the water dimer and water pentamer, we can afford ab initio molecular dynamics driven by MP2/6-311++G**, which is known to work well for water clusters [72]. In case we are interested in a chemical reaction, as is the case in this project, we should also include structures on the product side of the process. Thus, for the final optimal value of γ, we need to give equal weight in the tuning ensemble to structures of reactants and products. Performing the tuning for reactants and products will provide further information on the error of the resulting functional. An example of the average error as a function of γ for an ensemble of structures of the neutral water pentamer, is given in Figure 3.3. Even though these are preliminary results, it is encouraging that the lowest root mean square deviation from the ionization potential the-

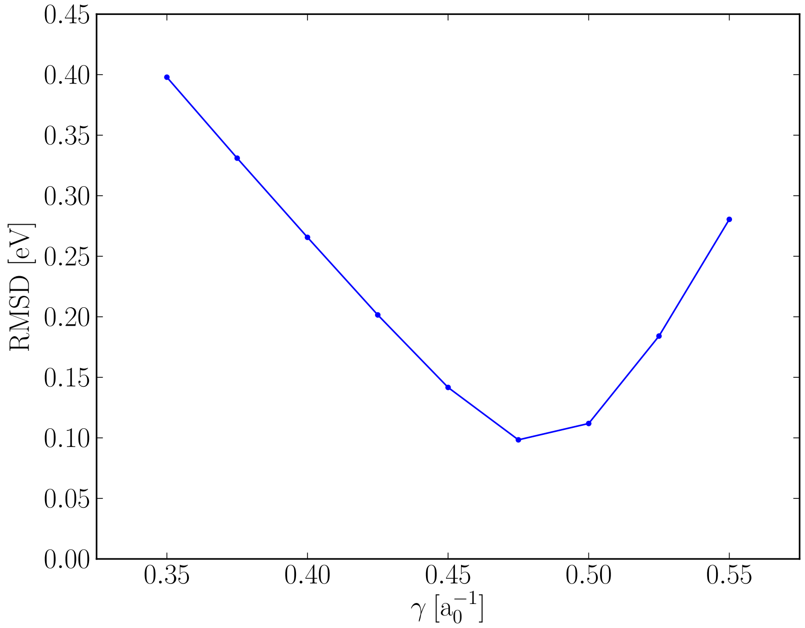

Figure 3.3 The root mean square deviation from the ionization potential theorem as a function of the range separation parameter γ calculated using the LC-BLYP functional over an ensemble of structures obtained with ab initio molecular dynamics at the MP2/6-311++G** level. Preliminary data is shown, final calculations will use a finer resolution in γ to better locate the minimum of the curve.

orem is less than 0.1 eV, suggesting that a single value of γ can be used for an ensemble of structures.

It is known from previous work that the optimal range separation parameter changes with the size of the system, even if the composition is the same. Although the method is in principle usable for the treatment of condensed systems in periodic boundary conditions, this is complicated by the problem of obtaining the ionization potential in periodic systems. Fortunately, an empirical relationship between the optimal γ and the optical dielectric constant of the material has been discovered [21], offering an easier, if less robust, way to set the parameter. Using the experimentally known ionization potential of liquid water as a target for the value of ϵ_{HOMO} (which is readily accessible even in periodic calculations) could be another alternative to the self-tuning performed in clusters.

This work is currently being prepared for publication in collaboration with Roi Baer from the Fritz Haber Research Center for Molecular Dynamics at the Hebrew University in Jerusalem.

CHAPTER

FOUR

DYNAMICS, STRUCTURE, AND REACTIVITY OF THE HYDRATED ELECTRON

In this chapter, we will present results of several related projects exploring the properties of an excess electron in aqueous systems — the hydrated electron. A total of five published papers containing most of these results is attached to the thesis. The process of vertical electron attachment to neat clusters of 32 water molecules at ambient temperature and its differences from the same process in clusters at cold temperatures are studied in reference 120. The details of vertical electron attachment to cold neat water clusters of the same size as before and the properties of the resulting cold anionic clusters are presented in reference 121. Reference 119 focuses on the reaction between a hydrated electron and a hydrated proton in a cluster of 32 water molecules. The same process is approached differently, starting from microhydration of the hydronium radical, in reference 123. The microhydration shows that there can be no localized hydronium radical in water, as already the addition of two water molecules displaces most of the spin density away from the hydronium species, creating a hydronium cation and a hydrated electron. These can then undergo the same hydrogen-forming reaction as was studied in the larger cluster. The review article 122 presents an overview of our work on ab initio molecular dynamics of anionic water clusters. Animations of some of the simulations are available on the attached DVD and they will be referenced where appropriate. All of the animations are provided in two different formats.

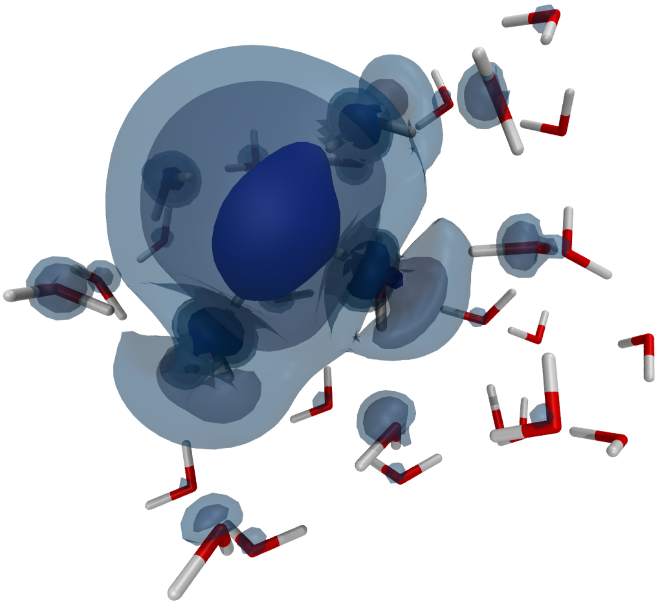

Figure 4.1 A snapshot of an anionic water cluster from a trajectory at 300 K. Isosurfaces of the spin density of the system show spatial distribution of the excess electron.

4.1 Anionic water clusters at ambient temperature

Let us start our treatment of the hydrated electron by looking at the properties of anionic water clusters. There are two aspects that we are interested in — equilibrium properties and the dynamics following vertical electron attachment. Throughout this work, we focus on a single cluster size, 32 water molecules, choosing to treat it in the best way affordable, rather than attempt to explore size dependence in a less rigorous way.

4.1.1 Equilibrium anionic water clusters at ambient temperature

First, let us consider equilibrium properties of such anionic water clusters. We need to obtain an equilibrated configuration, which can be achieved easily by using a halide anion, swapping it for an electron and equilibrating this new system. The electron always localizes in the cavity formed originally by the ion and that cavity needs to adapt to the new species. Then we run the system at 300 K with the CSVR thermostat, sampling the configurations of the equilibrium ensemble. This can be done in parallel using several independent trajectories in order to increase the total length of production simulation time obtained in a given amount of real time.

We monitor the total energy of the system to check the quenching of the transition from the configuration with the ion. Once the system is equilibrated, usually in several picoseconds, we collect data from the equilibrium ensemble. A total of roughly 25 ps of production simulation time was obtained. A representative snapshot of the system is show in Figure 4.1. In all the snapshots and animations presented in this thesis and in the published papers, two or more isosurfaces are used to display the contours of the spatial distribution of the spin density of the system. Figure 2 of reference 122 shows the radial distribution function of the spin density (green) and both the oxygen (red) and hydrogen (black) atoms around the center of the electron, which was calculated using (2.19). The curves are somewhat noisy due to limited statistics and compared to usual radial distribution functions in bulk solutions exhibit considerable smearing, which is due to increased disorder at the surface of the cluster. Nevertheless, they do feature clear peaks showing the structure of the solvation shell of the electron. An animation of one of the equilibrium runs is included on the attached DVD in the directory `animations/W32/anion/`. To characterize the excess electron in the cluster, we look at its radius of gyration, vertical detachment energy, and distances from the center of the cluster, as defined by (2.27) and (2.28). We examine the correlations of these quantities. The two panels of Figure 3 of reference 122 show the different behavior of the distance of the electron from the water cluster and the radius of gyration of the electron, calculated using (2.21). While VDE and r_g of the excess electron correlate strongly, there is little or no correlation between VDE and the distance of the electron from the cluster. This is true for both definitions of the distance of the two parts of the system, d_{COM} and d_{avg}. This result is qualitatively consistent with the results of single-electron pseudopotential models and is important for the interpretation of measured photoelectron spectra of anionic water clusters, where only the binding energy is available. These spectra should be understood in terms of the size of the electron, rather than its distance from the center of mass of the cluster.

We note that although evaporation of water molecules does occur in clusters at this temperature, it typically happens on the timescale of hundreds of picoseconds. In our simulations, we observe no evaporation and thus do not need to take any measures to deal with it. In simulations where this is an issue, a reflective spherical potential around the cluster would help to mitigate the problem.

These cluster simulations provide information on the local solvation structure of the first, and to some extent the second solvent shell. This is clearly confirmed by comparison to our latest work on the hydrated electron in bulk liquid water discussed at the end of this chapter. An important property of the results is the lack of any strong features in the distributions, for example the correlation of the radius of gyration and the vertical detachment energy. This is very typical for hydrated species, with the possible exception of multiply-charges ions, and is important for the interpretation of cluster experiments, as discussed below. These results serve as a reference for the non-equilibrium simulations of vertical electron attachment to both warm and cold clusters.

4.1.2 Vertical electron attachment to water clusters at ambient temperatures

To explore the relaxation dynamics of electrons in water clusters, to better understand their equilibrium properties and to shed light on experiments on anionic water clusters, we performed non-equilibrium simulations of vertical electron attachment to neutral water clusters. The results of these simulations were published in [120]. While the choice of a vertical process is an approximation, we opt for it for reasons stated in the chapter on methodology.

To perform these simulations, we start with neutral water clusters equilibrated at T=300 K using ab inito molecular dynamics. We take sample configurations from this distribution and use each as an initial condition of a new simulation, together with the attachment of an excess electron. It is important that this electron is attached simply by increasing the number of electrons in the density functional theory calculation by one and its distribution in the cluster is dictated entirely by what the ground state of this new system is. Thus no prejudice the author may hold about how the simulations should behave can influence the result, which is given entirely by the interactions in the system. Then, the system evolves in time from this vertical attachment and its properties are monitored the same way as before. This time, however, they are recorded as time-dependent quantities, as we are interested in the progress of this non-equilibrium process.

Let us first look at the radius of gyration as a way to characterize the size of the electron in the cluster. The distribution of the initial radii is shown in Figure 3 [120] on the left (in red), together with their subsequent evolution for six different trajectories (in different colors) and the average (in black). We can see a fast relaxation that is complete at about 1.5 ps. After that, the radii simply fluctuate around an equilibrium value. By comparing to the distribution of radii of gyration from the previously discussed equilibrium anionic water clusters, shown on the right of the same figure (in green), we can see that the relaxation is complete. Thus, after no more than 1.5 ps, the electrons attached to these warm water clusters relax to the equilibrium distribution and are indistinguishable from pre-equilibrated anionic water clusters. This is confirmed also by the same analysis of vertical detachment energies, as expected from the $r_g - VDE$ correlation discussed above. The data is shown in Figure 4 of reference 122. The comparison to the situation in cold anionic water clusters is discussed below.

Animations of two different trajectories are provided on the attached DVD in the directory `animations/W32/localize/`. Snapshots from one trajectory are also show as Figure 1 of the published paper [120]. By looking at the animations of trajectories, we can see a lot of disorder coming from the thermal fluctuations of the cluster. The excess electron is initially strongly delocalized over the surface of the cluster, but gradually moves to one patch of OH bonds that it reorients outwards. Then, it goes on to penetrate the fluctuating hydrogen-bonding network of the cluster, forming a cavity. The time scale of this process is seen in the above evolution of the radius of gyration — the cavity is formed in less than 1.5 ps.

Although most of the excess electron configurations in this medium-sized cluster of 32 water molecules are close to the surface for purely entropic reasons, they are bulk-like in their local structure, with a clear main lobe of the electron and an oriented first solvent shell. True surface states do exist during the localization dynamics, but only in its initial stages. These have an excess electron density that is very diffuse and exterior to the cluster, with no cavity formed by water molecules, only dangling OH bonds on the surface of the cluster.

Even though the attachment process studied here is relevant to measurements on anionic water clusters, it is very difficult to obtain clusters of this temperature experimentally. The reason for this is that on the timescale of the experiments, clusters created using supersonic expansion of similar techniques undergo evaporative cooling, decreasing their temperature significantly and becoming amorphous solid in the process [44]. To make direct contact with experimental results on clusters, we must modify our simulations to account for this.

4.2 Anionic water clusters at cold temperatures

To compute properties of clusters that are present in experiments, we perform analogous simulations as above, this time at significantly lower temperatures. We prepare the initial conditions by taking snapshots from the same neat water cluster trajectory at 300 K as before and energy-minimizing each such configuration. We then vertically attach an electron to each in the same way as above and initialize new velocities from a Maxwell distribution at low temperatures of 30–50 K. Starting independent simulations in this way, we simulate vertical electron attachment to cold water clusters. We do not mean to match the experimental conditions precisely, as they are not known very well anyway. It has been shown before that the details also depend on the thermal history of the neutral clusters before the attachment [66]. We merely want to achieve conditions that are in qualitative agreement with the experimental situation, which will help us interpret the general features of cold cluster experiments. We have published a detailed study using this computational setup [121].

The initial stages of the dynamics are similar to the case of the above clusters at ambient temperature, although everything is clearly slowed down at these cold temperatures. An animation of one trajectory is available at two different playback speeds on the attached DVD in the directory `animations/W32/localize-cold/`. Snapshots along this trajectory are displayed as Figure 1 of the published article [121]. The excess electron gradually moves to one part of the surface of the cluster, forming a cushion-like state that is diffuse and exterior to the cluster. However, in contrast with the previous case at ambient temperature, it does not go on to form a cavity, as the water hydrogen-bonding network stays rigid. This has implications for both the size and the binding energy of the electron. Looking at the time evolution of these quantities for different trajectories in Figures 3 and 4 of reference 121, it is clear that they do not approach the equilibrium distributions obtained previously. More importantly, if we plot the $r_g - VDE$ correlation and compare it to the equilibrium data, shown in Figure 6 of the same paper, we see that there is a gap that these cold trajectories never cross. Their excess electrons are generally larger and more weakly bound, when compared to the reference.

To account for some annealing that can occur in the experiments, we also prepare cold clusters in a different way. We take snapshots from the equilibrium distribution of anionic water clusters obtained previously, where a clearly defined cavity is almost always present, cool them to a low temperature and run molecular dynamics. The resulting cluster and its excess electron have a comparable temperature but very different properties from the clusters prepared by vertical electron attachment. The data is shown in blue for two different trajectories in Figures 3, 4 and 6 of the published paper. These electrons are generally more tightly bound and smaller in size. Their dynamics is completely unremarkable, as the solvation shell is fixed by the rigid hydrogen-bonding network, so the system only vibrates with a small amplitude around this local minimum.

For a comparison of the four different types of simulations, see Figures 4 and 5 of reference 122. The contrast between the two different types of electron attachment simulation is apparent in Figure 4. Figure 5 illustrates the possible annealing process by showing how the localization trajectories in warm clusters connect the distribution from localization in cold clusters with the equilibrium distribution.

As expected, all the clusters remain amorphous solid at these temperatures, as clearly seen from the time evolution of the root mean square deviation from the initial configuration depicted in Figure 8 of the published paper.

4.3 Interpretation of cluster experiments

As explained before, water clusters in experimental setups are always cold and amorphous solid. For this reason, we must look at the simulations of cold clusters if we want to interpret these measurements, including the assignment of the different isomers seen in the spectra. From our results, it is clear that the weakly bound experimental type II isomers are of the surface type — diffuse and weakly bound excess electrons, sitting at the exterior of the clusters. Type I isomers then correspond to the annealed localized electrons that we have prepared, with the detailed structure reported by Ma et al. [65] being beyond the resolution we can achieve with the extent of our simulations. Importantly, we see that the extrapolations to the aqueous bulk are not meaningful, as they implicitly change the temperature and cross a phase boundary. For isomer I, there is the possibility of a match, as the local structure is similar, only more compact and therefore more tightly bound. Incidentally, the experiment by Ma et al. [65] puts the clusters in contact with dilute helium close to room temperature. The abundance of the weakly bound isomers is significantly lower when compared to previous experiments that use a a different setup, which is interpreted as a result of this transient heating of the clusters. In second harmonic generation spectroscopy, which is surface sensitive, no evidence of excess electron density significantly protruding from the liquid is seen [82]. Detailed time-resolved photoelectron spectroscopy in a liquid microjet setup shows only a transient signal that could be attributed to surface electrons [11], which is consistent with the results of simulations of electron attachment to clusters at ambient temperatures.

Although one liquid microjet photoelectron spectroscopy experiment reported a signal at 1.6 eV that they attributed to a surface state of the hydrated electron [90], the statistics of that experiment is not entirely conclusive and the interpretation is inconsistent with both our computational results and recent experimental results. To explain the lifetime of their surface electron, reported to be more than 100 ps, the authors propose a barrier for the transition of the electron into the liquid. Finding a suitable mechanism for a barrier of this size does not seem to be easy. In reference 1 the authors admit that the originally proposed barrier to the transition is unlikely to exist, citing our published results. We note that such a claim could be made even based on well-known properties of liquid water and ions in solution. They suggest that the electron on the surface exists in an ion pair with H_2O^+, which is in turn stabilized by its solvation shell. Such explanation, however, does not seem to be any more plausible than the previous one, due to the extreme reactivity of the H_2O^+ species.

4.4 Atomic hydrogen formation

The importance of reactions of hydrated electrons with other solutes has been explained in the introduction. With this motivation, we have performed simulations of the most elementary of these reactions — that of the hydrated electron and a hydrated proton, forming a hydrogen atom. The results have been published [119].

As this is the earliest project concerning the hydrated electron, some aspects of the density functional setup are somewhat different from the other cluster calculations — certain changes were introduced over the years. The PBE functional is used with a triple-ζ polarized basis set with additional diffuse functions. No dispersion correction is applied. At the end of this chapter we provide a comparison of some of these different settings to estimate their influence on the results of our simulations.

We start with a cluster simulated using an empirical force field. The cluster comprises 31 water molecules, one H_3O^+ ion and one iodide ion, although any other halide anion would work. Taking sample configurations from this simulation and replacing the iodide with an electron, we start ab initio molecular dynamics trajectories at constant energy. Although more trajectories were simulated for the project, with slightly different settings, we report in the paper a set of ten consistent trajectories, out of which three end in a reaction of the two species, after roughly 1.7, 1, and 3.5 ps. Animations of all three reactive trajectories are available on the attached DVD in the directory `animations/W32/electron-proton/`. The other trajectories remained unreactive for the duration of time afforded by our computational resources, which was about 5 ps per trajectory.

Let us now proceed to the analysis of those three trajectories where the reaction has occured. All the trajectories have similar features, although they obviously differ due to different initial conditions and thermal noise. We start by visual inspection of the trajectory, both as an animation and as snapshots together with radial profiles in Figure 1 of the paper. Qualitatively, the electron behaves in a way similar to the clusters without an excess proton. It is notable that there is no direct attraction of the two oppositely charged species, as they are well hydrated by the cluster and their interaction is screened. The excess proton hops around the cluster and its identity changes, as covalent bonds emerge and disappear. This structural diffusion of the hydrated proton is well-understood [69]. It approaches the electron through one of the waters in its first solvent shell. At that moment, the distribution of the the excess electron is significantly distorted in a prolate shape, the proton transfers to the center of the original solvation cavity of the the excess electron and a hydrogen atom is formed. The process is therefore clearly a proton transfer, rather than electron transfer. This is surprising at first sight, due to the bare masses of the two species. In solution, however, it is the electron that is the heavier species, as its effective mass is determined by its solvent shell. This is confirmed when we look at two-dimensional projections of the positions of the two species in Figure 2 of the paper. Note that the triangular shapes are caused by vibrations of the hydronium cation. The two species coming into close contact is not sufficient — as can be seen in the electron-proton distances in the bottom two panels of the figure, there are times in both reactive and non-reactive trajectories when a reaction is attempted, but does not occur.

Seeking further insight, we examine the evolution of the spin density along the trajectory, quantified using the eigenvalues of the gyration tensor introduced earlier. Figure 3 of the published paper shows, for one particular trajectory, the three values in time, together with snapshots of configurations of different types. Looking at how much these values vary at different times, we can begin to understand what happens during the reaction. It is clear that one of the three values is much higher than the other two during the sharp decrease in size at the moment of the reaction. This impression can be best quantified when we calculate the radius of gyration and the relative shape anisotropy and plot their correlation for all the three trajectories, as shown in Figure 4 of the paper. The picture that then emerges is one of an equilibrium distribution at small but non-zero values of

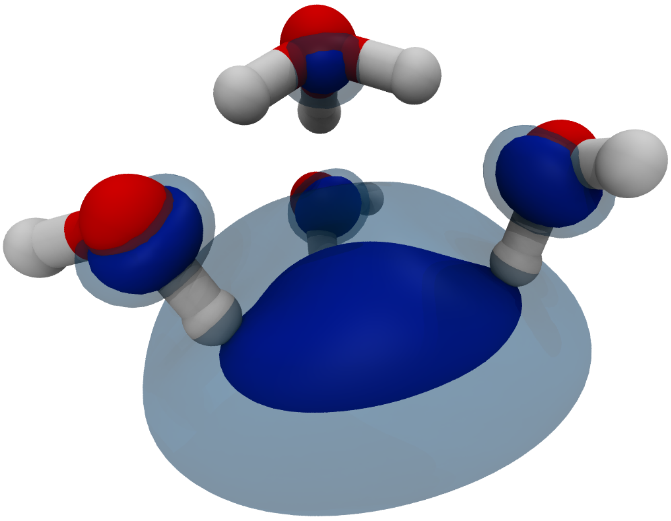

Figure 4.2 The initial structure of the $H_3O^+(H_2O)_3e^-_{aq}$ cluster.

κ^2 and values of r_g around 2.5 Å. From this distribution, there are attempted reactions in the direction of somewhat smaller sizes and significantly larger asymmetries. Three of those, in the different trajectories, result in a reaction, during which the asymmetry peaks and then returns almost to a zero value together with the shrinking of the spatial extent of the spin distribution to that of the hydrogen atom. These protrusions in the direction of the reaction exist also before the reaction occurs and in trajectories where no reaction occurs. The natural quesiton then is, are these an intrinsic feature of the hydrated electron, or are the induced by the presence of the proton? This question can be answered with the help of data that was obtained after this project was finished. Figure 7 of our review paper [122] show the same data together with the equilibrium distribution from anionic water clusters with no excess proton present. This distribution shows no sign of the fluctuations in the direction of the reaction. From this, we can conclude that they are induced by the presence of the proton, which initiates the reaction in this way.

Although the system gains a significant amount of potential energy, the ground-state energy of 13.6 eV of the newly formed hydrogen atom, it is not seen in the kinetic energy of the new atom or the rest of the water cluster. Indeed, experimentally, the free energy released in the reaction is only about 50 kJ mol^{-1} = 0.52 eV [86]. This is due to the significant hydration energies of the two charged reactant species, which are lost in the reaction, where the product is a neutral hydrogen atom.

Let us now turn to a much smaller cluster in which the same reaction can occur. Due to the decreased computational demands and lower complexity of the system, we can afford a rigorous search for the reaction coordinate and a more expensive electronic structure method — RI-MP2. These results have been published as part of our study of microhydration of the hydronium radical [123].

The small cluster comprises a hydronium cation, three water molecules and a hydrated electron. The structure that we start from is depicted in Figure 4.2. This is not the lowest energy structure of this cluster, as the excess proton and the excess electron can form a hydrogen atom. It is the process connecting these two states that we are interested in. For this, we perform nudged elastic band calculations [41, 40] connecting the two local minima using two different electronic structure methods. This reaction path-finding method uses a set of connected replicas of the system to obtain the minimum energy path between two local minima on a potential energy hypersurface, which is the ideal, 0 K reaction path of the process. Importantly, no assumptions need to be made on the reaction coordinate. We compare results from our DFT setup to those obtained using RI-MP2/aug-cc-pVTZ, which serve as a reference. Thanks to the small size of the system, we can afford to optimize self-consistent geometries of the reaction path with both methods.

The resulting energy profile along the reaction coordinate is shown in the top panel of Figure 7 of the published paper, together with some relevant interatomic distances in the bottom panel. Let us restrict the discussion of method comparison to noting that the DFT setup compares well to the much more expensive correlated method, especially for the barrier height, and leave the discussion of the details to the separate section on benchmarking below. Characteristics of the spin density are displayed in Figure 8 of the paper. An animation of the system moving along the minimum energy path from the reactants to the products, calculated using RI-MP2 is available on the attached DVD in the directory `animations/W3-H3O-RI-MP2/`. Looking at these results, it is remarkable that the reaction in this small cluster has all the features of the same process studied previously in a much larger cluster at a finite temperature. At the very beginning, the whole cluster compresses and the spin density shrinks in size. The reaction proceeds as a concerted transfer of two protons, with the one in the hydronium cation being the first to move. Capturing such a process smoothly without jumps in geometry would be problematic without a chain-of-states method like nudged elastic band. From the three eigenvalues of the gyration tensor, we can see that the spin distribution goes from oblate at the beginning to prolate during the reaction to spherical at the end. Relative shape anisotropy peaks clearly when the spin density is most distorted during the reaction, although it is interesting to note that this happens only after the reaction saddle point is passed. The potential energy difference between reactants and products is about -0.6 eV, comparable to the free energy released in the same reaction in bulk, as stated earlier. Snapshots showing maximum asymmetry for both the larger and smaller cluster are shown in Figure 4.3 for comparison. Although the approach take here does not capture temperature effects, it allow rigorous identification of the reaction coordinate and detailed analysis of the process along this coordinate without the noise introduced by a finite temperature. In this sense, this study is complementary to our previous treatment of the same process in the larger cluster.

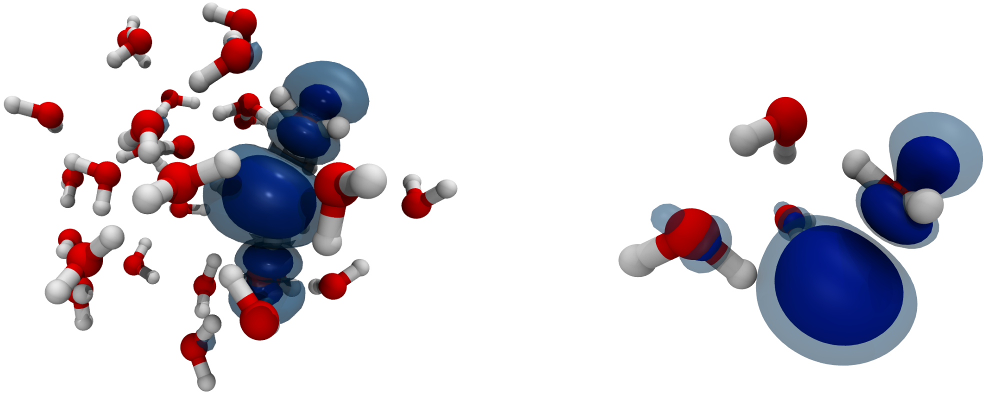

Figure 4.3 On the left, snapshot at the moment of maximum asymmetry of the spin density in the larger cluster taken from one of the reactive trajectories. On the right, snapshot at a value of reaction coordinate with maximum asymmetry of the spin density of the smaller cluster.

4.5 Bulk hydrated electron

The latest work on the hydrated electron performed in our group focuses on its structure in bulk liquid water and is yet unpublished. The actual calculations are being performed by Frank Uhlig. To increase the size of the periodic box and decrease the interaction of the excess electron with its periodic images, we employ a QM/MM setup with 32 or 64 water molecules treated with density functional theory and about 1000 water molecules treated with an empirical force field. This translates to a cubic box with edge length just over 30 Å. The electron needs to be contained entirely in the QM region, which is just about possible with 32 waters and certainly possibly with 64 waters. This setup allows us to obtain the radial distribution function of oxygen and hydrogen atoms around the center of the electron. The shape of the excess electron distribution can be characterized as before, but we focus on identifying the different regions of the system in which the electron density resides, as outlined in the chapter on methods. One of the results of this work is the confirmation that the local solvation structure of the excess electron in the medium-sized clusters that this thesis focuses on is very much like that in the bulk liquid. Preliminary results from a slab setup with an open surface also confirm the lack of stable diffuse surface states.

4.6 Benchmarking the computational setup

There are several aspects of our density functional theory setup that should be checked carefully to make sure that it provides an adequate description of the hydrated electron.

For sufficiently small systems we can compare directly to post-HF methods. We have done this for the small cluster that we use as a model for the electron-proton reaction — all the results are calculated independently using both RI-MP2 and the density functional theory setup described above. As Figure 7 of the published paper [123] shows, the methods match well, except for a small shift on the product side. In Figure 10, we show energy profiles along the reaction coordinate calculated using the original setup (blue) and its various modifications. Specifically, we can see that using the original SIC parameters a=0.2, b=0.0 (green), the barrier is lower and products are somewhat favored, but the overall reaction profile is preserved. Omitting the self-interaction correction entirely, on the other hand, completely distorts the profile and places the reactants and products at roughly the same energy. Omitting the diffuse basis functions provided by the ggg approach (cyan) compromises the description of the reactant state, increasing its energy by more than 0.5 eV. If both diffuse functions and SIC are left out of the calculation (gray), there is a certain amount of error cancellation, but the resulting energy profile is still far from satisfactory. This test clearly shows the importance of both the self interaction correction and diffuse basis functions.

A similar test can also be performed by using different settings to evaluate energies along a pre-calculated molecular dynamics trajectory. Results of such “replays” of one of our three reactive trajectories of the 32 water molecule cluster are shown in Figure 4.4. All the energies are shifted relative to the original calculation, which is therefore a constant zero, shown in black. The original calculation was performed with a traditionally augmented basis set and the blue curve shows that switching th molopt-TZV2P+ggg has almost no effect on the energy profile, apart from a constant shift and very small fluctuations. Using only the molopt-TZV2P basis set with no augmentation (cyan) destabilizes reactants relative to products, although not as much as in the previous case, where the excess electron density was more diffuse. The effects of modifying (red) or leaving out (green) the self-interaction correction are the most significant. In the case without SIC, products are severely destabilized by about 1 eV. Using the parameters a=0.3, b=0.2 has a smaller effect in the same direction.

In Figures 4.5 and 4.6 we show the convergence of two primary characteristics of the hydrated electron — its radius of gyration and vertical detachment energy. The plots use the same data as Figures 9 and 10 of our published paper [121], but show it in a better way — a spherical cutoff of the positions of the added ghost atoms (which hold the diffuse functions) increases along the horizontal axes, while the corresponding number of functions is shown at the top of the plot. For this benchmark, we use two very different geometries.

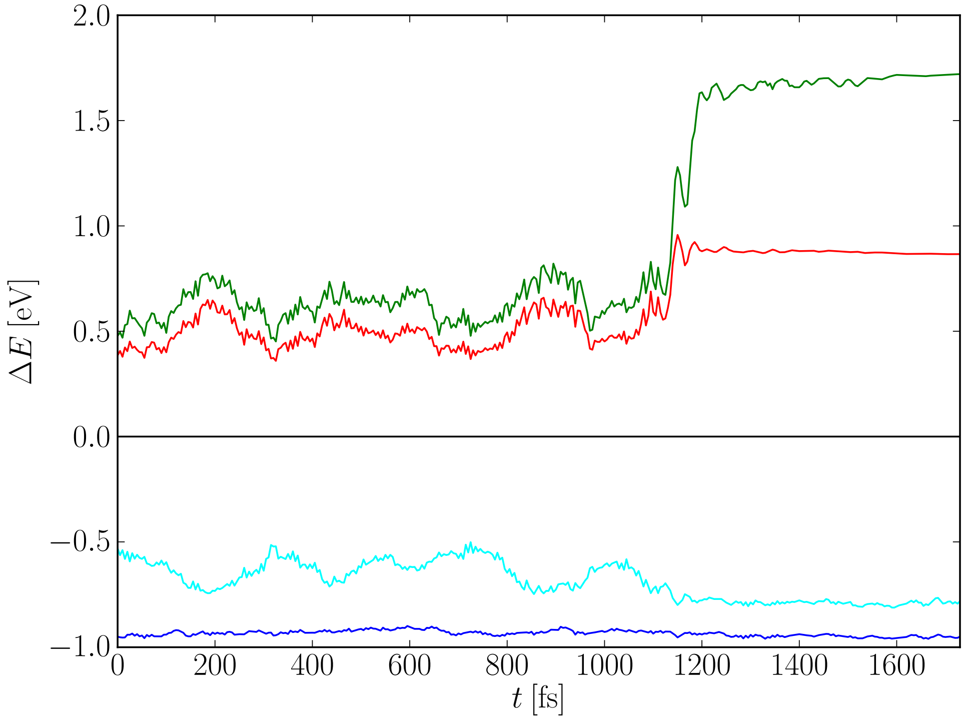

Figure 4.4 Relative energies for a reactive trajectory recalculated separately with different DFT setups. The original calculation (employed also to generate the trajectory) used ROKS with the augmented basis set and default settings (a=0.2, b=0) of the SIC (black). Change of basis to molopt-TZV2P (cyan), change of basis to molopt-TZV2P+ggg (blue), no SIC (green), and different SIC settings (a=0.3, b=0.2, red).

In Figure 4.5 the electron is localized in a cavity and is compact. In Figure 4.6 it is diffuse and exterior to the cluster, attached to three OH bonds on its surface. It is clear from the plots that diffuse functions are not important for the compact structure — convergence is relatively fast and the values do not change much. In the diffuse state, on the other hand, the use of diffuse functions is critical for correct description of the excess electron. This is also illustrated by the snapshots. We can conclude that although compact states could be represented quite well without augmentation, its use is needed for a balanced description of the hydrated electron.

This balance is especially important for the process of vertical electron attachment that we have studied. Therefore, we check the properties of the hydrated electron along one of the trajectories where an electron is attached to a cold water cluster, using different basis sets. In Figure 4.7 we plot three properties of the excess electron as a function of time along the trajectory. Clearly, just as before, the difference between traditional augmentation and ggg is negligible, although the latter is preferable for efficiency reasons, as explained earlier. Not using any augmentation has significant influence on the properties — the electron is smaller, more weakly bound and closer to the cluster. The impact would likely be even more severe in a trajectory that is actually evolved with such a setup.

The last issue that we will address as part of this benchmarking section is the application of the self-interaction correction to the singly occupied orbital in a restricted open-shell Kohn-Sham calculation. Using the same trajectory, we plot the same properties in Figure 4.8 for different setups. Not using the self-interaction correction changes the values substantially. Even this type of plain GGA density functional calculation is known to overbind the electron due to an unbalanced description of the anionic and neutral states. Clearly, this issue is made worse by the use of the self-interaction correction with the default parameters. Changing the parameters of the self-interaction correction causes only small changes to the radius of gyration and the distance and it almost entirely restores the binding energy. Based on these results, the new parameters for the self-interaction correction a=0.3, b=0.2 should be used in the future. Finally, we check that the use of unrestricted Kohn-Sham equations and a self-interaction correction applied to the spin density give results comparable to our restricted open-shell Kohn-Sham equations with the self-interaction applied to the spin density, which is also the density of the singly occupied orbital. The rerun with UKS is shown in blue and we can see that there is no influence on the binding energy. There is a noticeable decrease of the radius of gyration (which also transfers to the distance from the cluster), which comes from the fact that in the UKS calculations, the spin density has negative values in some regions of the system, whereas in ROKS, it can only be positive. This effect could be decreased for example by using the magnitude of the spin density in (2.22), which defines the radius of gyration, but it is not needed. The exact value of r_g is not important, we only need a measure of the spatial extent of the hydrated electron that is consistent across all the results.

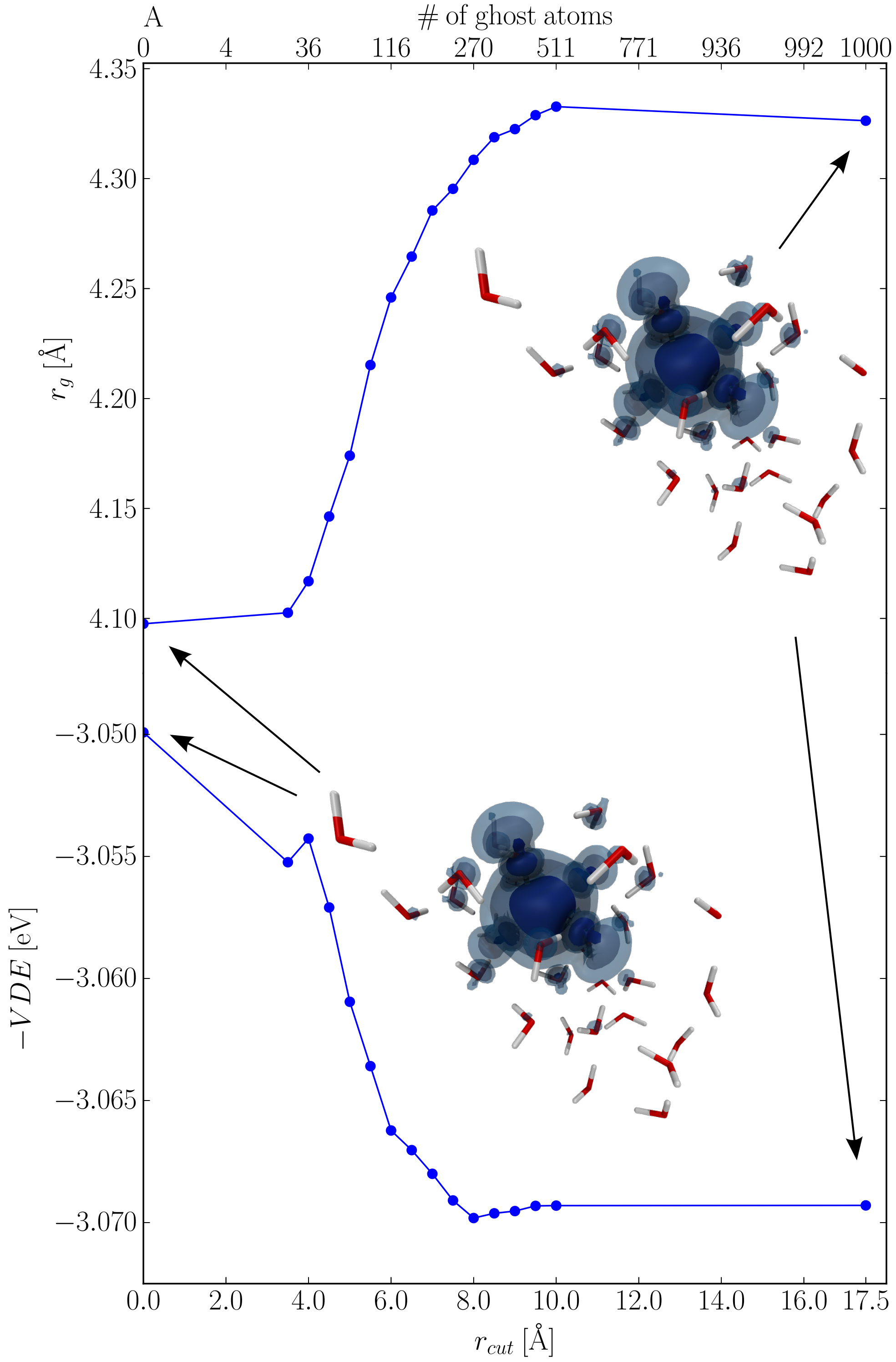

Figure 4.5 Radius of gyration (top panels) and vertical detachment energy (bottom panel) for a representative cluster geometry with the electron in a cavity as a function of the length of the spherical cutoff used for the generation of the additional diffuse Gaussian grid functions. The corresponding number of grid functions is shown at the top.

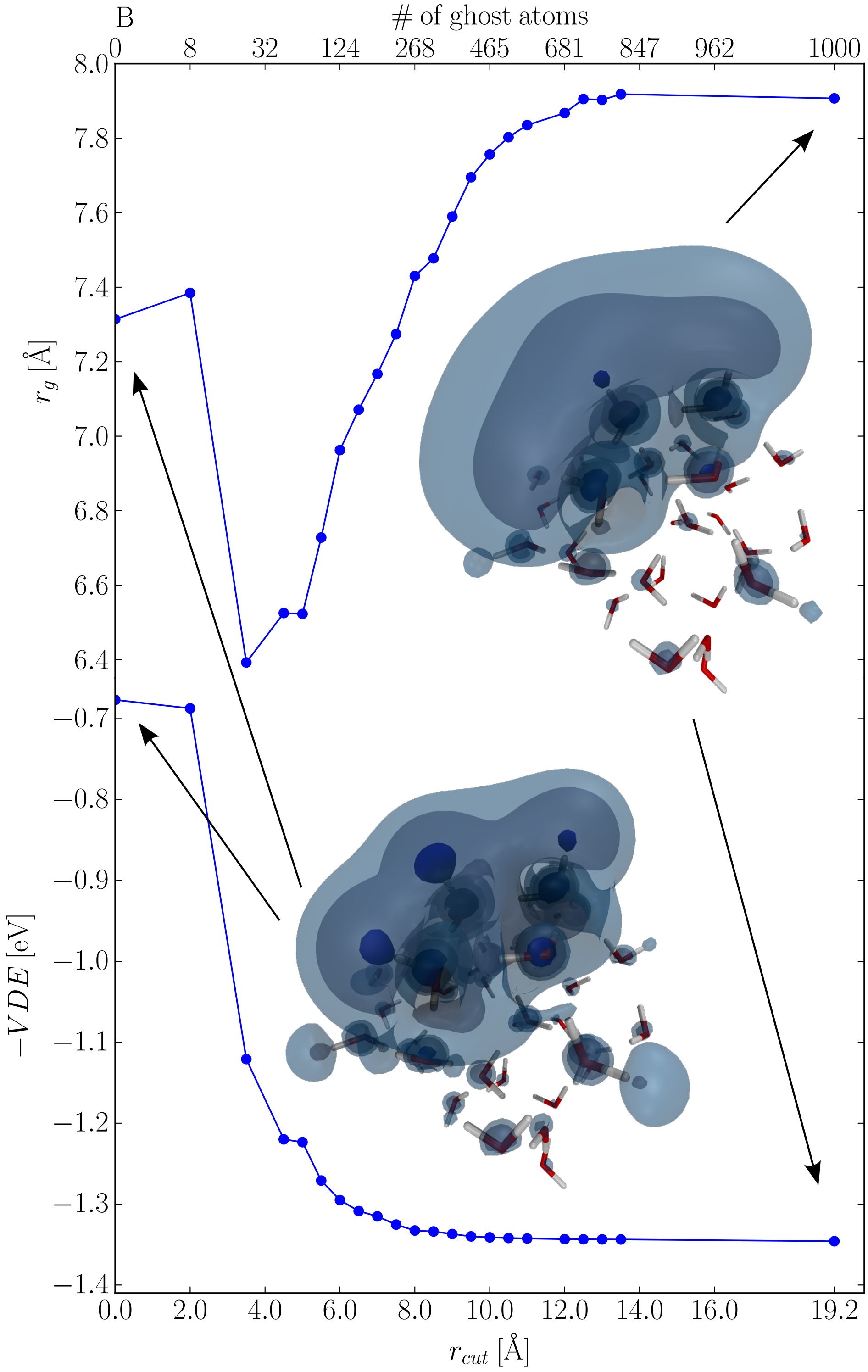

Figure 4.6 Radius of gyration (top panels) and vertical detachment energy (bottom panel) for a representative cluster geometry with a diffuse electron on the surface as a function of the length of the spherical cutoff used for the generation of the additional diffuse Gaussian grid functions. The corresponding number of grid functions is shown at the top.

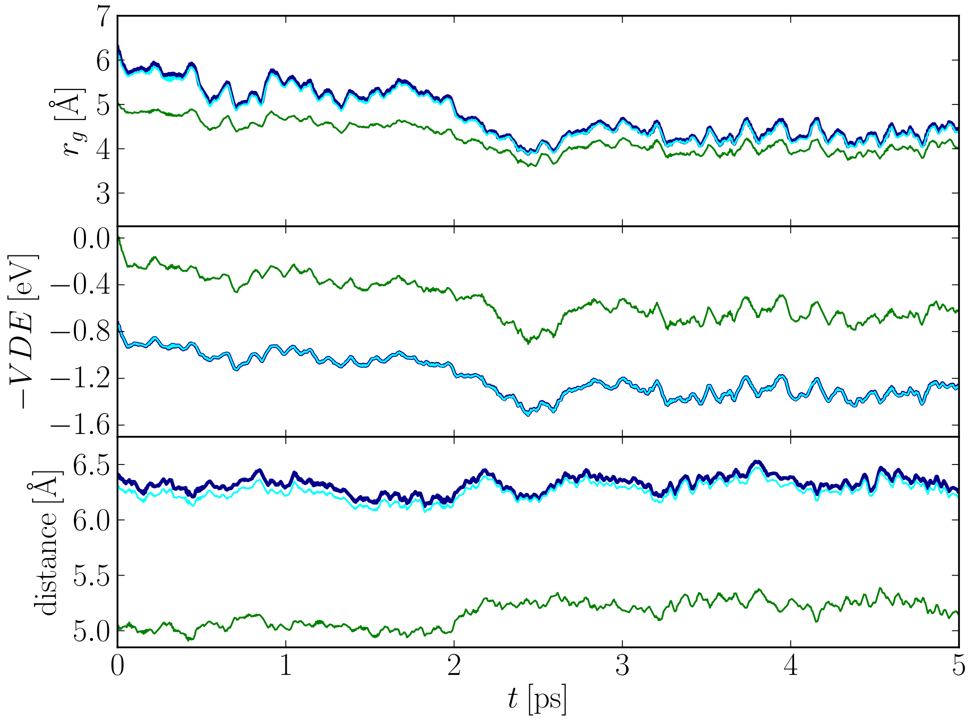

Figure 4.7 Time evolution of radius of gyration (top panel), vertical detachment energy (middle panel), and average distance of the excess electron from the cluster center of mass (bottom panel) for a selected cold localization trajectory, comparing different basis sets. The original calculation (employed also to generate the trajectory) used the molopt-TZV2P+ggg basis set and is shown in thick dark blue. A calculation using molopt-TZV2P without ggg is shown in green and a calculation using the aug-TZV2P basis set is shown in cyan.

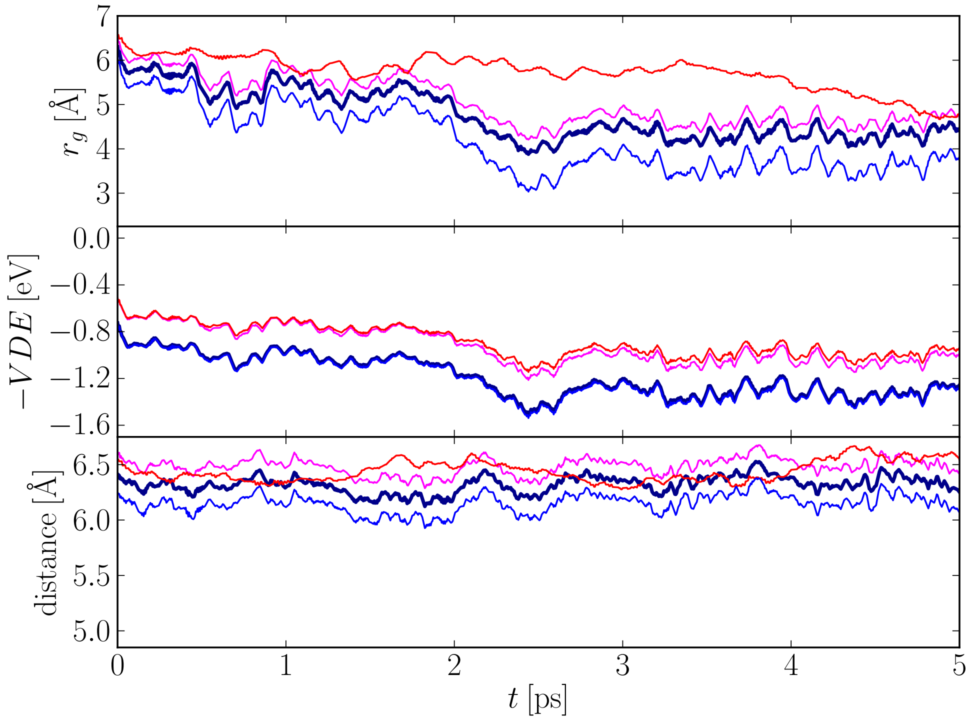

Figure 4.8 Time evolution of radius of gyration (top panel), vertical detachment energy (middle panel), and average distance of the excess electron from the cluster center of mass (bottom panel) for the same trajectory as in Figure 4.7, recalculated separately with different DFT setups. The original calculation (employed also to generate the trajectory) used ROKS and default SIC settings (a=0.2, b=0.0) and is shown in thick dark blue. A calculation with reparametrized SIC (a=0.3, b=0.2) is shown in magenta, a calculation without SIC is shown in red and a calculation with UKS instead of ROKS is shown in blue. All calculations were performed with the molopt-TZV2P+ggg basis.

While there is some freedom in the specific settings of our calculations, these tests show that our choices are justified and that they benchmark well where reference data is available.

CHAPTER

FIVE

CONCLUSIONS AND OUTLOOK

In this thesis, we have presented results on two different but related electronic charge defects in water — the cationic hole and the hydrated electron. These results have been published in a set of articles, which are attached to the thesis.

5.1 Summary of work done

Our primary method of choice was ab initio molecular dynamics, although it was supplemented by other methods as needed. For the calculation of electronic structure, we have focused on density functional theory, motivated by its favorable price-to-performance ratio. Its overall computational expense as well as the scaling of its implementation make it suitable for the description of extended condensed systems, including the use for ab initio molecular dynamics, which requires many calculations that need to be run in sequence. The quality of description of the energetics of many molecular systems is comparable to more expensive methods and superior to empirical force fields. With proper benchmarking against high-quality post-Hartree-Fock correlated methods, density functional theory can be used for the description of the challenging open-shell systems treated in this work. In both cases, the self-interaction correction for the singly-occupied orbital emerges as a crucial component of the setup used. Molecular simulations provide a high degree of control over the system together with spatial and temporal resolution unavailable in experiments. Taking advantage of these features, we have tried to address issues that arise in the interpretation of available data and provide information that is complementary to experiments.

After careful benchmarking, we have performed simulations of the process of photoionization of liquid water [118]. We have seen that the initial cationic hole is partially delocalized and that it is the localization of that hole that limits the time scale of the subsequent proton transfer reaction. In collaboration with our colleagues who have provided high-quality spectroscopic calculations, we have modelled the time-dependent optical spectrum of the process. Comparison to measured spectra shows that the ultrafast nature of the reaction keeps it just outside the reach of currently available experimental techniques, emphasizing the importance of simulations in cases like this one.

Our work on the hydrated electron focused on anionic water clusters [122]. One reason for this choice is the amount of work that has been done on anionic water clusters experimentally. Another reason is purely practical. The system that we have chosen, a cluster of 32 water molecules, is large enough to provide bulk-like local solvation structure of ionic species, yet reasonably computationally expensive, compared to what would be needed for a bulk condensed system. This allowed us to obtain a longer total simulation time and explore different aspects of the system and in more detail, compared to what would be possible for a much larger system. It also allowed us to fine-tune the computational setup so that when large calculations are performed, no computational resources are wasted. Calculations of the hydrated electron in bulk liquid water are currently under way in our group and they are among the most expensive simulations we have ever performed. In clusters, we have looked at equilibrium properties, attachment processes and a reaction of the hydrated electron with a proton. We have seen that the equilibrium hydrated electron at ambient temperature lacks any distinct structure in its photoelectron spectrum and that there are no distinct isomers [120]. This is in contrast with most experiments on anionic water clusters, where several different isomers are observed. To address this, we have performed simulations of cold anionic water clusters prepared in different ways, to mimic the experimental conditions [121]. We have identified different types of structures that we have assigned to the experimentally observed isomers. This difference between cold and warm anionic clusters has important consequences for the non-existence of diffuse weakly-bound surface states of hydrated electrons in liquid water. The conclusion that we draw is consistent with several different experimental techniques, including photoelectron spectroscopy on the liquid microjet, surface-sensitive second harmonic generation spectroscopy and photoelectron spectroscopy on anionic water clusters in an ion trap. The data that we get from our simulations can also be used as a reference for one-electron models of the hydrated electron, which are significantly cheaper computationally, but also rather sensitive to the way they are parametrized. We have also simulated the reaction of a hydrated electron with an excess proton at a finite temperature in the cluster of 32 water molecules [119] and we have examined the same process more carefully and with higher-quality methods in a much smaller cluster [123]. Surprisingly, the small model already has all the crucial features of the process in the larger cluster.

5.2 Future outlook

One aspect of the systems studied here that was not addressed in our treatment is the quantum nature of atomic nuclei. While considering them to be point particles with a charge and a mass is usually a very good approximation at ambient conditions, it has its limitations.

For hydrogen atoms or protons, there are appreciable nuclear quantum effects even at room temperature. This can be seen for example on the diffusion of excess protons in water, where the diffusion coefficient is underestimated by a factor of about 2 if the nuclei are treated classically. The different physical properties of normal and deuterated water point to the same issue. It is also known computationally that accounting for nuclear quantum effects changes the radial distribution functions, due to the smearing of the hydrogen positions.

In our simulations, there are several areas where the inclusion of nuclear quantum effects should be considered. Proton dynamics in both the electron-proton reaction and the reaction following photoionization of liquid water is certainly affected by the quantum nature of the proton. In simulations of cold clusters, the impact of quantum effects increases. The delocalization of protons increases and a portion of the degrees of freedom freeze out, which has significant effect on the heat capacity of the clusters. This effect is not captured in our setup at all, classical nuclei have a heat capacity of $k_B T/2$ per degree of freedom regardless of temperature.

Capturing nuclear quantum effects in large systems is both challenging and computationally expensive. One possible direction would be path integral molecular dynamics, which is only suitable for sampling equilibrium ensembles. The related methods of centroid molecular dynamics and ring polymer molecular dynamics can describe dynamic processes as well, but have their own limitations. In any case, addressing this aspect of the simulations is not a realistic goal in the near future.

There are several directions of future development suggested by the current status of the projects.

One issue that is not entirely resolved is the calculation of vertical detachment energy in periodic boundary conditions. Although methods to do this rigorously do exists, they either need significantly more simulation data to be able extrapolate to infinite box size, or are problematic for disordered systems like water.

The study of quenching reactions with species other than the excess proton would be interesting in the context of radiation chemistry, but is currently limited to closed-shell species. The treatment of two radical species in the same system is not possible with the current self-interaction correction method and new functionals would have to be developed to address this.

In general, the development of better density functionals could improve some of the results. While hybrid functionals show promise, they are significantly more expensive than GGA functionals.

Perhaps this work has seen at least some of the dreams of the future of ab initio molecular dynamics of previous authors [50] become reality. The author of this thesis is optimistic that with the increasing global computational resources and the methodological advances that can be expected soon, even the near future will bring many things not even dreamed of.

BIBLIOGRAPHY

[1] B Abel, U Buck, A L Sobolewski, and W Domcke. On the nature and signatures of the solvated electron in water. *Physical chemistry chemical physics : PCCP*, 14(1):22–34, January 2012. 1.3, 4.3

[2] M P Allen and D J Tildesley. *Computer Simulation of Liquids*. Oxford University Press, USA, June 1989. 2.1, 2.1.6

[3] Hans C Andersen. Molecular dynamics simulations at constant pressure and/or temperature. *The Journal of Chemical Physics*, 72(4):2384–2393, 1980. 2.1.5

[4] Marcel D Baer, Christopher J Mundy, Matthew J McGrath, I-F Will Kuo, J Ilja Siepmann, and Douglas J Tobias. Re-examining the properties of the aqueous vapor-liquid interface using dispersion corrected density functional theory. *The Journal of chemical physics*, 135(12):124712, September 2011. 2.5.1

[5] Roi Baer, Ester Livshits, and Ulrike Salzner. Tuned range-separated hybrids in density functional theory. *Annual review of physical chemistry*, 61(October 2009):85–109, March 2010. 3.3

[6] Roi Baer and Daniel Neuhauser. Density Functional Theory with Correct Long-Range Asymptotic Behavior. *Physical Review Letters*, 94(4):2–5, February 2005. 2.2.3, 3.3

[7] Robert N Barnett, Rina Giniger, Ori Cheshnovsky, and Uzi Landman. Dielectron Attachment and Hydrogen Evolution Reaction in Water Clusters. *The journal of physical chemistry. A*, June 2011. 1.4.1

[8] A D Becke. Density-functional exchange-energy approximation with correct asymptotic behavior. *Physical Review A*, 38(6):3098–3100, September 1988. 2.2.3, 2.5.1

[9] Mauro Boero. Excess electron in water at different thermodynamic conditions. *The journal of physical chemistry. A*, 111(49):12248–56, December 2007. 1.4.1

[10] Mauro Boero, Michele Parrinello, Kiyoyuki Terakura, Tamio Ikeshoji, and Chee Liew. First-Principles Molecular-Dynamics Simulations of a Hydrated Electron in Normal and Supercritical Water. *Physical Review Letters*, 90(22), June 2003. 1.4.1

[11] Franziska Buchner, Thomas Schultz, and Andrea Lübcke. Solvated electrons at the water-air interface: surface versus bulk signal in low kinetic energy photoelectron spectroscopy. *Physical chemistry chemical physics : PCCP*, 14(16):5837–42, April 2012. 1.3, 4.3

[12] Giovanni Bussi, Davide Donadio, and Michele Parrinello. Canonical sampling through velocity rescaling. *The Journal of chemical physics*, 126(1):014101, January 2007. 2.1.5

[13] Klaus Capelle. A bird's-eye view of density-functional theory. *eprint arXiv:cond-mat/0211443*, November 2002. 2.2

[14] R Car and M Parrinello. Unified Approach for Molecular Dynamics and Density-Functional Theory. *Physical Review Letters*, 55(22):2471–2474, November 1985. 2.3

[15] J V Coe, G H Lee, J G Eaton, S T Arnold, H W Sarkas, K H Bowen, C Ludewigt, H Haberland, and D R Worsnop. Photoelectron spectroscopy of hydrated electron cluster anions, (H[sub 2]O)[sup -][sub n = 2–69]. *The Journal of Chemical Physics*, 92(6):3980–3982, 1990. 1.3

[16] James V Coe, Susan T Arnold, Joseph G Eaton, Gang Ho Lee, and Kit H Bowen. Photoelectron spectra of hydrated electron clusters: Fitting line shapes and grouping isomers. *The Journal of chemical physics*, 125(1):014315, July 2006. 1.3

[17] C J Cramer. *Essentials Of Computational Chemistry: Theories And Models*. Wiley, 2004. 2, 2.2, 2.4

[18] Glenisson de Oliveira and Clifford E. Dykstra. Bond functions in the description of the water dimer. *Journal of Molecular Structure: THEOCHEM*, 337(1):1–7, July 1995. 2.2.2

[19] M. Dion, H. Rydberg, E. Schröder, D. C. Langreth, and B. I. Lundqvist. Van der Waals Density Functional for General Geometries. *Physical Review Letters*, 92(24):22–25, June 2004. 2.2.3

[20] Mayeul D'Avezac, Matteo Calandra, and Francesco Mauri. Density functional theory description of hole-trapping in SiO2: A self-interaction-corrected approach. *Physical Review B*, 71(20):1–5, May 2005. 2.2.3

[21] Helen R Eisenberg and Roi Baer. A new generalized Kohn-Sham method for fundamental band-gaps in solids. *Physical chemistry chemical physics : PCCP*, 11(22):4674–80, June 2009. 3.3

[22] J Enkovaara, C Rostgaard, J J Mortensen, J Chen, M Dułak, L Ferrighi, J Gavnholt, C Glinsvad, V Haikola, H a Hansen, H H Kristoffersen, M Kuisma, a H Larsen, L Lehtovaara, M Ljungberg, O Lopez-Acevedo, P G Moses, J Ojanen, T Olsen, V Petzold, N a Romero, J Stausholm-Mø ller, M Strange, G a Tritsaris, M Vanin, M Walter, B Hammer, H Häkkinen, G K H Madsen, R M Nieminen, J K Nø rskov, M Puska, T T Rantala, J Schiø tz, K S Thygesen, and K W Jacobsen. Electronic structure calculations with GPAW: a real-space implementation of the projector augmented-wave method. *Journal of physics. Condensed matter : an Institute of Physics journal*, 22(25):253202, June 2010. 2.2.2

[23] Enrico Fermi. Un Metodo Statistico per la Determinazione di alcune Priopriet à dell'Atomo. *Rend. Accad. Naz. Lincei*, 6:602–607, 1927. 2.2

[24] Richard Feynman, Robert Leighton, and Matthew Sands. *The Feynman Lectures on Physics*, volume 1. Addison-Wesley, Boston, second edition, 1963. 2.1.6

[25] Daan Frenkel and B Smit. *Understanding Molecular Simulation (Computational Science Series, Vol 1)*. Academic Press, October 2001. 2.1

[26] Tomaso Frigato, Joost VandeVondele, Burkhard Schmidt, Christof Schütte, and Pavel Jungwirth. Ab initio molecular dynamics simulation of a medium-sized water cluster anion: from an interior to a surface-located excess electron via a delocalized state. *The journal of physical chemistry. A*, 112(27):6125–33, July 2008. 1.4.1

[27] A Furuhama, M Dupuis, and K Hirao. Reactions associated with ionization in water: a direct ab initio dynamics study of ionization in (H2O)17. *The Journal of chemical physics*, 124(16):164310, 2006. 1.4.2

[28] Bruce C Garrett, David A Dixon, Donald M Camaioni, Daniel M Chipman, Mark A Johnson, Charles D Jonah, Gregory A Kimmel, John H Miller, Thomas N Rescigno, Peter J. Rossky, Sotiris S Xantheas, Steven D Colson, Allan H Laufer, Douglas Ray, Paul F. Barbara, David M. Bartels, Kurt H Becker, Kit H Bowen, Stephen E. Bradforth, Ian Carmichael, James V Coe, L Rene Corrales, James P Cowin, Michel Dupuis, Kenneth B Eisenthal, James A Franz, Maciej S Gutowski, Kenneth D Jordan, Bruce D Kay, Jay A Laverne, Sergei V Lymar, Theodore E Madey, C William McCurdy, Dan Meisel, Shaul Mukamel, Anders R Nilsson, Thomas M Orlando, Nikolay G Petrik, Simon M Pimblott, James R Rustad, Gregory K Schenter, Sherwin J Singer, Andrei Tokmakoff, Lai-Sheng Wang, Curt Wettig, and Timothy S

Zwier. Role of water in electron-initiated processes and radical chemistry: issues and scientific advances. *Chemical reviews*, 105(1):355–90, 2005. 1, 1.1

[29] Y. Gauduel, S. Pommeret, A. Migus, and A. Antonetti. Some evidence of ultrafast H2O+-water molecule reaction in femtosecond photoionization of pure liquid water: Influence on geminate pair recombination dynamics. *Chemical Physics*, 149(1-2):1–10, December 1990. 1.3

[30] Luigi Genovese, Thierry Deutsch, and Stefan Goedecker. Efficient and accurate three-dimensional Poisson solver for surface problems. *The Journal of Chemical Physics*, 127(5):054704–6, August 2007. 2.5.1

[31] Luigi Genovese, Thierry Deutsch, Alexey Neelov, Stefan Goedecker, and Gregory Beylkin. Efficient solution of Poisson's equation with free boundary conditions. *The Journal of chemical physics*, 125(7):074105, August 2006. 2.5.1

[32] S. Goedecker, M. Teter, and Jürg Hutter. Separable dual-space Gaussian pseudopotentials. *Physical Review B*, 54(3):1703–1710, 1996. 2.5.1

[33] Stefan Grimme. Accurate description of van der Waals complexes by density functional theory including empirical corrections. *Journal of computational chemistry*, 25(12):1463–73, September 2004. 2.2.3

[34] Stefan Grimme. Semiempirical GGA-type density functional constructed with a long-range dispersion correction. *Journal of computational chemistry*, 27(15):1787–99, 2006. 2.2.3, 2.5.1

[35] Stefan Grimme, Jens Antony, Stephan Ehrlich, and Helge Krieg. A consistent and accurate ab initio parametrization of density functional dispersion correction (DFT-D) for the 94 elements H-Pu. *The Journal of chemical physics*, 132(15):154104, April 2010. 2.2.3

[36] Stefan Grimme, Stephan Ehrlich, and Lars Goerigk. Effect of the damping function in dispersion corrected density functional theory. *Journal of computational chemistry*, 32(7):1456–65, May 2011. 2.2.3

[37] Manuel Guidon, Jürg Hutter, and Joost VandeVondele. Robust Periodic Hartree-Fock Exchange for Large-Scale Simulations Using Gaussian Basis Sets. *Journal of Chemical Theory and Computation*, 5(11):3010–3021, November 2009. 2.2.3

[38] Manuel Guidon, Jürg Hutter, and Joost VandeVondele. Auxiliary Density Matrix Methods for Hartree-Fock Exchange Calculations. *Journal of Chemical Theory and Computation*, 6(8):2348–2364, August 2010. 2.2.3

[39] Trygve Helgaker and Jan Almlöf. Molecular wave functions and properties calculated using floating Gaussian orbitals. *The Journal of Chemical Physics*, 89(8):4889, 1988. 2.2.2

[40] Graeme Henkelman and Hannes Jónsson. Improved tangent estimate in the nudged elastic band method for finding minimum energy paths and saddle points. *The Journal of Chemical Physics*, 113(22):9978, 2000. 4.4

[41] Graeme Henkelman, Blas P. Uberuaga, and Hannes Jónsson. A climbing image nudged elastic band method for finding saddle points and minimum energy paths. *The Journal of Chemical Physics*, 113(22):9901, 2000. 4.4

[42] John M Herbert and Martin Head-Gordon. Accuracy and limitations of second-order many-body perturbation theory for predicting vertical detachment energies of solvated-electron clusters. *Physical chemistry chemical physics : PCCP*, 8(1):68–78, January 2006. 1.4.1

[43] John M Herbert and Leif D Jacobson. Structure of the aqueous electron: assessment of one-electron pseudopotential models in comparison to experimental data and time-dependent density functional theory. *The journal of physical chemistry. A*, 115(50):14470–83, December 2011. 1.4.1

[44] C. Hock, M. Schmidt, R. Kuhnen, C. Bartels, L. Ma, H. Haberland, and B. V.Issendorff. Calorimetric Observation of the Melting of Free Water Nanoparticles at Cryogenic Temperatures. *Physical Review Letters*, 103(7):1–4, August 2009. 4.1.2

[45] P. Hohenberg. Inhomogeneous Electron Gas. *Physical Review*, 136(3B):B864–B871, November 1964. 2.2

[46] William G Hoover. Canonical dynamics: Equilibrium phase-space distributions. *Physical Review A*, 31(3):1695+, March 1985. 2.1.5

[47] Leif D Jacobson and John M Herbert. A one-electron model for the aqueous electron that includes many-body electron-water polarization: Bulk equilibrium structure, vertical electron binding energy, and optical absorption spectrum. *The Journal of chemical physics*, 133(15):154506, October 2010. 1.4.1

[48] Leif D Jacobson and John M Herbert. Comment on ”Does the hydrated electron occupy a cavity?”. *Science*, 331(6023):1387, March 2011. 1.4.1

[49] Leif D Jacobson, Christopher F Williams, and John M Herbert. The static-exchange electron-water pseudopotential, in conjunction with a polarizable water model: a new Hamiltonian for hydrated-electron simulations. *The Journal of chemical physics*, 130(12):124115, March 2009. 1.4.1

[50] Pavel Jungwirth. Ab Initio Molecular Dynamics - Dreams and Reality (Study of Selected Thermal Chemical Processes in Solution Using Classical Computer Simulations and ab initio Quantum Chemical Methods). *Candidate of Sciences Thesis*, 1993. 5.2

[51] Petr Jurečka, Jiří Černý, Pavel Hobza, and Dennis R Salahub. Density functional theory augmented with an empirical dispersion term. Interaction energies and geometries of 80 noncovalent complexes compared with ab initio quantum mechanics calculations. *Journal of computational chemistry*, 28(2):555–69, January 2007. 2.2.3

[52] W Koch and M C Holthausen. *A chemist's guide to density functional theory*. Wiley-VCH, 2000. 2.2

[53] W. Kohn and L. J. Sham. Self-Consistent Equations Including Exchange and Correlation Effects. *Physical Review*, 140(4A):A1133–A1138, November 1965. 2.2

[54] Jiří Kolafa. Time-reversible always stable predictor-corrector method for molecular dynamics of polarizable molecules. *Journal of computational chemistry*, 25(3):335–42, February 2004. 2.3, 2.5.1

[55] Anna I Krylov. Equation-of-motion coupled-cluster methods for open-shell and electronically excited species: the Hitchhiker's guide to Fock space. *Annual review of physical chemistry*, 59:433–62, January 2008. 1.4.2, 3.1

[56] Thomas Kühne, Matthias Krack, Fawzi Mohamed, and Michele Parrinello. Efficient and Accurate Car-Parrinello-like Approach to Born-Oppenheimer Molecular Dynamics. *Physical Review Letters*, 98(6):1–4, February 2007. 2.3

[57] R. E. Larsen, W. J. Glover, and B. J. Schwartz. Does the Hydrated Electron Occupy a Cavity? *Science*, 329(5987):65–69, July 2010. 1.4.1

[58] R. E. Larsen, W. J. Glover, and B. J. Schwartz. Response to Comments on "Does the Hydrated Electron Occupy a Cavity?". *Science*, 331(6023):1387–1387, March 2011. 1.4.1

[59] Chengteh Lee, Weitao Yang, and Robert G Parr. Development of the Colle-Salvetti correlation-energy formula into a functional of the electron density. *Physical Review B*, 37(2):785–789, January 1988. 2.2.3, 2.5.1

[60] Lippert G., Jürg Hutter, Parrinello M., Gerald Lippert, and Michele Parrinello. A hybrid Gaussian and plane wave density functional scheme. *Molecular Physics*, 92(3):477–488, October 1997. 2.2.2

[61] Yi Liu and Dawn a. Yarne. Ab initio molecular dynamics calculations with simple, localized, orthonormal real-space basis sets. *Physical Review B*, 68(12):1–8, September 2003. 2.2.2

[62] Ester Livshits and Roi Baer. A density functional theory for symmetric radical cations from bonding to dissociation. *The journal of physical chemistry. A*, 112(50):12789–91, December 2008. 3.3

[63] Ester Livshits, Rebecca S Granot, and Roi Baer. A density functional theory for studying ionization processes in water clusters. *The journal of physical chemistry. A*, 115(23):5735–44, June 2011. 1.4.2, 3.3

[64] Andrea Lübcke, Franziska Buchner, Nadja Heine, Ingolf V Hertel, and Thomas Schultz. Time-resolved photoelectron spectroscopy of solvated electrons in aqueous NaI solution. *Physical chemistry chemical physics : PCCP*, 12(43):14629–34, November 2010. 1.3

[65] Lei Ma, Kiran Majer, Fabien Chirot, and Bernd von Issendorff. Low temperature photoelectron spectra of water cluster anions. *The Journal of chemical physics*, 131(14):144303, 2009. 1.3, 4.3

[66] Ádám Madarasz, Peter J. Rossky, and László Turi. Response of observables for cold anionic water clusters to cluster thermal history. *The journal of physical chemistry. A*, 114(6):2331–7, February 2010. 4.2

[67] G.J. Martyna, Mark E. Tuckerman, D.J. Tobias, and M.L. Klein. Explicit reversible integrators for extended systems dynamics. *Molecular Physics*, 87(5):1117–1157, April 1996. 2.1.6

[68] Glenn J Martyna, Michael L Klein, and Mark E. Tuckerman. Nosé–Hoover chains: The canonical ensemble via continuous dynamics. *The Journal of Chemical Physics*, 97(4):2635, 1992. 2.1.5

[69] D Marx, ME Tuckerman, and J Hutter. The nature of the hydrated excess proton in water. *Nature*, pages 601–604, 1999. 4.4

[70] Dominik Marx and Jürg Hutter. *Ab Initio Molecular Dynamics: Basic Theory and Advanced Methods*. Cambridge University Press, 2009. 2.3

[71] Yifat Miller, Barbara J Finlayson-Pitts, and R Benny Gerber. Ionization of N2O4 in contact with water: mechanism, time scales and atmospheric implications. *Journal of the American Chemical Society*, 131(34):12180–5, September 2009. 2.3

[72] Yifat Miller and R Benny Gerber. Dynamics of proton recombination with NO3- anion in water clusters. *Physical chemistry chemical physics : PCCP*, 10(8):1091–3, February 2008. 2.3, 3.3

[73] R G Parr and W Yang. *Density-Functional Theory of Atoms and Molecules*. International Series of Monographs on Chemistry. Oxford University Press, 1994. 2.2

[74] M Parrinello and A Rahman. Crystal Structure and Pair Potentials: A Molecular-Dynamics Study. *Phys. Rev. Lett.*, 45(14):1196–1199, October 1980. 2.1.5

[75] J E Pask and P a Sterne. Finite element methods in ab initio electronic structure calculations. *Modelling and Simulation in Materials Science and Engineering*, 13(3):R71–R96, April 2005. 2.2.2

[76] J. P. Perdew. Self-interaction correction to density-functional approximations for many-electron systems. *Physical Review B*, 23(10):5048–5079, May 1981. 2.2.3

[77] Jp Perdew, K Burke, and M Ernzerhof. Generalized Gradient Approximation Made Simple. *Physical review letters*, 77(18):3865–3868, October 1996. 2.2.3, 2.5.1

[78] Piotr A Pieniazek, Eric J Sundstrom, Stephen E. Bradforth, and Anna I Krylov. Degree of initial hole localization/delocalization in ionized water clusters. *The journal of physical chemistry. A*, 113(16):4423–9, April 2009. 1.4.2, 3.1, 3.2.1

[79] Piotr A Pieniazek, Joost VandeVondele, Pavel Jungwirth, Anna I Krylov, and Stephen E. Bradforth. Electronic structure of the water dimer cation. *The journal of physical chemistry. A*, 112(27):6159–70, 2008. 1.4.2, 3.1

[80] Eva Pluhařová, Pavel Jungwirth, Stephen E Bradforth, and Petr Slavíček. Ionization of purine tautomers in nucleobases, nucleosides, and nucleotides: from the gas phase to the aqueous environment. *The journal of physical chemistry. B*, 115(5):1294–305, February 2011. 2.4

[81] Peter J. Rossky and Jurgen Schnitker. The hydrated electron: quantum simulation of structure, spectroscopy, and dynamics. *The Journal of Physical Chemistry*, 92(15):4277–4285, July 1988. 1.4.1

[82] D M Sagar, Colin D Bain, and Jan R R Verlet. Hydrated electrons at the water/air interface. *Journal of the American Chemical Society*, 132(20):6917–9, May 2010. 1.3, 4.3

[83] Jochen Schmidt, Joost VandeVondele, I-F William Kuo, Daniel Sebastiani, J Ilja Siepmann, Jürg Hutter, and Christopher J Mundy. Isobaric-isothermal molecular dynamics simulations utilizing density functional theory: an assessment of the

structure and density of water at near-ambient conditions. *The journal of physical chemistry. B*, 113(35):11959–64, September 2009. 2.5.1

[84] Jürgen Schnitker and Peter J. Rossky. An electron–water pseudopotential for condensed phase simulation. *The Journal of Chemical Physics*, 86(6):3462, March 1987. 1.4.1

[85] A Seidl, A Görling, P Vogl, Ja Majewski, and M Levy. Generalized Kohn-Sham schemes and the band-gap problem. *Physical review. B, Condensed matter*, 53(7):3764–3774, February 1996. 2.2.1

[86] Hirotsugu Shiraishi, Geni R. Sunaryo, and Kenkichi Ishigure. Temperature Dependence of Equilibrium and Rate Constants of Reactions Inducing Conversion between Hydrated Electron and Atomic Hydrogen. *The Journal of Physical Chemistry*, 98(19):5164–5173, May 1994. 4.4

[87] Ilya a Shkrob. The structure of the hydrated electron. Part 1. Magnetic resonance of internally trapping water anions: a density functional theory study. *The journal of physical chemistry. A*, 111(24):5223–31, June 2007. 1.4.1

[88] Ilya a Shkrob, William J Glover, Ross E Larsen, and Benjamin J Schwartz. The structure of the hydrated electron. Part 2. A mixed quantum/classical molecular dynamics embedded cluster density functional theory: single-excitation configuration interaction study. *The journal of physical chemistry. A*, 111(24):5232–43, June 2007. 1.4.1

[89] Alexander T. Shreve, Terry a. Yen, and Daniel M. Neumark. Photoelectron spectroscopy of hydrated electrons. *Chemical Physics Letters*, 493(4-6):216–219, June 2010. 1.3

[90] Katrin R. Siefermann, Yaxing Liu, Evgeny Lugovoy, Oliver Link, Manfred Faubel, Udo Buck, Bernd Winter, and Bernd Abel. Binding energies, lifetimes and implications of bulk and interface solvated electrons in water. *Nature chemistry*, 2(4):274–9, April 2010. 1.3, 4.3

[91] Andrzej L Sobolewski and Wolfgang Domcke. Computational studies of aqueous-phase photochemistry and the hydrated electron in finite-size clusters. *Physical chemistry chemical physics : PCCP*, 9(29):3818–29, August 2007. 1.4.1

[92] Julia Stähler, Cornelius Gahl, and Martin Wolf. Dynamics and Reactivity of Trapped Electrons on Supported Ice Crystallites. *Accounts of chemical research*, 45(1):131–138, December 2012. 1.1

[93] William C Swope, Hans C Andersen, Peter H Berens, and Kent R Wilson. A computer simulation method for the calculation of equilibrium constants for the formation of physical clusters of molecules: Application to small water clusters. *The Journal of Chemical Physics*, 76(1):637–649, 1982. 2.1.6

[94] Ying Tang, Huan Shen, Kentaro Sekiguchi, Naoya Kurahashi, Tomoya Mizuno, Yoshi-ichi Suzuki, and Toshinori Suzuki. Direct measurement of vertical binding energy of a hydrated electron. *Physical chemistry chemical physics : PCCP*, 12(15):3653–5, April 2010. 1.3

[95] Doros N. Theodorou and Ulrich W. Suter. Shape of unperturbed linear polymers: polypropylene. *Macromolecules*, 18(6):1206–1214, November 1985. 2.4

[96] L H Thomas. The calculation of atomic fields. In *Mathematical Proceedings of the Cambridge Philosophical Society*, volume 23, pages 542–548. Cambridge Univ Press, 1927. 2.2

[97] Alexandre Tkatchenko and Matthias Scheffler. Accurate Molecular Van Der Waals Interactions from Ground-State Electron Density and Free-Atom Reference Data. *Physical Review Letters*, 102(7):6–9, February 2009. 2.2.3

[98] Teodora Todorova, Ari P Seitsonen, Jürg Hutter, I-Feng W Kuo, and Christopher J Mundy. Molecular dynamics simulation of liquid water: hybrid density functionals. *The Journal of Physical Chemistry B*, 110(8):3685–91, March 2006. 3.2.1

[99] M. Tuckerman, B. J. Berne, and G. J. Martyna. Reversible multiple time scale molecular dynamics. *The Journal of Chemical Physics*, 97(3):1990, 1992. 2.1.6

[100] Mark E. Tuckerman. *Statistical Mechanics: Theory and Molecular Simulation*. Oxford Graduate Texts. Oxford University Press, 2010. 2.1

[101] László Turi and Daniel Borgis. Analytical investigations of an electron–water molecule pseudopotential. II. Development of a new pair potential and molecular dynamics simulations. *The Journal of Chemical Physics*, 117(13):6186, 2002. 1.4.1

[102] László Turi, Marie-Pierre Gaigeot, Nicolas Levy, and Daniel Borgis. Analytical investigations of an electron–water molecule pseudopotential. I. Exact calculations on a model system. *The Journal of Chemical Physics*, 114(18):7805, 2001. 1.4.1, 2.2.2

[103] László Turi and Adám Madarász. Comment on "Does the hydrated electron occupy a cavity?". *Science*, 331(6023):1387, March 2011. 1.4.1

[104] László Turi, Wen-Shyan Sheu, and Peter J Rossky. Characterization of excess electrons in water-cluster anions by quantum simulations. *Science (New York, N.Y.)*, 309(5736):914–7, August 2005. 1.4.1

[105] Eric Vanden-Eijnden and Giovanni Ciccotti. Second-order integrators for Langevin equations with holonomic constraints. *Chemical Physics Letters*, 429(1-3):310–316, September 2006. 2.1.5

[106] Joost VandeVondele, Urban Borštnik, and Jürg Hutter. Linear Scaling Self-Consistent Field Calculations with Millions of Atoms in the Condensed Phase. *Journal of Chemical Theory and Computation*, Article AS, March 2012. 2.5

[107] Joost VandeVondele and Jürg Hutter. An efficient orbital transformation method for electronic structure calculations. *The Journal of Chemical Physics*, 118(10):4365, 2003. 2.5.1

[108] Joost VandeVondele and Jürg Hutter. Gaussian basis sets for accurate calculations on molecular systems in gas and condensed phases. *The Journal of chemical physics*, 127(11):114105, 2007. 2.5.1

[109] Joost VandeVondele, M Krack, F Mohamed, M Parrinello, T Chassaing, and Jürg Hutter. Quickstep: Fast and accurate density functional calculations using a mixed Gaussian and plane waves approach. *Computer Physics Communications*, 167(2):103–128, 2005. 2.5

[110] Joost VandeVondele and Michiel Sprik. A molecular dynamics study of the hydroxyl radical in solution applying self-interaction-corrected density functional methods. *Physical Chemistry Chemical Physics*, 7(7):1363, 2005. 2.2.3, 3.1

[111] J R R Verlet, A E Bragg, A. Kammrath, O. Cheshnovsky, and D M Neumark. Observation of large water-cluster anions with surface-bound excess electrons. *Science*, 307(5706):93–6, 2005. 1.3

[112] Loup Verlet. Computer "Experiments" on Classical Fluids. I. Thermodynamical Properties of Lennard-Jones Molecules. *Phys. Rev.*, 159(1):98–103, July 1967. 2.1.6

[113] Victor P. Vysotskiy, Lorenz S. Cederbaum, Thomas Sommerfeld, Vamsee K. Voora, and Kenneth D. Jordan. Benchmark Calculations of the Energies for Binding Excess Electrons to Water Clusters. *Journal of Chemical Theory and Computation*, 8(3):893–900, March 2012. 1.4.1

[114] Adam P Willard and David Chandler. Instantaneous liquid interfaces. *The journal of physical chemistry. B*, 114(5):1954–8, February 2010. 2.4

[115] Bernd Winter. Liquid microjet for photoelectron spectroscopy. *Nuclear Instruments and Methods in Physics Research Section A: Accelerators, Spectrometers, Detectors and Associated Equipment*, 601(1-2):139–150, March 2009. 1.3

[116] Ryan M Young, Margaret a Yandell, Sarah B King, and Daniel M Neumark. Thermal effects on energetics and dynamics in water cluster anions (H2O)n(-). *The Journal of chemical physics*, 136(9):094304, March 2012. 1.3

[117] Tang-Qing Yu, José Alejandre, Roberto López-Rendón, Glenn J. Martyna, and Mark E. Tuckerman. Measure-preserving integrators for molecular dynamics in the isothermal–isobaric ensemble derived from the Liouville operator. *Chemical Physics*, 370(1-3):294–305, May 2010. 2.1.6

LIST OF ATTACHED PAPERS

[118] Ondrej Marsalek, Christopher G. Elles, Piotr A. Pieniazek, Eva Pluhařová, Joost VandeVondele, Stephen E. Bradforth, and Pavel Jungwirth. Chasing charge localization and chemical reactivity following photoionization in liquid water. *The Journal of Chemical Physics*, 135(22):224510, 2011.

[119] Ondrej Marsalek, Tomaso Frigato, Joost VandeVondele, Stephen E. Bradforth, Burkhard Schmidt, Christof Schütte, and Pavel Jungwirth. Hydrogen forms in water by proton transfer to a distorted electron. *The Journal of Physical Chemistry B*, 114(2):915–20, January 2010. 4, 4.4

[120] Ondrej Marsalek, Frank Uhlig, Tomaso Frigato, Burkhard Schmidt, and Pavel Jungwirth. Dynamics of Electron Localization in Warm versus Cold Water Clusters. *Physical Review Letters*, 105(4):043002, July 2010. 4, 4.1.2

[121] Ondrej Marsalek, Frank Uhlig, and Pavel Jungwirth. Electrons in Cold Water Clusters: An ab Initio Molecular Dynamics Study of Localization and Metastable States. *The Journal of Physical Chemistry C*, 114:20489–20495, July 2010. 4, 4.2, 4.6

[122] Ondrej Marsalek, Frank Uhlig, Joost Vandevondele, and Pavel Jungwirth. Structure, Dynamics, and Reactivity of Hydrated Electrons by Ab Initio Molecular Dynamics. *Accounts of Chemical Research*, 45(1):23–32, 2012. 4, 4.1.1, 4.1.2, 4.2, 4.4

[123] Frank Uhlig, Ondrej Marsalek, and Pavel Jungwirth. From a localized H(3)O radical to a delocalized H(3)O(+)e(-) solvent-separated pair by sequential hydration. *Physical chemistry chemical physics : PCCP*, 13:14003–14009, July 2011. 4, 4.4

APPENDIX

A

ATTACHED PAPERS

THE JOURNAL OF CHEMICAL PHYSICS **135**, 224510 (2011)

Chasing charge localization and chemical reactivity following photoionization in liquid water

Ondrej Marsalek,[1] Christopher G. Elles,[2,a)] Piotr A. Pieniazek,[2,b)] Eva Pluhařová,[1]
Joost VandeVondele,[3,c),d)] Stephen E. Bradforth,[2,c)] and Pavel Jungwirth[1,c)]
[1]*Institute of Organic Chemistry and Biochemistry, Academy of Sciences of the Czech Republic and Center for Biomolecules and Complex Molecular Systems, Flemingovo nám. 2, 16610 Prague 6, Czech Republic*
[2]*Department of Chemistry, University of Southern California, Los Angeles, California 90089-0482, USA*
[3]*Physical Chemistry Institute, Zürich University, Winterthurerstrasse 190, CH-8057 Zürich, Switzerland*

(Received 7 July 2011; accepted 8 November 2011; published online 12 December 2011)

The ultrafast dynamics of the cationic hole formed in bulk liquid water following ionization is investigated by *ab initio* molecular dynamics simulations and an experimentally accessible signature is suggested that might be tracked by femtosecond pump-probe spectroscopy. This is one of the fastest fundamental processes occurring in radiation-induced chemistry in aqueous systems and biological tissue. However, unlike the excess electron formed in the same process, the nature and time evolution of the cationic hole has been hitherto little studied. Simulations show that an initially partially delocalized cationic hole localizes within ~30 fs after which proton transfer to a neighboring water molecule proceeds practically immediately, leading to the formation of the OH radical and the hydronium cation in a reaction which can be formally written as $H_2O^+ + H_2O \rightarrow OH + H_3O^+$. The exact amount of initial spin delocalization is, however, somewhat method dependent, being realistically described by approximate density functional theory methods corrected for the self-interaction error. Localization, and then the evolving separation of spin and charge, changes the electronic structure of the radical center. This is manifested in the spectrum of electronic excitations which is calculated for the ensemble of *ab initio* molecular dynamics trajectories using a quantum mechanics/molecular mechanics (QM/MM) formalism applying the equation of motion coupled-clusters method to the radical core. A clear spectroscopic signature is predicted by the theoretical model: as the hole transforms into a hydroxyl radical, a transient electronic absorption in the visible shifts to the blue, growing toward the near ultraviolet. Experimental evidence for this primary radiation-induced process is sought using femtosecond photoionization of liquid water excited with two photons at 11 eV. Transient absorption measurements carried out with ~40 fs time resolution and broadband spectral probing across the near-UV and visible are presented and direct comparisons with the theoretical simulations are made. Within the sensitivity and time resolution of the current measurement, a matching spectral signature is not detected. This result is used to place an upper limit on the absorption strength and/or lifetime of the localized $H_2O^+{}_{(aq)}$ species. © *2011 American Institute of Physics*. [doi:10.1063/1.3664746]

INTRODUCTION

The radiation chemistry of pure water initiated by ionization leads to formation of an excess electron which leaves behind a cationic hole.[1] Each of these two charged radical species formed by ionizing radiation follows its own route of chemical reactivity. On one hand, H_2O^+ is an extremely unstable radical cation which reacts with a neighboring water molecule by proton transfer, forming the H_3O^+ cation and the OH radical. The latter species is involved in further oxidative processes.[1] On the other hand, the excess electron relaxes to a localized solvated electron, which can go on to reduce impurities such as ions, free radicals, or dissolved oxygen on the submicrosecond timescale.[1–4] Even in pure water, the solvated electron can react with other hydronium ions, with other solvated electrons formed in the spur, and with water itself which results in an inherent lifetime which does not exceed several milliseconds.[1,5–7] How far away the solvated electron localizes determines the yield of these strongly oxidizing and reducing radicals available for subsequent chemistry. If trapped close by (<3 nm), the electron may recombine back with either the OH radical or the H_3O^+ at the hole site. The preferred geminate recombination partner and the kinetics of recombination is, in turn, be governed by the precise interaction and correlation of the motions of the H_3O^+ and OH pair formed in the primary proton transfer step.[8,9] For the brief period before full solvation, the electron exhibits enhanced reactivity and this has been suggested to also affect the recombination yield and the production of H_2.[10]

[a)] Present address: Department of Chemistry, University of Kansas, Lawrence, Kansas 66045, USA.

[b)] Present address: Department of Chemistry, University of Wisconsin–Madison, 1101 University Avenue, Madison, Wisconsin 53706-1322, USA.

[c)] Authors to whom correspondence should be addressed. Electronic addresses: joost.vandevondele@mat.ethz.ch, stephen.bradforth@usc.edu, and pavel.jungwirth@uochb.cas.cz.

[d)] Present address: Nanoscale Simulations, ETH Zurich, HCI E 486.1, Wolfgang-Pauli-Strasse 10, 8093 Zurich, Switzerland.

The products of ionization of water, in particular the OH radical, are important species involved in the indirect radiation damage of materials and biomolecules including DNA.[11] Therefore, numerous kinetic studies have been devoted to elucidating the rates of processes induced by water ionization.[12] At ultrafast times and at the molecular level, unlike for the solvated electron product, the information about the chemical dynamics of the cationic hole leading to formation of OH is not so clear and subject to far fewer investigations.[8,9] It is usually assumed that the proton transfer reaction happens faster than 100 fs and this value is given in nearly all introductory texts on radiation damage of water and biological tissues.[13] This number derives from a pioneering photoionization study soon after the availability of amplified sub-picosecond pulses when an attempt was made to capture this primary step in the radiation chemistry of water. Gauduel *et al.*[14] claimed detection of H_2O^+ and its decay time, measured as 100 fs (and 170 fs in D_2O), through transient absorption. Their experiment used photolysis at 8 eV, but recent experimental evidence[15] and theoretical insight into the electronic structure of water indicate that 8 eV is not, in fact, sufficient to generate the H_2O^+ cation directly, and that the mechanism for ionization at this energy involves hydrogen atom motion in the excited state neutral water molecule to reach a solvated electron.[16–18] For such ionization pathways around 8 eV, it is now understood that H_2O^+ cannot be an intermediate and photodissociation dominates. The interpretation of the origin of signals in Ref. 14 is discussed later. Regardless, the important questions remain about over what timescale the proton transfer reaction happens and what electronic signature would be expected for the turnover of H_2O^+ into OH.

On the computational side, quantum chemical methods have recently[19–23] been employed to map the potential energy surface, dynamics, and spectroscopic properties of the simplest cluster model—the water dimer cation. These studies all show it is essentially a barrierless process for the system to convert from $H_2O^+ \ldots H_2O$ to $H_3O^+ \ldots OH$ after removal of the electron. Based on the shape of the potential surface, it was suggested that starting from the optimal geometry of the neutral water dimer, the distance between the oxygens of the two water molecules decreases upon ionization from 2.9 to 2.5, after which a proton hops from H_2O^+ to H_2O forming the above products.[20] A more recent work following the dynamics using quantum mechanical wave packet propagation reveals that the proton can oscillate between the two oxygens several times as the waters come closer together but the reaction is essentially complete in 50 fs.[23] In both the papers, it is predicted that these chemical changes are accompanied by shifts in the electronic spectrum, which is, in principle, accessible to ultrafast UV/visible transient absorption spectroscopy. In subsequent studies, ionization was modeled in larger clusters with up to five water molecules, which allowed investigation in a limited sense, i.e., for small systems, of the character of the charge delocalization upon ionization.[24–26] A partial delocalization (which is not present in the ionized water dimer, where the charge is initially fully localized on the hydrogen bond donating water molecule) was observed in these small water clusters.[25] Additionally, an *ab initio* molecular dynamics study of ionization in a cluster with 17 water molecules was performed recently which, however, due to the use of the Hartree-Fock (HF) method leads to a localized charge already at the instant of ionization.[27]

The previously studied ionized water clusters allow investigation of the onset of the medium effects; nevertheless, they are still very far from the condensed phase. A natural question therefore arises as to what is the degree of charge delocalization upon ionization in liquid water (i.e., what is the nature of the nascent bulk "H_2O^+") and whether this delocalization can play a role in slowing reaction from the cationic hole toward H_3O^+ and OH products in the aqueous bulk. To address this issue, we have employed *ab initio* molecular dynamics (AIMD) simulations of ionization in bulk water by removing the least bound electron. Dynamics following vertical ionization to the lowest ionized state was followed on the 1 ps timescale, which was sufficient to observe both hole localization and chemical reactivity. As with the water dimer cation studies, we correlate the changing electronic structure of the radical cation as its structure evolves along the reaction coordinate with the changes in the electronic absorption spectrum computed with the equation of motion coupled-clusters (EOM-IP-CCSD) method. A clear spectral evolution is predicted as the system moves toward the OH product.

These encouraging theoretical predictions suggest that a renewed attempt at experimental measurement of the lifetime of H_2O^+ in liquid water is warranted, particularly as factor of $\sim$3 times higher time resolution and full broadband probing is now possible compared to earlier experiments.[14] Such experiments would provide an important benchmark for verifying the AIMD spin localization and proton transfer dynamics. The short-lived water cation is still an extremely experimentally challenging target, in part because the spectroscopic signature of hydrated H_2O^+ remains a theoretical prediction that has never been experimentally observed in clusters or the bulk. Additionally, the timescales predicted for the proton transfer reaction are still right at the current state of the art in ultrafast time resolution, and a relatively weak electronic absorption is expected for H_2O^+ compared to absorption in the electron channel. Despite these concerns, a new experimental search to detect the initial hole and its evolution into OH is reported here. Our approach is to photoionize at energies where we expect strong coupling to the ionization continuum; the H_2O^+ species can be expected to be formed at a high quantum yield by two-photon excitation of bulk water once sufficiently high photolysis energies are used.[16] Recent studies by Crowell and co-workers[28] suggest that excitation near 11 eV strongly favors ionization over the competing dissociation channel, and 11 eV is near the vertical ionization potential of liquid water corresponding to the first $1b_1{}^{-1}$ ionization continuum.[16,29] However, we should bear in mind the fact that the absorption spectrum of liquid water at these energies is dominated by several electronic resonance states which means that ionization might either take place to the $1b_1{}^{-1}$ continuum or possibly by autoionization into the next higher ionization continuum, the $3a_1{}^{-1}$.[30,31] Based on our current assignment of the two-photon absorption (TPA) spectroscopy,[31] we expect the formation of a $1b_1{}^{-1}$ hole to be the most likely outcome following two-photon excitation at 11 eV with H_2O^+ formed within the pulse duration.

One other complication for a direct comparison of theory and experiment is that *ab initio* MD follows the dynamics of the lowest state of the system after removal of the least bound electron of the whole system. At the neutral geometry, there is a plethora of low-lying (excited) states of the cationic systems forming the quasi-continuous $1b_1{}^{-1}$ band. In the experiment, the intra-band relaxation also contributes to the localization process. A similar situation is observed when an electron is added to a neutral water system.[32–37] To describe this part of the process, one would need to perform non-adiabatic dynamics involving many electronic states, a calculation beyond those currently feasible within the all electron description.

In the following, we start by describing the *ab initio* molecular dynamics methodology for modeling the ultrafast chemical dynamics of the cationic hole in water and the quantum mechanics/molecular mechanics (QM/MM) coupled cluster calculations used to simulate the corresponding time-evolving electronic absorption spectra. Then we describe AIMD results for the localization and proton transfer dynamics of the cationic hole, benchmarked against highly accurate *ab initio* calculations for small water clusters. Simulations of the time-dependent electronic spectrum using the structural configurations from the AIMD trajectories are then presented, illustrating how they can be used to track the evolving reaction dynamics. The key spectral signature of the reaction $H_2O^+ + H_2O \rightarrow OH + H_3O^+$ is a blueshift of an absorption line from about 2.5 to 4 eV, corresponding to a conversion of a localized cationic hole to the OH radical. Finally, an attempt to experimentally monitor the transient spectroscopy initiated after photoionization is described with time resolution and probe spectral range such that a one-to-one comparison with the simulations is possible. The experimental result is used to bracket possible outcomes of the reaction dynamics in the system.

METHODS

We performed Born-Oppenheimer dynamics simulations of a cationic hole in a periodic box of 64 or 128 water molecules. Forces and energies were calculated from Kohn-Sham density functional theory (DFT), using functionals of the generalized gradient approximation (GGA) type [Becke-Lee-Yang-Parr (BLYP) or Perdew-Burke-Ernzerhof (PBE)] and, for several trajectories, including an empirical dispersion correction (BLYP-D).[38] The canonical constant temperature and volume (NVT) ensemble was simulated, with the volume based on experimental water density and the temperature set to $T = 350$ K for pure GGA DFT and $T = 300$ K for BLYP-D. The hybrid Gaussians and plane waves scheme was used with a TZV2P basis set for the Kohn-Sham orbitals and a 280 Ry cutoff for the auxiliary plane wave basis set.

After equilibration of a neutral water system, snapshots from a further trajectory separated by 500 fs were taken as different initial conditions for simulations of the dynamics following ionization. To this end, one electron was removed by changing the total charge of the system at $t = 0$ to model vertical ionization of the system. Since this procedure leads to an open shell system, the self-interaction correction (SIC) was used for the singly occupied orbital in a restricted open-shell formulation of the Kohn-Sham equations. The SIC parameters, a = 0.2 and b = 0, were tested previously for the solvated OH radical,[39] as well as for the water dimer cation, yielding results comparable to highly accurate wavefunction-based methods.[20,21]

For comparison, further calculations (both single-point energy evaluations and test dynamical runs), were performed with the HSE hybrid functional,[40] the "half-and-half" hybrid functional (BH&HLYP),[41] and, for the sake of completeness, also with pure Hartree-Fock exchange (HFX). As shown previously,[42] the admixture of a significant fraction of exact exchange in the density functional can improve the description of cationic radical systems. The optimal fraction of exchange is system dependent and, for example, the BH&HLYP functional contains 50% HFX, while the more common B3LYP functional only contains 20% HFX. For the condensed phase, functionals that employ screened exchange have a computational advantage.[40,42] In the present notation, e.g., HSE(0.5) refers to the HSE functional in which the fraction of exchange is 50%. Additional benchmark single-point calculations were also performed on a small cluster of five water molecules for comparison with available results calculated using the very accurate EOM-IP-CCSD method.[25,43] The DFT calculations for the cluster were set analogously to the bulk calculations, except that open boundary conditions were used. All *ab initio* molecular dynamics simulations were performed using the CP2K package and its DFT module Quickstep.[44]

Spectral calculations using EOM-IP-CCSD/6-311++G** focused on the excited states of a reactive subsystem (*vide infra*) below 6 eV excitation energy. Such a high level of theory is necessary to properly describe the excitation energies and the associated transition properties.[20] However, at the coupled cluster level only a small core of the molecular system can be included quantum mechanically. Excitations lower than 6 eV will only originate from the open shell part of the system; therefore, such a division of the system into a QM and MM part is only meaningful once the spin has partially localized. Our model defines a reactive trimer core by (i) the oxygen atom of the water molecule that transfers the proton, and (ii) two oxygen atoms closest to the hydrogens of the proton transfering molecule. Hydrogen atoms are included in the trimer if they are less than 1.5 Å from either of the oxygens. We chose a trimer, rather than a dimer, as our basic quantum mechanical core as in the molecular dynamics we observed several large amplitude vibrations of either OH bond in the central water molecule, before the actual reactive step takes place. Further, dynamically defining the trimer allowed to account for subsequent proton hops (from H_3O^+ to neighboring H_2O). Static selection of the oxygen trimer framework is justified by the long time scale of water diffusion. Thus, in effect quantum mechanical calculations were performed either on $(H_2O)_3{}^+$ or $OH(H_2O)_2$, with the remaining water molecules treated as point charges taken from the SPC/E water model (−0.8476 and 0.4238 for oxygen and hydrogen, respectively).[45] Each trajectory was followed up to 500 fs. Along each trajectory, the EOM-IP-CCSD excitation energies were computed based on the closed-shell reference. In order to construct transient absorption spectra at each step a 0.6 eV FWHM Gaussian was applied to each transition. Experimental linewidths in electronic spectra of related systems such the spectra of OH(aq) and H_2O itself are 1 eV or greater,[31,43,46] due to the extremely strong solute-water coupling, and so this rather arbitrary choice of width is likely an underestimate. Essentially, the inclusion of additional broadening is necessary because of under-sampling of the distribution of liquid structures, assuming inhomogeneity is the major determinant of the lineshape. The calculations using wavefunction-based methods were performed using the Q-CHEM program.[47]

RESULTS AND DISCUSSION

Ab initio MD following photoionization in bulk water

We simulated over 20 trajectories following ionization of bulk water, started with different initial conditions. To this end, we employed the BLYP-SIC functional with the self-interaction correction optimized against accurate coupled cluster calculations for the water dimer cation. For illustration, Fig. 1 depicts three crucial snapshots from a representative trajectory. The first snapshot shows the cationic hole right after photoionization, i.e., with nuclei in the geometry of neutral water. We see that the spin density of the cationic hole is delocalized over several water molecules (a detailed discussion about which water mlecules are most prone to carry the spin initially is presented in the supplementary material[63] and in Refs. 48–50). However, the hole localizes very fast on a single water molecule (second snapshot in Fig. 1). Such a localized H_2O^+ moiety becomes extremely reactive, forming H_3O^+ and OH in a reaction with a neighboring water molecule, as depicted on the third snapshot in Fig. 1. The products are first formed as a contact pair, but later become separated by one or more solvent molecules due to proton hops from the originally formed hydronium moiety to neighboring waters.

For further description of the ultrafast dynamics of the cationic hole and in order to draw robust conclusions, we now provide data for the whole set of simulated trajectories. Figure 2 shows the time evolution of the largest Mulliken spin population found on an oxygen of a water molecule for all trajectories. At the instant of photoionization, this largest spin density amounts to 0.1–0.3, indicating significant spin delocalization over several water molecules (*vide infra*). However, with a mean time of 31 fs (with a mean deviation of 21 fs) 95% of the spin localizes on a single water molecule (see Table I). The progress of the chemical reaction toward H_3O^+ and OH is then monitored in Fig. 3, which depicts for all trajectories the time evolution of the distance between the center of spin and the center of charge. During the localization process and before the reaction, both spin and charge localize on a single water molecule forming H_2O^+; therefore, this distance equals to zero. Right after the reaction, which proceeds as a proton hop from H_2O^+ to a neighboring water molecule, charge (H_3O^+) and spin (OH) become separated by a short hydrogen bond of about 2.6 Å. The first proton hop occurs on average at 33 fs (with a mean deviation of 14 fs), which practically coincides with the 95% localization time (Table I). However, for many trajectories re-crossings back to reactants take place with the final stabilization of the products occurring on average 44 fs after the first proton transfer. Afterwards, the proton can hop to other water molecules and the products become separated by a larger distance with most of the $H_3O^+ \ldots$ OH contact pairs disappearing within 200 fs (Fig. 3). It is likely that due to the classical treatment of all nuclei the proton transfer time and the number of re-crossings are somewhat overestimated in the present calculations, which thus likely present a lower bound to the proton transfer rate.[51]

It is useful to combine the principal results presented in Figs. 2 and 3 into a single picture (Fig. 4), which correlates for each trajectory the localization time with the moment of occurrence of the first proton transfer. We clearly see from Fig. 4 that the first proton transfer proceeds at the instant of, or right after, the spin localization, with the reaction being over (i.e., no more re-crossings occurring, open circles) for most trajectories several tens of femtoseconds later. Another useful correlation for understanding the process is that of the

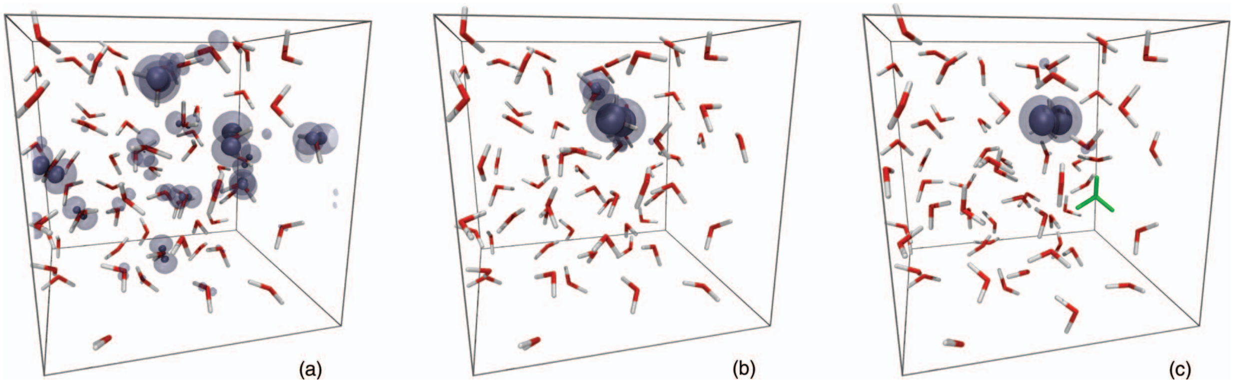

FIG. 1. Snapshots along a selected trajectory showing water molecules together with isosurfaces (at values of 0.01 and 0.001 au^{-3}) of the spin density. (a) The system right after ionization ($t = 0$) when the system is in the neutral geometry and the hole is partially delocalized. (b) The system after the hole localizes almost entirely on a single water molecule, forming transient H_2O^+ ($t = 40$ fs). This species reacts almost instantaneously with a neighboring water molecule, forming an OH radical and a hydronium cation (highlighted in green), which eventually become separated by water molecules, as shown in (c) ($t = 400$ fs).

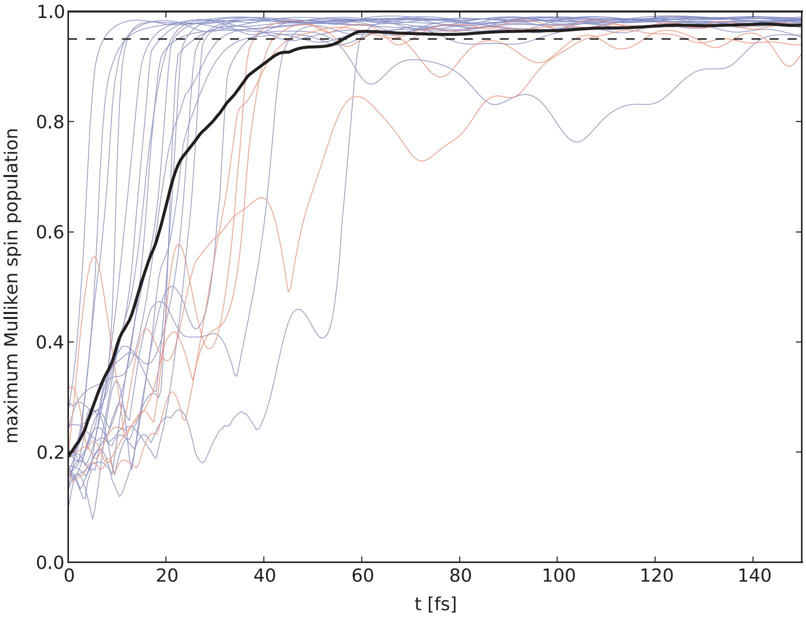

FIG. 2. Maximum Mulliken spin population (as a measure of localization of the hole) on a single oxygen atom, shown as a function of time for all trajectories. The dashed line is at the value of 0.95, its intersection with each line marking the time when the localization is practically complete. DFT trajectories are depicted in blue and DFT-D trajectories are in red. The black line is the average over all trajectories.

distance between the oxygen atoms involved in the proton transfer reaction with the distance between the transferring hydrogen atom and its new oxygen binding partner. This correlation is plotted for all simulated trajectories in Fig. 5. We see that in the initial stages of the reaction, both distances shrink simultaneously (blue segments in Fig. 5). Also, the shorter the initial O–O distance, the faster the system reaches the region where proton transfer starts occuring. Between the first proton hop and the time when the recrossings cease to occur the two oxygens stay close to each other (red segments). Once the two oxygens separate by more than 2.7 Å, the reaction is essentialy over with the nascent H_3O^+ and OH products forming first a contact pair and later being separated by water molecules. Note, that the shape of the trajectories in Fig. 5 corresponds to a potential energy surface which is remarkably similar to that of the water dimer cation,[20] indicating that after spin localization the reaction proceeds locally with H_2O^+ and one or at most two other water molecules directly involved.

Benchmarking the initial delocalization of the cationic hole

The initial degree of spin delocalization of the cationic hole is, from the computational point of view, a subtle issue which is dependent on the electronic structure method employed, as demonstrated in Fig. 6. The figure depicts, for a selected trajectory, the spin density in the unit cell of water right after ionization ($t = 0$), as obtained by different methods. As already discussed above, the BLYP-SIC functional yields a partially delocalized initial hole (Fig. 6). The importance of the self-interaction correction emerges from comparison to the uncorrected BLYP results (Fig. 6), which results in a spin density which is over-delocalized (*vide infra*). This over-delocalization is caused by the self-interaction error, leading to a spurious repulsion of the unpaired electron by itself.[42] The other extreme situation, i.e., complete localization of the initial cationic hole results from Hartree-Fock calculations (Fig. 6), where the artificial overlocalization is due to a symmetry breaking problem.[51] Hybrid functionals to a large degree cancel out these two errors. Figures 6(d) and 6(e) show the initial spin density following from calculations with the HSE functional with 25% or 50%[42] of exact exchange mixed in. While the first mixing value is similar to that used in most standard hybrid functionals, the second one matches best the EOM-IP-CCSD(T) energy of the water dimer cation.[20] In both the cases, we get a partially delocalized hole with its delocalization decreasing with increasing mixed-in fraction of exact exchange. The degree of initial delocalization from BLYP-SIC, employed in the dynamical calculations, is comparable to that obtained using the hybrid functional, being actually bracketed by the two HSE calculations. Further discussion of benchmarking along the dynamical trajectories is presented in the supplementary material.[63]

TABLE I. Spin localization and proton hopping times in fs.

	95% localization	First reactive proton hop	Final reactive proton hop
Mean value	31	33	77
Standard deviation	21	14	45

The fact that the structure and dynamics of the cationic hole in water sensitively depends on the approximations employed in the electronic structure calculations demonstrates

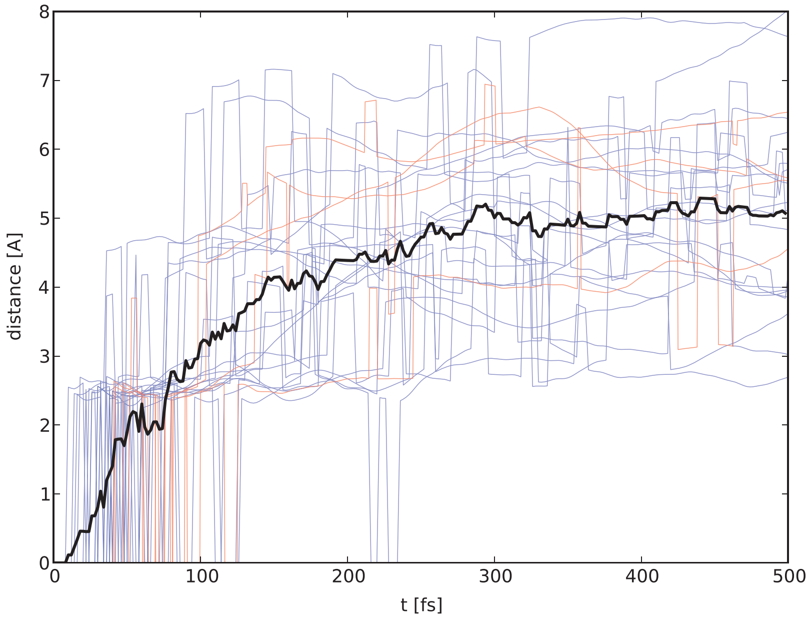

FIG. 3. The distance between the center of spin and the center of charge, shown as a function of time for all the trajectories. This distance between an oxygen atom with the highest Mulliken spin population and that to which the excess proton is the closest monitors the progress of the proton transfer reaction. It is zero initially, becoming non-zero after the first proton hop. DFT trajectories are depicted in blue and DFT-D trajectories are in red. The black line is the average over all trajectories.

the big challenges of the present problem and calls for benchmarking against a very accurate method such as the EOM-IP-CCSD.[20] Such calculation can only be performed for a small cluster model. We chose the smallest system with a tetrahedrally coordinated water molecule, i.e., the water pentamer cation in the geometry of a neutral cluster with one central water molecule hydrogen bonded to four others.[25] Figure 7 shows the spin densities after ionization of the neutral water pentamer using all the methods discussed here. The benchmark EOM-IP-CCSD spin density is partially delocalized over the two water molecules with no accepting hydrogen bonds. It is reassuring that the "workhorse" for the present

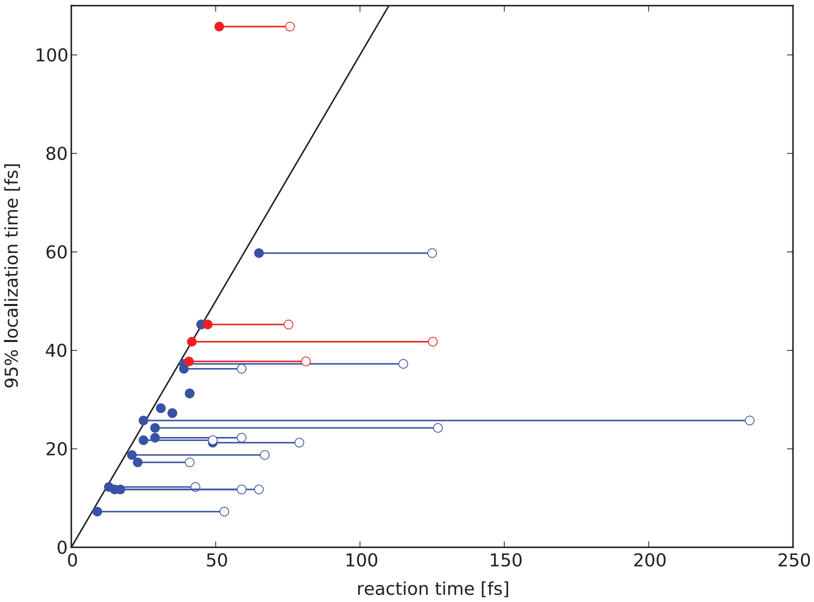

FIG. 4. Correlation between the time of localization and the time of reaction. The former is defined as the time when the maximum Mulliken spin population on a single oxygen atom reaches 0.95 (dashed line in Fig. 2). The latter is characterized by the reaction interval (depicted by a line) that starts at the moment of the first proton transfer (full circles) and ends when no more back transfer to the original hole occurs (open circles). DFT trajectories are depicted in blue and DFT-D trajectories are in red. The full line shows direct proportion between the two times for reference.

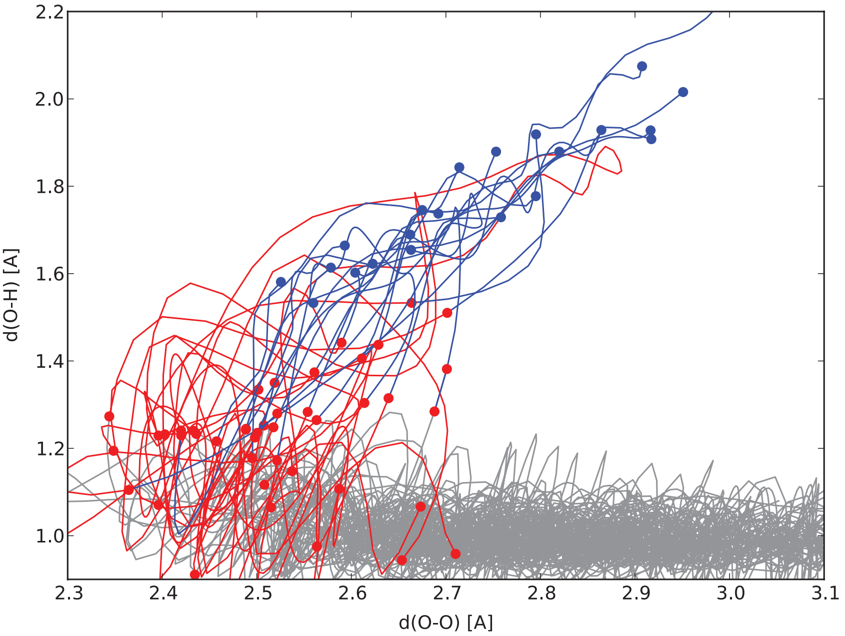

FIG. 5. Correlations between the distance between the oxygen atoms involved in the proton transfer reaction and the distance between the transferring hydrogen atom and its new oxygen bonding partner along all simulated trajectories. Blue circles mark the initial conditions and blue lines denote the trajectory segments until the reaction starts. Red segments with red circles at their boundaries mark the reaction intervals (as defined in Fig. 4). Gray segments show the rest of the trajectories after the reaction.

study, i.e., the BLYP-SIC methods compares very well to EOM-IP-CCSD. The hybrid HSE functionals also perform satisfactorily, with HSE 25% slightly overestimating and HSE 50% slightly underestimating the spin delocalization. In contrast, BLYP overdelocalizes and HF overlocalizes the initial spin density compared to the benchmark result.

Modeling of the absorption spectra

In order to facilitate connection to ultrafast electronic spectroscopy, we have evaluated electronic spectra along the AIMD trajectories. In our earlier work,[20] we calculated the absorption of the water dimer cation at various geometries along the proton transfer coordinate and this provides a

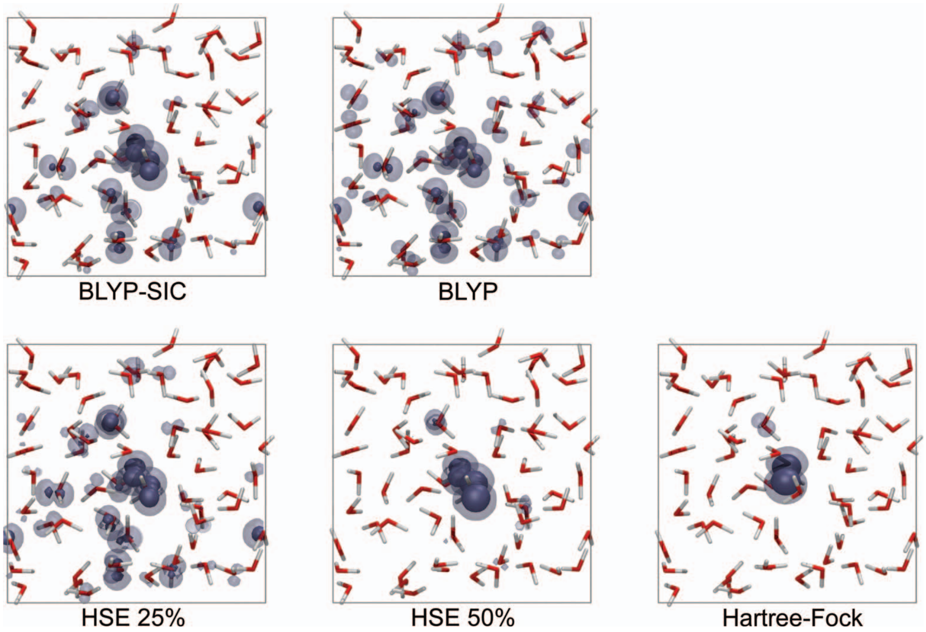

FIG. 6. Snapshots of the aqueous bulk system right after ionization ($t = 0$) for a selected trajectory using different electronic structure methods. Water molecules are shown together with isosurfaces of the spin density.

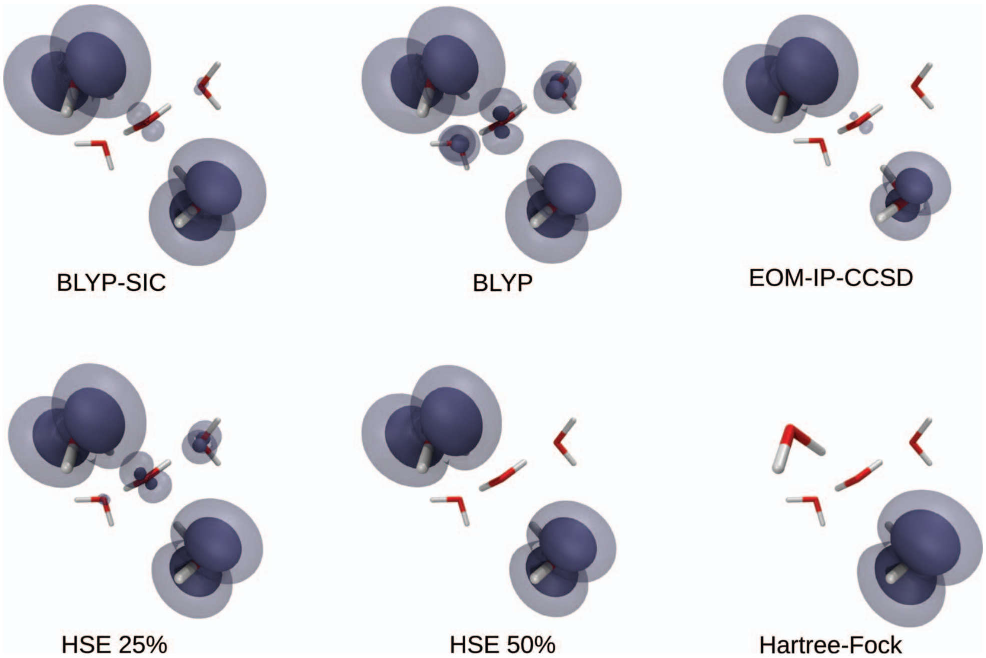

FIG. 7. Water pentamer as a benchmark cluster system, calculated with different methods (see text for detail). Water molecules are shown together with isosurfaces of the spin density.

helpful starting point for the bulk liquid ionization. The dimer cation is the simplest model of the proton transfer reaction in bulk water, where fully *ab initio* high-level calculations of the absorption spectrum are tractable.[20] We found that at the geometry of the neutral water dimer, the dimer cation has a calculated absorption near 620 nm that is associated with the H_2O^+ moiety and decays with the timescale of the proton transfer reaction. Following the reaction coordinate downhill to a weakly bound $H_3O^+ \ldots OH$ pair, a calculated absorption band in the UV corresponds to a purely valence transition on the OH radical.[20] A similar evolution of the optical signature is found for the gas phase dimer cation with wave packet time dynamics computed explicitly.[23]

Here we have generalized this approach to follow the bulk AIMD trajectories presented above and tried to include as much of the effect of the extended solvent on the electronic excitations as possible. As discussed in the Methods section, we have done this using a QM/MM approach. The reactive trimer is described by the EOM-IP-CCSD electronic structure method, while the rest of the system is described by point charges. While this limits the description of the delocalization, we can still follow how the reactive process influences the spectroscopy as the proton transfer reaction proceeds. In addition, we are sampling a range of initial H-bonding geometries in the liquid and structural changes of the network along the AIMD trajectories contain the collective effects of the liquid (e.g., "solvent drag") in modulating purely ballistic motions. In the AIMD simulations, the hole is initially partially delocalized, whereas here, the forced localization from the very earliest times allows us to obtain a clear picture of the spectral signature of the localized hole and thus a means to disentangle the spectroscopy from the localization dynamics.

At early times ($t = 0$–30 fs), we observe a very strong absorption spanning the entire 1–5 eV energy range [Fig. 8(a)]. Very little nuclear dynamics has occurred up to this point; consequently, the electronic states of all three water molecules are approximately degenerate. In particular, the configuration of the two hydrogen bond accepting molecules is conducive to the formation of an intense charge-resonance band.[25] Due to the absence of symmetry constraints, this transition couples to all the other excitations yielding intense bands throughout the entire spectral range. As the reaction proceeds, a close degeneracy between the two accepting molecules, one of which becomes H_3O^+, is lifted, the charge-resonance transition disappears, and lower intensity is observed throughout the entire spectrum.

Subsequently, as this broad absorption dies away, a new absorption band is seen, weak at first and rapidly blue shifting as it grows. By extrapolating to early times [more easily seen in Fig. 8(b)], this feature starts at ~2.3 eV (540 nm) at 30–50 fs and evolves to ~4 eV (310 nm) by the end of the computed time window. The band is not fully developed in intensity until ~150 fs. We note that a rising, blue shifting band is similar to predictions for the dimer cation.[20,23] This evolving band has been assigned as the H-bond donor $a_1 \rightarrow b_1$ (or $(a_1/b_1)^*$ and $(a_1/b_1) \rightarrow (b_1/0)$ in the dimer molecular orbital formalism introduced in Ref. 20) transition at the vertical ionization geometry turning into the $\sigma \rightarrow \pi$ valence transition on OH with increased oscillator strength.[20] In the bulk simulation, the $a_1 \rightarrow b_1$ transition starting out near 2.3 eV, which we are assigning to localized H_2O^+, is considerably weaker than in the dimer work. There is another noticeable difference in the time-evolving spectrum between the gas phase dimer and the bulk. In the wave packet simulations of Kamarchik

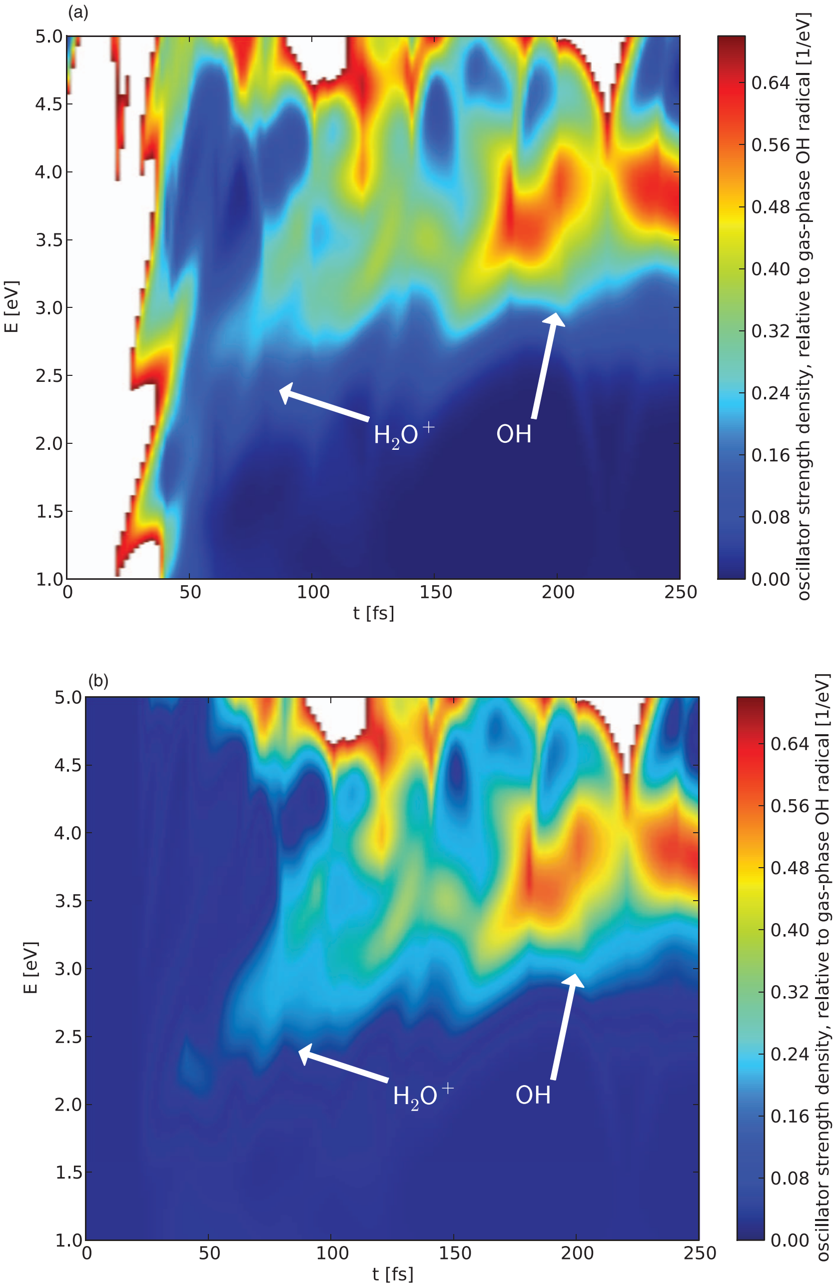

FIG. 8. (a) Time evolution of electronic excitation spectrum for ionized bulk water. Average of 22 AIMD trajectories with excitations computed for core trimer at the EOM-IP-CCSD level (see text). Stick spectra for each trajectory are broadened with 0.6 eV FWHM Gaussian. Excitations shown only for 1–5 eV, the optically accessible range. (b) As panel (a) except that the computed spectral intensity is turned on for each trajectory only when the spin is 95% localized as judged by analysis of the BLYP-SIC density, see Fig. 4. Intensity scale bar in both the plots is the oscillator strength density relative to that of the corresponding gas phase OH radical transition (0.00312).

et al.,[23] the proton is first transferred in ~10 fs and the spectral shift from 3 to 4 eV is over in 30 fs. This suggests that the delayed onset of proton transfer events in the bulk simulations, brought about by a rate limiting localization step, is manifested by slower spectral shifting in the electronic spectra. The influence of the surrounding waters (included as point charges) seems to introduce only modest changes to the basic spectral features, for example slightly red shifting the terminal OH(aq) band compared to the gas phase dimer.

It is perhaps understandable that the current spectral predictions map so well to the dimer cation spectra (with the exception of the timescales) because there is an artificial localization inherent to the present computational procedure. Although the nuclear motions are dictated by the full AIMD and proton transfer is inhibited until spin localization has taken place, the small size of the QM core (and particularly the fact we carve out a trimer with a central double H-bonded donor[25]) in the EOM-IP-CCSD calculations is prematurely forcing the electronic structure to localize in the spectral calculations. As we do not know what the spectral signature of an initial hole spread throughout the water network is, we turn on the spectra only after 95% localization is achieved for each individual DFT trajectory, where we expect the coupled cluster trimer to be a reasonable starting point for predicting the electronic spectrum [Fig. 8(b)]. This removes the strong initial feature, while the rest of the spectrum is not affected. Spectrally ignoring the first phase can be further justified when making a comparison to experiment as this temporal region is obscured by a separate coherent spectroscopic transition (*vide infra*) due to pulse overlap. This *ad hoc* procedure has the advantage of highlighting the weak early feature in the spectral simulations between 2 and 2.5 eV which we have assigned as the spectrum of the localized H_2O^+ hole. Clearly, an improved description of the electronic spectroscopy including a large quantum mechanical region is highly desirable to determine the spectroscopic signal of the early delocalized hole, but such an approach is beyond current computational capabilities.

Experimental search for the cationic hole and its evolution by femtosecond transient absorption

The ratio of the calculated oscillator strength at the proton-transferred geometry to the experimental[46] extinction coefficient of the OH_{aq} ($\sigma \rightarrow p$) transition in liquid water gives a scaling factor that can also be used to estimate the transition strength for a localized hole. Due to the uncertainties described in the preceding paragraph, we use for this estimate the earlier value[20,25] for $(H_2O)_2{}^+$ at the vertical dimer cluster geometry. This crude analysis suggests an experimental extinction coefficient of at least 80–100 $M^{-1}\,cm^{-1}$ at peak for localized H_2O^+, equivalent to about 0.4% of the maximum absorptivity of the equilibrium solvated electron (and comparable to the OH radical valence band absorption near 310 nm) originating from the photoionization process.[52] Note that we make our comparison with the long wavelength part of the OH(aq) absorption that has been assigned to the valence transition rather than the stronger charge transfer component at wavelengths shorter than 300 nm. The experimental extinction coefficient at the maximum of the OH ($A \leftarrow X$) transition in water is $\sim$125 $M^{-1}\,cm^{-1}$ at 350 °C (see Ref. 46), where hydrogen bonding is significantly reduced from room temperature, approximating the dimer. The calculated UV absorption band in the proton-transferred geometry of the dimer is $\sim$1.5 to 1.7 times stronger than the calculated absorption of the cation dimer at the initial geometry.

The solvated electron absorption takes 2–3 ps to reach its maximum value due to trapping and relaxation dynamics,[16,53] leaving a potential window (despite this unfavorable detection contrast ratio) to probe the newly localized hole. Assuming then that ionization produces equal numbers of H_2O^+ and solvated electron, the estimated extinction coefficient puts the H_2O^+ absorbance very close to experimental detection limits in favorable cases where the solvated electron signal exceeds 20 mOD. In addition, a fraction of the electrons are likely to undergo geminate recombination during the 2–3 ps before the solvated electron signal reaches its maximum, suggesting a higher initial concentration of H_2O^+ than implied by the electron signal.[54] So, although the H_2O^+ absorption is almost certainly weak, the fact that it is quite possibly within our detection limits convinced us to attempt a search for the experimental signal in the transient absorption spectrum.

Broadband pump-probe measurements were therefore performed that probe the range from 300 to 800 nm. Our experimental apparatus has been described in detail previously.[16,17,31] Briefly, 30 fs pulses centered between 223 and 227 nm derived from four-wave mixing in a hollow-core fiber[55] are focused into a 70 μm thin flowing film of neat liquid water.[56] At the focus, two-photon absorption of the pump by water leads to prompt ionization, and a broadband white light continuum brought to a narrower focus probes the absorption of products. The differential absorption from the continuum is measured on a photodiode array with the pump blocked every other shot. Figures 9(a) and 9(c) show two datasets covering different parts of the continuum probe transient absorption spectrum. A strong two-photon (pump + probe) absorption at short wavelengths dominates the signal near time-zero, where the pump and probe pulses overlap in time,[31] while the absorption at longer wavelengths rises with a timescale of $\sim$1 to 2 ps due to the formation of solvated electrons[57,58] neither of which is accounted for in the present AIMD simulations. Although well understood, these two strong features complicate the search for a weak transient absorption by a localized H_2O^+. As shown in the representations of the computed spectrum in the panels (b) and (d) of the figure, the H_2O^+ species is expected to absorb from 600 to 500 nm, with a lifetime determined by the proton-transfer reaction, and then evolve into an OH radical that absorbs in the near-UV (most clearly seen in panel (b)). Comparing panels (a) with (b) and (c) with (d) in Fig. 9, as well as their cuts (Fig. 10), shows that there is no clear experimental signature for a localized H_2O^+ which would appear sandwiched between these two other intense features in the dispersed 2D dataset. From comparison of panels (a) and (b), it is clear that even the signal from the final product OH radical (expected with intensity $\sim$0.2 to 0.3 mOD is itself difficult to discern the above continuous tail of the rising electron band, surprisingly already present at short wavelengths just after the 30 fs ionization pulse). Figures S3 and S4 in the supplementary material show additional data and the OH spectral band contribution expected (based on that detected from H_2O_2 photolysis).[63]

Careful examination of the pump-probe anisotropy and power dependence of the signal do not reveal any sign of a spectroscopic signature of H_2O^+. Weak absorption by the short-lived H_2O^+ transient species is the most likely explanation for the absence of an experimental signal. Another possible experimental limitation is the short lifetime of the H_2O^+ species, because the strong two-photon absorption peak dominates the transient spectrum up to about 40 fs. This experimental complication means that regardless of our uncertainty in the spectral signature prior to localization [and omitted in Figs. 8(b), 9(a), and 9(c)], the experiment will not

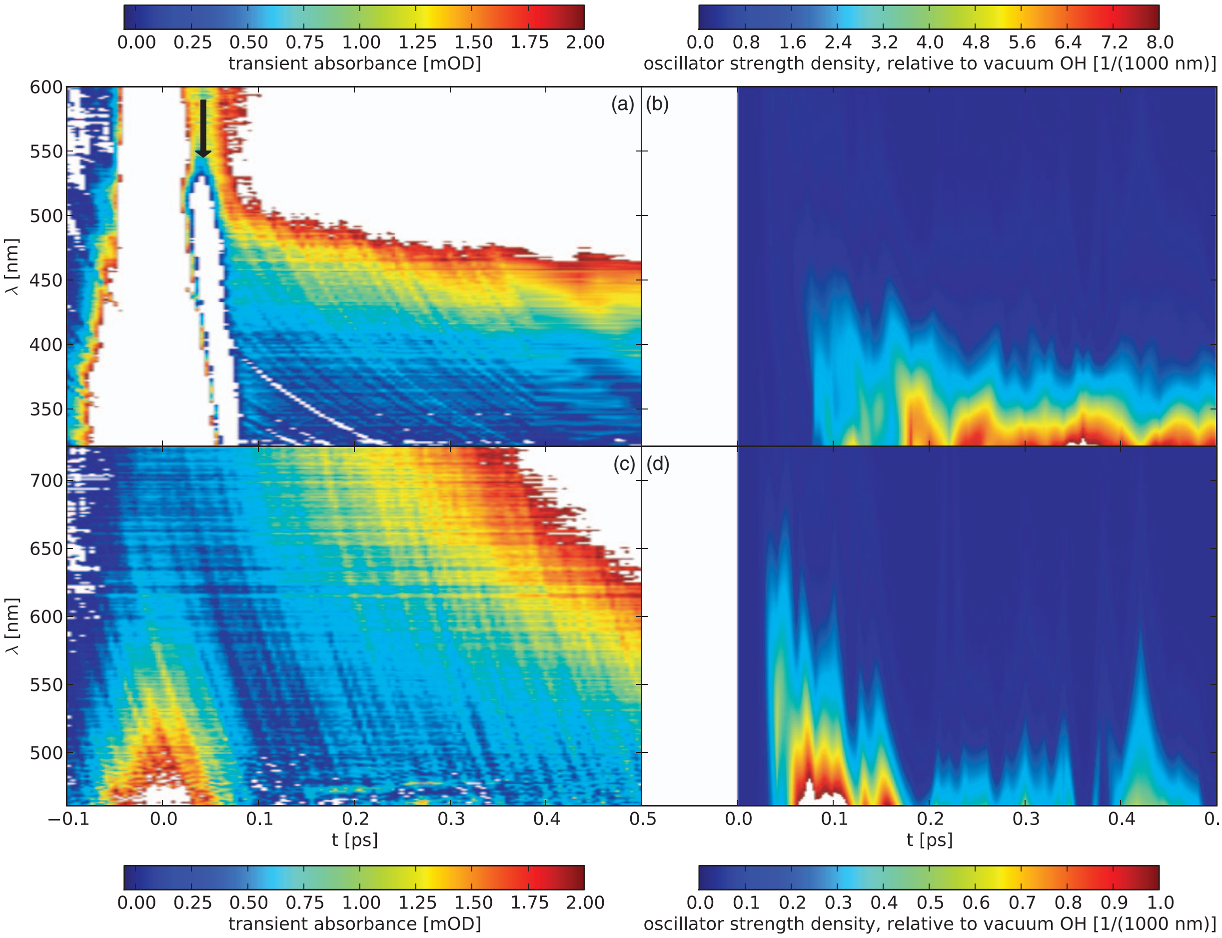

FIG. 9. Comparing spectral predictions and experiment. (a) and (c) Experimental transient absorption spectra with a continuum probe and time resolution of 40–50 fs. Photoionization of pure liquid water achieved with 2 photons giving a total excitation energy ∼11 eV. Scale bar is transient absorbance in mOD. The signal aligned along zero delay is coherent pump + probe absorption and is observed in absence of ionization (see text). In (a), cross phase modulation between the pump and 800 nm driven probe continua is observed (see arrow)—this is minimized by driving the continuum at 1350 nm (c). Signal rising to maximum at 500 fs delay most prominently at 700 nm is from the solvated electron; when fully developed, the absorbance at 720 nm is 20 mOD. (b) and (d) Simulated spectrum for ground state cationic hole in bulk water, reproduced from Fig. 8(b) but now shown matching experimental range of probe wavelengths and normalized to peak spectral intensity. Recall that the spectral simulation shows only signals attributable to the ionized and localized hole. These signals are not apparent in the experimental datasets.

be able to comment on the spectral evolution during this earliest period. The best case experimental time-resolution of ∼40 fs is determined by the duration of the pump laser pulse; this limits our observation window to transient species with lifetimes longer than about 30–40 fs. Cross-phase modulation and non-linear dispersion of the broadband probe pulses further complicate the signal at very short delay. This can be seen in the data in panel (a) using continuum light generated at 800 nm; we obtained better time resolution and stronger signal using this continuum but significant cross phase modulation artifacts (marked on plot with arrow) can be seen in this data which complicate its interpretation. The data in panel (c) were recorded using broadband probe light generated at a central wavelength of 1350 nm, where the cross-phase modulation and dispersion effects are minimal. Overall, analysis of all of our data suggests we find no evidence for H_2O^+, including where the time resolution is as short as 40 fs and where the solvated electron signal exceeds the target 20 mOD. Although our experiments fail to reveal a signature we can associate with a H_2O^+ species, based on our experiments we can rule out the previous measurement of Gauduel as an observation of H_2O^+ or its reported lifetime.[14] We have also been able to place limits on the cross section and/or the lifetime of this species.

The earlier[14] pump-probe experiments delivered 8 eV of energy into water, as compared to 11 eV employed here. As remarked on in the Introduction, we now know that two-photon photolysis of water near 11 eV yields a much higher fraction of ionization events (compared to dissociation events) than two-photon excitation at 8 eV[28,59] and at much lower pump intensity due to the much higher 2PA cross section.[31] In that case, if the proton transfer reaction timescale was 100 fs, the decaying signal assigned to H_2O^+ by Gauduel near 400 nm probe would then be readily seen here [Fig. 9(a)] with shorter pulses and at 11 eV total excitation energy. The signal in Ref. 14 instead of being due to H_2O^+ is most likely due to

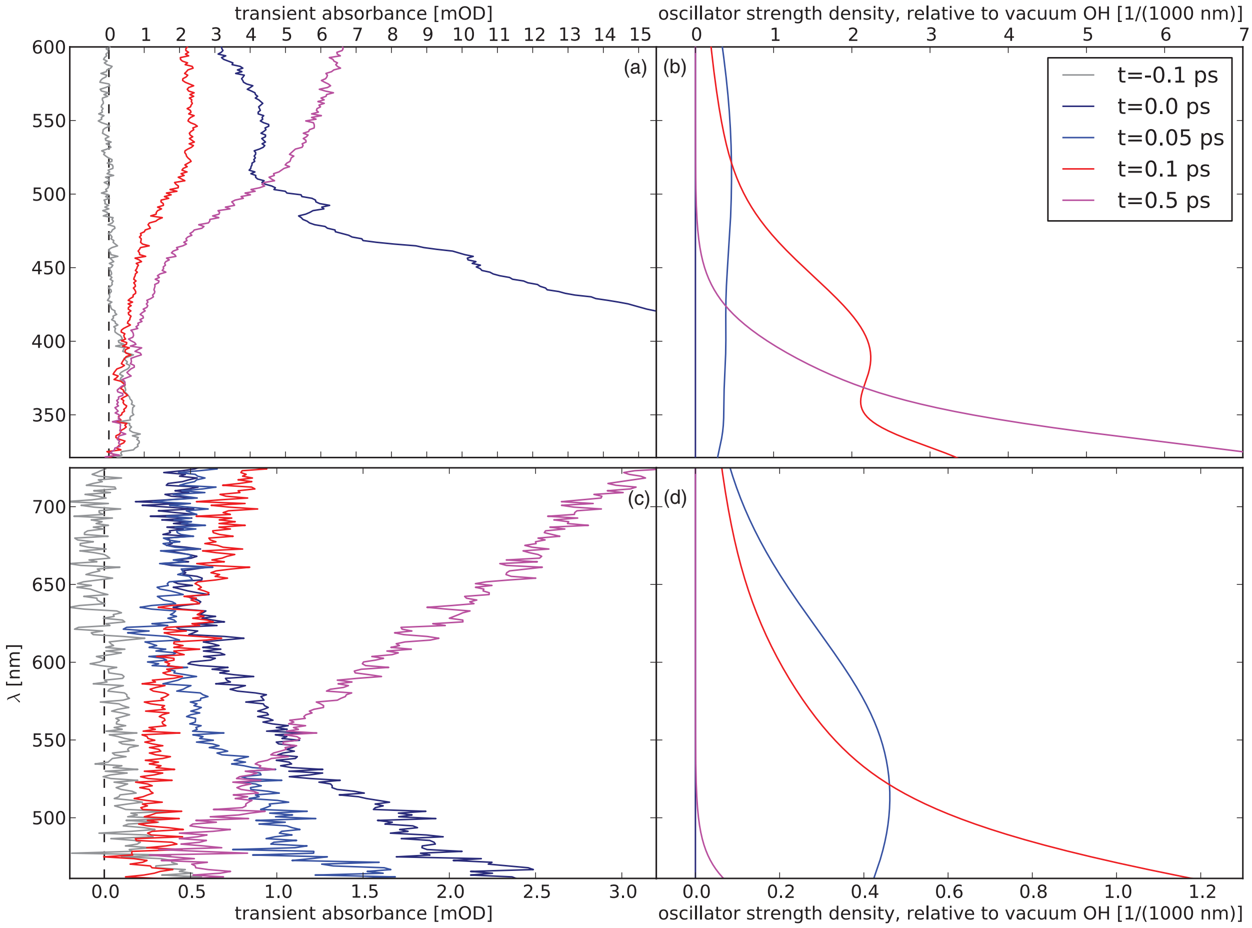

FIG. 10. Spectral cuts from the four panels of Fig. 9 at four pump-probe delays comparing theoretical prediction (b and d) and experimental reality (a and c). No blue shifting feature is picked up experimentally.

simultaneous absorption of one pump and one probe photon when the two laser pulses are overlapped in time.[31] No excited state is formed in this pathway and the width of the feature is instead determined by the cross correlation of the two pulses. If any of the signal is due to population formed by absorption of two pump photons (no intensity dependent data are given in Ref. 14), this part of the signal must originate from absorption from the excited state of neutral H_2O and the free[43,46] OH radicals formed very rapidly by direct dissociation.[28] Preliminary measurements in our laboratory show rotationally hot OH radicals, formed in greater yield by photodissociating H_2O_2 than two-photon water photolysis, absorbing out to 400 nm (Figure S4).[60] We reiterate that H_2O^+ is not formed with 8 eV total energy deposition.

If the lifetime of H_2O^+ is as short as the current AIMD trajectories indicate, more intense pump pulses would increase the likelihood of observing the proton-transfer reaction directly. Shorter pulses give better time-resolution but at the expense of increased cross-phase modulation artifacts. More intense pulses would increase the population of H_2O^+ (quadratic in pump intensity), and thus, the signal relative to the 2PA feature which is linear in the pump. However, if (as indicated by AIMD calculations) the initial cationic hole is delocalized and upon localization reacts fast, this means that the population of the localized H_2O^+ will be small at any time, and that even shorter pulses may not resolve the problem of its detection.

There are some additional factors we should consider. In the calculations, we have made an assumption that H_2O^+ is formed in its ground electronic state, since excited state dynamics would involve calculations of the higher states and non-adiabatic couplings, which are both highly non-trivial tasks in the condensed phase. It is possible that it is also non-trivial experimentally to produce a ground state H_2O^+. It may be that in the experiment ionization at 11 eV does not exclusively lead to H_2O^+ with a $(1b_1)^{-1}$ hole and consideration of the excited resonance state of water prepared would then be necessary.[31,61] In this scenario, excitation would promote an electron from the second highest occupied orbital, $3a_1$ (just as in the gas phase $\tilde{B} \leftarrow \tilde{X}$ band) and this is more likely to autoionize to give an excited state $(3a_1)^{-1}$ cation, or decay through a neutral dissociative mechanism that does not produce H_2O^+ as a transient. The dynamics subsequent to ejection of a $3a_1$ electron from the water dimer has recently been considered by Kamarchik *et al.*[23] The excited H_2O^+ cation so formed is metastable to proton transfer, and also has a very different excited state spectrum compared to the ground state localized cation here so far considered. The dissociation scenario is analogous to the neutral pathway that we have previously indicated plays a role at lower excitation energies near 8 eV, except that OH radicals will be formed in an electronically excited state. Therefore, neither of these putative $3a_1$ promotion channels produces the ground state H_2O^+ we have sought here. The relative two-photon cross sections for the various $(1b_1)^{-1}$ and $(3a_1)^{-1}$ excited states and also for direct ionization determine the importance of each of these channels. Despite this possible explanation for the non-observation of ground state H_2O^+ signal, our current assignment of the liquid water spectrum still suggests that at 11 eV transitions to $(1b_1)^{-1}$ dominate over any $(3a_1)^{-1}$ excitation pathway.[31]

CONCLUSIONS

We have investigated in detail the reaction dynamics of the cationic hole formed in water after ionization by high energy radiation. Not only is this reaction of fundamental importance in radiation chemistry, but this is also an excellent test case for *ab initio* molecular dynamics, complementing the numerous studies that have considered the excess electron in water. We find that from a theoretical perspective, there is an initially partially delocalized state and that the localization transition is of key importance in determining the overall timescale for the reaction process. The degree of delocalization and the timescale for localization, however, are critically determined by the amount of HF exchange included in the DFT treatment. We have carefully benchmarked a self-interaction correction for BLYP against varying amounts of exact HF exchange and EOM-IP-CCSD for small clusters.[20,25,62] For such a benchmarked DFT model, the average localization time is ~30 fs and proton transfer starts practically immediately. Although the proton transfer step may proceed even faster if quantum tunneling is accounted for, as localization is found to be rate limiting here, tunneling should not influence the overall kinetics.

Simulated electronic spectra are constructed using a QM/MM scheme based on EOM-IP-CCSD and the structural snapshots from the set of AIMD trajectories. These predict an electronic signature shifting across the visible into the near-ultraviolet and intensifying with time that provides a means to track the reaction $H_2O^+ + H_2O \rightarrow OH + H_3O^+$. A transient absorption experiment with 40 fs time resolution was carried out but did not see any such signature of reaction in the visible and near UV. The spectral simulations make clear that determining a reaction time by monitoring transient absorbance in the ultraviolet (in the stronger charge transfer part of the OH spectrum[43]) is not an unambiguous marker for the appearance time, as the system absorbs in this region even prior to proton transfer. This experimental result definitively overturns the prior value of 100 fs based on pump-probe spectroscopy and very often quoted in the literature and introductory texts on radiation chemistry for this reaction.

Several points concerning the experiment should be acknowledged: (i) Our sensitivity to a localized H_2O^+ based on its visible band oscillator strength may not be sufficient. (ii) Because the localization step is rate-limiting for the overall reaction, the localized H_2O^+ starts reacting immediately and so is never strongly populated. This, together with the distribution of the starting times of the reaction (equivalent to the localization times), makes it difficult for the experiment to detect. (iii) In the experiment, due to complexities of the photoionization process itself, which are yet to be fully understood, the system may not start out on the ground state cation surface considered by AIMD. (iv) It is possible that the reaction time is indeed at the lower limit of the theoretical prediction and is, therefore, not resolvable with current temporal resolution of the experiment.

In summary, we have characterized the ultrafast dynamics following photoionization in bulk water with AIMD simulations. These calculations provide a detailed molecular picture of the cationic hole localization and subsequent proton transfer and a <40 fs timescale for the overall reaction is consistent, but not proven, by a new time-resolved study.

ACKNOWLEDGMENTS

J.V. acknowledges fruitful discussions with Michiel Sprik and O.M. acknowledges stimulating discussions with Roi Baer. Support from the Czech Science Foundation (Grant Nos. 203/08/0114), the Czech Ministry of Education (Grant No. LC512), and the Academy of Sciences (Praemium Academie) is gratefully acknowledged. Part of the work in Prague was supported via Project Z40550506. O.M. and E.P. acknowledge support from the International Max-Planck Research School for Dynamical Processes in Atoms, Molecules and Solids. Generous allocation of computer time from the Swiss National Supercomputer Centre (CSCS) is gratefully acknowledged. Experimental and theoretical work at the University of Southern California was supported by the U.S. National Science Foundation via CHE-0617060 and CHE-0957869 as well as the iOpenShell Center for the Computational Studies of Electronic Structure and Spectroscopy of Open-Shell and Electronically Excited Species (CRIF:CRF CHE-0625419+0624602+0625237).

[1] B. C. Garrett, D. A. Dixon, D. M. Camaioni, D. M. Chipman, M. A. Johnson, C. D. Jonah, G. A. Kimmel, J. H. Miller, T. N. Rescigno, P. J. Rossky, S. S. Xantheas, S. D. Colson, A. H. Laufer, D. Ray, P. F. Barbara, D. M. Bartels, K. H. Becker, H. Bowen, S. E. Bradforth, I. Carmichael, J. V. Coe, L. R. Corrales, J. P. Cowin, M. Dupuis, K. B. Eisenthal, J. A. Franz, M. S. Gutowski, K. D. Jordan, B. D. Kay, J. A. LaVerne, S. V. Lymar, T. E. Madey, C. W. McCurdy, D. Meisel, S. Mukamel, A. R. Nilsson, T. M. Orlando, N. G. Petrik, S. M. Pimblott, J. R. Rustad, G. K. Schenter, S. J. Singer, A. Tokmakoff, L. S. Wang, C. Wittig, and T. S. Zwier, Chem. Rev. **105**, 355 (2005).

[2] G. V. Buxton, C. L. Greenstock, W. P. Helman, and A. B. Ross, J. Phys. Chem. Ref. Data **17**, 513 (1988).

[3] P. Kambhampati, D. H. Son, T. W. Kee, and P. F. Barbara, J. Phys. Chem. A **106**, 2374 (2002).

[4] J. A. Kloepfer, V. H. Vilchiz, V. A. Lenchenkov, X. Y. Chen, and S. E. Bradforth, J. Chem. Phys. **117**, 766 (2002).

[5] G. Stein, Israel J. Chem. **9**, 413 (1971).

[6] O. Marsalek, T. Frigato, J. VandeVondele, S. E. Bradforth, B. Schmidt, C. Schutte, and P. Jungwirth, J. Phys. Chem. B **114**, 915 (2010).

[7] K. H. Schmidt and D. M. Bartels, Chem. Phys. **190**, 145 (1995).

[8] S. M. Pimblott, J. Phys. Chem. **95**, 6946 (1991).

[9] T. Goulet and J.-P. Jay-Gerin, J. Chem. Phys. **97**, 5076 (1992).

[10] J. A. LaVerne and S. M. Pimblott, J. Phys. Chem. A **14**, 9820 (2000).

[11] C. von Sonntag, *Free-Radical-Induced DNA Damage and Its Repair: A Chemical Perspective* (Springer, Berlin, 2006).

[12] C. D. Jonah, D. M. Bartels, and A. C. Chernovitz, International Journal of Radiation Applications and Instrumentation. Part C. Radiation Physics and Chemistry **34**, 145 (1989).
[13] T. Ellenberger, *DNA Repair and Mutagenesis* (ASM, Washington, 2005).
[14] Y. Gauduel, S. Pommeret, A. Migus, and A. Antonetti, Chem. Phys. **149**, 1 (1990).
[15] B. Winter, R. Weber, W. Widdra, M. Dittmar, M. Faubel, and I. V. Hertel, J. Phys. Chem. A **108**, 2625 (2004).
[16] C. G. Elles, A. E. Jailaubekov, R. A. Crowell, and S. E. Bradforth, J. Chem. Phys. **125**, 044515 (2006).
[17] X. Chen, D. S. Larsen, S. E. Bradforth, and I. H. M. van Stokkum, J. Phys. Chem. A **115**, 3807 (2011).
[18] P. Han and D. M. Bartels, J. Phys. Chem. **94**, 5824 (1990).
[19] H. Tachikawa, J. Phys. Chem. A **106**, 6915 (2002).
[20] P. A. Pieniazek, J. VandeVondele, P. Jungwirth, A. I. Krylov, and S. E. Bradforth, J. Phys. Chem. A **112**, 6159 (2008).
[21] Q. Y. Cheng, F. A. Evangelista, A. C. Simmonett, Y. Yamaguchi, and H. F. Schaefer, J. Phys. Chem. A **113**, 13779 (2009).
[22] G. H. Gardenier, M. A. Johnson, and A. B. McCoy, J. Phys. Chem. A **113**, 4772 (2009).
[23] E. Kamarchik, O. Kostko, J. M. Bowman, M. Ahmed, and A. I. Krylov, J. Chem. Phys. **132**, 194311 (2010).
[24] H. Tachikawa, J. Phys. Chem. A **108**, 7853 (2004).
[25] P. A. Pieniazek, E. J. Sundstrom, S. E. Bradforth, and A. I. Krylov, J. Phys. Chem. A **113**, 4423 (2009).
[26] A. Furuhama, M. Dupuis, and K. Hirao, Phys. Chem. Chem. Phys. **10**, 2033 (2008).
[27] A. Furuhama, M. Dupuis, and K. Hirao, J. Chem. Phys. **124**, 164310 (2006).
[28] C. G. Elles, I. A. Shkrob, R. A. Crowell, and S. E. Bradforth, J. Chem. Phys. **126**, 164503 (2007).
[29] X. Chen and S. E. Bradforth, Annu. Rev. Phys. Chem. **59**, 203 (2008).
[30] P. A. Pieniazek, E. J. Sundstrom, S. E. Bradforth, and A. I. Krylov, J. Phys. Chem. A **113**, 4423 (2009).
[31] C. G. Elles, C. A. Rivera, Y. Zhang, P. A. Pieniazek, and S. E. Bradforth, J. Chem. Phys. **130**, 084501 (2009).
[32] A. Madarasz, P. J. Rossky, and L. Turi, J. Chem. Phys. **126** (2007).
[33] D. Borgis, P. J. Rossky, and L. Turi, J. Chem. Phys. **127** (2007).
[34] A. A. Mosyak, O. V. Prezhdo, and P. J. Rossky, J. Chem. Phys. **109**, 6390 (1998).
[35] G. B. Griffin, R. M. Young, O. T. Ehrler, and D. M. Neumark, J. Chem. Phys. **131** (2009).
[36] A. E. Bragg, J. R. R. Verlet, A. Kammrath, O. Cheshnovsky, and D. M. Neumark, Science **306**, 669 (2004).
[37] A. R. Menzeleev and T. F. Miller, J. Chem. Phys. **132** (2010).
[38] S. Grimme, J. Comput. Chem. **27**, 1787 (2006).
[39] J. VandeVondele and M. Sprik, Phys. Chem. Chem. Phys. **7**, 1363 (2005).
[40] J. Heyd, G. E. Scuseria, and M. Ernzerhof, J. Chem. Phys. **118**, 8207 (2003).
[41] A. D. Becke, J. Chem. Phys. **98**, 1372 (1993).
[42] M. Sodupe, J. Bertran, L. Rodriguez-Santiago, and E. J. Baerends, J. Phys. Chem. A **103**, 166 (1999).
[43] D. M. Chipman, J. Phys. Chem. A **112**, 13372 (2008).
[44] J. VandeVondele, M. Krack, F. Mohamed, M. Parrinello, T. Chassaing, and J. Hutter, Comput. Phys. Commun. **167**, 103 (2005).
[45] H. J. C. Berendsen, J. R. Grigera, and T. P. Straatsma, J. Phys. Chem. **91**, 6269 (1987).
[46] I. Janik, D. M. Bartels, and C. D. Jonah, J. Phys. Chem. A **111**, 1835 (2007).
[47] Y. Shao, L. F. Molnar, Y. Jung, J. Kussmann, C. Ochsenfeld, S. T. Brown, A. T. B. Gilbert, L. V. Slipchenko, S. V. Levchenko, D. P. O'Neill, R. A. DiStasio, R. C. Lochan, T. Wang, G. J. O. Beran, N. A. Besley, J. M. Herbert, C. Y. Lin, T. Van Voorhis, S. H. Chien, A. Sodt, R. P. Steele, V. A. Rassolov, P. E. Maslen, P. P. Korambath, R. D. Adamson, B. Austin, J. Baker, E. F. C. Byrd, H. Dachsel, R. J. Doerksen, A. Dreuw, B. D. Dunietz, A. D. Dutoi, T. R. Furlani, S. R. Gwaltney, A. Heyden, S. Hirata, C. P. Hsu, G. Kedziora, R. Z. Khalliulin, P. Klunzinger, A. M. Lee, M. S. Lee, W. Liang, I. Lotan, N. Nair, B. Peters, E. I. Proynov, P. A. Pieniazek, Y. M. Rhee, J. Ritchie, E. Rosta, C. D. Sherrill, A. C. Simmonett, J. E. Subotnik, H. L. Woodcock, W. Zhang, A. T. Bell, A. K. Chakraborty, D. M. Chipman, F. J. Keil, A. Warshel, W. J. Hehre, H. F. Schaefer, J. Kong, A. I. Krylov, P. M. W. Gill, and M. Head-Gordon, Phys. Chem. Chem. Phys. **8**, 3172 (2006).
[48] P. Hunt and M. Sprik, ChemPhysChem **6**, 1805 (2005).
[49] M. J. McGrath, J. I. Siepmann, I. F. W. Kuo, C. J. Mundy, J. VandeVondele, J. Hutter, F. Mohamed, and M. Krack, J. Phys. Chem. A **110**, 640 (2006).
[50] E. R. Davidson and W. T. Borden, J. Phys. Chem. **87**, 4783 (1983).
[51] D. Marx, M. E. Tuckerman, J. Hutter, and M. Parrinello, Nature **397**, 601 (1999).
[52] P. M. Hare, E. A. Price, and D. M. Bartels, J. Phys. Chem. A **112**, 6800 (2008).
[53] V. H. Vilchiz, J. A. Kloepfer, A. C. Germaine, V. A. Lenchenkov, and S. E. Bradforth, J. Phys. Chem. A **105**, 1711 (2001).
[54] M. K. Fischer, H. Rossmadl, and H. Iglev, J. Chem. Phys. **134**, 214507 (2011).
[55] A. E. Jailaubekov and S. E. Bradforth, Appl. Phys. Lett. **87**, 021107 (2005).
[56] M. J. Tauber, R. Mathies, X. Chen, and S. E. Bradforth, Rev. Sci. Instrum. **74**, 4958 (2003).
[57] R. Lian, R. A. Crowell, and I. A. Shkrob, J. Phys. Chem. A **109**, 1510 (2005).
[58] V. H. Vilchiz, J. A. Kloepfer, A. C. Germaine, V. A. Lenchenkov, and S. E. Bradforth, J. Phys. Chem. A **105**, 1711 (2001).
[59] D. M. Bartels and R. A. Crowell, J. Phys. Chem. A **104**, 3349 (2000).
[60] Y. Zhang, L. Cass, C. G. Elles, and S. E. Bradforth (unpublished).
[61] P. C. do Couto and D. M. Chipman, J. Chem. Phys. **132**, 244307 (2010).
[62] E. Livshits, R. S. Granot, and R. Baer, J. Phys. Chem. A **115**, 5735 (2011).
[63] See supplementary material at http://dx.doi.org/10.1063/1.3664746 for additional experimental and computational data and figures.

Dynamics of Electron Localization in Warm versus Cold Water Clusters

Ondrej Marsalek,[1] Frank Uhlig,[2] Tomaso Frigato,[3] Burkhard Schmidt,[3] and Pavel Jungwirth[1,*]
[1]*Institute of Organic Chemistry and Biochemistry, Academy of Sciences of the Czech Republic and Center for Biomolecules and Complex Molecular Systems, Flemingovo nám. 2, CZ-16610 Prague 6, Czech Republic*
[2]*Wilhelm-Ostwald-Institut für Physikalische und Theoretische Chemie, Linnéstraße 2, D-04103 Leipzig, Germany*
[3]*Institut für Mathematik, Freie Universität Berlin, Arnimallee 6, D-14195 Berlin, Germany*

(Received 5 March 2010; published 21 July 2010)

The process of electron localization on a cluster of 32 water molecules at 20, 50, and 300 K is unraveled using *ab initio* molecular dynamics simulations. In warm, liquid clusters, the excess electron relaxes from an initial diffuse and weakly bound structure to an equilibrated, strongly bound species within 1.5 ps. In contrast, in cold, glassy clusters the relaxation processes is not completed and the electron becomes trapped in a metastable surface state with an intermediate binding energy. These results question the validity of extrapolations of the properties of solvated electrons from cold clusters of increasing size to the liquid bulk.

DOI: 10.1103/PhysRevLett.105.043002 PACS numbers: 31.15.es, 33.15.Ry, 33.80.Eh

Interaction of ionizing radiation with water leads to formation of a quasifree electron and a partially delocalized cationic hole. Both of these species undergo ultrafast reactive dynamics. H_2O^+ reacts on a 100 fs time scale with a neighboring water molecule forming H_3O^+ and OH [1,2]. The latter is a key radical involved in indirect radiation damage of DNA. In this process, the quasifree electron also plays a role [1,3]; however, the aqueous environment causes its localization and formation of a solvated electron on a picosecond time scale [4,5]. Depending on water purity, solvated electrons survive for up to microseconds or milliseconds before reacting with salt ions, dissolved oxygen molecules, OH radicals, protons, or water molecules themselves [1,6–10]. These are fundamental reactions in radiation chemistry, which are important, among others, in nuclear waste treatment [1].

A very detailed molecular insight into the structure of an electron in aqueous environment has been gained from cluster studies. Both experiments and calculations show that the character of this species changes from a weakly (dipole) bound electron in small water clusters to a more bulklike solvated electron in larger clusters [11–19]. This behavior has been utilized for extrapolating the binding energy and other properties of the electron from clusters of increasing size into the aqueous bulk [12,20]. These extrapolations are, however, not free of contradictions, which concern the occurrence of several isomers and electron binding motifs, as well as surface vs interior location of the electron in water clusters of different sizes [12,14,19]. A crucial issue, which has gained more attention recently [15,21] and will be addressed in this study, is the fact that extrapolations to liquid water are done using clusters at very low (typically below 100 K) temperatures. Under these conditions, clusters with tens to hundreds of water molecules are unlikely to be liquid, but rather resemble amorphous solids [22]. In such a glassy state, translational motion is dramatically slowed down. Therefore, kinetically trapped electron-cluster geometries which depend on preparation conditions, rather than fully relaxed structures, can prevail in the experiment [12,15]. Measurements and simulations show that the observed state sensitively depends on the history of the cluster both before and after electron attachment [15,21].

Here, we address the question of electron localization on medium-size water clusters at warm vs cold conditions using *ab initio* molecular dynamics (AIMD) simulations. Initially, an electron is vertically (i.e., without any geometry change) attached to a neutral cluster comprising 32 water molecules and its subsequent dynamics is followed at cluster temperatures ranging from 20 to 300 K. We show below that the resulting localization process dramatically depends on temperature, which puts a question mark over extrapolations from cold clusters to the liquid bulk.

The computational methodology has been described in detail in our recent paper on electron-proton recombination in water [9]. Briefly, we perform AIMD using the BLYP density functional [23,24] with a dispersion correction [25]. Pseudopotentials [26] replace the oxygen core electrons and the hybrid Gaussian plane wave scheme is used for efficient evaluation of the energies and forces [27]. The self-interaction correction is employed for the singly-occupied orbital in a restricted open-shell Kohn-Sham framework [28]. The Kohn-Sham orbitals are represented using a TZV2P basis set [29] augmented with diffuse Gaussian functions placed on a regular grid spanning the whole simulation box. Open boundary conditions together with a suitable electrostatic solver [30] are used, as is appropriate for a cluster system. The vertical detachment energy (VDE) is calculated directly from the energy difference between the anionic and the neutral system at the same geometry. The excess electron is plotted as the unpaired spin density of the system [31]. Comparison to RIMP2 calculations suggests that the present DFT calculations only slightly overestimate the VDE of the excess electron [31]. The present way of correcting the self-interaction error improves the description of the anionic cluster at the expense of artificially increasing the VDE. Compared to previously used one-electron models [19,32] the all (valence) electron AIMD approach adopted here explicitly accounts for coupling between the excess electron and valence electrons of water molecules [33].

All the localization trajectories were started from the geometry of a neutral water cluster. For comparison, equilibrium trajectories were also performed, started with a preexisting polarized cavity [31]. Initial geometries for localization at low temperatures were obtained by energy minimization, while the 300 K simulations used snapshots from dynamics at 300 K as their initial condition. All production simulations were performed at constant total energy using the CP2K package [34].

We simulated six localization trajectories with an electron added to a cluster of 32 water molecules equilibrated at 300 K. Figure 1 shows three snapshots from a representative trajectory, taken at 0, 950, and 4250 fs. Upon attachment to the neutral cluster, the excess electron is initially delocalized over the outer surface of the water cluster [Fig. 1(a)], with a radius of gyration of about 6 Å. However, the excess electron immediately starts to shrink, polarizing neighboring water molecules. This localization process can be roughly separated into two steps. First, water molecules locally reorient forming the initial solvation structure within less than a picosecond [Fig. 1(b)]. The structure then becomes even more favorable for electron binding by translational and further rotational motion of water molecules. This process creates a polarized cavity and moves the electron deeper into the cluster. Nevertheless, for most of the simulation time the electron remains solvated asymmetrically with respect to the center of the cluster, i.e., close to the surface [Fig. 1(c)]. In less than 1.5 ps the electron thus acquires its final size of about 2.75 Å and becomes indistinguishable from an equilibrated solvated electron in a 32 water cluster, as investigated in our previous study [31].

The main physical characteristics, i.e., radius of gyration, VDE, and average distance from the cluster center of mass (COM) [31] of the excess electron along the trajectory depicted in Fig. 1 are plotted in Fig. 2. The top panel shows the process of shrinking of the excess electron from its initial size of 6 Å to about 5 Å in less than 1 ps, and then to the final value of ~2.75 Å in another 0.5 ps. The middle panel depicts the VDE, the negative value of which strongly correlates with the radius of gyration of the excess electron, as observed also for the equilibrated solvated electron [31]. The initial delocalized electron is bound to the neutral water cluster by less than 1 eV; however, within 1.5 ps its vertical binding energy triples, fluctuating around its final value of about 3 eV. The last panel of Fig. 2 shows the time evolution of the average distance of the excess electron from the COM of the water cluster [31]. This distance decreases from its initial value of 6 Å to about 5 Å. The excess electron is thus brought closer to the COM of the cluster by the localization process. Nevertheless, it remains to be situated predominantly in the interfacial region, in agreement with previous studies of an equilibrium solvated electron in a cluster of the same size [19,31]. Finally, note that there is little correlation between the position of the excess electron within the cluster and its vertical binding energy [31].

Time evolution of the radius of gyration of the excess electron [9] for the six simulated trajectories at 300 K is depicted in Fig. 3. Because of different geometries of the neutral clusters at the moment of electron attachment, the localization process is unique for each trajectory. Nevertheless, the feature common to all of them is that the excess electron shrinks from ~6 Å to roughly 2.75 Å in less than 1.5 ps. For comparison, the red plot at the left hand side of Fig. 3 shows the distribution of radii of gyration of electrons attached to neutral water clusters at 200 different geometries, while the green plot at the right hand side

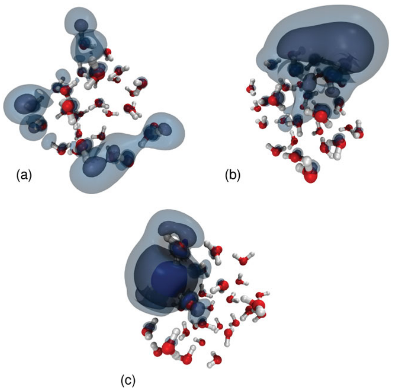

FIG. 1 (color). Snapshots from a representative trajectory at times (a) 0, (b) 950, and (c) 4250 fs after the vertical attachment of the excess electron to a cluster of 32 water molecules at 300 K.

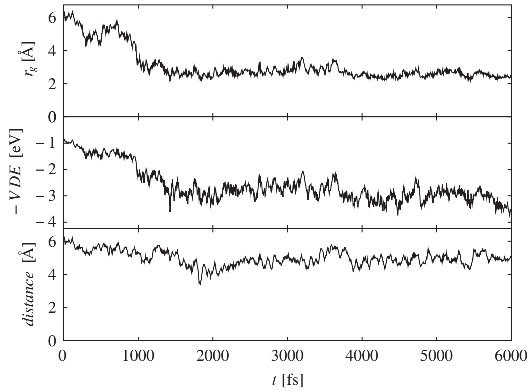

FIG. 2. Time evolution of the radius of gyration (top panel), vertical detachment energy (middle panel), and average distance of the excess electron from the cluster center of mass (bottom panel) for a representative localization trajectory at 300 K.

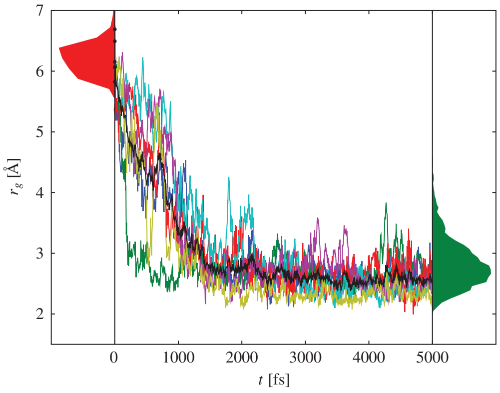

FIG. 3 (color). Time evolution of the radius of gyration of the excess electron in the six localization trajectories at 300 K. Black curve shows the average of these trajectories. Black dots mark the values at $t = 0$ fs. Left, red: distribution of radii of gyration of electrons attached to neutral water clusters. Right, green: distribution of radii of gyration of the solvated electron in equilibrium trajectories.

corresponds to radii of gyration obtained from 40 ps of simulation time of an equilibrium solvated electron. Note that the initial and final distributions of radii of gyration of the localization trajectories match the former and the latter plot, despite the fact that the final distribution is taken from entirely independent simulations.

Let us now move from clusters at ambient temperature to very cold ones. Figure 4 shows the time evolution of the radius of gyration of the excess electron for clusters with mean temperature of 20 or 50 K, compared to those at 300 K. We see that upon moving from warm liquid to cold solid clusters the situation changes dramatically. The initial (subpicosecond) electron localization phase is similar for all temperatures, except that the vertical electron affinity at $t = 0$ is slightly lower in cold clusters. However, at later stages the electron on cold clusters does not localize further, but rather gets trapped in geometries with a radius of gyration between 4 and 5 Å and VDE of 1.3–1.5 eV. Clearly, the initial (partial) reorientation of water molecules is feasible also in the cold glassy clusters, but further stabilization of the electron solvation structure by translational motion of water molecules is hindered at low temperatures. The cold clusters thus get trapped in a metastable situation about half way between the initial geometry and the equilibrated solvated electron. This trapping will persist on much longer time scales than those of the present simulations (up to 15 ps). This is due to the extremely small diffusion rate in amorphous solid water, which is at least 6 orders of magnitude below that in liquid water [35,36]. Therefore, excess electrons attached to cold water clusters are likely to be kinetically trapped in metastable geometries for the micro to millisecond time scales pertinent to the experiment [12,15].

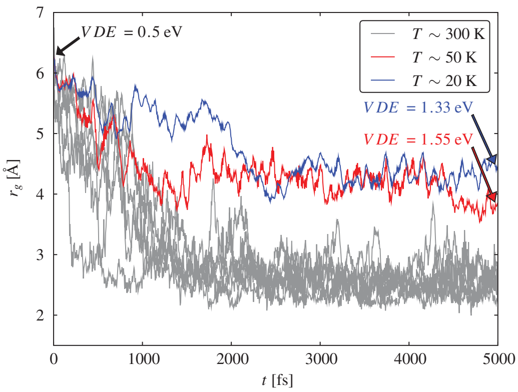

FIG. 4 (color). Time evolution of the radius of gyration of the excess electron in localization trajectories at 20 and 50 K. Arrows with labels show the VDE for both trajectories at the beginning (same geometry for both) and at $t = 5$ ps. Data for 300 K are shown for comparison (gray).

The trapping and nonergodic behavior in cold water clusters is further demonstrated in Fig. 5, which shows the correlation between the radius of gyration of the excess electron and its average distance from the COM of the cluster at different temperatures. Comparison to simulations of an equilibrated solvated electron at 300 K shows again the pronounced difference between localization in warm vs cold clusters. During electron localization at 300 K the system explores the same phase space region as the equilibrated electron (actually an even broader one thanks to the initially strongly delocalized geometries). In cold clusters, however, the excess electron remains localized in a narrow phase space region corresponding to large distances from the cluster center and large to medium values of the radius of gyration. Most notably, at 20 or 50 K the system never visits the region of small radii of gyration, which are characteristic for equilibrium solvated electrons, nor does it leave the outer surface of the cluster. Note that this is not the only possible scenario of formation of cold anionic clusters [15,21], but it is pertinent to cluster experiments used for extrapolations to the liquid bulk [12,20].

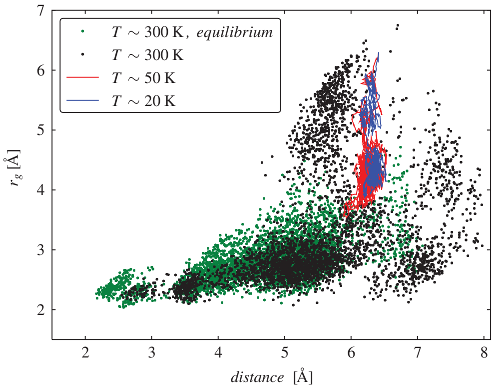

FIG. 5 (color). Correlation between the average distance of the electron from the cluster center of mass and the radius of gyration of the electron. Green: data from equilibrium trajectories at 300 K. Black: data from the first 3 ps of the six localization trajectories at 300 K. Red, blue: data from localization trajectories at 20 and 50 K.

Our simulations shed new light on attempts to extrapolate electron binding energies of different isomers from cold water clusters to the liquid bulk [12,20]. Different experimental conditions lead to effective temperatures of the clusters between 10 and 150 K, where they are solid or at most partially melted [37]. The present simulations of clusters at 20–50 K are most relevant for experiments performed in the lower temperature range, where isomers with weakly bound electrons exist. Experiments show that in such cold clusters several isomers of the excess electron with distinct binding energies can be found [12]. Our simulations support previous suggestions [12,15,19] that most of these isomers are metastable structures kinetically trapped in the glassy clusters. The most stable isomer probably represents an exception, being close to a relaxed structure. This is indicated by the fact that its VDE extrapolates reasonably to the bulk value [15,20,38]. Still, these clusters are about 200 K colder than the liquid bulk and, moreover, at these temperatures, all the less stable isomers are kinetically trapped structures. The present calculations show that in liquid clusters at ambient conditions, which are, however, not readily accessible to experiment due to evaporative cooling, no such distinct isomers exist. The electron, initially attached to a neutral system at 300 K, always relaxes within 1.5 ps into its equilibrated state. Only for this situation, extrapolation of the properties of the excess electron with increasing cluster size to the aqueous bulk is fully justified.

We thank Barbara Kirchner, Joost VandeVondele, Steve Bradforth, Bernd Winter, Katrin Siefermann, and Bernd Abel for fruitful discussions. Support from the Czech Science Foundation (Grant 203/08/0114) and from the Czech Ministry of Education (Grant LC 512) is gratefully acknowledged. O. M. thanks the IMPRS for support.

---

*pavel.jungwirth@uochb.cas.cz

[1] B. C. Garrett *et al.*, Chem. Rev. **105**, 355 (2005).
[2] P. A. Pieniazek, J. VandeVondele, P. Jungwirth, A. I. Krylov, and S. E. Bradforth, J. Phys. Chem. A **112**, 6159 (2008).
[3] J. Simons, Acc. Chem. Res. **39**, 772 (2006).
[4] P. Kambhampati, D. H. Son, T. W. Kee, and P. F. Barbara, J. Phys. Chem. A **106**, 2374 (2002).
[5] V. H. Vilchiz, J. A. Kloepfer, A. C. Germaine, V. A. Lenchenkov, and S. E. Bradforth, J. Phys. Chem. A **105**, 1711 (2001).
[6] E. Hart and M. Anbar, *The Hydrated Electron* (Wiley-Interscience, New York, 1970).
[7] G. V. Buxton, C. L. Greenstock, W. P. Helman, and A. B. Ross, J. Phys. Chem. Ref. Data **17**, 513 (1988).
[8] R. A. Crowell and D. M. Bartels, J. Phys. Chem. **100**, 17713 (1996).
[9] O. Marsalek, T. Frigato, J. VandeVondele, S. E. Bradforth, B. Schmidt, C. Schütte, and P. Jungwirth, J. Phys. Chem. B **114**, 915 (2010).
[10] C. G. Elles, A. E. Jailaubekov, R. A. Crowell, and S. E. Bradforth, J. Chem. Phys. **125**, 044515 (2006).
[11] J. V. Coe, G. H. Lee, J. G. Eaton, S. T. Arnold, H. W. Sarkas, K. H. Bowen, C. Ludewigt, H. Haberland, and D. R. Worsnop, J. Chem. Phys. **92**, 3980 (1990).
[12] J. R. R. Verlet, A. E. Bragg, A. Kammrath, O. Cheshnovsky, and D. M. Neumark, Science **307**, 93 (2005).
[13] G. B. Griffin, R. M. Young, O. T. Ehrler, and D. M. Neumark, J. Chem. Phys. **131**, 194302 (2009).
[14] N. I. Hammer, J.-W. Shin, J. M. Headrick, E. G. Diken, J. R. Roscioli, G. H. Weddle, and M. A. Johnson, Science **306**, 675 (2004).
[15] L. Ma, K. Majer, F. Chirot, and B. von Issendorff, J. Chem. Phys. **131**, 144303 (2009).
[16] R. N. Barnett, U. Landman, C. L. Cleveland, and J. Jortner, J. Chem. Phys. **88**, 4429 (1988).
[17] J. Xu and K. D. Jordan, J. Phys. Chem. A **114**, 1364 (2010).
[18] H. M. Lee, S. B. Suh, P. Tarakeshwar, and K. S. Kim, J. Chem. Phys. **122**, 044309 (2005).
[19] L. Turi, W.-S. Sheu, and P. J. Rossky, Science **309**, 914 (2005).
[20] K. R. Siefermann, Y. Liu, E. Lugovoy, O. Link, M. Faubel, U. Buck, B. Winter and B. Abel, Nature Chem. **2**, 274 (2010).
[21] A. Madarasz, P. J. Rossky, and L. Turi, J. Phys. Chem. A **114**, 2331 (2010).
[22] V. Buch, B. Sigurd, J. Paul Devlin, U. Buck, and J. K. Kazimirski, Int. Rev. Phys. Chem. **23**, 375 (2004).
[23] A. D. Becke, Phys. Rev. A **38**, 3098 (1988).
[24] C. Lee, W. Yang, and R. G. Parr, Phys. Rev. B **37**, 785 (1988).
[25] S. Grimme, J. Comput. Chem. **27**, 1787 (2006).
[26] S. Goedecker, M. Teter, and J. Hutter, Phys. Rev. B **54**, 1703 (1996).
[27] G. Lippert, J. Hutter, and M. Parrinello, Mol. Phys. **92**, 477 (1997).
[28] J. VandeVondele and M. Sprik, Phys. Chem. Chem. Phys. **7**, 1363 (2005).
[29] J. VandeVondele and J. Hutter, J. Chem. Phys. **127**, 114105 (2007).
[30] L. Genovese, T. Deutsch, and S. Goedecker, J. Chem. Phys. **127**, 054704 (2007).
[31] T. Frigato, J. VandeVondele, B. Schmidt, C. Schütte, and P. Jungwirth, J. Phys. Chem. A **112**, 6125 (2008).
[32] R. N. Barnett, U. Landman, and A. Nitzan, J. Chem. Phys. **91**, 5567 (1989).
[33] I. A. Shkrob, J. Phys. Chem. A **111**, 5223 (2007).
[34] J. VandeVondele, M. Krack, F. Mohamed, M. Parrinello, T. Chassaing, and J. Hutter, Comput. Phys. Commun. **167**, 103 (2005).
[35] K.-H. Jung, S.-C. Park, J.-H. Kim, and H. Kang, J. Chem. Phys. **121**, 2758 (2004).
[36] R. S. Smith, Z. Dohnalek, G. A. Kimmel, K. P. Stevenson, and B. D. Kay, Chem. Phys. **258**, 291 (2000).
[37] C. Hock, M. Schmidt, R. Kuhnen, C. Bartels, L. Ma, H. Haberland, and B. v. Issendorff, Phys. Rev. Lett. **103**, 073401 (2009).
[38] A. T. Shreve, T. A. Yen, and D. M. Neumark, Chem. Phys. Lett. **493**, 216 (2010).

J. Phys. Chem. C **2010,** *114,* 20489–20495 **20489**

Electrons in Cold Water Clusters: An ab Initio Molecular Dynamics Study of Localization and Metastable States[†]

Ondrej Marsalek,[‡] Frank Uhlig,[§] and Pavel Jungwirth*,[‡]

Institute of Organic Chemistry and Biochemistry, Academy of Sciences of the Czech Republic and Center for Biomolecules and Complex Molecular Systems, Flemingovo nám. 2, 16610 Prague 6, Czech Republic, and Wilhelm-Ostwald-Institut für Physikalische und Theoretische Chemie, Linnéstrasse 2, 04103 Leipzig, Germany

Received: May 28, 2010; Revised Manuscript Received: July 2, 2010

Ab initio molecular dynamics simulations were performed with the aim to follow two scenarios for an excess electron in cold water clusters. In the first one, an electron is attached to a quenched neutral cluster. Such an electron, initially very delocalized and loosely bound, shrinks somewhat and increases its vertical detachment energy to 1−1.5 eV within several picoseconds. Unlike in warm liquid clusters, the electron in this cold system does not, however, reach a more compact and strongly bound structure. In contrast, if an equilibrated negatively charged water cluster with a well-localized excess electron is instantaneously quenched to ∼0 K, the electron remains strongly bound in a water cavity and practically does not change its size and binding energy. These results have important consequences for detailed interpretation of photoelectron spectroscopy measurements of electrons solvated in aqueous clusters and liquid water microjets.

Introduction

One of the pressing questions concerning the structure and dynamics of a hydrated electron[1−5] concerns the relation of its properties in water clusters and in the liquid bulk. This question is not only how clusters of increasing size approach the bulk limit but also how different the experimental conditions in the two situations are.[6−12] A crucial property of a solvated electron is its vertical binding energy, i.e., the negative of the vertical detachment energy (VDE) of the anionic system. Its importance is also reflected in the fact that experiments on negatively charged water clusters[6,8,12] have been used to extrapolate its value to the bulk limit, which has been hard to obtain directly. Most recently, direct VDE measurements in the aqueous bulk have become feasible thanks to the technique of liquid microjets.[13−15] In this context it is imperative to properly establish the relation between cluster and microjet experiments. While the former systems are solid, having effective temperatures below 150 K,[12] the latter are liquid with temperatures above the freezing point.[13,15]

A typical feature of the experiments on negatively charged water clusters is that several isomers with distinct VDEs are observed for a given system size.[8,12] Depending on the particular way of cluster preparation, these isomers are populated with varying abundances.[12] There is ongoing discussion about the structural interpretation in terms of either the position (surface vs interior) or different surface states of the electron.[8,12,16−21] Attempts have also been made to extrapolate the VDEs of these isomers to infinite size and interpret the extrapolated values in terms of different structures (bulk vs surface) of an electron solvated in liquid water.[8,12,13] There is, however, a potential problem with such interpretations. Namely, in the microjet experiment, equilibrium liquid state conditions can be assumed for the solvated electron.[13,15] However, the isomers observed in the solid clusters do not necessarily correspond to an equilibrium situation but can reflect metastable situations pertinent to their experimental preparation.[11,12,20,21] The issues to be addressed in such extrapolations are, therefore, connected not only with different temperatures and phases (liquid vs amorphous solid or crystalline) but also with thermodynamic vs kinetically trapped states.

Problems connected with the metastability of the cluster states of the solvated electron and the corresponding dependence of the result on the method of preparation have been addressed both in experiments[12] and in simulations.[20,21] Comparison between two experiments with different ways of formation and storing of the water cluster anions is revealing.[8,12] Some isomers are present in both measurements, while others show up only in one experiment, which again points to their metastable nature. Related calculations, treating the electron as a quantum particle and water molecules classically, confirm that the occurrence and population of different isomers reflect the thermal history of the cluster.[20] Most recently, we have performed ab initio molecular dynamics simulations of the localization process following electron attachment to cold or warm neutral water clusters.[21] Using a density functional theory based all (valence) electron approach, we have shown that at 300 K the excess electron attached to a neutral water cluster relaxes to an equilibrium solvated state within 1.5 ps, while at 20−50 K it becomes trapped in a metastable state about half way between the initial and the fully relaxed state.[21] Here, we employ similar computational techniques to investigate and analyze electrons in cold water clusters prepared in different ways. Out of the various possibilities,[20] we chose to compare two very different scenarios. In the first one, the electron attaches to a cold neutral cluster and localizes afterward, while in the second one an equilibrated warm negatively charged water cluster is quenched to 0 K. This comparison allows us to characterize in detail the nature of electrons localized in or on cold water clusters prepared under different conditions.

[†] Part of the "Mark A. Ratner Festschrift".

* Corresponding author, pavel.jungwirth@uochb.cas.cz.

[‡] Academy of Sciences of the Czech Republic and Center for Biomolecules and Complex Molecular Systems.

[§] Wilhelm-Ostwald-Institut für Physikalische und Theoretische Chemie.

10.1021/jp1049028

Methods

We performed ab initio molecular dynamics (AIMD) simulations for anionic clusters consisting of 32 water molecules. Initial conditions for the trajectories were prepared in two different ways. In the first one, structures from an AIMD of a neutral water cluster were taken and energy minimized and, at $t = 0$, the number of electrons was increased by 1. Eight trajectories were launched from these initial geometries with velocities sampled from Maxwell−Boltzmann distributions at 30−50 K. In the second one, geometries were obtained by energy minimization of 47 structures obtained in previous AIMD simulations of $(H_2O)_{32}^-$ at 300 K.[21] Subsequently, two of these were used as initial conditions for MD trajectories. Classical equations of motion for the nuclei were propagated with a time step of 0.5 fs with no temperature coupling.

Energies and forces were evaluated using the Becke, Lee, Yang, and Parr (BLYP) exchange-correlation functional.[22,23] Dispersion interactions were accounted for using empirical pairwise damped London terms.[24] It was shown previously that this combination provides a very good description of liquid water.[25] To correct for the self-interaction error, which is an important issue for open shell systems, the functional was augmented with an additional term depending on the electron density of the unpaired electron.[26,27] To this end, we worked within a restricted open shell formulation of the density functional theory. The Kohn−Sham orbitals were expanded into an atom-centered triple-ζ basis set with two polarization functions, optimized for condensed molecular systems,[28] in conjunction with an auxiliary plane wave basis with a cutoff of 280 Ry for the electronic density. The Goedecker−Teter−Hutter norm-conserving pseudopotentials[29] replaced the oxygen core electrons. The system was placed in a $20 \times 20 \times 20$ Å^3 box, and an open boundary conditions Poisson's solver,[30] appropriate for clusters, was employed. For a proper description of the diffuse part of the spin density, an additional grid of 1000 Gaussian functions with width of 0.189 Å^{-1} and spacing of 2 Å was placed within the box.[21] VDE was evaluated as the difference between ground state energies of the cluster before and after electron detachment, in the geometry of the anion. Calculations were performed using the Quickstep module of the freely available CP2K program package.[31]

Below, we provide for reference definitions of various quantities monitored during the AIMD runs. Due to the restricted open-shell formalism employed, the total spin density of the system coincides with the density of the singly occupied molecular orbital (SOMO):

$$s(\mathbf{r}) = \Phi_{\mathrm{SOMO}}(\mathbf{r})\Phi_{\mathrm{SOMO}}{}^*(\mathbf{r})$$

The spin density itself is normalized as

$$\int s(\mathbf{r})\,\mathrm{d}^3r = 1$$

The two main observables monitored throughout all of the simulations are the first and second moments of the spin distribution. Whereas the first moment $\mathbf{r}_\mathrm{c}$ provides the center of the spin distribution

$$\mathbf{r}_\mathrm{c} = \int \mathbf{r}s(\mathbf{r})\,\mathrm{d}^3r$$

the second moment corresponds to the gyration tensor

$$\mathbf{S} = \int (\mathbf{r} - \mathbf{r}_\mathrm{c})(\mathbf{r} - \mathbf{r}_\mathrm{c})s(\mathbf{r})\,\mathrm{d}^3r$$

This tensor has three eigenvalues, denoted as λ_x^2, λ_y^2, and λ_z^2. For a description of the size of the excess electron, we use the radius of gyration $\mathbf{r}_\mathrm{g}$ which can either be defined as

$$r_\mathrm{g} = \sqrt{\int s(\mathbf{r})(\mathbf{r} - \mathbf{r}_\mathrm{c})^2\,\mathrm{d}^3r}$$

or using the three eigenvalues of the gyration tensor

$$r_\mathrm{g} = \sqrt{(\lambda_x{}^2 + \lambda_y{}^2 + \lambda_z{}^2)}$$

The gyration tensor is symmetric and positive-definite; hence all its eigenvalues are positive as well. Thus, we can approximate the shape of the spin distribution as an ellipsoid with its half-axes equal to λ_x^{-1}, λ_y^{-1}, and λ_z^{-1}. Several shape descriptors are available for such an ellipsoid.[32] The asphericity b determines the deviation from a perfect sphere

$$b = \lambda_z{}^2 - \frac{1}{2}(\lambda_x{}^2 + \lambda_y{}^2)$$

It acquires non-negative values and it is zero for a perfect sphere. The deviation from cylindric symmetry (acylindricity) is

$$c = (\lambda_y{}^2 - \lambda_z{}^2)$$

which is also always non-negative and zero for cylindric symmetry. The relative shape anisotropy, given by

$$\kappa^2 = \frac{b^2 + \frac{3}{4}c^2}{r_\mathrm{g}{}^4}$$

is an overall measure of the deviation from any kind of symmetry of the ellipsoid. It is bounded between 0 and 1, with zero corresponding to a perfect sphere.

Results and Discussion

In this study, we compare the behavior of the excess electron in cold water clusters prepared in two different ways: (i) by attaching an electron to a neutral system which has been thermally equilibrated and then instantaneously quenched to 0 K or (ii) by instantaneously cooling to 0 K a previously thermally equilibrated negatively charged cluster, with the electron occupying a well-developed cavity and being strongly bound. In each case, we monitor the dynamics started from these initial conditions with the total energy of the system kept constant. Figures 1 and 2 show representative sets of snapshots from these trajectories (for animations of these trajectories see Supporting Information). We see that the two different ways of preparation of the cold clusters lead to qualitatively different structure and dynamics of the excess electron. When the electron is attached to a cold cluster (Figure 1), it is initially strongly delocalized over the cluster surface and within several picoseconds partially localizes at one side of the outer surface of the water clusters. As also discussed in previous studies,[21,33] this partial localization is due to a slight reorganization of the

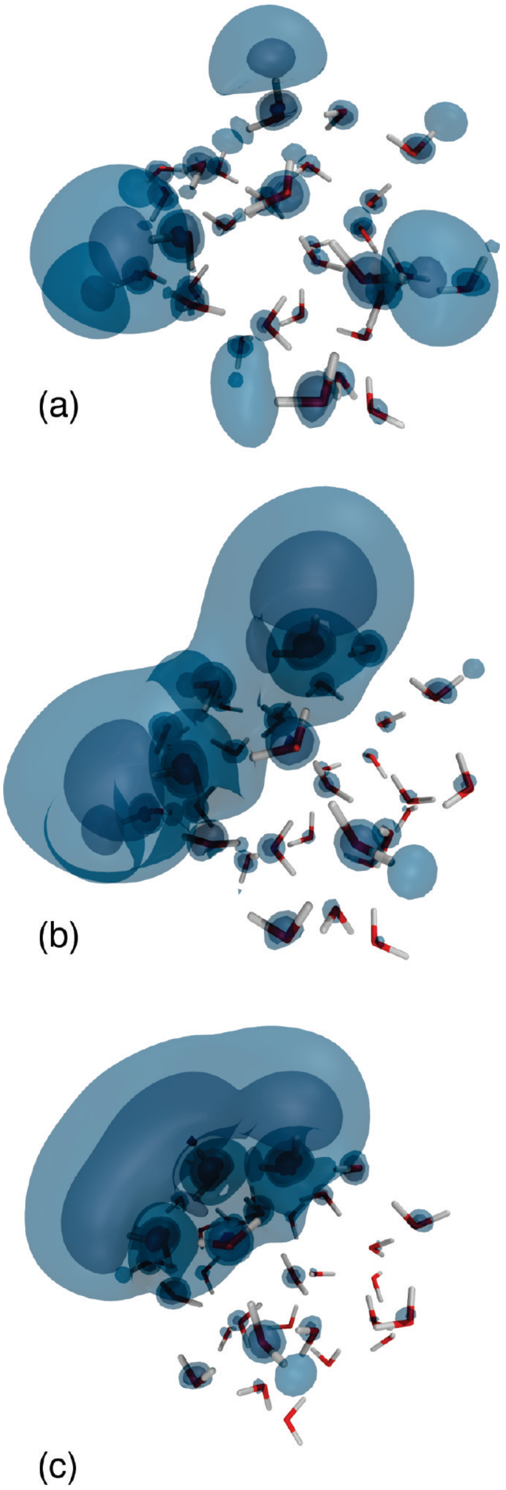

Figure 1. Snapshots of the localization process following the attachment of an electron to a cold neutral water cluster: (a) the moment of electron attachment ($t = 0$ fs); (b) snapshot after partial localization on the surface ($t = 1.75$ ps); (c) after further relaxation to a metastable state ($t = 5$ ps). Isovalues correspond to electron densities of 0.003, 0.0005, and 0.0002 au.

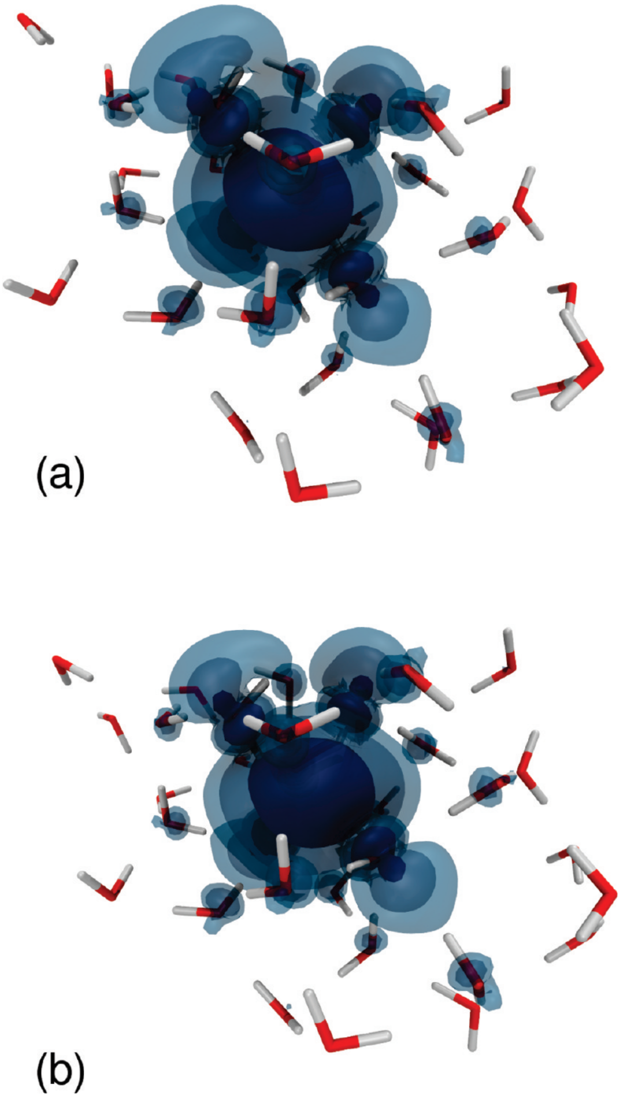

Figure 2. Snapshots from a run of an anionic water cluster equilibrated at 300 K and then instantaneously quenched to 0 K. (a) $t = 0$ fs and (b) after 5 ps molecular dynamics at constant energy.

dangling hydrogens of surface water molecules. However, in the cold water cluster there is not enough flexibility to allow for a creation of a polarized cavity, which would lead to a fully solvated electron. Such an equilibrated cavity electron forms in a warm cluster and remains largely intact upon cooling of this structure (Figure 2). Moreover, the shape of the excess electron prepared in this way mostly does not change during dynamics after cooling (Figure 2). It is worth mentioning at this point that the excess electron in the warm cluster, while strongly localized most of the time, can transiently acquire rather delocalized structures.[18] If such a structure is quenched to 30−50 K, we found that in the subsequent dynamics the electron remains delocalized at the cluster surface.

Time evolution of the radius of gyration of excess electrons prepared in the two ways described above is depicted in Figure 3. An electron attached to a quenched neutral water cluster starts gradually shrinking from its initial radius of more than 6 Å. However, on the time scale of the (several picosecond) simulations it remains significantly larger than an electron equilibrated at 300 K, with radius below 3 Å. In contrast, for an equilibrated negatively charged water cluster quenched to 0 K the already small electron further slightly shrinks and preserves its smaller size for the whole duration of the “cold” trajectory. The sizes of excess electrons prepared in these two ways thus appear on opposite tails of the equilibrium size distribution in the warm cluster (Figure 3). Figure 4 shows for

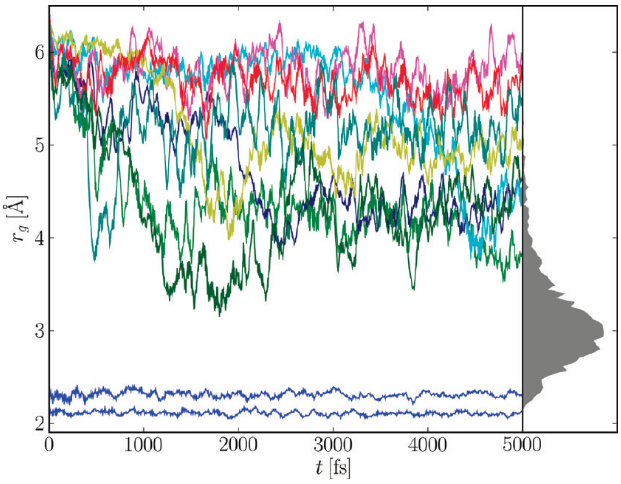

Figure 3. Radius of gyration of the excess electron as a function of time for different types of trajectories. Runs started from quenched equilibrated anionic water clusters are shown in blue (two trajectories), runs started by attachment of the electron to a quenched neutral water cluster are shown in other colors (eight trajectories). Equilibrium runs at $T = 300$ K are shown in gray for reference (six trajectories).

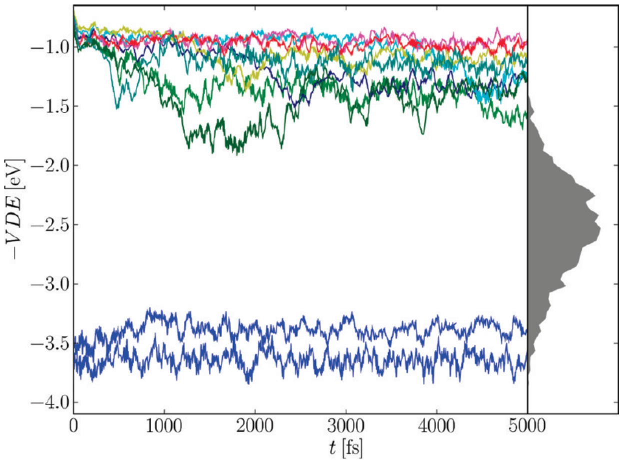

Figure 4. Vertical detachment energy of the excess electron as a function of time for different types of trajectories. Runs started from quenched equilibrated anionic water clusters are shown in blue (two trajectories), runs started by attachment of the electron to a quenched neutral water cluster are shown in other colors (eight trajectories). Equilibrium runs at $T = 300$ K are shown in gray for reference (six trajectories).

the same set of trajectories as in Figure 3 the corresponding time evolution of VDE. For electrons attached to cold water clusters, their vertical binding shifts from about −0.5 to −1 to −1.5 eV. These values are still rather far from the −2.5 to −3 eV binding of electrons in clusters equilibrated at 300 K, indicating that the clusters are kinetically trapped.[20,21] Note also that cooling of an equilibrated negatively charged cluster leads to small increase of electron binding, which then remains roughly constant as time evolves (Figure 4).

Figure 5 shows the time evolution of the radius of gyration, VDE, and the distance between the center of the electron and center of mass of the cluster for a representative trajectory started by attaching an electron to an instantaneously quenched equilibrated neutral water cluster. As in our previous studies,[18,21] we see a very strong correlation between the size of the excess electron and its vertical binding energy. In contrast, there is little correlation between the VDE and the position of the electron with respect to the water cluster. This indicates that photoelectron spectroscopy is an excellent tool for distinguishing between delocalized and compact excess electron structures. However, it does not provide direct information about the position (interior vs interfacial) of the excess electron.

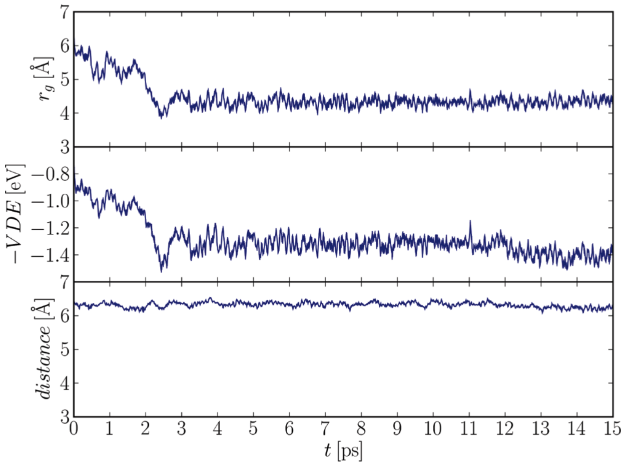

Figure 5. Time evolution of the radius of gyration (top panel), vertical detachment energy (middle panel), and average distance of the excess electron from the cluster center of mass (bottom panel) for a representative trajectory corresponding to initial attachment of the electron to a quenched neutral water cluster.

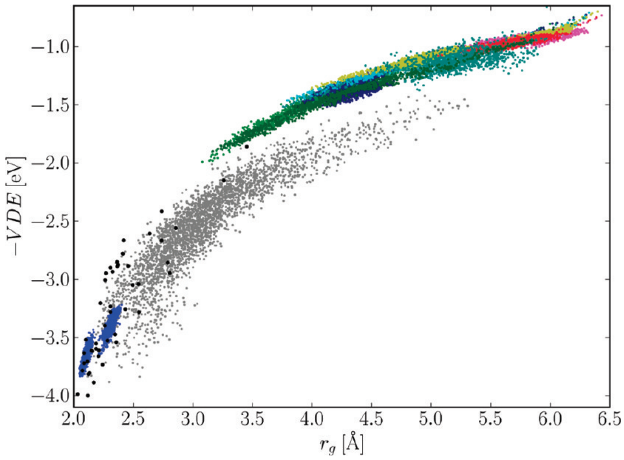

Figure 6. Correlation between the vertical detachment energy and the radius of gyration of the excess electron for different types of trajectories and configurations. A set of geometries obtained by cooling equilibrated anionic water clusters is shown in black, runs started from three of those geometries are depicted in blue, and runs started by attachment of an electron to a quenched neutral water cluster are shown in other colors (eight trajectories). For comparison, equilibrium runs at $T = 300$ K are shown in gray (25 ps total simulation time).

A direct presentation of the correlation between the radius of gyration and VDE of the excess electron is provided in Figure 6. We see that the two investigated ways of preparing cold excess electrons lead to filling separate regions of phase space. Electrons attached to equilibrated and then quenched clusters fill during subsequent dynamics a narrow region where the radius of gyration changes from 6.5 to 3 Å and, in concert, VDE moves from 0.5 to 2 eV. In contrast, when an equilibrated negatively charged water cluster is quenched to 0 K, the phase space region encompasses small radii of gyration (roughly 2−3 Å) and strong electron binding (about −2.5 to −4 eV) with zero overlap with the situation where the electron is attached to cold clusters (Figure 6). The phase space region corresponding

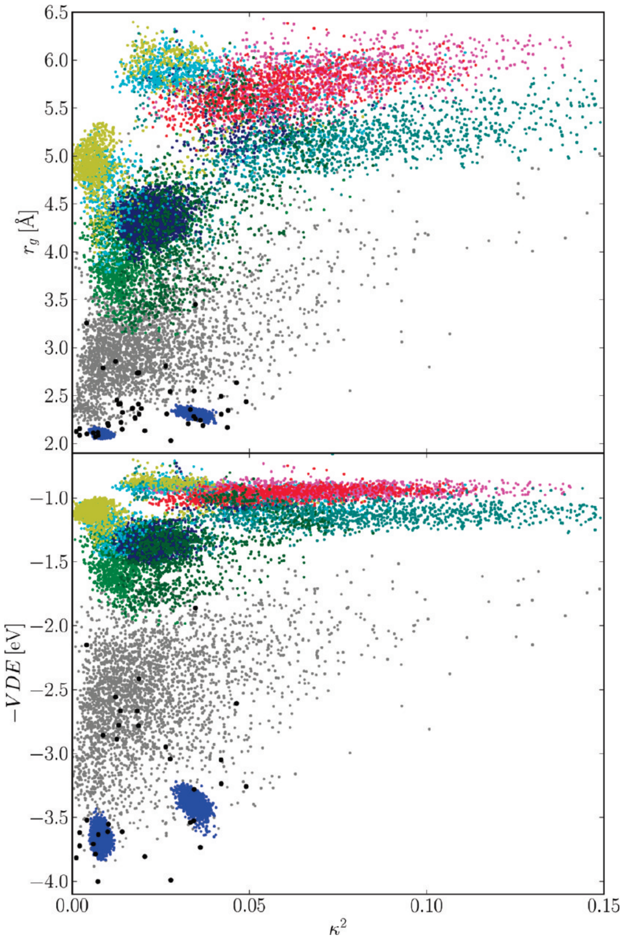

Figure 7. Correlation between shape anisotropy and radius of gyration (top panel) and vertical detachment energy (bottom panel) for different types of trajectories and configurations. A set of geometries obtained by cooling equilibrated anionic water clusters is shown in black, runs started from three of those geometries are depicted in blue, and runs started by attachment of an electron to a quenched neutral water cluster are shown in other colors (eight trajectories). For comparison, equilibrium runs at T = 300 K are shown in gray (25 ps total simulation time).

to equilibrated anion clusters at 300 K lies between these two sets, overlapping on one end with the quenched negatively charged clusters, while being separated by a gap from electrons attached to cold clusters (Figure 6). The latter confirms that attaching an electron to a cold cluster does not lead (at least on the time scale of the simulation) to an equilibrated strongly bound electron but rather to a weak electron binding energy of a kinetically trapped species. Figure 7 shows similar correlations as in Figure 6, but now between the asymmetry parameter of the excess electron[27] and its radius of gyration or VDE. We see that the extended, loosely bound structures, pertinent to electron attachment to a cold cluster, start as rather asymmetric distributions, which become more symmetric as the electron (partially) localizes. The more compact and more strongly bound structures, corresponding to equilibrated negatively charged clusters, both before and after cooling, tend to be also more symmetric as seen from lower values of the asymmetry parameter.

The kinetic trapping of the structures obtained from dynamics started by electron attachment to neutral clusters quenched to 0 K is further demonstrated in Figure 8, which shows the time evolution of the root-mean-square deviation (rmsd) from the t = 0 structure as a function of time for a representative trajectory. We see an increase of the rmsd from 0 to about 1 Å within the first few picoseconds, which corresponds to small rearrangements of the surface water molecules as the electron starts to localize. However, the reorientation of water molecules then stops as exemplified by the leveling of the rmsd. In contrast, at ambient conditions rmsd continues to increase (Figure 8) as the cavity for the strongly bound electron forms in sufficiently large water clusters (such as that investigated here) and moves by diffusion in the liquid cluster. This, however, does not happen in cold clusters and, consequently, the system becomes kinetically trapped. These observations have important implications concerning the validity of extrapolations of the properties of the excess electron from cold clusters to the bulk liquid. If experiments could be done for warm liquid clusters, such extrapolation would be well justified. However, since the kinetically trapped structures with weakly bound electrons tend to disappear upon heating, it is questionable whether such extrapolations to liquid water are justified. This in particular concerns the experimentally observed cold cluster isomers with less negative VDEs,[8,12] which do not seem to have an analogue in the ambient liquid.

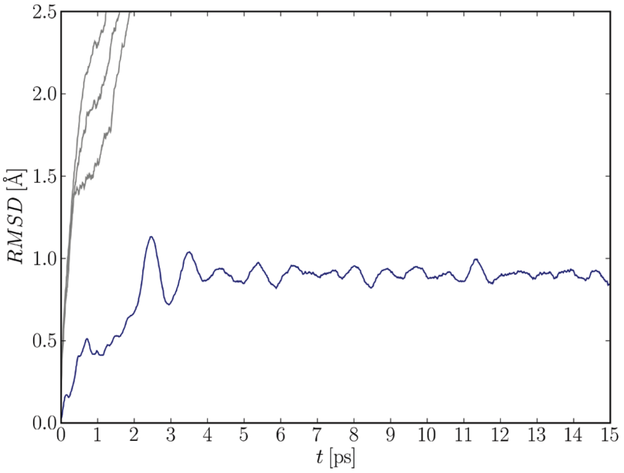

Figure 8. Root mean square deviation of the system from its initial geometry as a function of time for a representative trajectory, where the excess electron has been attached to a quenched neutral cluster at t = 0 (dark blue). For comparison, results for three equilibrium runs at 300 K are shown in gray.

Our results concerning the structure and dynamics of the excess electron are only as good as the underlying electronic structure description. It is, therefore, important to establish the reliability of the results with respect to the employed basis set and density functional method. The former issue is of particular importance for proper description of delocalized structures such as the excess electron. We found out that adding a regularly spaced grid of diffuse Gaussian functions is an effective and economic way of dealing with this problem. Figures 9 and 10 demonstrate the convergence of the crucial properties of the excess electron—its radius of gyration and VDE, with the number of Gaussian functions added. We see that for an excess electron in a well-developed cavity convergence is achieved at around 500 basis functions. For a more diffuse structure of the excess electron convergence is, as expected, somewhat slower, nevertheless 1000 basis functions (which in the present setup corresponds to a grid spanning the whole box) provide practically converged radius of gyration and VDE. Figure 11 shows the effects of additional Gaussian functions and the self-interaction correction[26,27] on the radius of gyration, position of the excess electron, and its VDE along a representative trajectory

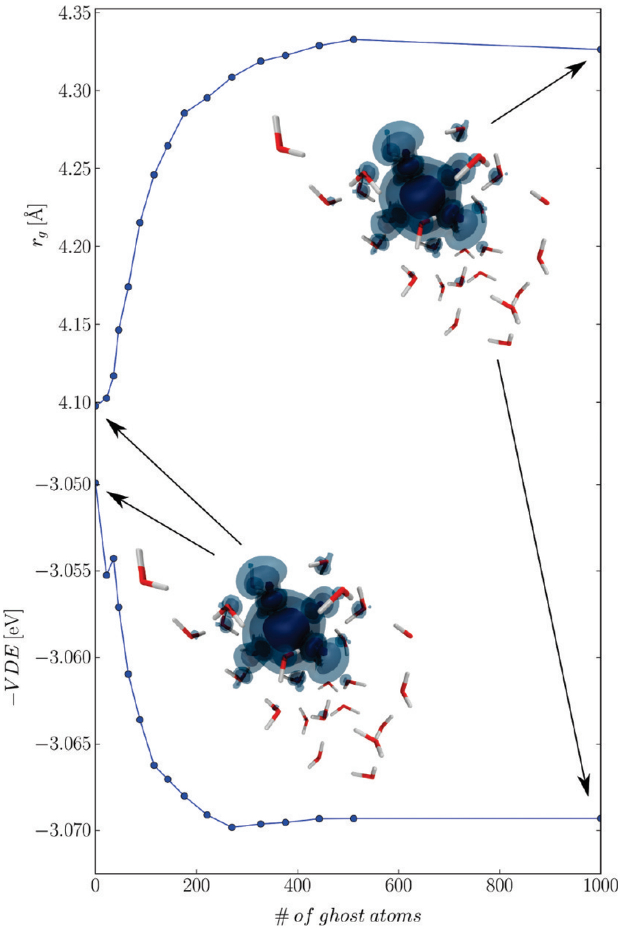

Figure 9. Radius of gyration (top panel) and vertical detachment energy (bottom panel) for a representative cluster geometry with the excess electron in a well-developed cavity, as a function of the number of ghost atoms used as additional diffuse basis functions. A spherical cutoff from the center of the excess electron is used to decrease the number of ghost atoms.

(same trajectory as in Figure 5; first 5 ps) corresponding to an electron attached to a quenched neutral cluster. We see that the effects of both the additional basis set and the self-interaction correction are important. Additional Gaussians allow accommodating better the excess electron, particularly in regions where no atoms of water molecules are present, which leads to its increase in size and distance from the center of cluster. At the same time a more complete basis set results in a more strongly bound excess electron.

Density functional methods within the generalized gradient approximation (such as BLYP) cannot provide an exact description of the excess electron.[34] They tend to overshoot the VDE of the excess electron, which may be partly due to an unbalanced description of system with varying number of electrons, i.e., before and after electron detachment. The self-interaction correction removes a significant part of the spurious self-repulsion of the excess electron. This allows the electron to better localize, leading to more compact and more strongly bound structures. Quantitatively, inclusion of the self-interaction correction increases the VDE by up to 0.5 eV. Since we do not correct for self-interaction error in the closed shell state after ionization, this increase may to some extent be artificial. Nevertheless, the structure and dynamics of the anionic clusters, which are in the focus of our study, should not be affected by this.

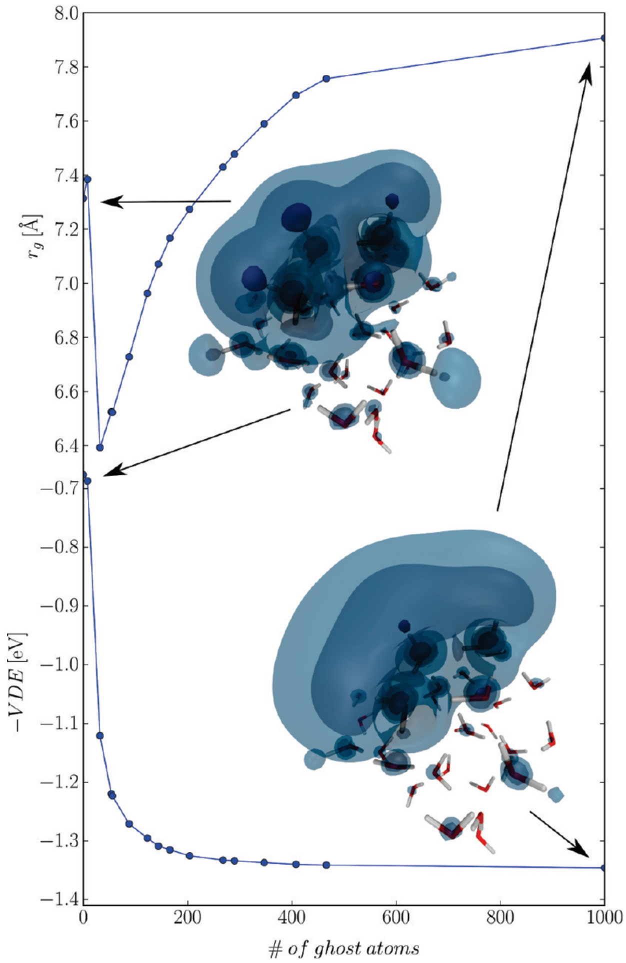

Figure 10. Radius of gyration (top panel) and vertical detachment energy (bottom panel) for a representative cluster geometry with the excess electron in a diffuse surface state, as a function of the number of ghost atoms used as additional diffuse basis functions. A spherical cutoff from the center of the excess electron is used to decrease the number of ghost atoms.

Conclusions

We performed ab initio molecular dynamics simulations of an excess electron in cold water clusters containing 32 water molecules, comparing two ways of preparation of the initial conditions of the system. Within the first scenario, we attached at $t = 0$ an excess electron to a neutral cluster, previously equilibrated (at 300 K) and then instantaneously quenched to 0 K. In the second approach, a negatively charged water cluster was first equilibrated at 300 K and then instantaneously quenched to 0 K, after which the dynamics was monitored. In the first case, the initially very delocalized and loosely bound electron partially relaxed, which is connected with a decrease of its size and increase of its vertical detachment energy from about 0.5 to $1 - 1.5$ eV within several picoseconds. However, at these cryogenic conditions the excess electron in a sufficiently large water cluster, such as the one investigated here, does not reach equilibrium (at least not on the picosecond time scale) but rather becomes kinetically trapped. In the second scenario, the excess electron remains well localized in a water cavity. As a matter of fact, cooling of equilibrated negatively charged water clusters, possessing a well-localized excess electron, even increases VDEs and decreases the electron size. The size and binding energy of such an excess electron change little during

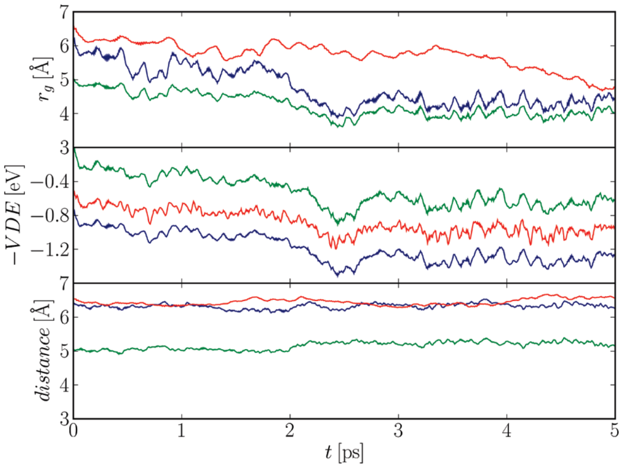

Figure 11. Time evolution of the radius of gyration (top panel), vertical detachment energy (middle panel), and average distance of the excess electron from the cluster center of mass (bottom panel) for the same trajectory as in Figure 5 comparing calculations with self-interaction correction and additional Gaussian basis functions (blue) to calculations lacking either the former (red) or the latter (green) item.

subsequent dynamics. Our results demonstrate, in agreement with previous studies,[12,20,21] that the properties of the excess electron in cryogenic water clusters depend on the details of the preparation of the system. This also raises questions concerning the validity of direct extrapolations of properties of electrons in cold water clusters to the bulk liquid.[13,21]

Acknowledgment. Support from the Czech Science Foundation (Grants 203/08/0114) and the Czech Ministry of Education (Grant LC512) is gratefully acknowledged. Part of the work in Prague was supported via Project Z40550506. O.M. acknowledges support from the International Max-Planck Research School for Dynamical Processes in Atoms, Molecules and Solids.

Supporting Information Available: Animations of the localization trajectories. This material is available free of charge via the Internet at http://pubs.acs.org.

References and Notes

(1) Hart, E.; Anbar, M. *The hydrated electron*; Wiley-Interscience: New York, 1970.

(2) Crowell, R. A.; Bartels, D. M. *J. Phys. Chem.* **1996**, *100*, 17713.

(3) Vilchiz, V. H.; Kloepfer, J. A.; Germaine, A. C.; Lenchenkov, V. A.; Bradforth, S. E. *J. Phys. Chem. A* **2001**, *105*, 1711.

(4) Kambhampati, P.; Son, D. H.; Kee, T. W.; Barbara, P. F. *J. Phys. Chem. A* **2002**, *106*, 2374.

(5) Garrett, B. C.; Dixon, D. A.; Camaioni, D. M.; Chipman, D. M.; Johnson, M. A.; Jonah, C. D.; Kimmel, G. A.; Miller, J. H.; Rescigno, T. N.; Rossky, P. J.; Xantheas, S. S.; Colson, S. D.; Laufer, A. H.; Ray, D.; Barbara, P. F.; Bartels, D. M.; Becker, K. H.; Bowen, H.; Bradforth, S. E.; Carmichael, I.; Coe, J. V.; Corrales, L. R.; Cowin, J. P.; Dupuis, M.; Eisenthal, K. B.; Franz, J. A.; Gutowski, M. S.; Jordan, K. D.; Kay, B. D.; LaVerne, J. A.; Lymar, S. V.; Madey, T. E.; McCurdy, C. W.; Meisel, D.; Mukamel, S.; Nilsson, A. R.; Orlando, T. M.; Petrik, N. G.; Pimblott, S. M.; Rustad, J. R.; Schenter, G. K.; Singer, S. J.; Tokmakoff, A.; Wang, L. S.; Wittig, C.; Zwier, T. S. *Chem. Rev.* **2005**, *105*, 355.

(6) Coe, J. V.; Lee, G. H.; Eaton, J. G.; Arnold, S. T.; Sarkas, H. W.; Bowen, K. H.; Ludewigt, C.; Haberland, H.; Worsnop, D. R. *J. Chem. Phys.* **1990**, *92*, 3980.

(7) Hammer, N. I.; Shin, J. W.; Headrick, J. M.; Diken, E. G.; Roscioli, J. R.; Weddle, G. H.; Johnson, M. A. *Science* **2004**, *306*, 675.

(8) Verlet, J. R. R.; Bragg, A. E.; Kammrath, A.; Cheshnovsky, O.; Neumark, D. M. *Science* **2005**, *307*, 93.

(9) Coe, J. V.; Arnold, S. T.; Eaton, J. G.; Lee, G. H.; Bowen, K. H. *J. Chem. Phys.* **2006**, 125.

(10) Coe, J. V.; Williams, S. M.; Bowen, K. H. *Int. Rev. Phys. Chem.* **2008**, *27*, 27.

(11) Ehrler, O. T.; Neumark, D. M. *Acc. Chem. Res.* **2009**, *42*, 769.

(12) Ma, L.; Majer, K.; Chirot, F.; von Issendorff, B. *J. Chem. Phys.* **2009**, 131.

(13) Siefermann, K. R.; Liu, Y. X.; Lugovoy, E.; Link, O.; Faubel, M.; Buck, U.; Winter, B.; Abel, B. *Nat. Chem.* **2010**, *2*, 274.

(14) Neumark, D. M. *Nat. Chem.* **2010**, *2*, 247.

(15) Tang, Y.; Shen, H.; Sekiguchi, K.; Kurahashi, N.; Mizuno, T.; Suzuki, Y. I.; Suzuki, T. *Phys. Chem. Chem. Phys.* **2010**, *12*, 3653.

(16) Roscioli, J. R.; Hammer, N. I.; Johnson, M. A. *J. Phys. Chem. A* **2006**, *110*, 7517.

(17) Turi, L.; Sheu, W. S.; Rossky, P. J. *Science* **2005**, *309*, 914.

(18) Frigato, T.; VandeVondele, J.; Schmidt, B.; Schutte, C.; Jungwirth, P. *J. Phys. Chem. A* **2008**, *112*, 6125.

(19) Madarasz, A.; Rossky, P. J.; Turi, L. *J. Chem. Phys.* **2009**, 130.

(20) Madarasz, A.; Rossky, P. J.; Turi, L. *J. Phys. Chem. A* **2010**, *114*, 2331.

(21) Marsalek, O.; Uhlig, F.; Frigato, T.; Schmidt, B.; Jungwirth, P. Submitted.

(22) Becke, A. D. *Phys. Rev. A* **1988**, *38*, 3098.

(23) Lee, C. T.; Yang, W. T.; Parr, R. G. *Phys. Rev. B* **1988**, *37*, 785.

(24) Grimme, S. *J. Comput. Chem.* **2006**, *27*, 1787.

(25) Schmidt, J.; VandeVondele, J.; Kuo, I. F. W.; Sebastiani, D.; Siepmann, J. I.; Hutter, J.; Mundy, C. J. *J. Phys. Chem. B* **2009**, *113*, 11959.

(26) VandeVondele, J.; Sprik, M. *Phys. Chem. Chem. Phys.* **2005**, *7*, 1363.

(27) Marsalek, O.; Frigato, T.; VandeVondele, J.; Bradforth, S. E.; Schmidt, B.; Schutte, C.; Jungwirth, P. *J. Phys. Chem. B* **2010**, *114*, 915.

(28) VandeVondele, J.; Hutter, J. *J. Chem. Phys.* **2007**, *127*, 114105.

(29) Goedecker, S.; Teter, M.; Hutter, J. *Phys. Rev. B* **1996**, *54*, 1703.

(30) Genovese, L.; Deutsch, T.; Neelov, A.; Goedecker, S.; Beylkin, G. *J. Chem. Phys.* **2006**, *125*, 074105.

(31) VandeVondele, J.; Krack, M.; Mohamed, F.; Parrinello, M.; Chassaing, T.; Hutter, J. *Comput. Phys. Commun.* **2005**, *167*, 103.

(32) Theodorou, D. N.; Suter, U. W. *Macromolecules* **1985**, *18*, 1206.

(33) Kim, S. K.; Park, I.; Lee, S.; Cho, K.; Lee, J. Y.; Kim, J.; Joannopoulos, J. D. *Phys. Rev. Lett.* **1996**, *76*, 956.

(34) Sommerfeld, T.; DeFusco, A.; Jordan, K. D. *J. Phys. Chem. A* **2008**, *112*, 11021.

JP1049028

J. Phys. Chem. B **2010,** *114,* 915–920

Hydrogen Forms in Water by Proton Transfer to a Distorted Electron

Ondrej Marsalek,[†,||] Tomaso Frigato,[‡,||] Joost VandeVondele,[§] Stephen E. Bradforth,[⊥] Burkhard Schmidt,[‡] Christof Schütte,[‡] and Pavel Jungwirth*,[†]

Institute of Organic Chemistry and Biochemistry, Academy of Sciences of the Czech Republic and Center for Biomolecules and Complex Molecular Systems, Flemingovo nám. 2, 16610 Prague 6, Czech Republic, Institut für Mathematik, Freie Universität Berlin, Arnimallee 6, D-14195, Berlin, Germany, Physical Chemistry Institute, Zürich University, Winterthurerstrasse 190, CH-8057 Zürich, Switzerland, and Department of Chemistry, University of Southern California, Los Angeles, California 90089-0482, U.S.A.

Received: September 17, 2009; Revised Manuscript Received: October 29, 2009

Solvated electrons are ubiquitous intermediates in radiation-induced processes, with their lifetime being determined by quenching processes, such as the direct reaction with protons under acidic conditions. Ab initio molecular dynamics simulations allow us to unravel with molecular resolution the ultrafast reaction mechanism by which the electron and proton react in water. The path to a successful reaction involves a distortion and contraction of the hydrated electron and a rapid proton motion along a chain of hydrogen bonds, terminating on the water molecule most protruding into the electron cloud. This fundamental reaction is thus decidedly shown to be of a proton-transfer rather than electron-transfer character. Due to the desolvation penalty connected with breaking of the hydration shells of these charged particles, the reaction is, however, not diffusion-limited, in agreement with the interpretation of kinetics measurements.

Introduction

Solvated electrons are formed when high-energy radiation passes through condensed material ranging from biological tissue to polymers, ceramics, or aqueous solutions used for nuclear waste storage and reprocessing. Water, in particular, has played a central role in radiation chemistry; understanding the chemical reactions that occur subsequent to the initial ionizing events is essential to model radiation-induced processes in the broader class of soft matter.[1,2] The electron in water polarizes the neighboring solvent molecules, creating a hydrated electron, which possesses a fluctuating structure with an average radius of gyration[3,4] of about 2.5 Å. When water is ionized, electrons are hydrated on a time scale shorter than 1 ps, and these species are highly reducing.[1,2] In pure deoxygenated water, the electron can survive for milliseconds, but its reaction with either added quenchers or (bio)chemical systems already dissolved within the liquid are key to the nature of radiation damage that occurs subsequently.

Acids are often used to quench (or scavenge) solvated electrons. For example, the proton quenching reaction plays an important role in the highly acidic media used for reprocessing spent nuclear material (PUREX process). Despite this ubiquitous role of quenching reactions in the radiation chemistry of aqueous systems and the fact that the kinetics of such quenching reactions have been known for decades,[5] a molecular picture for the mechanism of this intriguing class of fundamental reactions has remained elusive.

The electron−proton reaction leading to a hydrogen atom is seemingly the most elementary chemical process, at least in the gas phase, where 1312 kJ mol^{-1} are released upon association. In water, the strong solvation of both charged particles substantially reduces the exoergicity ($\Delta G^{\circ}_{298} = -50$ kJ mol^{-1}), and the reaction mechanism becomes correspondingly much more complex.[6] The reaction can be thought of as either a proton transfer from a hydronium ion to a weak base, forming the H atom in the former cavity of the electron,[7,8] or an electron transfer onto H_3O^+, forming transiently H_3O, which rapidly dissociates.[5] There has been considerable argument over which is the correct picture.[5,7,8] In either case, the process is a reaction between an aqueous H_3O^+ and a water shell polarized around a central negatively charged cavity of e^-_{aq}. It is the subtle way in which the solvent shells need to respond to the motion of each particle that holds the key to understanding the reaction mechanism. The reaction is fast ($k_{298} = 2.3 \times 10^{10}$ M^{-1} s^{-1}).[5,9,10] However, compared to the $H^+ + OH^- \rightarrow H_2O$ reaction, which similarly requires a large solvent rearrangement upon the loss of two ionic hydration shells, the electron−proton reaction in water is almost an order of magnitude slower.[2] Furthermore, despite the Coulomb attraction and the high mobility of H^+, the electron−proton reaction is slower than either of the $H + e^-_{aq} + H_2O \rightarrow H_2 + OH^-$ or $OH + e^-_{aq} \rightarrow OH^-$ reactions.[2] The comparison with the latter is significant since most solvated electrons produced in the ionization of water recombine with the geminate OH rather than the geminate hydronium.[11,12] Analysis of kinetic studies[6] suggests a barrier to the "contact" reaction of the electron−proton pair with passage time of ∼20 ps.

Although the solvated electron as an unusual quantum solute has been an attractive target for nonlinear spectroscopy in the liquid-phase and gas-phase spectroscopy of anionic water clusters, the reactivity of solvated electrons has mainly been charted by pulse radiolysis pump−probe spectroscopy.[1] On the theory side, calculations have dealt with the equilibrium structure and spectroscopy of the hydrated electron,[4,13−17] with its reaction with a proton addressed previously only with static calculations

---

* To whom correspondence should be addressed. E-mail: pavel.jungwirth@uochb.cas.cz. Fax: +420 220 410 320.

[†] Academy of Sciences of the Czech Republic and Center for Biomolecules and Complex Molecular Systems.

[‡] Freie Universität Berlin.

[§] Zürich University.

[⊥] University of Southern California.

[||] Both authors contributed equally.

10.1021/jp908986z

for a small model system of an isolated Eigen cation ($H_9O_4^+$).[18] The dynamical simulations reported here thus represent the first successful modeling of the quenching reaction of the hydrated electron in a system already possessing features pertinent to bulk water, using the full power of methods that compute the electronic structure as it evolves in time.

Methods Section

This section provides computational details pertinent to the present ab initio MD simulations of reactive quenching of the hydrated electron by an excess proton. A set of 10 independent initial conditions were prepared using a 500 ps classical molecular dynamics run of a water cluster containing 31 H_2O molecules and a single hydronium (H_3O^+) and the electron substituted by a negative ion of comparable size.[17] At $t = 0$, we switched to ab initio MD, simulating nominally a $H^+e^-(H_2O)_{32}$ system at the same geometry, employing the semilocal Perdew–Burke–Ernzerhof exchange-correlation functional empirically corrected for long-range dispersion interactions.[19] The Goedecker–Teter–Hutter norm-conserving pseudopotentials[20] replaced the oxygen core electrons. The Kohn–Sham orbitals were expanded in an atom-centered triple-ζ Gaussian basis set augmented with two polarization functions and additional diffuse functions[21] that are necessary for proper description of the solvated electron. The use of the restricted open-shell formalism allowed us to employ the self-interaction correction (SIC) for the unpaired electron.[22] Only with the use of the SIC do the results compare quantitatively to benchmark MP2 calculations.

The optimal values of the SIC parameters a and b were obtained by minimizing the mean-square difference (MSD) between SIC-DFT and RI-UMP2/aug-cc-pVDZ energies for geometries sampled along two different reactive trajectories. A total of 17 configurations were employed, and for each trajectory, energies were shifted to zero average before computing the MSD. The optimization procedure yielded the following values of the SIC parameters: $a = 0.313$ and $b = 0.180$. These were subsequently rounded to $a = 0.3$ and $b = 0.2$ as it was found that around these values, the choice of SIC parameters influenced only slightly the calculated energies. Note that comparing DFT calculations with and without SIC showed that the latter shifts up the energy of the reaction product (i.e., the H atom) with respect to the reactants by up to 80 kJ/mol, hindering therefore the recombination process.

The convergence of the employed basis set in terms of the description of the hydrated electron was checked by augmenting the m-TZV2P basis set[23] by diffuse Gaussian functions with an exponent of 0.1 distributed uniformly in space on a cubic grid with a lattice constant of 2 Å. Tests for one of the reactive trajectories show that this has only a minor effect of a relative stabilization of the reactants with respect to the products by about 30 kJ/mol (as compared to the basis set employed throughout the present study).

The system was placed in a $20 \times 20 \times 20$ Å^3 cubic box, and a cutoff of 280 Ry was used for the auxiliary plane wave basis set. The Poisson equation was treated with a wavelet-based solver with open boundary conditions, which are adequate for the investigated isolated system. Classical equations of motion were integrated with a time step of 0.5 fs within the microcanonical ensemble. Forces were obtained from an electronic structure calculation fully converged at each step. All dynamical calculations were performed using the CP2K package and its electronic structure module Quickstep,[21] employing a setup similar to that of our previous study that focused solely on the nonreactive behavior of the hydrated electron.[17]

The initial geometries for the presented simulations were obtained from classical molecular dynamics using an empirical force field. The system consisted of a cluster of 31 SPCE water molecules, a hydronium, and an iodide ion. For initiating each of the ab initio molecular dynamics simulations, we took a particular geometry along the classical trajctory, removed the iodide, and set the total charge of the system to 0. In this way, an initial cavity was created that is suitable for the solvated electron due to its size and polarization of the surrounding water molecules. Due to the presence of the proton, the electron does not exhibit such a strong tendency to drift fast to the surface via a delocalized state as in our previous study concerned with its nonreactive behavior (i.e., without the presence of the quenching proton).[17]

Finally, we provide here definitions of physical observables monitored during the simulations. The total spin density of the system is defined as the difference between electron densities of the two spin components

$$s(\mathbf{r}) = \rho_\alpha(\mathbf{r}) - \rho_\beta(\mathbf{r}) \tag{1}$$

Because of the restricted open-shell formalism used in the present work, the spin density actually coincides with the electron density of the singly occupied Kohn–Sham orbital

$$s(\mathbf{r}) = \phi_{SO}(\mathbf{r})\phi^*_{SO}(\mathbf{r}) \tag{2}$$

In the following, we work with a spin density normalized so that

$$\int s(\mathbf{r})\mathrm{d}^3r = 1 \tag{3}$$

From this spin density, further quantities are derived. The center of the spin density (i.e., the position of the electron) is the first moment of the distribution

$$\mathbf{r}_c = \int \mathbf{r}s(\mathbf{r})\mathrm{d}^3r \tag{4}$$

The radial distribution of the spin density relative to this center is then

$$4\pi r^2 s(R) = \int s(\mathbf{r} - \mathbf{r}_c)\mathrm{d}\Omega \tag{5}$$

where $R = |r - r_c|$ and dΩ denotes an integration over the angular variables. The second moment of the distribution is the gyration tensor, given by

$$\mathbf{S} = \int (\mathbf{r} - \mathbf{r}_c)(\mathbf{r} - \mathbf{r}_c)s(\mathbf{r})\mathrm{d}^3r \tag{6}$$

We denote the eigenvalues of this tensor as s_x^2, s_y^2, and s_z^2. The relative shape anisotropy, κ^2, is defined in terms of these eigenvalues in a standard way.[24]

For the excess proton, we use the following definition. First, two closest protons are assigned to each oxygen atom, forming a water molecule. Then, the excess proton is identified as the one left after this assignment. As a consequence, in H_3O^+, the excess proton is the one connected to the central oxygen by the longest of the three O–H bonds. Note that due to this

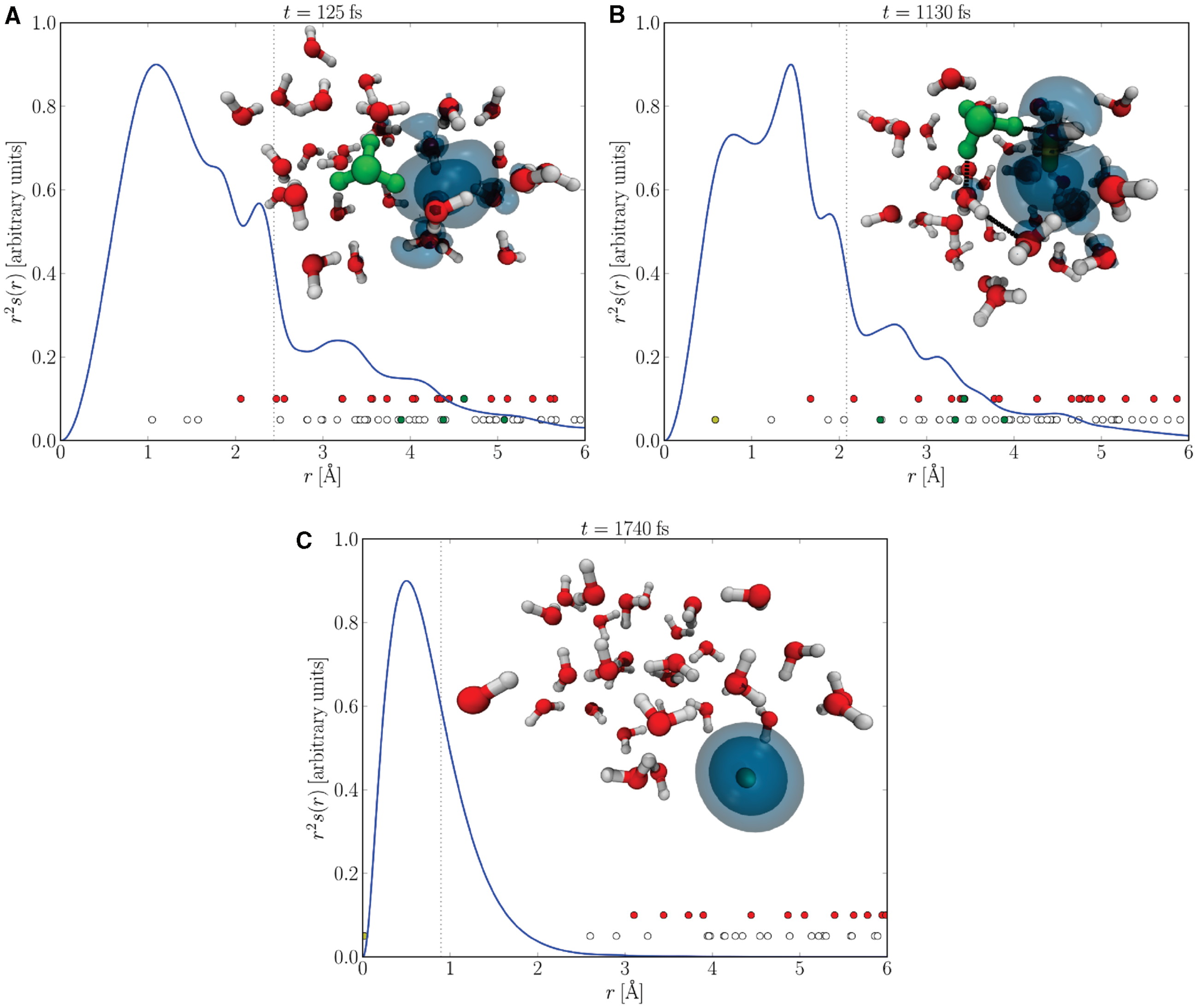

Figure 1. Electron distributions (spin densities) and snapshots of the system before (A), during (B), and after (C) the electron−proton reactive event. The vertical dotted line denotes the radius of gyration of the electron. White and red dots depict positions of water hydrogens and oxygens with respect to the electron, while the green color is used to label the atoms forming the hydronium cation. The single water hydrogen penetrating deep into the electron density just before the reaction and eventually becoming the product hydrogen atom is depicted in yellow in (B) and (C). The dashed black line in (B) highlights the hopping path of the proton along the chain of hydrogen-bonded water molecules prior to the reaction.

definition, the identity of the excess proton in H_3O^+ can change during vibrational motions of this ion.

Results

We chose a medium-sized cluster since it not only bears many similarities to the aqueous bulk but also allows for comparison to the extensive body of experimental data on photoionization and vibrational spectroscopy in electron-containing water clusters.[25−27] The present system with 32 water molecules is large enough to possess an interior region, in which the solvated electron initially resides in a pre-existing polarized cavity (see Figure 1A and Methods Section for details). At the same time, we can take advantage of the finite size of the system in the sense that it reduces the phase space that the excess proton, initially bound to a water molecule well separated from this cavity (Figure 1A), has to explore before the reaction. Another fact that makes the reaction more feasible in the cluster is the slightly lower binding energy of the electron,[17] which effectively destabilizes the reactants with respect to the products and thus accelerates the process. In summary, the reaction in the present cluster is a good proxy to that in the aqueous bulk, being at the same time computationally more accessible.

We obtained a total of 10 ab initio molecular dynamics (MD) trajectories, each propagated for several picoseconds (for computational details, see the Methods Section and for animations see the Supporting Information). Three of these trajectories captured a successful reaction event leading to formation of a hydrogen atom within 1−3.5 ps, while for the other seven trajectories, the reaction did not occur over this time scale. The reaction is most usefully described and quantified by analyzing these trajectories in terms of the concerted dynamical behavior of the excess proton and the hydrated electron. The three frames in Figure 1 depict for one of the reactive trajectories the excess electron (i.e., the total spin density) radial distribution function, together with snapshots taken before, at the moment of, and after the electron−proton reactive event. Before the reaction, the excess electron is localized from roughly 80%[15,16] in the polarized water cavity, with the remainder of its spin density

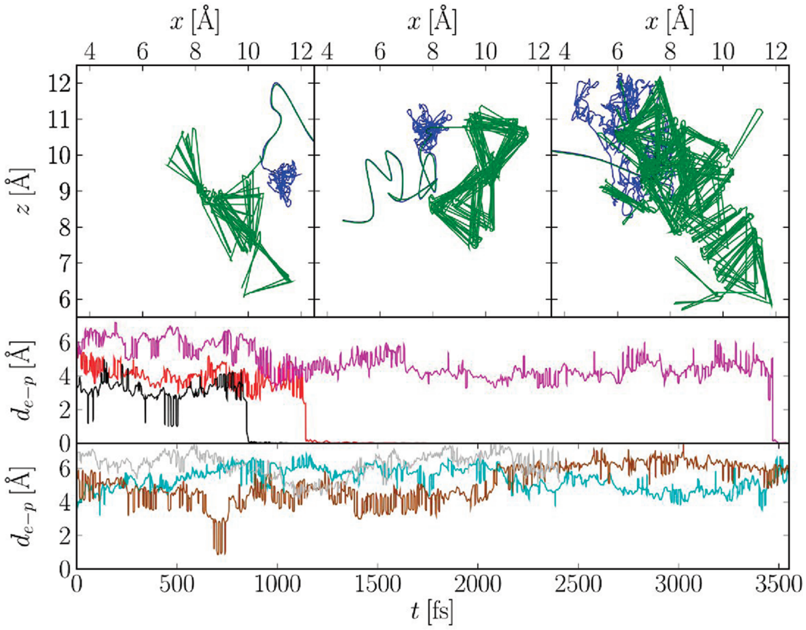

Figure 2. Projections of the electron (blue) and proton (green) trajectories on the xz-plane for the three reactive trajectories (upper panels) and time evolution of the mutual separation of the excess proton and the center of mass of the hydrated electron for three reactive (middle panel: black, red, and violet) and three nonreactive (bottom panel: brown, cyan, and gray) trajectories. The projections show that the electron smoothly diffuses within the system while the proton is more mobile, exhibiting frequent hops (note that the triangular parts of the trajectories correspond to shuffling of the excess proton within a single water molecule). These projections, together with plots showing that the electron−proton separation does not decrease until just before the reactive event (or attempts thereof), illustrate that the reaction is not diffusion-limited.

being distributed over the neighboring solvent molecules (Figure 1A). The cavity is spherical only on average, with large instantaneous fluctuations of its shape and size. Right before the reaction, the electron spin density changes shape, remaining elongated in the direction of a particularly strongly solvating water molecule (Figure 1B). The excess proton moves to this molecule, reacting with the electron and forming a hydrogen atom (Figure 1C).

The motion of the excess proton is qualitatively different from that of the hydrated electron. While the electron constantly reshapes but diffuses relatively slowly[28] within the system, the proton moves faster by a hopping mechanism.[29,30] Note that the excess proton is defined as the one that remains after each oxygen atom is assigned the two hydrogens nearest to it. This proton is then depicted as chemically bound to its nearest water molecule (Figure 1). Before the reaction, the identity of this excess proton changes frequently within a single hydronium, which makes it available for occasional proton transfer to neighboring water molecules.[30] The present classical description of nuclear motions provides a qualitatively correct description of the proton motion,[31] which can be further enhanced if quantum nuclear effects such as tunneling are taken into account.[32]

The relative motion of the two reactants in all three reactive trajectories, as well as in three representative unreactive trajectories, is demonstrated in Figure 2 (lower two panels), which plots the time evolution of the mutual separation of the proton and the center of the electron density. The upper panels of Figure 2 show for the reactive events a projection of the electron and proton trajectories onto the xz-plane. Figure 2 clearly demonstrates that the proton with its frequent hops is the "light" particle while the electron due to its relatively strongly bound solvent shell is the "heavy" one, which represents an interesting but understandable reversal of the usual roles of the electron and proton.

The reaction occurs only after many proton hops along the hydrogen-bonded chain of water molecules and several unsuccessful attempts at reacting with the electron (see Figures 2 and 3). The electron−proton reaction is thus not a diffusion-limited process since direct association of electron and proton into a hydrogen atom in water is hindered by the desolvation penalty of the two charged reactants. The sequence of events leading to the reaction is further illustrated by Figure 3, which presents (for the reactive trajectory shown in Figure 1) the time evolution of the mean sizes of the electron spin density along the three principal axes of its gyration tensor. Initially, the electron is roughly spherical; however, each attempt at reaction (marked by a decrease in electron size) is accompanied by its distortion toward a prolate shape. This can be understood in terms of an asymmetric solvation shell, with one or two water molecules penetrating deeper into the electronic cloud, being more reactive than a symmetric one. A successful reactive event is thus accompanied by a dramatic change from (on average) a spherical to a prolate shape of the electron density, after which the electron shrinks to the size of a hydrogen atom, becoming almost a perfect sphere. This effect is further exemplified in Figure 4, which shows for the three reactive trajectories the correlation between the radius of gyration and asymmetry of the electron. Note the anisotropic compression in two dimensions of the electron density occurring in the early stages of the electron−proton reaction. The electron distortion is, to a large extent, driven by the reacting proton. This also follows from comparison with previous simulations of an electron (without a proton) in a water cluster of the same size, where no such large asymmetries of the electron density were observed.[17]

Discussion

The fact that only 3 out of 10 trajectories led to a successful reaction emphasizes that the reactants do not simply diffuse

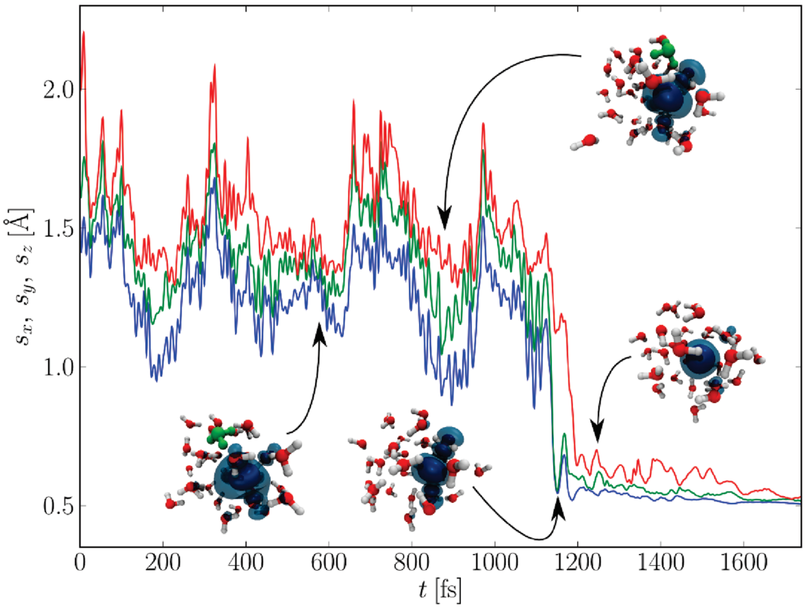

Figure 3. Time evolution of the square roots of the principal moments of the gyration tensor of the excess electron taken from one trajectory, characterizing the size and asymmetry of its distribution, together with representative snapshots of the system. Note the correlation between increased asymmetry, characterized by large differences between the three eigenvalues, and the tendency of the electron to react with the proton.

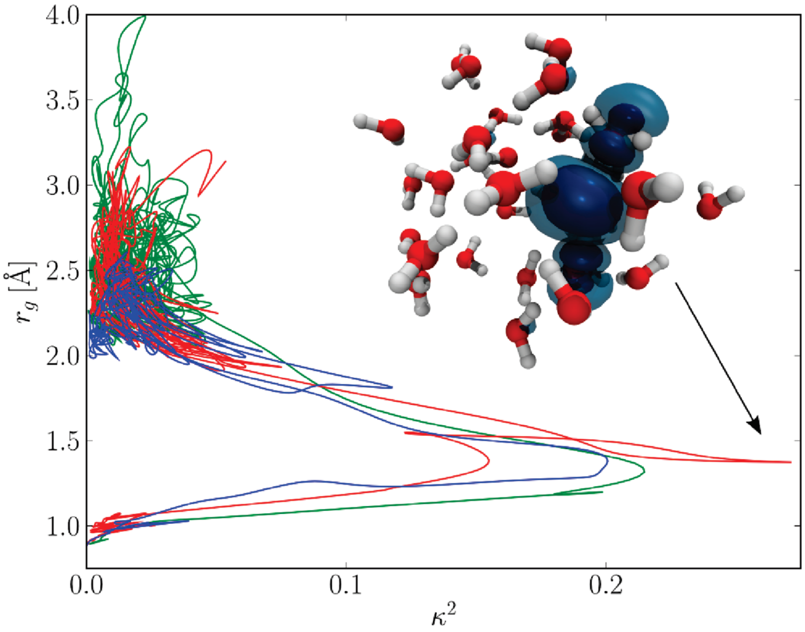

Figure 4. Correlation between the radius of gyration, r_g, and the relative shape anisotropy, κ^2, for the three reactive trajectories. Note the reactant basin of the hydrated electron (large radius and small asymmetry) connected with the product basin of the hydrogen atom (small radius and small asymmetry) via a transition structure (also shown as a snapshot) with an intermediate radius and large asymmetry.

toward each other and react, in which case the reaction would always occur in the simulated water cluster within several hundred femtoseconds. The reason for the slow-down of the reaction is that not only are two hydration shells around charged species lost but also the product H atom is hydrophobic, so there is a very large solvent rearrangement penalty. This picture of a barrier to reaction is fully consistent with the interpretation of the bulk experimental rate constant and its temperature dependence; namely, the reaction is only partially diffusion-controlled at all temperatures measured,[6] and the diffusion-limited rate would be at least 5 times higher at room temperature[2,6,12] (vide infra).

As expected from dielectric continuum theories, the room-temperature bimolecular rate constant decreases markedly from 2.3 × 10^{10} M^{-1} s^{-12} upon going to high ionic strength due to screening of the attractive Coulomb attraction between the reactants. The ionic strength dependence in quenching reactions, including this one, was the original evidence used to establish the solvated electron as the main reducing species produced by radiolysis by virtue of its charge.[34]

Although the number of trajectories computed here is not sufficient to predict a reaction rate for the cluster, simple use of the bulk rate constant adjusted for ionic strength,[2,10] along with the effective H_3O^+ concentration in the cluster suggests an average reaction time of ~50 ps.[35] The fact that only 30% of our trajectories have reacted over 3.5 ps indicates that the present ab initio MD methodology is semiquantitative in describing the reaction.

The quenching reaction by protons of the solvated electron has been investigated for at least 50 years due to its significance in condensed-phase radiation chemistry. From the thermodynamic and kinetic data established for this reaction, many significant mechanistic insights have been gained, although as mentioned in the Introduction, there have been long-standing arguments as to whether the electron moves onto the hydronium ion or whether the electron accepts a proton. The atomistic picture developed in the current work helps to amplify many of the kinetic observations and clarify the primary mechanism.

This electron−proton reaction in water is widely agreed not to be under diffusion control.[5,6,9] The ~11 kJ mol^{-1} activation energy is very close to the activation energy connected with the diffusion coefficient in water. However, Shiraishi and others have shown that, based on a Debye−Smoluchowski estimate, the rate is lower than the diffusion limit by a factor of 5−10 over a large range of temperatures.[6] The kinetic isotopic effect for the reaction is relatively large. Direct measurements in relatively concentrated acid solution show almost a factor of 2 slower bimolecular rate constant for D_2O.[33] This evidence has been cited in the past to support an electron-transfer mechanism producing a H_3O radical,[5] but substantial rearrangement of the solvent shell (as seen in the simulation here) has also been argued to explain the isotope effect in support of a proton-transfer mechanism.[8]

Conclusions

The present simulations show that formation of hydrogen from an electron and proton in water is fundamentally a proton-transfer reaction and that there is no H_3O intermediate. This differs from the assertion that the solvated electron always reacts by electron transfer,[5] which is found in most of the older, but still referenced, reviews and texts of the radiation chemistry field.[2] We are, however, in agreement with the more recent consensus[8] that in many solvated electron reactions with Brønsted acids, the electron is acting as a base.[7] The present ab initio MD simulations thus provide a detailed and contemporary picture of a token quenching process of a hydrated electron, that is, the electron−proton reaction in water, directly elucidating the molecular mechanism of this most fundamental process in radiation chemistry.

Acknowledgment. The authors thank David Bartels for valuable conversations about this reaction. Support from the Czech Science Foundation (Grants 203/08/0114) and the Czech Ministry of Education (Grant LC512) and is acknowledged. Part of the work in Prague was supported via Project Z40550506. O.M. acknowledges support from the International Max-Planck Research School for Dynamical Processes in Atoms, Molecules and Solids. S.E.B. thanks the U.S. National Science Foundation for support (CHE-0617060). T.F. acknowledges support from the Center of Scientific Simulations, FU Berlin. A part of the presented calculations has been performed on the HLRN supercomputer.

Supporting Information Available: Animations of the three reactive trajectories and details concerning these trajectories are provided as Supporting Information. This material is available free of charge via the Internet at http://pubs.acs.org.

References and Notes

(1) Garrett, B. C.; Dixon, D. A.; Camaioni, D. M.; Chipman, D. M.; Johnson, M. A.; Jonah, C. D.; Kimmel, G. A.; Miller, J. H.; Rescigno, T. N.; Rossky, P. J.; Xantheas, S. S.; Colson, S. D.; Laufer, A. H.; Ray, D.; Barbara, P. F.; Bartels, D. M.; Becker, K. H.; Bowen, H.; Bradforth, S. E.; Carmichael, I.; Coe, J. V.; Corrales, L. R.; Cowin, J. P.; Dupuis, M.; Eisenthal, K. B.; Franz, J. A.; Gutowski, M. S.; Jordan, K. D.; Kay, B. D.; LaVerne, J. A.; Lymar, S. V.; Madey, T. E.; McCurdy, C. W.; Meisel, D.; Mukamel, S.; Nilsson, A. R.; Orlando, T. M.; Petrik, N. G.; Pimblott, S. M.; Rustad, J. R.; Schenter, G. K.; Singer, S. J.; Tokmakoff, A.; Wang, L. S.; Wittig, C.; Zwier, T. S. *Chem. Rev.* **2005**, *105*, 355.

(2) Buxton, G. V.; Greenstock, C. L.; Helman, W. P.; Ross, A. B. *J. Phys. Chem. Ref. Data* **1988**, *17*, 513.

(3) Bartels, D. M.; Takahashi, K.; Cline, J. A.; Marin, T. W.; Jonah, C. D. *J. Phys. Chem. A* **2005**, *109*, 1299.

(4) Turi, L.; Sheu, W. S.; Rossky, P. J. *Science* **2005**, *309*, 914.

(5) Hart, E.; Anbar, M. *The hydrated electron*; Wiley-Interscience: New York, 1970.

(6) Shiraishi, H.; Sunaryo, G. R.; Ishigure, K. *J. Phys. Chem.* **1994**, *98*, 5164.

(7) Stein, G. *Isr. J. Chem.* **1971**, *9*, 413.

(8) Han, P.; Bartels, D. M. *J. Phys. Chem.* **1992**, *96*, 4899.

(9) Barker, G. C.; Fowles, P.; Sammon, D. C.; Stringer, B. *Trans. Faraday Soc.* **1970**, *66*, 1498.

(10) Kloepfer, J. A.; Vilchiz, V. H.; Lenchenkov, V. A.; Chen, X. Y.; Bradforth, S. E. *J. Chem. Phys.* **2002**, *117*, 766.

(11) Thomsen, C. L.; Madsen, D.; Keiding, S. R.; Thogersen, J.; Christiansen, O. *J. Chem. Phys.* **1999**, *110*, 3453.

(12) Goulet, T.; Jay-Gerin, J. P. *J. Chem. Phys.* **1992**, *96*, 5076.

(13) Boero, M. *J. Phys. Chem. A* **2007**, *111*, 12248.

(14) Barnett, R. N.; Landman, U.; Scharf, D.; Jortner, J. *Acc. Chem. Res.* **1989**, *22*, 350.

(15) Shkrob, I. A. *J. Phys. Chem. A* **2007**, *111*, 5223.

(16) Shkrob, I. A.; Glover, W. J.; Larsen, R. E.; Schwartz, B. J. *J. Phys. Chem. A* **2007**, *111*, 5232.

(17) Frigato, T.; VandeVondele, J.; Schmidt, B.; Schutte, C.; Jungwirth, P. *J. Phys. Chem. A* **2008**, *112*, 6125.

(18) Sobolewski, A. L.; Domcke, W. *Phys. Chem. Chem. Phys.* **2007**, *9*, 3818.

(19) Grimme, S. *J. Comput. Chem.* **2006**, *27*, 1787.

(20) Goedecker, S.; Teter, M.; Hutter, J. *Phys. Rev. B* **1996**, *54*, 1703.

(21) VandeVondele, J.; Krack, M.; Mohamed, F.; Parrinello, M.; Chassaing, T.; Hutter, J. *Comput. Phys. Commun.* **2005**, *167*, 103.

(22) VandeVondele, J.; Sprik, M. *Phys. Chem. Chem. Phys.* **2005**, *7*, 1363.

(23) VandeVondele, J.; Hutter, J. *J. Chem. Phys.* **2007**, *127*, 114105.

(24) Theodorou, D. N.; Suter, U. W. *Macromolecules* **1985**, *18*, 1206.

(25) Lee, G. H.; Arnold, S. T.; Eaton, J. G.; Sarkas, H. W.; Bowen, K. H.; Ludewigt, C.; Haberland, H. *Z. Physik D: At., Mol. Clusters* **1991**, *20*, 9.

(26) Verlet, J. R. R.; Bragg, A. E.; Kammrath, A.; Cheshnovsky, O.; Neumark, D. M. *Science* **2005**, *307*, 93.

(27) Roscioli, J. R.; Hammer, N. I.; Johnson, M. A. *J. Phys. Chem. A* **2006**, *110*, 7517.

(28) Schmidt, K. H.; Han, P.; Bartels, D. M. *J. Phys. Chem.* **1992**, *96*, 199.

(29) Boero, M.; Ikeshoji, T.; Terakura, K. *ChemPhysChem* **2005**, *6*, 1775.

(30) Marx, D.; Tuckerman, M. E.; Hutter, J.; Parrinello, M. *Nature* **1999**, *397*, 601.

(31) Marx, D.; Tuckerman, M. E.; Parrinello, M. *J. Phys.: Condens. Matter* **2000**, *12*, A153.

(32) Geissler, P. L.; Dellago, C.; Chandler, D.; Hutter, J.; Parrinello, M. *Science* **2001**, *291*, 2121.

(33) Bartels, D. M.; Craw, M. T.; Han, P.; Trifunac, A. D. *J. Phys. Chem.* **1989**, *93*, 2412.

(34) Czapski, G.; Schwarz, H. A. *J. Phys. Chem.* **1962**, *66*, 471.

(35) In the system simulated here, with a single hydronium and 31 water molecules approximating the cluster as having the density of room-temperature water, the simulations would thus have ~1.8 M ionic strength. The pseudo-first-order rate constant adjusted for ionic strength is $(50\ \mathrm{ps})^{-1}$ at $[H_3O^+] = 1.8$ M. Following Shiraishi,[6] and assuming the cluster effectively has the two reactants in an "association complex", we might alternatively predict a $(26\ \mathrm{ps})^{-1}$ rate for the reaction if it were to proceed as the bulk kinetics.

JP908986Z

PCCP

Dynamic Article Links

Cite this: *Phys. Chem. Chem. Phys.*, 2011, **13**, 14003–14009

www.rsc.org/pccp

PAPER

From a localized H_3O radical to a delocalized $H_3O^+\cdots e^-$ solvent-separated pair by sequential hydration†

Frank Uhlig, Ondrej Marsalek and Pavel Jungwirth*

Received 15th March 2011, Accepted 14th June 2011
DOI: 10.1039/c1cp20764d

The impact of microhydration on the electronic structure and reactivity of the H_3O moiety is investigated by *ab initio* calculations. In the gas phase, H_3O is a radical with spin density localized on its hydrogen end, which is only kinetically stable and readily decomposes into a water molecule and a hydrogen atom. When solvated by a single water molecule, H_3O preserves to a large extent its radical character, however, two water molecules are already capable to shift most of the spin density to the solvent. With three solvating water molecules this shift is practically completed and the system is best described as a solvent-separated pair of a hydronium cation and a hydrated electron. The electronic structure of this system and its proton transfer reactivity leading to formation of a hydrogen atom already resemble those of a proton–electron pair in bulk water.

1 Introduction

The strength of hydrogen bonding interactions between polar or ionic solutes and the solvating water molecules depends on the polarity and/or charge density of the dissolved species. From this perspective, a rather complex situation can occur when the electronic structure of the solute changes significantly upon hydration. In general, the highly polar water molecules tend to induce an increase in the polarity of the solute whenever its structure is sufficiently flexible to allow for such a change. An interesting example of such a shift in the electronic structure upon hydration is the H_3O radical, which has been suggested to be one of the key species involved in radiation chemistry processes in water.[1–6] This is a well-justified suggestion, but needs some clarification concerning the exact nature of this radical when interacting with water molecules. It was shown that in water a ground state radical with spin density localized at the H_3O moiety does not exist.[3,6,7] Instead, this species acquires the form of a solvent-separated $H_3O^+\cdots e^-$ pair, which raises the question whether it is actually adequate to call it an H_3O radical when dissolved in water. A solvent-separated $H_3O^+\cdots e^-$ pair is only kinetically stable, rapidly forming a hydrogen atom.[3,7] The proton–electron reaction is one of the fundamental processes in radiation chemistry of water.[8] It was shown both experimentally[9,10] and computationally[7] that this reaction is not diffusion limited, exactly because of the formation of the solvent-separated $H_3O^+\cdots e^-$ pair, and that it proceeds as proton transfer rather than electron transfer. Moreover, calculations did not point to a localized H_3O radical as a reactive intermediate during this process.[7] In other words, the rate-limiting process of the reaction is not the proton–electron recombination step but rather the deformation of the immediate solvent shell of the hydrated electron induced by the presence of the excess proton.[7]

For the gas phase radical the spin density must be localized on the H_3O moiety simply because there is no solvent to pass it to. Additionally, previous calculations showed that already three water molecules are sufficient to completely transfer the spin density from the H_3O to the solvent.[3,6,11] From this perspective it is of interest to explore the process of microhydration of H_3O. In the present study we investigate using *ab initio* quantum chemical methods clusters containing H_3O with up to three water molecules focusing on two mutually interconnected issues. The first one involves the gradual loss of the localized radical character of H_3O upon adding the first, second, and third water molecule. The second one concerns the reactivity leading to the loss of a hydrogen atom, either directly from the original H_3O moiety or indirectly *via* proton transfer to a water molecule involved in solvating the highly mobile excess electron.

2 Methods

We performed geometry optimizations and minimum energy path (MEP) calculations for differently sized $H_3O(H_2O)_n$ clusters, with $n = 0$–3. For the main part of the results, the electronic structure was calculated using the Møller–Plesset perturbation theory in the resolution of identity approximation (RI-MP2) in its spin-unrestricted formulation using Dunning's

---

Institute of Organic Chemistry and Biochemistry, Academy of Sciences of the Czech Republic and Center for Biomolecules and Complex Molecular Systems, Flemingovo nám. 2, 16610 Prague 6, Czech Republic. E-mail: pavel.jungwirth@uochb.cas.cz; Tel: +420 220 410 314

† Electronic supplementary information (ESI) available: Animation of the reaction presented in Fig. 7. See DOI: 10.1039/c1cp20764d

correlation-consistent triple-ζ split valence basis set augmented with diffuse functions (aug-cc-pVTZ).[12] The Turbomole[13] program package was used for all RI-MP2 calculations.

Geometry optimizations, relaxed scans of the potential energy surface (PES), and nudged elastic band (NEB)[14] calculations were performed using the above electronic structure method. Geometries of the local minima of the clusters were optimized with the Broyden–Fletcher–Goldfarb–Shanno (BFGS) algorithm.[15–18] MEPs for hydrogen abstraction from the clusters with n = 0, 1, 2 were obtained as relaxed PES scans, where the individual structures were optimized using the FIRE algorithm.[19] NEB calculations were performed for the clusters with two (16 images) and three (32 images) water molecules. A climbing image was used to ensure that one of the images is the transition state.[20] The FIRE algorithm was used for the optimization of the band. In the NEB method, a series of replicas of the system lying between the reactant and product states is connected atom-by-atom using harmonic bonds. Further, forces from the additional harmonic bonds perpendicular to the direction of the band are removed, preventing the band from "cutting corners". All the replicas are optimized simultaneously under the influence of both normal forces and forces from the harmonic bonds. The endpoints of the NEB were two local minima—one structure with the hydronium cation and the hydrated electron separated by solvent molecules and another with a hydrogen atom bound non-covalently to a relaxed cluster of two or three water molecules. Initial positions of the intermediate images were taken from the converged DFT calculations (see below). All these optimizations were performed using the Atomic Simulation Environment (ASE).[21] Its interface to Turbomole was modified to enable RI-MP2 calculations.

To check the effect of additional dynamic correlation we also performed CCSD(T) calculations employing the same aug-cc-pVTZ basis set on top of the RI-MP2 geometries of the hydrogen abstraction path in H_3O. The CCSD(T) calculations were carried out using the NWChem program package.[22]

In addition, benchmark calculations were performed using energies and forces obtained with density functional theory (DFT). We used the Becke, Lee, Yang and Parr (BLYP) exchange–correlation functional[23,24] with additional, pairwise additive London terms effectively accounting for dispersion effects.[25] We employed the scaled self-interaction correction (SIC) applied only to the singly-occupied orbital in a restricted open-shell calculation.[26] The scaling parameters used were a = 0.3 and b = 0.2, as previously parametrized for the proton–electron reaction in a cluster of 32 water molecules.[7] Other values were used as well for comparison purposes. A hybrid Gaussians and plane waves (GPW) scheme was used, where the Kohn–Sham orbitals are represented as a linear combination of Gaussian basis functions, while the electronic density is represented in a plane-wave basis. In this work, a molecularly optimized generally contracted triple-ζ basis set with two additional polarization functions (molopt-TZV2P) was used as the atom-centered Gaussian basis set,[27] possibly extended by a grid of Gaussian functions denoted as ggg.[7,28] The plane-wave cutoff for the density was set to 280 Ry and the Goedecker–Teter–Hutter norm-conserving pseudopotentials were employed.[29] A wavelet-based Poisson solver was used for correct treatment of electrostatics in open boundary conditions.[30] Although BLYP is generally not as accurate as MP2, this setup, once benchmarked properly, can be applied to much larger cluster systems as well as condensed phase problems.[7]

This electronic structure setup was used for NEB calculations of hydrogen abstraction from clusters with two and three water molecules. Improved tangent estimates[31] were used for better stability and a climbing image[20] was used to obtain the transition state. The band was optimized using molecular dynamics with the projected velocity Verlet modification of the propagator.[32] This propagator works in the same way as the original one used for molecular dynamics, but in addition, the relative direction of velocities and forces is checked in each step using a dot product. If the direction is opposite, velocities are set to zero. The endpoints of the NEB were prepared the same way as in the RI-MP2 setup. Initial conditions for the intermediate images were created by linear interpolation between the endpoints and one configuration in the vicinity of the transition state taken from a relaxed PES scan. All DFT-based calculations were performed with the CP2K program suite and its Quickstep module.[33]

3 Results and discussion

First, we focus on consequences of microhydration of the central H_3O moiety on its electronic structure. To this end we performed geometry optimizations of the $H_3O(H_2O)_n$ clusters with n = 0–3, leading to the structures shown in Fig. 1. Starting geometry of the largest $H_3O(H_2O)_3$ cluster was taken from ref. 2, while for $H_3O(H_2O)_n$ with n = 0, 1, 2 they were obtained by sequentially removing water molecules from the $H_3O(H_2O)_3$ cluster. These optimizations yielded structures (A), (C), (D), and (E). Except for structure (D), these were previously reported as the local minima lowest in energy with the constraint of preserving the hydronium species intact (*i.e.*, non-dissociating).[11] Note that structure (D) is 0.19 eV higher than the lowest local minimum with a preserved hydronium geometry for that system (which has a central water molecule with H_3O on one side and H_2O on the other).[11] In addition, we separately constructed and optimized a previously unnoticed

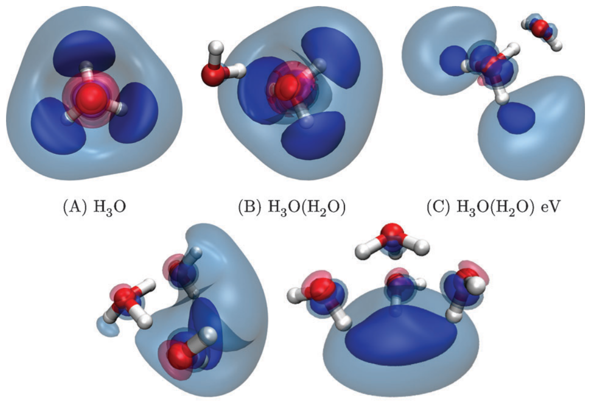
(A) H_3O (B) $H_3O(H_2O)$ (C) $H_3O(H_2O)$ eV

(D) $H_3O(H_2O)_2$ (E) $H_3O(H_2O)_3$

Fig. 1 Minimum energy structures of the $H_3O(H_2O)_n$ (n = 0…3) clusters. Depicted are contours of the spin density at four different values (±0.001 and ±0.003 e Bohr^{-3})

Table 1 Vertical ionization potentials for the five structures depicted in Fig. 1

	VIP/eV
(A) H_3O	5.88
(B) $H_3O(H_2O)_1$	5.65
(C) $H_3O(H_2O)_1$	4.56
(D) $H_3O(H_2O)_2$	4.11
(E) $H_3O(H_2O)_3$	4.09

structure (B), which has a water molecule donating rather than accepting a hydrogen bond, and which is about 0.30 eV higher in energy than structure (C).

Fig. 1 provides also graphical information on the electronic structure in terms of the unpaired spin density for each system. In isolated H_3O, the spin density of the system is localized on the hydrogen atoms and, to a lesser extent, also on the oxygen of the H_3O radical. The vertical ionization potential (VIP) of the isolated H_3O radical amounts to 5.88 eV (Table 1). Comparing the two structures with a single solvating water molecule, one can clearly see the difference between hydronium accepting a hydrogen bond from a water molecule and that donating a hydrogen bond to a water molecule. In the former case, hydronium remains practically intact as a spin-localized H_3O radical with only a slightly reduced VIP of 5.65 eV (structure (B) in Fig. 1 and Table 1). In the latter case, however, the spin density distorts (structure (C) in Fig. 1), leading to a significant reduction of the VIP to 4.56 eV (Table 1). Just as the first water molecule, the second and the third one also prefer to attach to the hydrogen side of the H_3O species (Fig. 1). In the process of increasing the number of solvent molecules in the cluster, the spin density further leaks away from H_3O and localizes near the dangling hydrogens of the water molecules. Already for two added water molecules, there is very little spin density left on the original H_3O radical (structure (D) in Fig. 1) and, consequently, the VIP further drops to 4.11 eV (Table 1). For three water molecules hydrating H_3O, the spin transfer to the solvent is practically completed. Hence, the hydronium loses its radical character and becomes a cation, donating hydrogen bonds to the surrounding water molecules. The excess electron localizes on the opposite side of the cluster between the free OH bonds. Thanks to the stabilization by the dangling water hydrogens, as well as by the presence of the H_3O^+ cation, the excess electron in the cluster with three water molecules already qualitatively resembles in its size and binding energy (4.09 eV) a bulk hydrated electron.

The gradual shift from an H_3O radical toward a solvent-separated $H_3O^+\cdots e^-$ pair affects also the reactivity of this species, as demonstrated by the minimum energy paths for the dissociation of $H_3O(H_2O)_n$ to $(H_2O)_{n+1}$ + H. The isolated H_3O radical can only dissociate by breaking one of its OH bonds. The energy profile of this process, obtained from a relaxed PES scan, is depicted in Fig. 2. In order to validate the employed RI-MP2 method, we compare it to CASPT2 calculations with a comparable basis set, taken from ref. 2, and, for comparison, we also present UHF results. Note that the CASPT2 method accounts for both static and dynamic correlation, while RI-MP2 essentially only for the latter. The bond lengths reported at the minimum are 1.01 Å with RI-MP2 and 0.98 Å for CASPT2. At the transition state the OH bonds are 1.2 and 1.19 Å and the barrier heights 0.11 and 0.13 eV, respectively. Also shown in Fig. 2 are CCSD(T) energies (red) calculated for the geometries obtained from the RI-MP2 relaxed scan. The close match in geometries and relative energies between CASPT2 and RI-MP2, as well as the non-negligible mismatch with the UHF results illustrates that for the cleavage of an OH bond of the H_3O radical, it is dynamic correlation that primarily needs to be accounted for. On the basis of the very good match between CCSD(T) and RI-MP2, especially in the transition state region, we can conclude that RI-MP2 is fully sufficient in describing the correlation effects in our systems. This conclusion has also been verified in previous studies for isolated H_3O, as well for the $H_3O(H_2O)_3$ cluster[1,34] and is in agreement with the observation that "the ground state of the hydronium radical is dominated by a single reference".[1] SIC-DFT (a = 0.3, b = 0.2) with the molopt-TZV2P + ggg basis set underestimates the barrier of the reaction (0.03 eV) in contrast to RI-MP2 or CCSD(T).

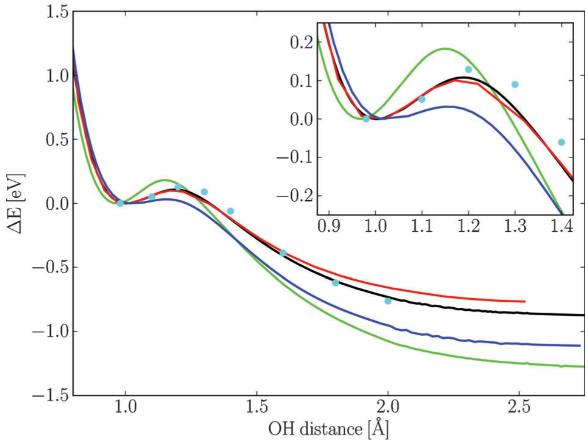

Fig. 2 Minimum energy paths for OH bond dissociation in a hydronium radical. Relaxed scan obtained with RI-MP2 (black) with the aug-cc-pVTZ basis set. Energies of the RI-MP2 geometries calculated with UHF with the aug-cc-pVTZ basis set (green), CCSD(T) with the aug-cc-pVTZ basis set (red) and SIC-DFT (a = 0.3, b = 0.2) with the molopt-TZV2P + ggg basis set (blue). CASPT2 (cyan dots) energies calculated with the double-ζ ANO-L split valence basis set augmented with additional diffuse s and p functions on the oxygen atoms (ζ = 0.02 Bohr^{-1}) are shown. The CASPT2 energies are taken from ref. 2.

By adding one water molecule that donates a hydrogen bond to H_3O the formation of a hydrogen atom is only favourable *via* the dissociation of an OH bond of the H_3O radical (Fig. 3). The energetics of the dissociation are essentially the same as for the isolated H_3O radical. The minimum is located at an OH bond length of 1.02 Å, the maximum at 1.18 Å and the barrier height is 0.08 eV. In contrast, dissociation of an OH bond of the water molecule donating a hydrogen bond to the H_3O radical proceeds only over a high barrier of 5.22 eV until the whole cluster undergoes rearrangements to form an H_2O dimer and a hydrogen atom. In the cluster with the H_3O radical donating a hydrogen bond to a water molecule, there are two practically identical low-barrier (~0.1 eV)

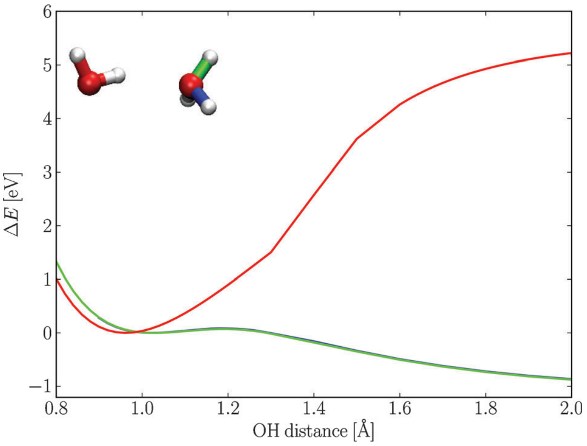

Fig. 3 Minimum energy paths for different OH bond dissociations in the $H_3O(H_2O)$ (B) cluster. Inset shows the minimum structure of the cluster. The color coding of the curves corresponds to colors of the bonds of the structure displayed.

pathways leading again to the formation of a hydrogen and a water dimer (Fig. 4). We can conclude that in both $H_3O(H_2O)$ clusters the lowest reaction paths are analogous to that in the H_3O radical.

For clusters containing more than one water molecule, the OH bond dissociation at the H_3O moiety is not favorable. In the $H_3O(H_2O)_2$ cluster, only one hydrogen of the H_3O does not form a hydrogen bond to a water molecule. For dissociation of the corresponding OH bond a barrier of about 0.22 eV has to be overcome, which is mainly due to necessary rearrangements of the cluster. The favorable process is, however, the dissociation of a water OH bond, which proceeds over a small ($<$0.1 eV) barrier connected with the proton transfer from H_3O to the water molecule. The almost simultaneous cleavage of the water OH bond which has the hydrogen atom penetrating into the excess electron density is practically barrierless. In contrast, the other water OH bond does not break so easily, since the cluster needs to rearrange first with respect to the excess electron. In these cases, the reaction proceeds *via* structures which have a highly distorted, but compact excess electron.

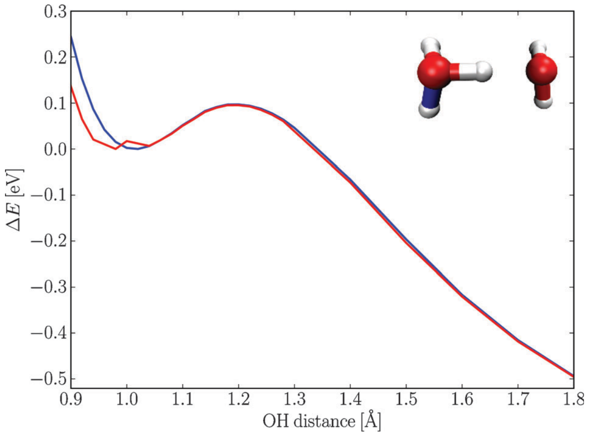

Fig. 4 Minimum energy paths for different OH bond dissociations in the $H_3O(H_2O)$ (C) cluster. Inset shows the minimum structure of the cluster. The color coding of the curves corresponds to colors of the bonds of the structure displayed.

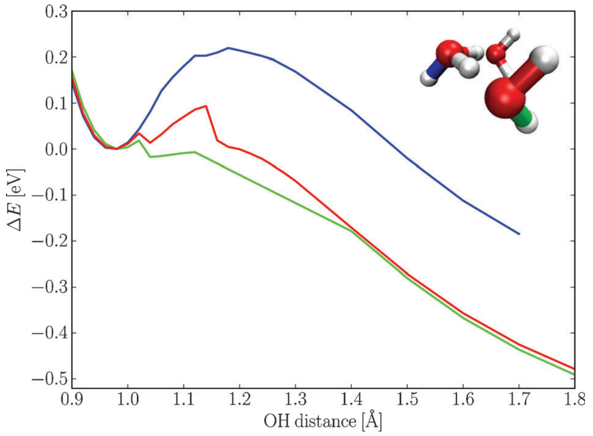

Fig. 5 Minimum energy paths for different OH bond dissociations in the $H_3O(H_2O)_2$ (D) cluster. Inset shows the minimum structure of the cluster. The color coding of the curves corresponds to colors of the bonds of the structure displayed.

A simple bond distance is not the best choice of a reaction coordinate for hydrogen abstraction reactions in clusters with more than one water molecule since it does not capture very well collective motion—relaxation of the whole cluster or coordinated transfer of two protons. One demonstration of this problem is the lack of smoothness in the reaction profiles presented in Fig. 5. In order to obtain the intrinsic reaction coordinate of these more difficult reactions, we performed calculations using the NEB method.[14]

For hydrogen abstraction from the $H_3O(H_2O)_2$ cluster, a total of 16 NEB images were used to obtain the MEP. Specifically, the OH bond to be dissociated corresponds to the green curve in Fig. 5. This choice corresponds to the OH bond that most significantly points into the electronic cloud of the excess electron. It was motivated by the fact that it shows the lowest barrier in the relaxed PES scans presented above and is, therefore, decisive for the stability of this cluster. RI-MP2 energies along the resulting MEP are shown in the top panel of Fig. 6 together with snapshots of selected configurations. In contrast with the case of the relaxed scan, the MEP obtained using NEB is smooth in energies and geometries. Moreover, as the climbing image extension of the NEB method was used, one of the replicas is in the transition state, which gives a good estimate of the barrier height. The barrier is negligible (5 meV) and would be practically non-existent if quantum nuclear effects were taken into account. The bottom panel of Fig. 6 shows relevant distances between atoms taking part in the reaction as a function of the reaction coordinate. The largest rate of change of all of these coordinates can be seen in the vicinity of the transition state.

The MEP for hydrogen abstraction from the $H_3O(H_2O)_3$ cluster was evaluated in two steps. First, a rough estimate of the reaction path was calculated using 8 images. These were then used as a basis for interpolation to a total of 32 images, which were again optimized using NEB. One of the three

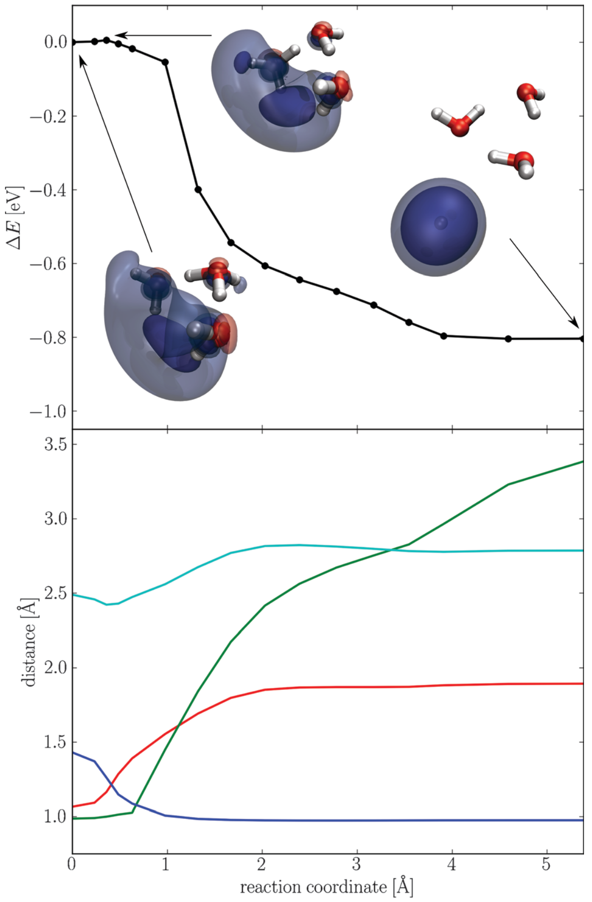

Fig. 6 MEP for $H_3O(H_2O)_2$ obtained with NEB and RI-MP2 and aug-cc-pVTZ basis set (top panel). Bottom panel shows distances of OH in hydronium cation (red), OH distance in water molecule (green), OO distance of before mentioned molecules (cyan) and OH distance in newly formed water molecule (blue).

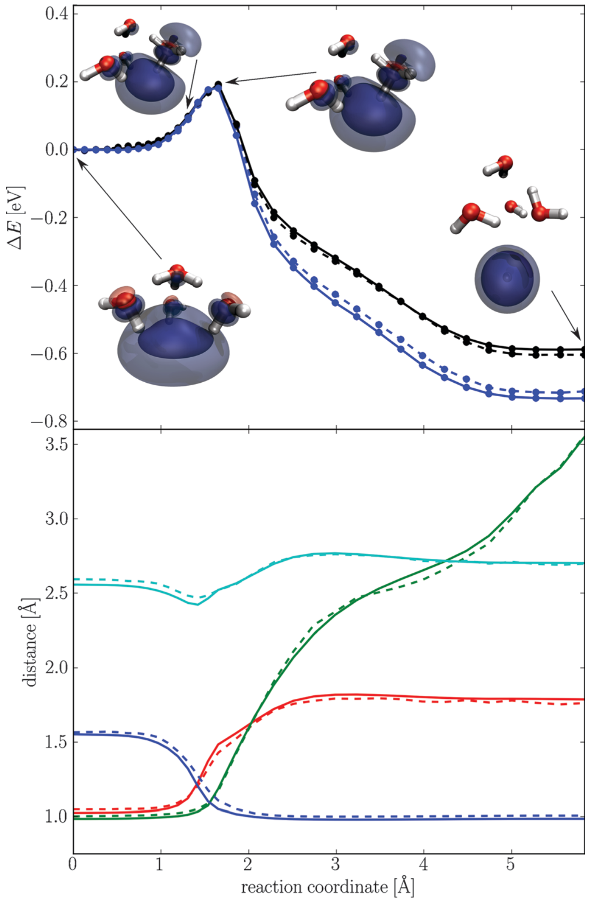

Fig. 7 Two MEPs for $H_3O(H_2O)_3$ obtained with NEB optimized using two different electronic structure setups. SIC-DFT (a = 0.3, b = 0.2) using the molopt-TZV2P + ggg basis set is shown in blue in top panel, RI-MP2 using the aug-cc-pVTZ basis set is shown in black. Energies at DFT and RI-MP2 geometries are shown using dashed and full lines, respectively. Bottom panel shows distances of OH in hydronium cation (red), OH distance in water molecule (green), OO distance of before mentioned molecules (cyan) and OH distance in newly formed water molecule (blue) from the DFT and RI-MP2 calculations using dashed and full lines, respectively.

equivalent OH bonds pointing into the electronic cloud of the excess electron was chosen as that to be dissociated. These NEB calculations were performed using SIC-DFT. The resulting geometries plus independently optimized end points were used in a second NEB calculation with RI-MP2. DFT and RI-MP2 energies along the resulting MEPs are shown in the top panel of Fig. 7 together with snapshots of selected configurations. It is notable that the MEPs of the $H_3O(H_2O)_3$ dissociation with SIC-DFT and RI-MP2 are now much closer to each other in energy compared to those of the dissociation of the bare H_3O moiety. DFT performs well in the reaction region and for the barrier height, while slightly overstabilizing the products. The improved performance of DFT upon increasing the cluster size (and thus enhancing hydrogen bonding interactions) indicates applicability of this method for large clusters and the condensed phase. The bottom panel of Fig. 7 shows distances between atoms, defined the same way as before. The selected interatomic distances again change appreciably only in the vicinity of the transition state. Closer inspection of the geometries in the reactive region (for animation of the reaction see ESI†) reveals that the initial part of the reaction entails an overall compression of the cluster on the side of the hydrated electron. Only after this compression can the proton transfer from the hydronium cation to the neighboring water molecule start, being closely followed by the transfer of the next proton from the water molecule to the center of the electronic cloud, where it forms a hydrogen atom.

It is useful to quantify the changes in the shape of the spin density of the system during the reaction. For this purpose, we evaluate the gyration tensor of the spin density and quantities derived from it, namely its principal moments s_x, s_y, s_z, the radius of gyration r_g, and relative shape anisotropy κ^2.[7] These are plotted as functions of the reaction coordinate in Fig. 8. The spatial extent of the spin density, as measured by its radius of gyration, decreases monotonically during the reaction. The principal axes of the ellipsoid corresponding to the gyration tensor show a transition from an oblate shape in the initial state to a prolate shape during the reaction and finally to the spherical shape of a hydrogen atom in the final stage. The relative shape

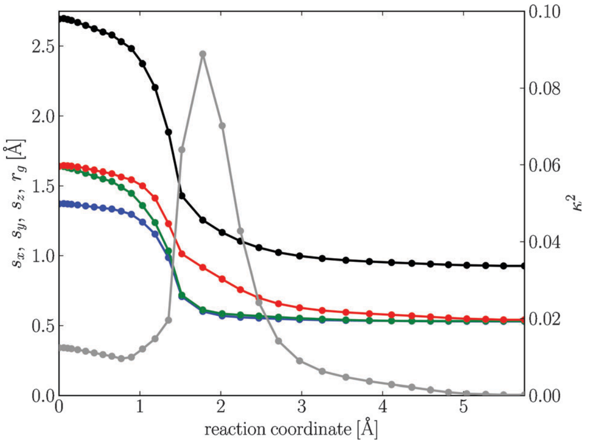

Fig. 8 Principal moments s_x, s_y and s_z of gyration tensor of the spin density along the MEP obtained with NEB calculations (red, green, blue). Radius of gyration r_g in black and relative shape anisotropy κ^2 in gray.

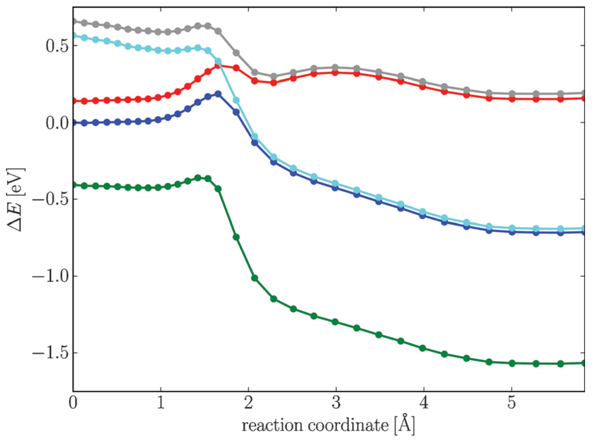

Fig. 10 Energies of the $H_3O(H_2O)_3$ cluster obtained using DFT with different basis sets and settings of the SIC calculated along the same MEP as shown in Fig 7 (obtained with molopt-TZV2P + ggg basis set and SIC (a = 0.3, b = 0.2), blue). Energies with molopt-TZV2P + ggg and SIC (a = 0.2, b = 0.0) are shown in green, with molopt-TZV2P + ggg and no SIC in red, with molopt-TZV2P and SIC (a = 0.3, b = 0.2) in cyan and with molopt-TZV2P and no SIC in gray.

anisotropy, which is calculated from the principal moments, demonstrates that the asymmetry of the spin density reaches its maximum just after the transition state when the hydrogen atom is being formed. It is notable that the reactive process in a model system with only three water molecules already has all the properties of the reaction identified in a much larger cluster of 32 water molecules at a finite temperature.[7] The effect of the finite temperature in those cluster systems does not change the qualitative picture of the reaction mechanism in the $H_3O(H_2O)_3$ cluster. Note that this reaction has been observed and investigated, although not in such mechanistic detail, in small clusters theoretically[3,6] and it has been invoked in interpreting measurements of kinetic energy distributions of H-fragments for water nanoparticles doped with hydrogen halides.[4,6]

For additional insight into the concerted proton transfer, we have performed a two-dimensional relaxed PES scan in the space of the two OH bonds that are being broken. The surface is shown in Fig. 9 together with points corresponding to geometries from the NEB calculation. There is an apparent curved pathway, which is exemplified by the NEB curve, leading from the initial minimum to the transition state.

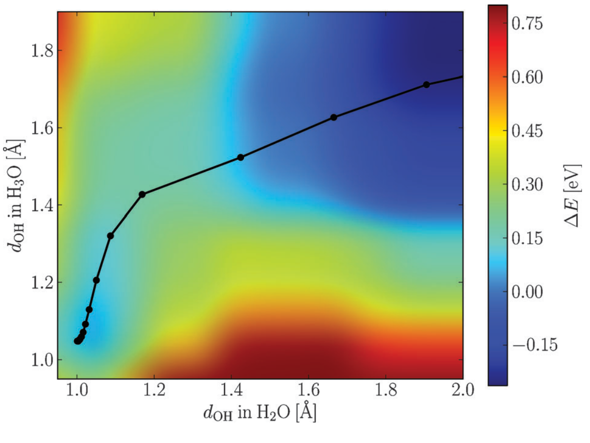

Fig. 9 Two-dimensional relaxed PES scan for $H_3O(H_2O)_3$ along OH bond distance in H_3O cation and OH bond distance in water molecule hydrogen-bonded to H_3O at corresponding OH bond (colored). Black dots are at values of the OH bond lengths at the geometries of the MEP obtained with NEB calculations.

In Fig. 10, we compare calculations at the MEP geometries for the $H_3O(H_2O)_3$ cluster with different DFT settings in order to better understand the influence of the SIC and basis sets extensions. Energies for the DFT setup that was also used for the optimization of the NEB (SIC (a = 0.3, b = 0.2), molopt-TZV2P + ggg) are shown in blue. We have already established that these compare well to RI-MP2 energies (Fig. 7), therefore the reaction path thus obtained should be a good approximation to that optimized with RI-MP2. We further note that RI-MP2 energies match full MP2 energies to within less than 1 meV, which justifies the use of the RI approximation for these calculations. Focusing first on the influence of basis set choice in our DFT calculations, we can see that the removal of diffuse basis functions (cyan) destabilizes reactants by about 0.6 eV and practically removes the barrier (0.02 eV). Comparison of the molopt-TZV2P + ggg basis set to an aug-TZV2P basis set (not shown) indicates comparable overall quality of the augmentation with diffuse functions, with variations in relative energies in the 10 meV range. Setting the SIC parameters is also important. Using the original parameters a = 0.2, b = 0.0[26] (green) introduces an overall bias, overstabilizing products by roughly 0.45 eV when compared to SIC (a = 0.3, b = 0.2). Not using the SIC at all (red) reshapes the PES significantly, reducing the reaction exothermicity roughly to zero, and introduces an additional spurious and rather broad barrier. This is a severe change when compared to the roughly 0.7 eV decrease in energy between reactants and products with the optimized SIC (a = 0.3, b = 0.2). Finally, note the rather accidental compensation of errors between the self-interaction error and insufficient basis set in a calculation that uses only the molopt-TZV2P basis set and no SIC (gray).

4 Conclusions

We investigated by means of *ab initio* calculations how the radical character and reactivity of the H_3O species change upon hydration by 1–3 water molecules. The first solvating water molecule has only a minor effect on the radical character of H_3O when accepting a hydrogen bond from it and virtually no effect when donating a hydrogen bond. As in the gas phase, in this smallest cluster with water H_3O remains a localized radical, which is metastable with respect to the loss of a hydrogen atom. The situation changes dramatically upon adding a second water molecule, which results in transfer of most of the spin density from H_3O to the solvent. Upon adding a third water molecule this transfer is practically completed and the cluster forms a solvent separated $H_3O^+\cdots e^-$ pair. Microhydration thus completely alters the electronic character of the H_3O moiety from a localized radical to an H_3O^+ cation separated by water molecules from a hydrated electron. This change has consequences also for reactivity, which in the larger cluster proceeds as a proton transfer to the excess electron, forming a hydrogen atom. Both the electronic structure and the reaction path in the cluster with three water molecules already bear all the salient features of the situation in the aqueous bulk.

Acknowledgements

Support from the Czech Science Foundation (grants 203/08/0114), the Czech Ministry of Education (grant LC512), and the Academy of Sciences (Praemium Academie) is gratefully acknowledged. OM and FU acknowledge support from the IMPRS Dresden.

References

1 A. L. Sobolewski and W. Domcke, *J. Phys. Chem. A*, 2002, **106**, 4158–4167.
2 A. L. Sobolewski and W. Domcke, *Phys. Chem. Chem. Phys.*, 2002, **4**, 4–10.
3 A. L. Sobolewski and W. Domcke, *Phys. Chem. Chem. Phys.*, 2007, **9**, 3818–3829.
4 V. Poterya, M. Farnik, P. Slavicek, U. Buck and V. V. Kresin, *J. Chem. Phys.*, 2007, **126**, 071101–071104.
5 V. Poterya, M. Farnik, M. Oncak and P. Slavicek, *Phys. Chem. Chem. Phys.*, 2008, **10**, 4835–4842.
6 V. Poterya, J. Fedor, A. Pysanenko, O. Tkac, J. Lengyel, M. Oncak, P. Slavicek and M. Farnik, *Phys. Chem. Chem. Phys.*, 2011, **13**, 2250–2258.
7 O. Marsalek, T. Frigato, J. VandeVondele, S. E. Bradforth, B. Schmidt, C. Schütte and P. Jungwirth, *J. Phys. Chem. B*, 2010, **114**, 915–920.
8 B. C. Garrett, D. A. Dixon, D. M. Camaioni, D. M. Chipman, M. A. Johnson, C. D. Jonah, G. A. Kimmel, J. H. Miller, T. N. Rescigno, P. J. Rossky, S. S. Xantheas, S. D. Colson, A. H. Laufer, D. Ray, P. F. Barbara, D. M. Bartels, K. H. Becker, H. Bowen, S. E. Bradforth, I. Carmichael, J. V. Coe, L. R. Corrales, J. P. Cowin, M. Dupuis, K. B. Eisenthal, J. A. Franz, M. S. Gutowski, K. D. Jordan, B. D. Kay, J. A. LaVerne, S. V. Lymar, T. E. Madey, C. W. McCurdy, D. Meisel, S. Mukamel, A. R. Nilsson, T. M. Orlando, N. G. Petrik, S. M. Pimblott, J. R. Rustad, G. K. Schenter, S. J. Singer, A. Tokmakoff, L. S. Wang, C. Wittig and T. S. Zwier, *Chem. Rev.*, 2005, **105**, 355–389.
9 D. M. Bartels, M. T. Craw, P. Han and A. D. Trifunac, *J. Phys. Chem.*, 1989, **93**, 2412–2421.
10 D. M. Bartels, A. R. Cook, M. Mudaliar and C. D. Jonah, *J. Phys. Chem. A*, 2000, **104**, 1686–1691.
11 A. N. Alexandrova, *J. Phys. Chem. A*, 2010, **114**, 12591–12599.
12 A. Wilson, T. vanMourik and T. Dunning, *THEOCHEM*, 1996, **388**, 339–349.
13 TURBOMOLE V6.2 2010, a development of University of Karlsruhe and Forschungszentrum Karlsruhe GmbH, 1989–2007, TURBOMOLE GmbH, since 2007; available from http://www.turbomole.com.
14 R. Elber and M. Karplus, *Chem. Phys. Lett.*, 1987, **139**, 375–380.
15 C. G. Broyden, *IMA J. Appl. Math.*, 1970, **6**, 76–90.
16 R. Fletcher, *Comput. J.*, 1970, **13**, 317–322.
17 D. Goldfarb, *Math. Comput.*, 1970, **24**, 23–26.
18 D. Shanno, *Math. Comput.*, 1970, **24**, 647.
19 E. Bitzek, P. Koskinen, F. Gähler, M. Moseler and P. Gumbsch, *Phys. Rev. Lett.*, 2006, **97**, 170201.
20 G. Henkelman, B. Uberuaga and H. Jonsson, *J. Chem. Phys.*, 2000, **113**, 9901–9904.
21 S. R. Bahn and K. W. Jacobsen, *Comput. Sci. Eng.*, 2002, **4**, 56–66.
22 M. Valiev, E. Bylaska, N. Govind, K. Kowalski, T. Straatsma, H. V. Dam, D. Wang, J. Nieplocha, E. Apra, T. Windus and W. de Jong, *Comput. Phys. Commun.*, 2010, **181**, 1477–1489.
23 A. Becke, *Phys. Rev. A: At., Mol., Opt. Phys.*, 1988, **38**, 3098–3100.
24 C. Lee, W. Yang and R. Parr, *Phys. Rev. B*, 1988, **37**, 785–789.
25 S. Grimme, *J. Comput. Chem.*, 2006, **27**, 1787–1799.
26 J. VandeVondele and M. Sprik, *Phys. Chem. Chem. Phys.*, 2005, **7**, 1363–1367.
27 J. VandeVondele and J. Hutter, *J. Chem. Phys*, 2007, **127**, 114105.
28 O. Marsalek, F. Uhlig and P. Jungwirth, *Structure, dynamics, and reactivity of hydrated electrons by ab initio molecular dynamics* submitted.
29 S. Goedecker, M. Teter and J. Hutter, *Phys. Rev. B: Condens. Matter*, 1996, **54**, 1703–1710.
30 L. Genovese, T. Deutsch, A. Neelov, S. Goedecker and G. Beylkin, *J. Chem. Phys.*, 2006, **125**, 074105.
31 G. Henkelman and H. Jonsson, *J. Chem. Phys.*, 2000, **113**, 9978–9985.
32 K. W. J. H. Jonsson and G. Mills, *Classical and Quantum Dynamics in Condensed Phase Simulations*, World Scientific, 1998.
33 J. VandeVondele, M. Krack, F. Mohamed, M. Parrinello, T. Chassaing and J. Hutter, *Comput. Phys. Commun.*, 2005, **167**, 103–128.
34 S. K. Chulkov, N. F. Stepanov and Y. V. Novakovskaya, *Russ. J. Phys. Chem. A*, 2009, **83**, 798–808.

ACCOUNTS
of chemical research

Structure, Dynamics, and Reactivity of Hydrated Electrons by Ab Initio Molecular Dynamics

ONDREJ MARSALEK,[†] FRANK UHLIG,[†]
JOOST VANDEVONDELE,[‡] AND PAVEL JUNGWIRTH[*,†]
[†]Institute of Organic Chemistry and Biochemistry, Academy of Sciences of the Czech Republic and Center for Biomolecules and Complex Molecular Systems, Flemingovo nám. 2, 16610 Prague 6, Czech Republic, and [‡]Physical Chemistry Institute, Zürich University, Winterthurerstrasse 190, CH-8057 Zürich, Switzerland

RECEIVED ON MARCH 1, 2011

CONSPECTUS

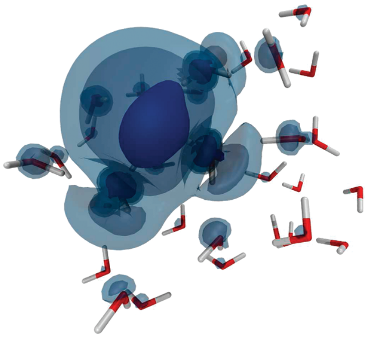

Understanding the properties of hydrated electrons, which were first observed using pulse radiolysis of water in 1962, is crucial because they are key species in many radiation chemistry processes. Although time-resolved spectroscopic studies and molecular simulations have shown that an electron in water (prepared, for example, by water photoionization) relaxes quickly to a localized, cavity-like structure ~2.5 Å in radius, this picture has recently been questioned. In another experimental approach, negatively charged water clusters of increasing size were studied with photoelectron and IR spectroscopies. Although small water clusters can bind an excess electron, their character is very different from bulk hydrated species. As data on electron binding in liquid water have become directly accessible experimentally, the cluster-to-bulk extrapolations have become a topic of lively debate. Quantum electronic structure calculations addressing experimental measurables have, until recently, been largely limited to small clusters; extended systems were approached mainly with pseudopotential calculations combining a classical description of water with a quantum mechanical treatment of the excess electron.

In this Account, we discuss our investigations of electrons solvated in water by means of ab initio molecular dynamics simulations. This approach, applied to a model system of a negatively charged cluster of 32 water molecules, allows us to characterize structural, dynamical, and reactive aspects of the hydrated electron using all of the system's valence electrons. We show that under ambient conditions, the electron localizes into a cavity close to the surface of the liquid cluster. This cavity is, however, more flexible and accessible to water molecules than an analogous area around negatively charged ions.

The dynamical process of electron attachment to a neutral water cluster is strongly temperature dependent. Under ambient conditions, the electron relaxes in the liquid cluster and becomes indistinguishable from an equilibrated, solvated electron on a picosecond time scale. In contrast, for solid, cryogenic systems, the electron only partially localizes outside of the cluster, being trapped in a metastable, weakly bound "cushion-like" state. Strongly bound states under cryogenic conditions could only be prepared by cooling equilibrated, liquid, negatively charged clusters. These calculations allow us to rationalize how different isomers of electrons in cryogenic clusters can be observed experimentally. Our results also bring into question the direct extrapolation of properties of cryogenic, negatively charged water clusters to those of electrons in the bulk liquid.

Ab initio molecular dynamics represents a unique computational tool for investigating the reactivity of the solvated electron in water. As a prototype, the electron−proton reaction was followed in the 32-water cluster. In accord with experiment, the molecular mechanism is a proton transfer process that is not diffusion limited, but rather controlled by a proton-induced deformation of the excess electron's solvent shell. We demonstrate the necessary ingredients of a successful density functional methodology for the hydrated electron that avoids potential pitfalls, such as self-interaction error, insufficient basis set, or lack of dispersion interactions. We also benchmark the density functional theory methods and outline the path to faithful ab initio simulations of dynamics and reactivity of electrons solvated in extended aqueous systems.

10.1021/ar200062m

1. Introduction

The blue color associated with dissolution of alkali metals in ammonia has been observed already in the 19th century, but it was not until 1918 that the phenomenon became connected with solvated electrons.[1] It is common knowledge that this process is much more vigorous in water.[2] Therefore, it turned out not to be a practical way to investigate hydrated electrons, which were first observed via pulse radiolysis of water only in 1962.[3] Since then, electrons in water were shown to act as key species in many radiation chemistry processes.[4] Their structure, dynamics, and reactivity have been, therefore, intensely studied by time-resolved spectroscopies.[4−7] In short, these studies showed that initially nonequilibrium electrons, prepared by photoexcitation of solvated electrons or UV ionization of water or host species such as halide anions, relax fast but in a complicated fashion (depending on their preparation) to a localized, cavity-like structure of a mean radius of 2.5 Å. At the same time, the electron in water can, as a chemically unstable species, geminately recombine with OH or H_3O^+ (or the halogen atom), or react with a whole plethora of scavengers such as N_2O or SF_6. Recently, the cavity model of the solvated electron and its ability to interpret optical and EPR spectra[8] has been questioned, and an alternative, diffuse electron model has been suggested[9] and immediately criticized.[10,11] In the course of this Account, we come back to this issue in more detail.

Another experimental approach to hydrated electrons is based on investigating negatively charged water clusters of increasing size by photoelectron and IR spectroscopies.[12−15] Already a water dimer is capable of binding an excess electron;[12] however, its character is very different from the bulk hydrated species. In small systems, these are weakly bound and very diffuse dipole-bound electrons, which reside at the exterior of the water cluster.[16] Upon increasing the cluster size, the binding energy of the excess electron increases and it is often assumed that it eventually approaches the aqueous bulk limit.[14,17] However, this issue can be rather subtle since water clusters prepared by supersonic jet expansion are not liquid but rather amorphous solids. As data on electron binding in liquid water have recently become directly accessible experimentally,[17−20] applicability of cluster to bulk extrapolations has been vividly discussed recently[14,15,17,21,22] and will be also one of the subjects of this Account.

Experiments on hydrated electrons are paralleled by molecular calculations. On the side of large system sizes, electrons in big clusters and extended aqueous systems have been described using a pseudopotential.[9,23−30] Within this approach, only the excess electron is treated as a quantum mechanical entity, while the rest of the system is described classically. The advantage is that the computationally most costly quantum mechanical part does not increase with system size, and therefore, large systems ranging from clusters with several hundreds of water molecules to "infinite" (via periodic boundary conditions) aqueous bulk or slab systems can be addressed. The problematic part is the purely effective account for the electronic structure of water molecules excluding thus exchange interactions between all the electrons in the system, which may account for about 10−20% of the excess electron binding.[8,31] Moreover, the results can only be as good as the underlying pseudopotential and can sensitively depend on its form and parameters.[10,11] Finally, description of the chemical reactivity of the excess electron is in principle out of reach of these pseudopotential methods.

For the above reasons, it makes good sense to try to describe the electronic structure of the whole electron−water system quantum mechanically. Small anionic water clusters with up to about 10 water molecules can be treated using accurate ab initio quantum chemical methods.[32,33] Methods such as coupled clusters with very diffuse basis sets, which account satisfactorily for electron correlation effects (in particular dispersion), are required for a quantitative description of the diffuse electrons weakly bound to small water clusters.[33] Upon increasing the cluster size, the character of the excess electron gradually changes from such an external dipole-bound electron to a more strongly bound and compact species which starts to resemble the electron solvated in extended aqueous systems. Due to increase in binding and decrease in size of the electron, its description becomes easier as system size increases. This is fortunate, since one can hope that density functional theory (DFT) methods, applicable to large systems, could take over when coupled clusters and similar approaches are no more practical.[21,22,34−38] One has to, however, keep in mind the possible pitfalls of DFT such as problems with dispersion interactions and the self-interaction error (SIE), the latter being particularly relevant for open-shell systems such as the solvated electron.[37,39] Nevertheless, as we show in this Account, when the potentially problematic issues with DFT are properly addressed, one can obtain a practical and faithful method for the description of the structure, dynamics, and reactivity of electrons solvated in large aqueous systems.

2. DFT Simulations and Analysis of the Hydrated Electron

The workhorse for our studies of the hydrated electron has been a negatively charged cluster comprising 32 water molecules.[21,22,36,37] There is nothing particular about this number; the important thing is that such a cluster is already large enough to host a species that semiquantitatively resembles an electron solvated in the aqueous bulk. While the size of the cluster is still far from allowing a fully quantitative modeling of extended systems, the cluster is big enough to possess both surface and interior regions. Therefore, it is possible to investigate preferred locations of the solvated electron and their correlation with its size and binding energy. At the same time, such a cluster is small enough to allow for a statistically converged dynamical description of the solvated electron using adequate DFT methods.

A typical computational setup for our ab initio molecular dynamics (AIMD) simulations for anionic clusters consisting of 32 water molecules is as follows (for more details, see refs 21, 22, 36, and 37). Energies and forces are evaluated using the Becke, Lee, Yang, and Parr (BLYP) exchange-correlation functional, with dispersion interactions accounted for using empirical pairwise damped London terms.[40] Self-interaction error is corrected by augmenting the BLYP functional with an additional term depending on the electron density of the unpaired electron within the restricted open-shell formulation of DFT.[41] The Kohn–Sham orbitals are expanded into an atom-centered triple-ζ basis set with two polarization functions, optimized for condensed molecular systems (molopt-TZV2P),[42] augmented by an additional grid of up to 1000 space-fixed Gaussian functions. An auxiliary plane wave basis with a cutoff of 280 Ry is used for the electronic density. The Goedecker–Teter–Hutter norm-conserving pseudopotentials[43] are employed. The cluster is placed in a $20 \times 20 \times 20$ Å^3 box and an open boundary conditions Poisson solver is used.[44] Classical equations of motion for the nuclei are propagated with a time step of 0.5 fs with initial conditions sampled from thermal distribution at the desired temperature and with no subsequent temperature coupling. All calculations are performed using the Quickstep module of the CP2K program package.[45]

Vertical detachment energy (VDE) of the electron, that is, the negative of its vertical binding energy, is evaluated as the difference between ground state energies of the cluster before and after electron detachment, in the geometry of the anion. Within the restricted open-shell formalism, the total spin density of the system coincides with the density of the singly occupied molecular orbital. Two important observables are the first and second moments of the spin distribution. The first moment $\mathbf{r}_c$ provides the center of the spin distribution. The second moment corresponds to the gyration tensor, of which we monitor the trace, the radius of gyration r_g, and the relative shape anisotropy κ.[22]

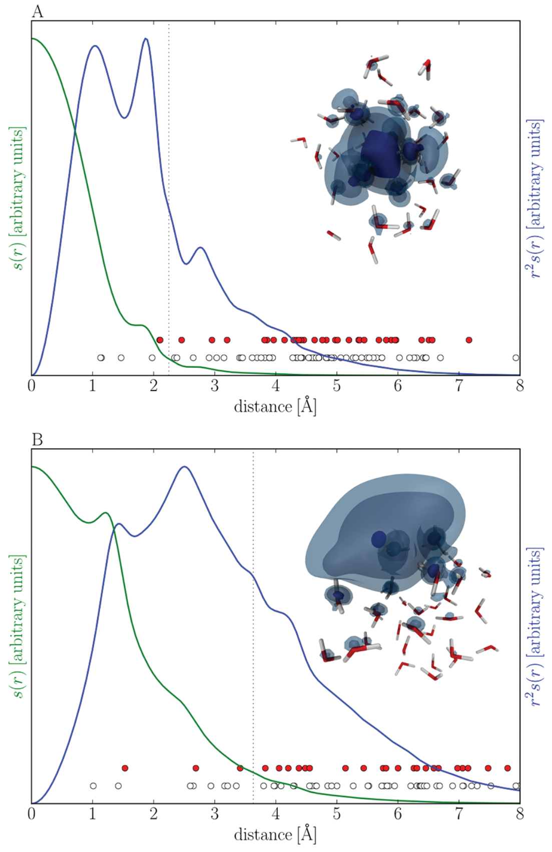

FIGURE 1. Snapshots and radial density of the excess electron as a function of the distance from its center averaged (green) and integrated (blue) over the angular variables for (A) a configuration with a well-developed cavity taken from an equilibrium simulation at $T = 300$ K and (B) a configuration sampled soon after attachment to a cold (30 K) water cluster with the electron on the surface of the cluster in a cushion-like state. Dashed vertical line shows the radius of gyration of the electron. Red and white dots show the positions of the oxygen and hydrogen atoms, respectively.

3. Structural Aspects of Hydrated Electrons

The structure of an excess electron equilibrated in a liquid 32-water cluster at 300 K is presented in Figure 1A.[21] Simply scrutinizing the snapshot, which displays the water molecules and the unpaired spin density corresponding to the excess electron at three different isodensity values,[22] leads to the conclusion that the electron occupies a cavity at the

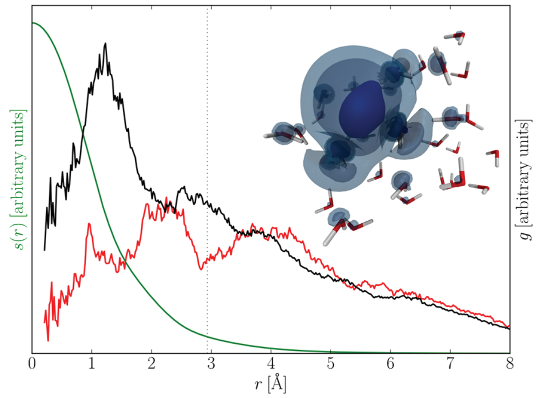

FIGURE 2. Radial density of the excess electron averaged over the angular variables (green) and radial distribution function of water oxygen (red) and hydrogen (black) atoms relative to the center of the excess electron from equilibrium configurations at $T = 300$ K.

exterior region of the cluster. However, this cavity is quantitatively different from that formed by atomic anions. In both cases, the water cavity is polarized, with water molecules pointing one of their hydrogen atoms inside. However, since the excess electron density is "softer" than that of negative ions due to the lack of a positive nucleus, it more readily deforms from the spherical shape and water molecules can penetrate deeper into it. This is also seen from the radial density of the excess electron and the positions of the water molecules (Figure 1A), where there is sizable overlap between the solvated electron and the nearest ∼4 water molecules. When the excess electron is attached to a cold amorphous solid 32-water cluster at 30−50 K, the situation is very different.[21,22] The electron slightly reorients water molecules at the surface of the cluster; however, a cavity cannot be formed at these cryogenic conditions. The result is a rather surface-delocalized "cushion-like" excess electron at the periphery of the cluster (Figure 1B).

The statistically averaged (over 25 ps equilibrium trajectory at 300 K) structure of the excess electron cavity and its radial density at ambient conditions is depicted in Figure 2. These plots exemplify the overlap between the excess electron and the radial distributions of the hydrogen and oxygen atoms of the surrounding water molecules. The hydrogen distribution exhibits a peak ∼1.2 Å from the center of the electron, followed by an oxygen peak around 2−3 Å. Due to limited statistics (particularly at small distances), these curves are rather noisy; nevertheless, there is a large degree of similarity with analogous distribution functions from a recent pseudopotential model interpreted as a noncavity electron.[9] This is striking, since visual inspection and analysis of our spin densities present a rather convincing picture of an electron cavity, albeit a soft one, into which water molecules can easily penetrate.[21,36]

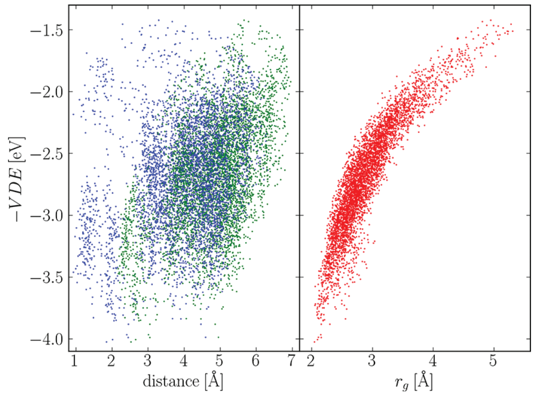

FIGURE 3. (Left) Lack of correlation between vertical detachment energy of the excess electron and its distance from the cluster (measured in two different ways) and (right) correlation between vertical detachment energy of the excess electron and its radius of gyration, both for equilibrium configurations at $T = 300$ K. On the left, data using the average distance of the electron from the cluster center of mass are shown in green, whereas those using the distance between the center of the electron and the cluster center of mass are shown in blue.

Suggestions have been made in the literature that VDE of the electron can be related to its position with respect to the solvating water system.[14,17] To a limited extent, this is substantiated. Namely, the "cushion-like" structures occurring in cryogenic clusters have small values of VDE and are always located at the exterior of the cluster.[14,15,21,22] However, the situation concerning the more strongly bound structures, which appear both in cryogenic solids[14,15] and in warmer aqueous systems,[17−20] is more complicated. Our DFT calculations,[21,36] as well as earlier pseudopotential calculations,[27,46,47] show that in general there is little correlation between VDE and position of the hydrated electron (Figure 3, left) and that strongly bound hydrated electrons can be found both in the interior and within the aqueous interface. There is, however, a remarkable inverse correlation between the size of the excess electron and its VDE: the smaller the electron, the more strongly bound it is (see Figure 3, left and also ref 48). Both DFT and pseudopotential calculations thus indicate that photoelectron spectroscopy is a powerful tool for determining the size of the excess electron rather than its position.

4. Dynamical Aspects of Hydrated Electrons

Electrons attached to neutral water clusters relax very differently at ambient conditions of 300 K and at cryogenic temperatures of 30−50 K. Figure 4A shows the time evolution of the radius of gyration of the excess electron for three

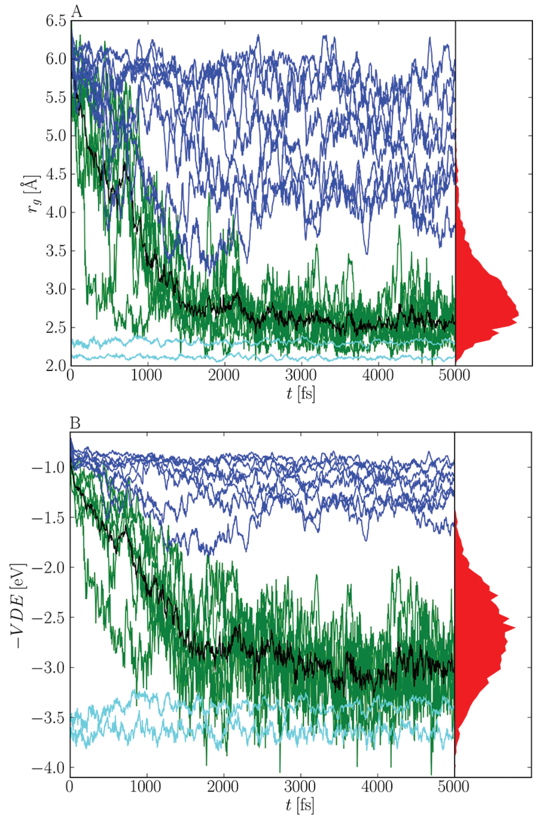

FIGURE 4. Time evolution of (A) radius of gyration and (B) vertical detachment energy of the excess electron for different simulation setups, together with the equilibrium distribution at $T = 300$ K (red). Simulations following electron attachment to cold (30−50 K) water clusters are shown in blue (8 trajectories). Simulations following electron attachment to water clusters at $T = 300$ K are shown in green (6 trajectories), and their average in black. Simulations of cold (30−50 K) anionic clusters with a preformed cavity are shown in cyan (2 trajectories).

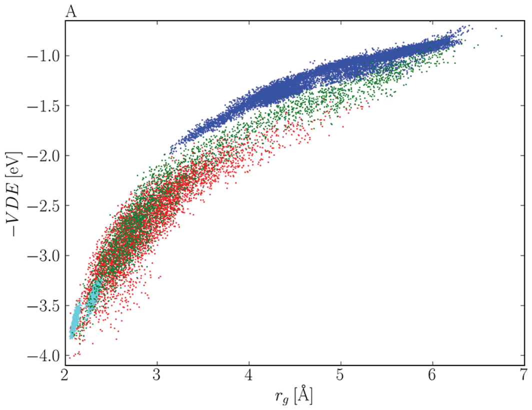

FIGURE 5. Correlation between vertical detachment energy of the excess electron and its radius of gyration for different simulation setups. Simulations following electron attachment to cold (30−50 K) water clusters are shown in blue (8 trajectories). Simulations following electron attachment to water clusters at $T = 300$ K are shown in green (6 trajectories). Simulations of cold (30−50 K) anionic clusters with a preformed cavity are shown in cyan (2 trajectories). Equilibrium simulations of anionic clusters at $T = 300$ K are shown in red.

different types of trajectories, and Figure 4B depicts the corresponding time evolution of the VDEs. In green, a set of trajectories corresponding to electron attachment to liquid water clusters at 300 K is presented. Initially, the electron is rather delocalized and weakly bound since the neutral cluster geometry is not particularly favorable for electron binding. However, the electron polarizes the surrounding aqueous environment very quickly, first rotating neighboring water molecules so that hydrogens point to it and second building a cavity in the hydrogen bonding structure of the cluster. As a result, its size shrinks, VDE increases, and within ~1.5 ps properties of an equilibrated solvated electron (red distributions in Figure 4) are reached. It should be noted that DFT is only able to describe relaxation on the electronic ground state surface of the system. This may not fully capture the localization process, particularly its early stages, when the nuclear and excess electron dynamics may be happening on a comparable time scale. Nevertheless, the simulated localization times are comparable to the experimentally observed picosecond time scale relaxation of the excess electron in water.[6]

The localization process of electrons attached to cold (30−50 K) neutral clusters is depicted in blue in Figure 4. The initial stage of electron localization is similar to that in ambient clusters, albeit a bit slower. Within the first picosecond, the excess electron polarizes the surface water molecules and, as a result, it starts to shrink and becomes more strongly bound. While at ambient conditions the excess electron subsequently creates a cavity in the liquid water structure, this does not happen in the cold solid clusters. As a result, the electron remains trapped in metastable states less than halfway from the initial condition to a fully localized structure. The situation is very different if the excess electron is first equilibrated at 300 K and then cooled to cryogenic conditions (cyan lines in Figure 4). Upon cooling to 30−50 K, the electron becomes even more strongly bound and smaller in size than at 300 K. During subsequent dynamics at low temperature, virtually nothing happens with this structure. This indicates that strongly and weakly bound excess electrons can coexist in ensembles of cryogenic clusters depending on their way of formation, as observed in the experiment.[14,15]

The correlation between radius of gyration and VDE for the same data sets and using the same color coding as in

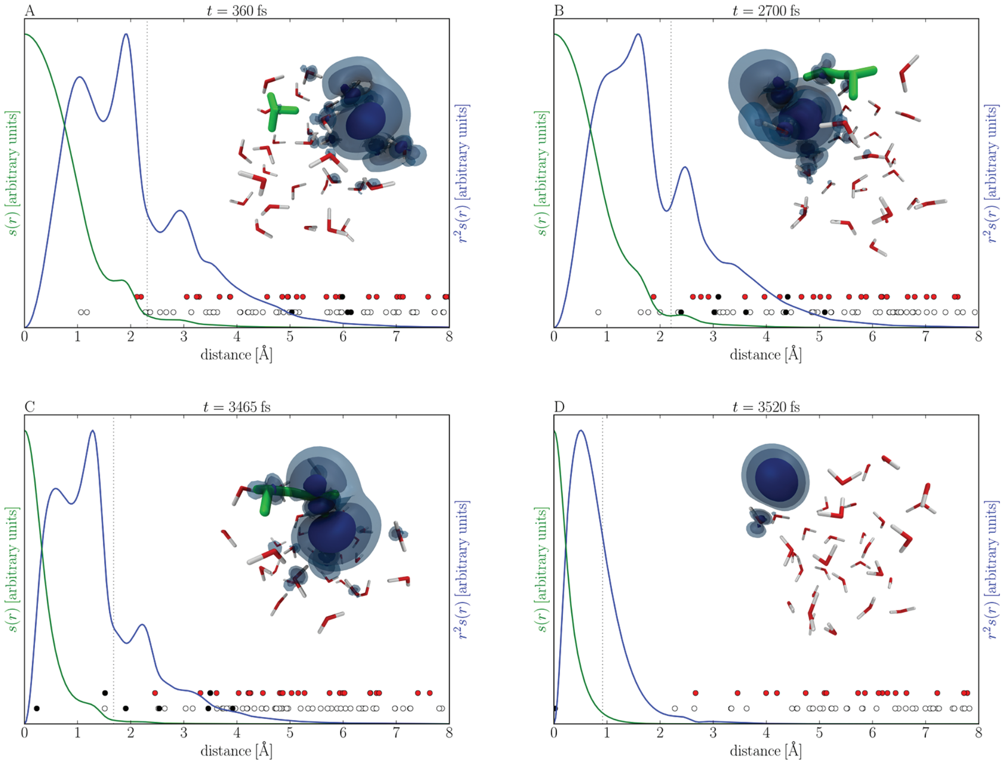

FIGURE 6. Radial density of the excess electron as a function of the distance from its center averaged (green) and integrated (blue) over the angular variables for configurations along a reactive trajectory. Dashed vertical line shows the radius of gyration of the electron. Red and white dots show the positions of the water oxygen and hydrogen atoms.

Figure 4 is presented in Figure 5. The first thing to note is the very good overlap between the equilibrium points and data from localization trajectories at 300 K. The only part that is missing from the equilibrium data corresponds to the strongly delocalized and loosely bound structures from the onsets of the localization trajectories. This region is close to that explored during cold localization at 30–50 K, except that the latter exhibits even weaker electron binding. This corresponds to the exterior "cushion-like" states which form at the surface of cold clusters. On the other side of the distribution, large binding energies and small sizes are signatures of equilibrated and consequently quenched electrons (cyan).

5. Reactivity of Hydrated Electrons

The excess electron in water is a chemically unstable entity which can react with various impurities and, very slowly, also with water itself.[4] An important quencher of the hydrated electron, in particular at acidic conditions, is the hydronium cation. The electron–proton reaction in water leading to formation of a hydrogen atom was shown experimentally to be slower than a purely diffusion limited process.[4,49] Also, measurements in deuterated water indicated that the reaction is a proton transfer to the solvated electron[49] rather than electron transfer to the hydronium cation connected with transient formation of a localized H_3O radical, as suggested earlier.[50] Note that the H_3O radical has also been invoked recently in rationalizing ground and excited state processes involving hydrated electrons.[51,52] However, in these studies, the key species is not a genuine radical with the spin localized at the H_3O moiety but rather a $H_3O^+ \cdots e^-_{aq}$ solvent-separated pair.[51,52]

We used AIMD to elucidate the detailed molecular mechanism of the electron–proton reaction in water. In order to prepare the reactants, we first equilibrated a 32-water system with an added proton and iodide anion. The latter was then replaced by an excess electron, which filled the iodide cavity, and the course of the reaction was then monitored for a set of trajectories.[37] In Figure 6, we analyze four snapshots along one of the reactive trajectories. The first snapshot, from the beginning of the trajectory, corresponds to a solvated electron which is only weakly perturbed by the presence of the hydronium cation at a distance of 4–5 Å (compare to equilibrated solvated electron in

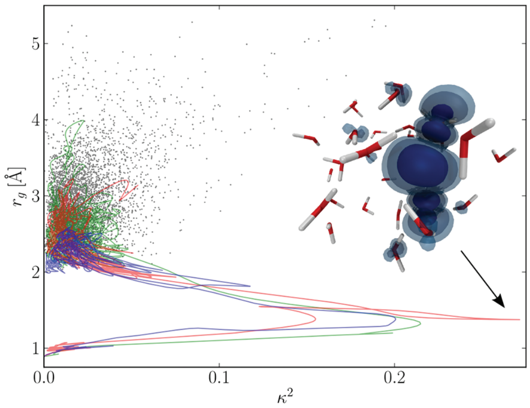

FIGURE 7. Correlation between radius of gyration and relative shape anisotropy of the excess electron for three reactive trajectories. Data from equilibrium simulations of the anionic cluster (i.e., without the excess proton) are shown for reference in gray.

Figure 1A). Subsequently, the proton moves close to the water shell around the excess electron (Figure 6B). However, it does not react immediately but rather moves around this shell by proton hopping for more than a picosecond, confirming that the electron–proton reaction in water is not diffusion limited.[4,49] Only after a suitable perturbation in the solvent shell occurs or is induced by the proton (Figure 6C), the reaction takes place and a hydrogen atom is formed (Figure 6D). The simulations also clearly show that it is the proton which moves to the hydrated electron, having a lower effective mass in water, in accord with the experimentally suggested proton transfer mechanism.[49]

Does the proton have to wait for a perturbation of the solvent shell of the excess electron or does it induce it? The answer is clear from Figure 7 which depicts the correlation between the radius of gyration of the excess electron and its relative shape anisotropy along three reactive trajectories (lines), compared to equilibrium simulation without the excess proton (dots). An equilibrated electron is only weakly asymmetric, except for instances when it is rather delocalized. These geometries are, however, not relevant for the reaction requiring simultaneous localization and distortion of the excess electron, which only happens in the presence of the hydronium cation. For a successful reaction, it is necessary that one water molecule penetrates deep into the excess electron density and donates a proton, which then becomes the nucleus of the newly formed hydrogen atom. At the same time, this donating water molecule acquires the excess proton, its integrity being preserved.

6. Method Development

From the methodological point of view, providing an accurate picture of the solvated electron is an interesting and open challenge. When one of the prime targets is the study of its reactivity in the bulk liquid, only electronic structure methods that are able to describe the dynamics of hundreds of atoms in periodic boundary conditions are ultimately suitable. However, several problems have to be solved in order to reliably describe the subtle balance between localized and delocalized electronic states.

Approximate variants of density functional theory, in particular the computationally efficient generalized gradient approximations (GGA) employed in our work, are known to suffer from the self-interaction error. This error, which is more severe for systems with unpaired electrons, tends to artificially delocalize electronic states. It can be partially corrected for using a self-interaction correction (SIC) which, in a recent formulation, is only applied to the unpaired electron and scaled to reproduce benchmark results.[41] Depending on the parametrization (we mostly used the standard values of $a = 0.2$ and $b = 0$[41]), the SIC causes an overestimation of the VDE, which is most likely caused by the imbalance introduced by applying this correction only to the anionic state in the VDE calculation. This, however, changes little on the fact that the description of the structure and dynamics of the hydrated electron should be improved by introducing the SIC. As a matter of fact, the effect of SIC on the structure and dynamics of the hydrated electron is modest; however, it becomes crucial for the description of its reactivity. For example, the electron–proton reaction toward the hydrogen atom does not run in water with GGA functionals without SIC.[37]

A second important technical aspect is the choice of the basis set. In CP2K, one uses an auxiliary plane-wave basis set and a primary Gaussian basis set which has to be sufficiently flexible and diffuse. For example, localized interior states can be more easily described with an atom-centered basis than delocalized surface states, and as such will be favored unless a suitable basis is employed. Three basis sets have been tested: a split valence basis set with diffuse functions (aug-TZV2P), a molecularly optimized basis set which contracts diffuse primitives with tighter valence orbitals (molopt-TZV2P), and a combination of the molopt-TZV2P basis with a regular grid of Gaussian basis function. The latter two basis sets do not suffer from linear dependencies and are thus more suitable and more efficient for MD simulations of large systems, especially in periodic boundary conditions.

However, only with the addition of the Gaussian grid functions within a 10−13 Å cutoff (500−750 basis functions), a faithful description (equivalent to the use of the aug-TZV2P basis) of the diffuse surface bound electron can be obtained.

In future work, we plan to extend our studies to the properties and reactivity of the electron in the aqueous bulk and address new challenges which may arise there. The first challenge will be the significant size effects that can be expected for the simulation of charged species and estimating VDE in periodic boundary conditions. Also, investigating reactions of the solvated electron with radicals (rather than with a closed-shell hydronium cation) will introduce another level of complexity in the electronic structure. Indeed, these systems are open-shell singlet biradicals having a multiconfigurational character. Since multiconfigurational wave function approaches are currently computationally intractable for large systems, this calls for DFT functionals with terms specifically describing static correlation.

7. Conclusions

We employed ab initio molecular dynamics to characterize the structure, dynamics, and reactivity of an excess electron solvated in water. Using a negatively charged 32-water cluster as a model system, we reached the following principal conclusions:

(i) At ambient conditions, the excess electron resides in a cavity close to the surface of the cluster. This cavity is softer and more flexible than that around atomic anions, and water molecules penetrate rather deep into it, underscoring the importance of all (valence) electron description of the system which includes exchange interactions.

(ii) The process of electron attachment to a neutral water system and subsequent localization is very different at ambient versus cryogenic conditions. In the former, liquid, system, the cluster quickly reaches an equilibrated structure which corresponds to a well localized and strongly bound solvated electron. However, in the latter, solid, system, the electron gets trapped in a metastable "cushion-like" state at the periphery of the cluster, which is more weakly bound. Strongly bound states are observed in the cryogenic solid only if initially prepared at ambient conditions and subsequently quenched. This rationalizes the observation of several isomers in cryogenic cluster experiments and raises a question mark over extrapolations of excess electron properties from these clusters to the liquid bulk.

(iii) The electron−proton reaction in water, as the simplest example of chemical quenching of the solvated electron, is shown to be, unlike in the gas phase, a complex many-body process. Adding more detail to the general experimentally derived mechanism, we demonstrate that the reaction is not diffusion limited and it is a proton transfer rather than electron transfer process where a localized H_3O radical does not play a role of a key intermediate. The rate-limiting step of the reaction is a deformation of the excess electron induced by the hydronium cation within which a single water molecule penetrates deep into the electron cavity.

As a final note, we mention that after submission of this Account a new AIMD study of an electron attached to a cluster containing 105 water molecules has been published.[53] Despite the fact that the system is almost three times bigger than that investigated in our group (and the DFT method employed is similar but not identical), the results are qualitatively the same. Namely, the authors of the new study also found a stable localized cavity electron, the binding energy of which does not strongly depend on its position within the cluster, as well as a weakly bound delocalized electron, which is kinetically trapped at the cold cluster surface (see Figure 3 in ref 53). These findings, together with earlier pseudopotential calculations performed for large clusters and extended systems,[9,23−28] support our claim that the results for the 32-water cluster anion presented here have direct implications also for electron solvated in larger aqueous systems.

Support from the Czech Science Foundation (Grants 203/08/0114), the Czech Ministry of Education (Grant LC512), and the Academy of Sciences (Praemium Academie) is gratefully acknowledged. O.M. and F.U. acknowledge support from the IMPRS Dresden.

BIOGRAPHICAL INFORMATION

Ondrej Marsalek was born in 1981. In 2008, he received a master's degree in theoretical physics at the Faculty of Mathematics and Physics, Charles University in Prague. Since 2008, he has been a doctoral student in the group of Pavel Jungwirth at the Institute of Organic Chemistry and Biochemistry of the Academy of Sciences of the Czech Republic.

Frank Uhlig was born in 1985. He received a Bachelor of Science from the Faculty of Chemistry at the University of Leipzig in 2008 and a Master of Science at the same institution in 2010. He is currently a doctoral student in the group of Pavel Jungwirth at the

Institute of Organic Chemistry and Biochemistry of the Academy of Sciences of the Czech Republic.

Joost VandeVondele was born in 1975. He obtained a degree in engineering physics at the University of Ghent in Belgium. He received his doctoral degree in natural sciences from the ETH Zurich. As a postdoctoral fellow at the universities of Zurich and Cambridge, he became one of the leading developers of the CP2K simulation package. His current research in the Institute of Physical Chemistry at the University of Zurich targets the development and application of new tools for accurate simulations of large and complex systems.

Pavel Jungwirth graduated in physics from the Charles University in Prague and completed his doctoral thesis in computational chemistry in 1993. During 1994–1995 he was a Golda Meir Fellow at the Hebrew University in Jerusalem and a postdoc at the University of California at Irvine. During 1995–2003 he was a research group leader at the Heyrovský Institute and in 2004 he moved with his group to the Institute of Organic Chemistry and Biochemistry of the Academy of Sciences in Prague. Since 2000 he is also an Associate Professor at the Charles University (full professor since 2011). In 2009 he was elected a member of the Learned Society of the Czech Republic. He has educated more than a dozen Ph.D. and M.S. students in computational chemistry, focusing primarily on modeling of ions at biologically and atmospherically relevant aqueous interfaces.

FOOTNOTES

*To whom correspondence should be addressed. E-mail: pavel.jungwirth@uochb.cas.cz.

REFERENCES

1 Gibson, G. E.; Argo, W. L. The Absorption Spectra of the Blue Solutions of Certain Alkali and Alkaline Earth Metals in Liquid Ammonia and in Methylamine. *J. Am. Chem. Soc.* **1918**, *40*, 1327–1361.

2 Cotton, F. A.; Wilkinson, G. *Advanced Inorganic Chemistry*; John Wiley & Sons: New York, 1988.

3 Hart, E. J.; Boag, J. W. Absorption Spectrum of Hydrated Electron in Water and in Aqueous Solutions. *J. Am. Chem. Soc.* **1962**, *84*, 4090–4095.

4 Garrett, B. C. e. a. Role of water in electron-initiated processes and radical chemistry: Issues and scientific advances. *Chem. Rev.* **2005**, *105*, 355–389.

5 Bartels, D. M.; Cook, A. R.; Mudaliar, M.; Jonah, C. D. Spur decay of the solvated electron in picosecond radiolysis measured with time-correlated absorption spectroscopy. *J. Phys. Chem. A* **2000**, *104*, 1686–1691.

6 Kambhampati, P.; Son, D. H.; Kee, T. W.; Barbara, P. F. Solvation dynamics of the hydrated electron depends on its initial degree of electron delocalization. *J. Phys. Chem. A* **2002**, *106*, 2374–2378.

7 Chen, X. Y.; Bradforth, S. E. The ultrafast dynamics of photodetachment. *Annu. Rev. Phys. Chem.* **2008**, *59*, 203–231.

8 Shkrob, I. A. The structure of the hydrated electron. Part 1. Magnetic resonance of internally trapping water anions: A density functional theory study. *J. Phys. Chem. A* **2007**, *111*, 5223–5231.

9 Larsen, R. E.; Glover, W. J.; Schwartz, B. J. Does the Hydrated Electron Occupy a Cavity? *Science* **2010**, *329*, 65–69.

10 Turi, L.; Madarasz, A. Comment on "Does the Hydrated Electron Occupy a Cavity? *Science* **2011**, *331*, 1387.

11 Jacobson, L. D.; Herbert, J. M. Comment on "Does the Hydrated Electron Occupy a Cavity? *Science* **2011**, *331*, 1387–d.

12 Coe, J. V.; Lee, G. H.; Eaton, J. G.; Arnold, S. T.; Sarkas, H. W.; Bowen, K. H.; Ludewigt, C.; Haberland, H.; Worsnop, D. R. Photoelectron-Spectroscopy of Hydrated Electron Cluster Anions, $(H_2O)^-_{n=2-69}$. *J. Chem. Phys.* **1990**, *92*, 3980–3982.

13 Hammer, N. I.; Shin, J. W.; Headrick, J. M.; Diken, E. G.; Roscioli, J. R.; Weddle, G. H.; Johnson, M. A. How do small water clusters bind an excess electron? *Science* **2004**, *306*, 675–679.

14 Verlet, J. R. R.; Bragg, A. E.; Kammrath, A.; Cheshnovsky, O.; Neumark, D. M. Observation of large water-cluster anions with surface-bound excess electrons. *Science* **2005**, *307*, 93–96.

15 Ma, L.; Majer, K.; Chirot, F.; von Issendorff, B. Low temperature photoelectron spectra of water cluster anions. *J. Chem. Phys.* **2009**, *131*, 144303.

16 Sommerfeld, T.; Jordan, K. D. Electron binding motifs of $(H_2O)_n^-$ clusters. *J. Am. Chem. Soc.* **2006**, *128*, 5828–5833.

17 Siefermann, K. R.; Liu, Y. X.; Lugovoy, E.; Link, O.; Faubel, M.; Buck, U.; Winter, B.; Abel, B. Binding energies, lifetimes and implications of bulk and interface solvated electrons in water. *Nat. Chem.* **2010**, *2*, 274–279.

18 Shreve, A. T.; Yen, T. A.; Neumark, D. M. Photoelectron spectroscopy of hydrated electrons. *Chem. Phys. Lett.* **2010**, *493*, 216–219.

19 Tang, Y.; Shen, H.; Sekiguchi, K.; Kurahashi, N.; Mizuno, T.; Suzuki, Y. I.; Suzuki, T. Direct measurement of vertical binding energy of a hydrated electron. *Phys. Chem. Chem. Phys.* **2010**, *12*, 3653–3655.

20 Sagar, D. M.; Bain, C. D.; Verlet, J. R. R. Hydrated Electrons at the Water/Air Interface. *J. Am. Chem. Soc.* **2010**, *132*, 6917–6919.

21 Marsalek, O.; Uhlig, F.; Frigato, T.; Schmidt, B.; Jungwirth, P. Dynamics of Electron Localization in Warm versus Cold Water Clusters. *Phys. Rev. Lett.* **2010**, *105*, 043002.

22 Marsalek, O.; Uhlig, F.; Jungwirth, P. Electrons in Cold Water Clusters: An ab Initio Molecular Dynamics Study of Localization and Metastable States. *J. Phys. Chem. C* **2010**, *114*, 20489–20495.

23 Barnett, R. N.; Landman, U.; Cleveland, C. L.; Jortner, J. Electron Localization in Water Clusters 0.1. Electron-Water Pseudopotential. *J. Chem. Phys.* **1988**, *88*, 4421–4428.

24 Barnett, R. N.; Landman, U.; Cleveland, C. L.; Jortner, J. Electron Localization in Water Clusters 0.2. Surface and Internal States. *J. Chem. Phys.* **1988**, *88*, 4429–4447.

25 Barnett, R. N.; Landman, U.; Scharf, D.; Jortner, J. Surface and Internal Excess Electron-States in Molecular Clusters. *Acc. Chem. Res.* **1989**, *22*, 350–357.

26 Nicolas, C.; Boutin, A.; Levy, B.; Borgis, D. Molecular simulation of a hydrated electron at different thermodynamic state points. *J. Chem. Phys.* **2003**, *118*, 9689–9696.

27 Turi, L.; Sheu, W. S.; Rossky, P. J. Characterization of excess electrons in water-cluster anions by quantum simulations. *Science* **2005**, *309*, 914–917.

28 Sommerfeld, T.; DeFusco, A.; Jordan, K. D. Model Potential Approaches for Describing the Interaction of Excess Electrons with Water Clusters: Incorporation of Long-Range Correlation Effects. *J. Phys. Chem. A* **2008**, *112*, 11021–11035.

29 Jacobson, L. D.; Herbert, J. M. A one-electron model for the aqueous electron that includes many-body electron-water polarization: Bulk equilibrium structure, vertical electron binding energy, and optical absorption spectrum. *J. Chem. Phys.* **2010**, *133*, 154506.

30 Madarasz, A.; Rossky, P. J.; Turi, L. Response of Observables for Cold Anionic Water Clusters to Cluster Thermal History. *J. Phys. Chem. A* **2010**, *114*, 2331–2337.

31 Shkrob, I. A.; Glover, W. J.; Larsen, R. E.; Schwartz, B. J. The structure of the hydrated electron. Part 2. A mixed quantum/classical molecular dynamics embedded cluster density functional theory: Single-excitation configuration interaction study. *J. Phys. Chem. A* **2007**, *111*, 5232–5243.

32 Herbert, J. M.; Head-Gordon, M. First-principles, quantum-mechanical simulations of electron solvation by a water cluster. *Proc. Natl. Acad. Sci. U.S.A.* **2006**, *103*, 14282–14287.

33 Xu, J.; Jordan, K. D. Application of the Diffusion Monte Carlo Method to the Binding of Excess Electrons to Water Clusters. *J. Phys. Chem. A* **2010**, *114*, 1364–1366.

34 Boero, M. Excess electron in water at different thermodynamic conditions. *J. Phys. Chem. A* **2007**, *111*, 12248–12256.

35 Renault, J. P.; Vuilleumier, R.; Pommeret, S. Hydrated electron production by reaction of hydrogen atoms with hydroxide ions: A first-principles molecular dynamics study. *J. Phys. Chem. A* **2008**, *112*, 7027–7034.

36 Frigato, T.; VandeVondele, J.; Schmidt, B.; Schutte, C.; Jungwirth, P. Ab initio molecular dynamics simulation of a medium-sized water cluster anion: From an interior to a surface-located excess electron via a delocalized state. *J. Phys. Chem. A* **2008**, *112*, 6125–6133.

37 Marsalek, O.; Frigato, T.; VandeVondele, J.; Bradforth, S. E.; Schmidt, B.; Schutte, C.; Jungwirth, P. Hydrogen Forms in Water by Proton Transfer to a Distorted Electron. *J. Phys. Chem. B* **2010**, *114*, 915–920.

38 Boero, M.; Parrinello, M.; Terakura, K.; Ikeshoji, T.; Liew, C. C. First-principles molecular-dynamics simulations of a hydrated electron in normal and supercritical water. *Phys. Rev. Lett.* **2003**, *90*, 226403.

39 Herbert, J. M.; Head-Gordon, M. Calculation of electron detachment energies for water cluster anions: An appraisal of electronic structure methods, with application to $(H_2O)_{20}$ and $(H_2O)_{24}$. *J. Phys. Chem. A* **2005**, *109*, 5217–5229.

40 Grimme, S. Semiempirical GGA-type density functional constructed with a long-range dispersion correction. *J. Comput. Chem.* **2006**, *27*, 1787–1799.

41 VandeVondele, J.; Sprik, M. A molecular dynamics study of the hydroxyl radical in solution applying self-interaction-corrected density functional methods. *Phys. Chem. Chem. Phys.* **2005**, *7*, 1363–1367.

42 VandeVondele, J.; Hutter, J. Gaussian basis sets for accurate calculations on molecular systems in gas and condensed phases. *J. Chem. Phys.* **2007**, *127*, 114105.

43 Goedecker, S.; Teter, M.; Hutter, J. Separable dual-space Gaussian pseudopotentials. *Phys. Rev. B* **1996**, *54*, 1703–1710.

44 Genovese, L.; Deutsch, T.; Neelov, A.; Goedecker, S.; Beylkin, G. Efficient solution of Poisson's equation with free boundary conditions. *J. Chem. Phys.* **2006**, *125*, 074105.

45 VandeVondele, J.; Krack, M.; Mohamed, F.; Parrinello, M.; Chassaing, T.; Hutter, J. QUICKSTEP: Fast and accurate density functional calculations using a mixed Gaussian and plane waves approach. *Comput. Phys. Commun.* **2005**, *167*, 103–128.

46 Bartels, D. M. Moment analysis of hydrated electron cluster spectra: Surface or internal states? *J. Chem. Phys.* **2001**, *115*, 4404–4405.

47 Madarasz, A.; Rossky, P. J.; Turi, L. Interior- and surface-bound excess electron states in large water cluster anions. *J. Chem. Phys.* **2009**, *130*, 124319.

48 Turi, L.; Madarasz, A.; Rossky, P. J. Excess electron localization sites in neutral water clusters. *J. Chem. Phys.* **2006**, *125*, 014308.

49 Han, P.; Bartels, D. M. H/D Isotope Effects in Water Radiolysis. 4. The Mechanism of $(H)_{aq} \rightleftharpoons (e^-)_{aq}$ Interconversion. *J. Phys. Chem.* **1992**, *96*, 4899–4906.

50 Hart, E.; Anbar, M. *The hydrated electron*; Wiley-Interscience: New York, 1970.

51 Sobolewski, A. L.; Domcke, W. Computational studies of aqueous-phase photochemistry and the hydrated electron in finite-size clusters. *Phys. Chem. Chem. Phys.* **2007**, *9*, 3818–3829.

52 Poterya, V.; Fedor, J.; Pysanenko, A.; Tkac, O.; Lengyel, J.; Oncak, M.; Slavicek, P.; Farnik, M. Photochemistry of HI on argon and water nanoparticles: Hydronium radical generation in HI(H2O)n. *Phys. Chem. Chem. Phys.* **2011**, *13*, 2250–2258.

53 Barnett, R. N.; Giniger, R.; Cheshnovsky, O. Dielectron attachment and hydrogen evolution reaction in water clusters. *J. Phys. Chem. A* **2011**, *115*, 7378–7391.